EXPERIMENTAL EVALUATION OF A CARBON SLURRY DROPLET
COMBUSTION MODEL

Gerald A. Szekely, Jr.

Technical Memorandum
File No. TM 81-253
December 14, 1981
Contract No. N00024-79-C-6043

Copy No. _6_

The Pennsylvania State University
Intercollege Research Programs and Facilities
APPLIED RESEARCH LABORATORY
Post Office Box 30
State College, PA 16801

APPROVED FOR PUBLIC RELEASE
DISTRIBUTION UNLIMITED

NAVY DEPARTMENT

NAVAL SEA SYSTEMS COMMAND

REPORT DOCUMENTATION PAGE

1. REPORT NUMBER	2. GOVT ACCESSION NO.	3. RECIPIENT'S CATALOG NUMBER
TM 81-253	AD-A112 379	

4. TITLE (and Subtitle)	5. TYPE OF REPORT & PERIOD COVERED
EXPERIMENTAL EVALUATION OF A CARBON SLURRY DROPLET COMBUSTION MODEL	Ph.D., Thesis, March 1982
	6. PERFORMING ORG. REPORT NUMBER
	TM 81-253

7. AUTHOR(s)	8. CONTRACT OR GRANT NUMBER(s)
Gerald A. Szekely, Jr.	N00024-79-C-6043

9. PERFORMING ORGANIZATION NAME AND ADDRESS	10. PROGRAM ELEMENT, PROJECT, TASK AREA & WORK UNIT NUMBERS
The Pennsylvania State University Applied Research Laboratory, P.O. Box 30 State College, PA 16801	

11. CONTROLLING OFFICE NAME AND ADDRESS	12. REPORT DATE
Naval Sea Systems Command	December 14, 1981
Department of the Navy	13. NUMBER OF PAGES
Washington, DC 20362	265 pages

14. MONITORING AGENCY NAME & ADDRESS(if different from Controlling Office)	15. SECURITY CLASS. (of this report)
	Unclassified, Unlimited
	15a. DECLASSIFICATION/DOWNGRADING SCHEDULE

16. DISTRIBUTION STATEMENT (of this Report)

Approved for public release, distribuiton unlimited,
per NSSC (Naval Sea Systems Command), 6/23/81.

17. DISTRIBUTION STATEMENT (of the abstract entered in Block 20, if different from Report)

18. SUPPLEMENTARY NOTES

19. KEY WORDS (Continue on reverse side if necessary and identify by block number)

thesis, combustion, carbon, slurry, droplets

20. ABSTRACT (Continue on reverse side if necessary and identify by block number)

A theoretical and experimental investigation of the combustion process of carbon slurry fuels is described. The combustion of individual drops (400-1000 μm in diameter) supported at various positions within an open turbulent diffusion flame was observed. When a slurry drop was exposed to the flame, the liquid fuel evaporated in the first stage of the process leaving a porous carbon agglomerate formed from the carbon particles in the slurry. The second stage involved heat-up and reaction or quenching of the agglomerate. Consumption of the agglomerate
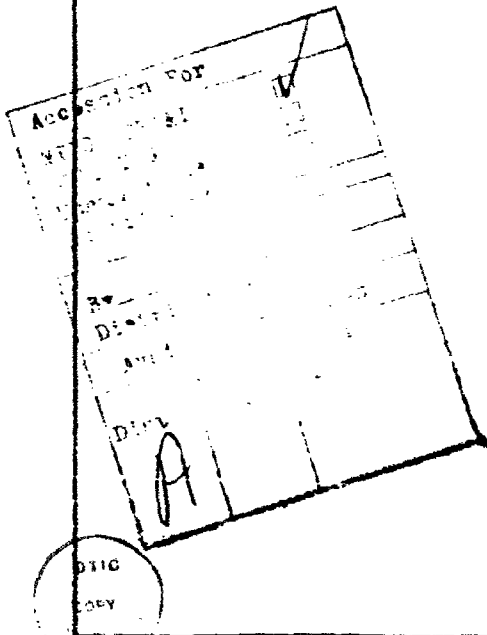
DD $_{1 \text{ JAN } 73}^{\text{FORM}}$ 1473   EDITION OF 1 NOV 65 IS OBSOLETE

was the slowest step in the process, requiring 90-95 percent of the drop life-time, even in regions where maximum agglomerate reaction rates were observed. An analysis was developed to provide predictions of both liquid and agglomerate heat-up and reaction. Area-reactivity factors were used in the carbon-agglom-erate reaction analysis to account for the effects of pores, reaction within the particle, intrinsic variations of carbon-black reactivity and catalysts. Transport-rate enhancement factors were also employed in the carbon-agglomerate reaction analysis to account for the increased mass and energy transport due to the flow percolating through the open porous structure of the carbon agglomerate. Two separate models were examined. The first considered oxygen and hydroxal reacting with carbon, and the second involved oxygen, carbon dioxide and water vapor reacting with carbon. The analysis yielded good predictions of both particle size and temperature variations for flame equivalence ratios of 0.272-1.350. The use of a catalyzed slurry was found to increase agglomerate burning rates in the lean portions of the flame, extending the lean limit of agglomerate reaction.

A laminar-premixed flame apparatus was also constructed, in order to examine the variation of the empirical factors over a broader range of test conditions. These tests emphasized smaller freely moving particles, more representative of practical slurry sprays, and test conditions in the kinitically-controlled regime. The apparatus consisted of a particle generator which produced a stream of carbon agglomerate particles, with initial initial diameters in the 10-100 μm range, which passed through the post flame region of a flat-flame burner. Measurements were made of particle size, mass, temperature and velocity as a function of position above the burner.

A relationship between apparent particle density and reacted-mass fraction was obtained which was relatively independent of particle size and local particle environment. The variation of both the transport-enhancement factors and the area-reactivity multiplication factors, for both reaction mechanisms, were found to depend on particle diameter and reacted-mass fraction to some degree. However, constant values similar to those found for the large supported particles, also yielded a reasonable correlation of the measurements. The burning rate increased with increasing flame temperature and with decreasing equivalence ratio.

ABSTRACT

A theoretical and experimental investigation of the combustion process of carbon slurry fuels is described. The combustion of individual drops (400-1000 μm in diameter) supported at various positions within an open turbulent diffusion flame was observed. When a slurry drop was exposed to the flame, the liquid fuel evaporated in the first stage of the process leaving a porous carbon agglomerate formed from the carbon particles in the slurry. The second stage involved heat-up and reaction or quenching of the agglomerate. Consumption of the agglomerate was the slowest step in the process, requiring 90-95 percent of the drop lifetime, even in regions where maximum agglomerate reaction rates were observed. An analysis was developed to provide predictions of both liquid and agglomerate heat-up and reaction. Area-reactivity factors were used in the carbon-agglomerate reaction analysis to account for the effects of pores, reaction within the particle, intrinsic variations of carbon-black reactivity, and catalysts. Transport-rate enhancement factors were also employed in the carbon-agglomerate reaction analysis to account for the increased mass and energy transport due to the flow percolating through the open porous structure of the carbon agglomerate. Two separate models were examined. The first considered oxygen and hydroxyl reacting with carbon, and the second involved oxygen, carbon dioxide and water vapor reacting with carbon. The analysis yielded good predictions of both particle size and

temperature variations for flame equivalence ratios of 0.272-1.350. The use of a catalyzed slurry was found to increase agglomerate burning rates in the lean portions of the flame, extending the lean limit of agglomerate reaction.

A laminar-premixed flame apparatus was also constucted, to examine the variation of the empirical factors over a broader range of test conditions. These tests emphasized smaller freely moving particles, more representative of practical slurry sprays, and test conditions in the kinetically-controlled regime. The apparatus consisted of a particle generator which produced a stream of carbon agglomerate particles, with initial initial diameters in the 10-100 µm range, which passed through the post-flame region of a flat-flame burner. Measurements were made of particle size, mass, temperature and velocity as a function of position above the burner.

A relationship between apparent particle density and reacted-mass fraction was obtained which was relatively independent of particle size and local particle environment. The variation of both the transport-enhancement factors and the area-reactivity multiplication factors, for both reaction mechanisms, were found to depend on particle diameter and reacted-mass fraction to some degree. However, constant values similar to those found for the large supported particles, also yielded a reasonable correlation of the measurements. The burning rate increased with increasing flame temperature and with decreasing equivalence ratio.

TABLE OF CONTENTS

TABLE OF CONTENTS (Continued)

TABLE OF CONTENTS (Continued)

LIST OF TABLES

LIST OF FIGURES

LIST OF FIGURES (Continued)

LIST OF FIGURES (Continued)

LIST OF FIGURES (Continued)

LIST OF FIGURES (Continued)

LIST OF FIGURES (Continued)

NOMENCLATURE

Symbol	Description
a_i	Area-reactivity factor
A_i	Preexponential factor
B	Mass transfer potential
B_o	Oxidation transfer number
B_T	Heat transfer number
B_Y	Mass transfer number
B_{Y_c}	Combustion transfer number
C	Carbon
CO	Carbon monoxide
CO_2	Carbon dioxide
C_D	Drag coefficient
C_p	Specific heat
d	Flame jet diameter, equivalent diameter of an ellipsoid
d_p	Particle diameter
D	Effective binary diffusivity
E_i	Activation energy
h	Heat transfer coefficient
H_2	Diatomic hydrogen
H_2O	Water
i	Enthalpy
i_f	Enthalpy of formation
i_{fg}	Enthalpy of vaporization
k	Boltzmann constant

Symbol	Description
K	Dimensionless mass burning rate
K_e	Evaporation rate constant
K_{pi}	Equilibrium constant
K_{ri}	Reaction rate constant
Le	Lewis number
m	Total particle mass
m_i	Mass of species i in particle
$\dot{m}''$	Net mass flux
$\dot{m}''_i$	Mass flux of species i
$\dot{m}_t$	Total drop evaporation rate
M	Mixture molecular weight
M_i	Molecular weight of species i
n_i	Reaction order
Nu	Nusselt number parameter, Equation (3.10)
O_2	Diatomic oxygen
OH	Hydroxyl
P	Total pressure
P_i	Partial pressure of species i
Pr	Prandtl number
q''_c	Convective heat flux at particle surface
q''_r	Radiative heat flux at particle surface
r	Radial distance
R	Universal gas constant
Re	Reynolds number
R_i	Reaction rate of species i

Symbol	Description
Sc	Schmidt number
Sh	Sherwood number parameter, Equation (3.10)
t	Time
T	Temperature
u	Velocity
v	Element velocity from particle
x	Axial distance from exit of flame jet
X_i	Mole fraction of species i
Y_i	Mass fraction of species i
$\tilde{Y}_i$	Mass fraction of element i
α	Average property factor, Equation (3.1)
ϵ	Surface emissivity, reacted mass fraction
ϵ'	Characteristic energy
ϵ_i	Mass flux fraction
λ	Thermal conductivity
μ	Dynamic viscosity
μ_{ij}	Stoichiometric parameters, Equation (3.48)
ν	Kinematic viscosity
ν_i^0	Stoichiometric coefficient, Equation (3.25)
ρ	Density
σ	Stefan-Boltzmann constant, molecular diameter
ϕ	Equivalence ratio, generic property representing both temperature and species mass fractions
ϕ_{ij}	Parameter, Equation (A.3)
χ	Reaction parameter, Equation (3.52)
ψ	Transport-enhancement factor

Subscripts	Description
a	Nonfuel gas
avg	Average condition
b	Boiling point
c	Carbon
cr	Critical
e	Final
f	Liquid phase
F	Fuel
i	Initial
g	Gas phase
m	Mean
Max	Maximum condition
Min	Minimum condition
p	Particle surface
r	Radiative, resident, reduced
ref	Reference condition
s	Support probe, drop surface
T	Energy boundary
w	Surface of enclosure
o	Initial condition
∞	Surroundings of particle

Superscripts

—	Time-averaged quantity

ACKNOWLEDGMENTS

CHAPTER I

INTRODUCTION

1.1 General Statement of the Problem

A promising technology for coal utilization is to mix finely crushed carbon or coal in oil and then directly burn the resulting slurry in stationary combustors such as furnaces and boilers. This concept is attractive since it directly substitutes coal for oil as an energy source. Also, the crushing and mixing processes involved in the slurry preparation are far more economical than energy-expensive coal-liquefaction and gasification processes. Finally, the slurry is pumpable and can readily be used in conventional combustors with minimal equipment modifications.

In addition to economy, the high density of the combustible solid carbon gives the slurry a significantly higher volumetric energy density than conventional liquid fuels. Because of its high energy density, a carbon slurry is a very promising military fuel for air-breathing propulsion systems, such as cruise missiles, where compactness is an important design criterion [1].

In order to meet the high energy density requirements of cruise-missile applications a low-volatile, low-ash solid carbon fuel suspended in a high energy density liquid fuel was desired. The fuel proposed was a medium-thermal carbon black--liquid JP-10 mixture. JP-10 or exo-tetrahydrodi (cyclopentadiene) is a pure hydrocarbon with

the chemical formula of $C_{10}H_{16}$, and its properties and structure are given in Appendix A. A 50% by mass solid--50% by mass liquid fuel mixture is believed to be a good compromise between high energy density, greater than 50,000 MJ/m^3, and low viscosity to maintain the fuel's liquid characteristics [2]. The formulation would also have to contain additives to deflocculate the thermal black, stabilize the dispersion, and promote combustion [2].

The general combustion properties of carbon slurries have been examined in gas turbine combustors [2,3] and well-stirred reactors [4]. The substitution of slurries for liquid fuels in combustors, however, is not without problems. The liquid fuel tends to burn off before the medium-thermal black can ignite, especially in low-temperature combustors [2]. Furthermore, the carbon residue remaining after the liquid evaporates is difficult to burn out. Therefore, new combustion-chamber designs optimizing the combustor aerodynamics are required to accommodate the dual burning nature of slurry fuels [2].

The present study emphasized fundamental aspects of the carbon-slurry combustion problem by observing and analyzing the combustion properties of individual slurry drops. The droplet combustion process is fundamental to successful operation of a combustor since it affects the residence-time requirements and combustion efficiency. Thus, the combustion of carbon-slurry droplets has been studied under conditions which simulate those of a combustion chamber.

1.2 Description of Slurry Drop Combustion

Slurries have not been widely used in the past and the existing literature on their combustion characteristics is limited. A recent paper by Law et al. [5] reports some results on the combustion characteristics of single, supported coal slurry drops. Combustion was accomplished in still air under natural convection conditions. The slurry consisted of dried, 200 mesh, coal powder (coal type unidentified) in No. 2 heating oil. The drops were suspended from a small probe (initial drop diameters of 850-1250 µm) and ignited. The initial combustion process was fueled by the liquid. As the liquid continued to evaporate, small masses of material (presumably containing coal particles) were intermittently ejected from the drop. After all the oil had vaporized, the flame extinguished, leaving an irregularly shaped agglomerate of coal particles on the support. The mass of material remaining on the probe increased as the initial percentage of coal in the slurry was increased. For initial coal weight percentages greater than 15-20%, the mass of the coal agglomerate remaining after extinction reached 70-80% of the initial mass of coal in the drop.

Based on existing information on coal combustion [6-10], it is likely that persistent combustion of a coal-slurry drop in air involves three major processes: (1) evaporation and combustion of the liquid fuel, (2) devolatilization of the coal with subsequent oxidation, and (3) reaction of the remaining solid carbon-ash particle. In contrast, the present slurry fuels employ carbon black

as the solid phase; thus, a devolatilization stage is not expected. Judging from the results of Law et al. [5], carbon levels in the present test slurries are sufficiently high to result in significant agglomeration.

1.2.1 Preliminary Test Apparatus

In order to gain further insight into the combustion processes of a carbon-slurry droplet, a single fuel drop (50.4% dispersed carbon by weight in JP-10) suspended from a quartz fiber in still air was ignited with a match. As a baseline a pure JP-10 droplet was also burned in the same manner. The drop combustion process was observed with a 16 mm Photosonics, model 16-B, motion picture camera. The camera optics provided a 2:1 magnification. The camera was powered with a Kepco, SM 36-5 AM d.c. power supply. The framing rate was indicated with a timing light on the camera, activated with an Adtrol Electronic pulse generator, model 501. Kodak Plus-X reversal film was used for all tests.

Backlighting for shadowgraph measurements was provided by a Pek, model 401A, 75W mercury arc lamp. The light from the arc was collimated and directed toward the drop location. A diffuser screen was employed behind the drop to equalize the light intensity of the background. The background intensity was adjusted so that envelope flames around the drop could also be observed.

The film records were analyzed on a frame-by-frame basis, using a Vanguard motion picture analyzer. Photographs of objects of known size at the drop location provided a calibration of distances on the film.

Carbon residue left on the probe after combustion was examined with a scanning electron microscope (SEM), International Scientific Instruments, model M-7. Permanent records of the appearance of the residue were obtained with Polaroid film.

1.2.2 Preliminary Test Observations

The pure JP-10 drop burned in a conventional manner for a liquid fuel [11]. An envelope flame was observed around the droplet until all the fuel was consumed. After an initial heat-up period, the square of the droplet diameter decreased in a linear fashion, which is typical behavior for supported drops under natural convection conditions.

The initial phase of combustion of the slurry drops was similar to that of pure JP-10. An envelope flame was observed around the drop and the drop diameter decreased. This phase appeared to involve the combustion of the JP-10 in the slurry. However, after a time, the envelope flame was extinguished and a black residue remained on the probe. Although gravimetric measurements were not made, it appeared that most of the original solid carbon in the drop remained unburned.

A slurry with a catalyst to initiate carbon combustion was also burned. The catalyzed slurry drops exhibited the most interesting combustion behavior in air. A typical dark field motion picture for this case appears in Figure 1. The early frames clearly show the envelope flame around the drop persisting for nearly a second. After this flame was extinguished, a small amount of luminosity was present for a period of 2.8 s. Then the residue itself began to glow,
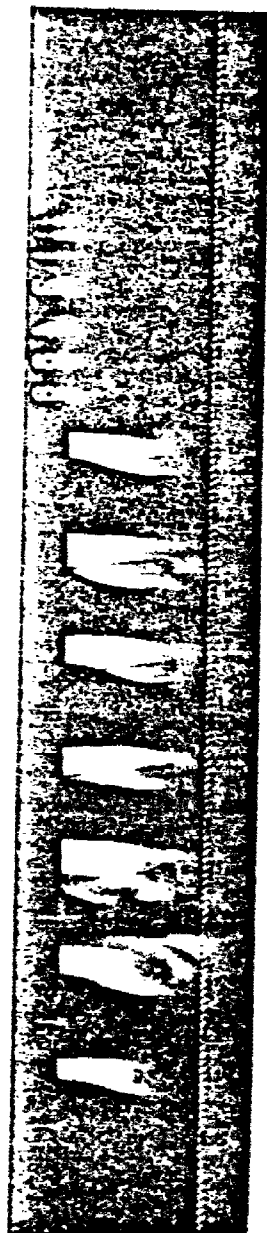
Timing Frequency = 100 Hz
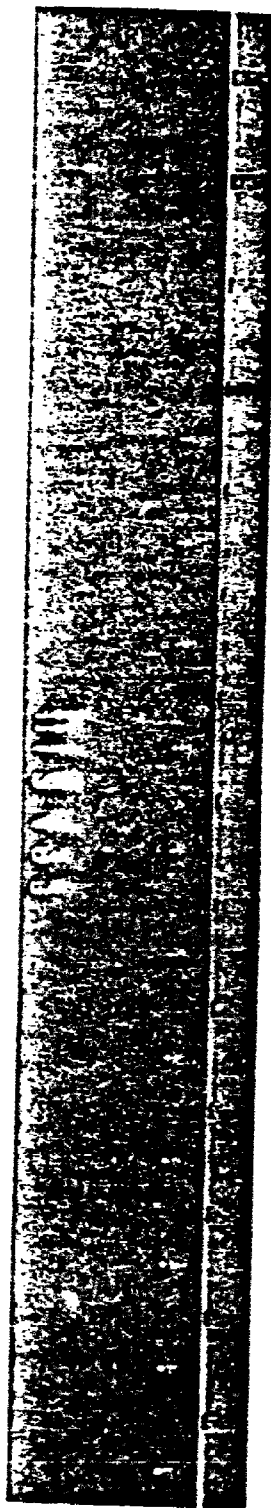
Figure 1. Dark field motion picture photographs of a catalyzed slurry droplet burning in air.

indicating reaction of the carbon. After a period of glowing (12.6 s, of which only the last 2.5 s are shown in the figure) the particle extinguished again, which left a carbon residue suspended from the probe.

The dark period prior to the glowing period probably involved reaction of the carbon, causing it to become heated. Glowing was observed where heating has proceeded to a temperature high enough for the particle to emit significant radiation in the wavelength range for which the photographic system is sensitive. Thus the absence of glowing is not necessarily indicative of no reaction, and even the uncatalyzed drop may have undergone significant reaction during the dark period.

These results indicate that the catalyst has an important effect on the carbon reaction rate. The catalyst increased the reactivity of the carbon, and thus combustion was sustained at higher rates in spite of heat losses to the surroundings, at least for a time. The slow step in the reaction process involved combustion of the carbon, which will be the controlling step during spray combustion in a practical combustion chamber.

These observations indicate that the overall behavior of the present carbon-slurry drops was qualitatively similar to the behavior observed for coal slurries [5]. In the present case, however, there was less disruption of the particles during combustion, probably due to the absence of the volatilization step for the solid.

Further insight concerning the slurry combustion mechanism was obtained by observing the carbon residue with the SEM. As a baseline, Figure 2a is a photograph of the residue from a catalyzed slurry drop, which was evaporated in air without combustion. In this case, the surface of the agglomerate is very smooth. The smoothness suggests that the particles in the slurry tend to pack together in a close array, with perhaps the smallest sized particles more prevalent at the surface.

A SEM photograph of the uncatalyzed slurry residue, after combustion in air, is shown in Figure 2b. In this case, the residue appears smooth in some regions and rough in others. The residue also appears to be partly hollow. It was difficult to prevent some disturbance of the sample while it was transported to and mounted in the SEM; therefore, the fractured zones may be due to handling problems. Certainly some areas are very similar to the appearance of the surface when no reaction occurred, e.g., as shown in Figure 2a. The rough areas could be typical of the subsurface structure in cases of little reaction or could result from consumption of smaller particles.

Figure 3a is an illustration of SEM photographs of the residue of the catalyzed slurry drop following combustion in air. This structure is very different from the preceding cases. The residue has a more open structure and no smooth regions are observed. The reaction of the solid appears to extend a significant distance below the outermost surface of the particle. The smallest elements, observed at a
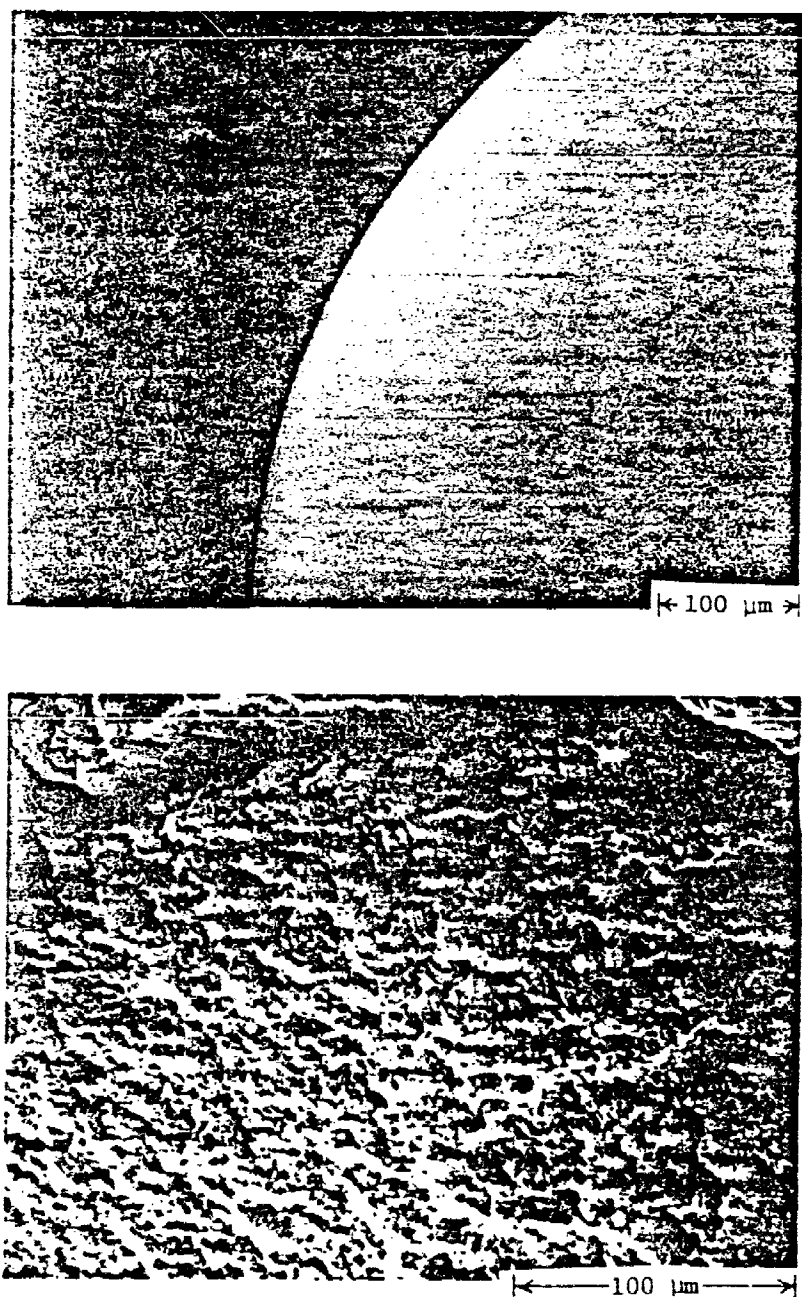
Figure 2.   SEM photographs of the carbon residue following
the evaporation in air of a catalyzed slurry
droplet (upper) and the combustion of an
uncatalyzed slurry droplet in air (lower).

|←200 μm→|

|←——100 μm——→|
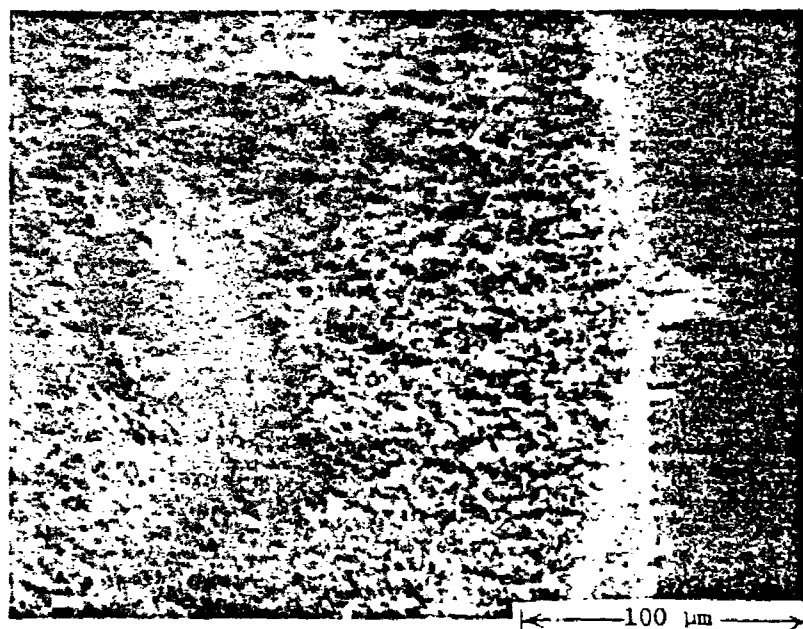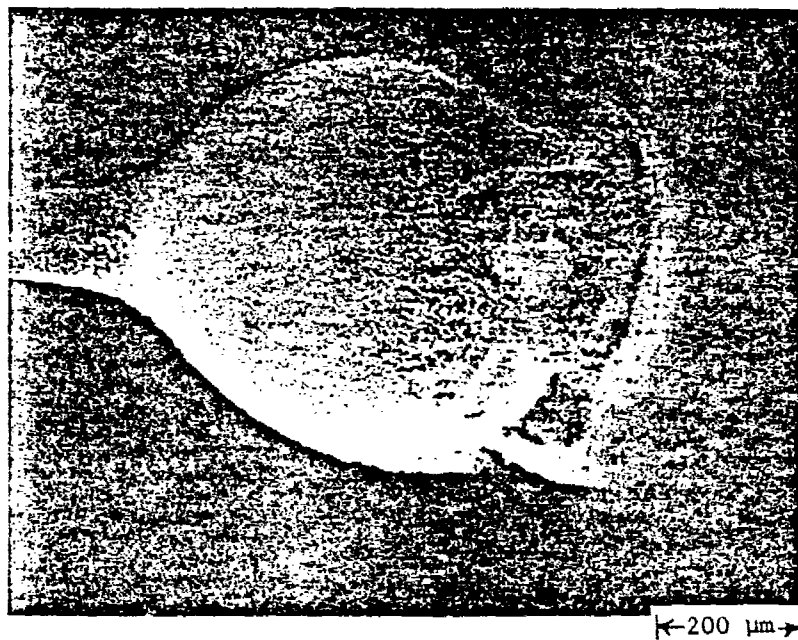
Figure 3. SEM photographs of the carbon residue following
the combustion of a catalyzed slurry droplet in air.

magnification of 10,000, appear to have a characteristic diameter of approximately 0.3 μm, which corresponds to the ultimate particle size of the slurry. These sub-elements are arranged in groups having a grape-cluster appearance. The protuberance visible in Figure 3b has a diameter of roughly 25 μm, which would be more typical of the residue from a drop produced under combustion-chamber conditions. It is evident that particles of this size are irregular in shape and relatively porous.

1.2.3 Burning Rates in Air

Figure 4 is an illustration of the variation of particle diameter as a function of time after ignition in air for three test fuels: pure JP-10, noncatalyzed slurry and catalyzed slurry. Throughout the suspended-particle test of this investigation, the reported particle diameter is the equivalent diameter of an ellipsoid having the same volume, i.e.,

$$d = (d_{min}^2 \; d_{max})^{1/3} \qquad (1.1)$$

where d is the reported diameter, and d_{max} and d_{min} are the major and minor diameters of the particle.

After ignition, the diameter of the pure JP-10 droplet decreased at an accelerated rate until all of the fuel was consumed. An envelope flame was observed to surround the liquid droplet as the diameter was decreasing. The slurry drops also exhibited a reduction
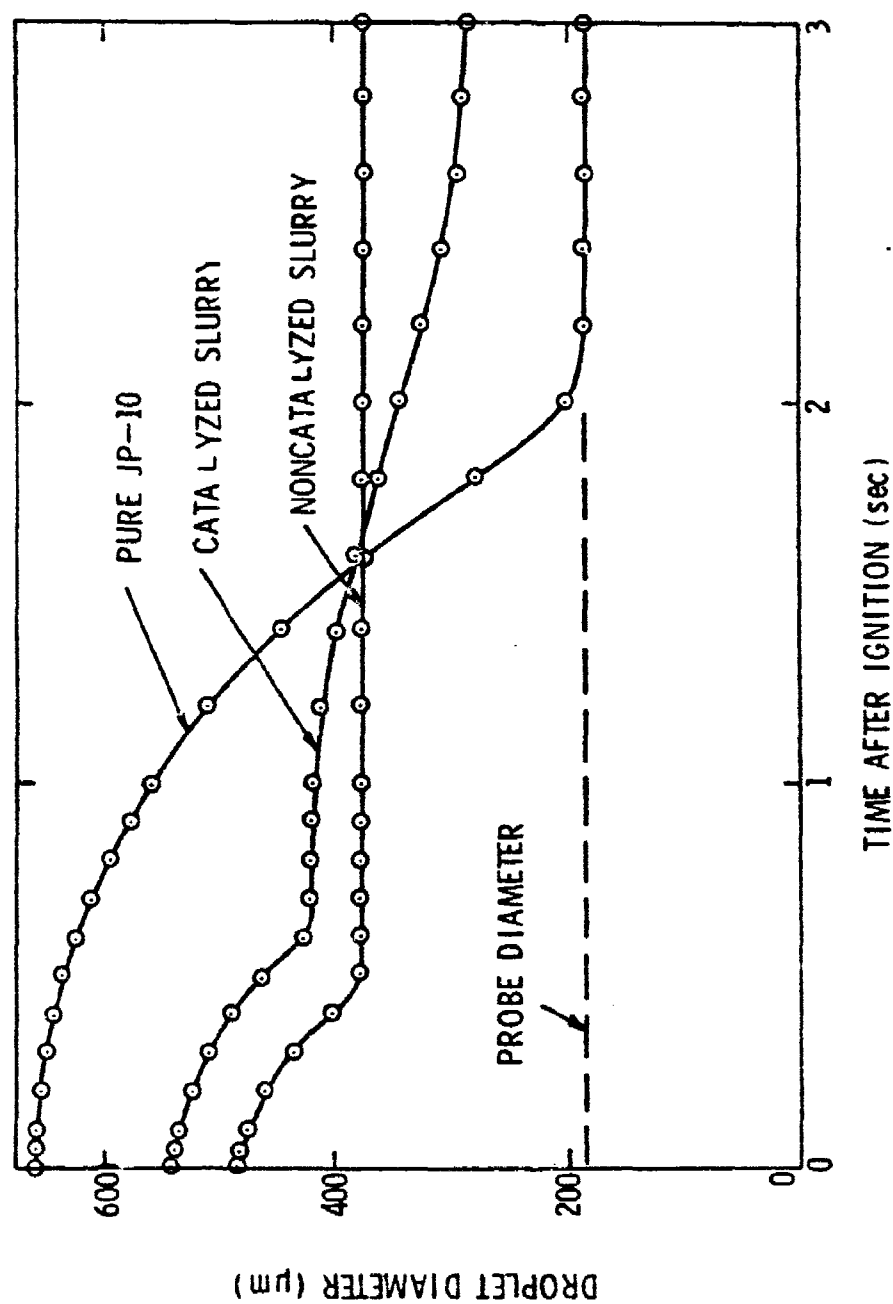
Figure 4. Droplet diameter as a function of time for pure JP-10, noncatalyzed and catalyzed slurry droplets burned in air.

in diameter in the region just after ignition, when an envelope flame was observed. This initial diameter reduction was due to the combustion of liquid JP-10, and the rate of diameter decrease was approximately equal to that for the pure JP-10 droplet.

Once the envelope flame of the noncatalyzed slurry drop extinguished, no further luminosity was observed and the particle diameter remained constant. With a catalyst present, however, the particle glowed after a dark period, and then extinguished again leaving a residue. During the glowing period, however, there was relatively little variation in the diameter of the particle. This agrees with the SEM observations where the structure was rather porous following combustion of a catalyzed slurry drop, suggesting reaction in depth rather than just at the surface. The bulk of the reaction in the glowing period is probably confined to the subsurface region where heat losses are reduced. As the reaction proceeds, the structure becomes more porous while the outer portions remain in place. Final extinguishment then becomes a complex process dependent upon heat losses, oxidant penetration into the pores of the structure, and perhaps loss of the catalyst.

The variation of droplet diameter observed in Figure 4 can be explained with the combustion mechanism of a slurry droplet presented in Figure 5. After ignition and the establishment of an envelope flame surrounding the drop, the droplet begins to heat up. As the liquid temperature increases, the rate of evaporation increases due to the increased vapor pressure of the fuel at the liquid surface.
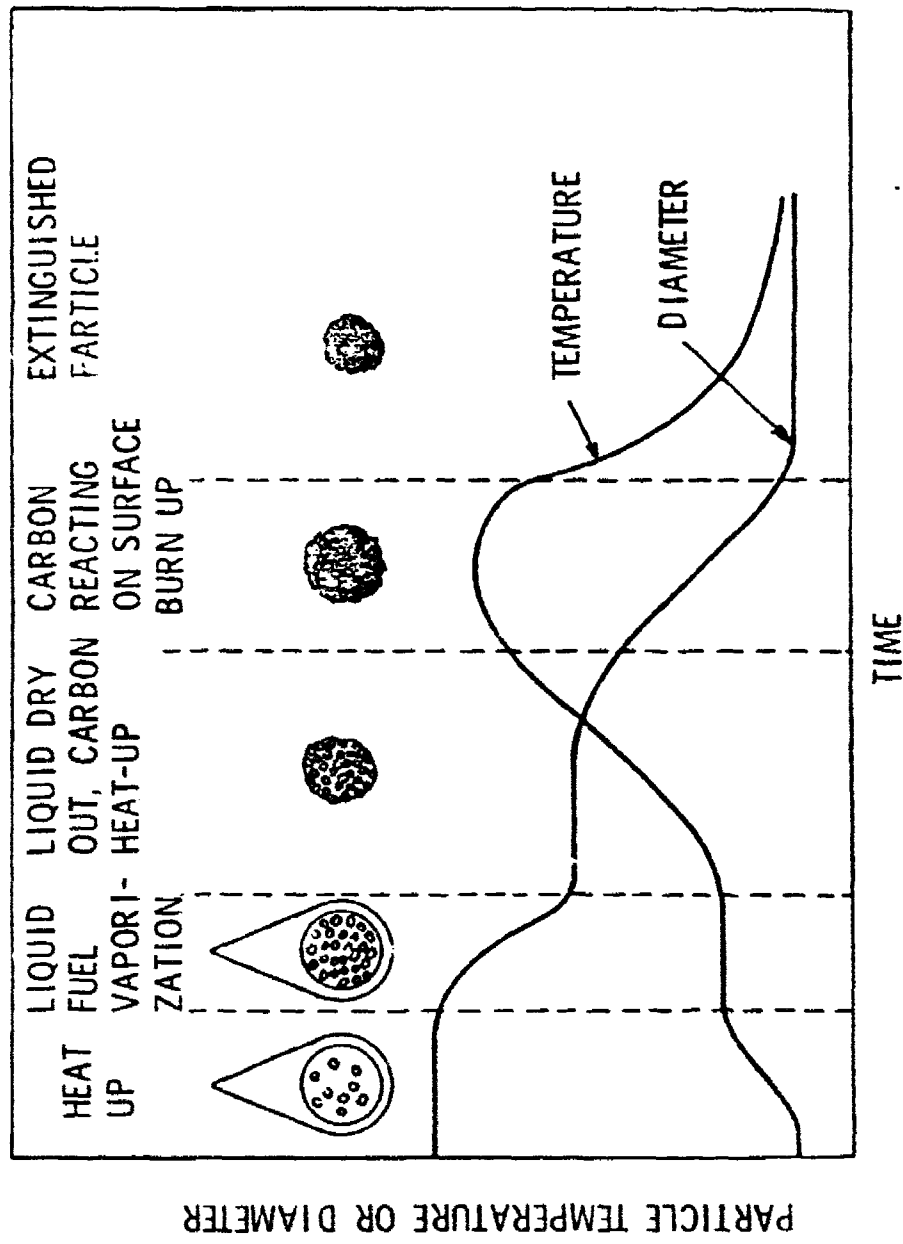
Figure 5. Sketch illustrating the details of the slurry combustion process.

Eventually a condition is reached where all the heat transferred from the flame to the drop surface is utilized for the heat of vaporization of the evaporating fuel, and the liquid temperature stabilizes at what is termed the wet-bulb temperature. The wet-bulb temperature is generally somewhat below the boiling temperature of the fuel at the ambient pressure. The vaporization rate is greatest at the wet-bulb temperature. Therefore, while the drop diameter decreases through the period of liquid combustion, the rate of decrease is greatest at the wet-bulb condition.

As the liquid evaporates, the solid carbon particles pack together to form an agglomerate. Eventually, the remaining liquid fuel can only be found in the pores of the agglomerate, and although liquid is evaporating and fueling the flame, the diameter of the agglomerate remains constant. When all the liquid fuel has evaporated the envelope flame is extinguished. At this point the particle will either extinguish as in the noncatalyzed slurry case; or the temperature will begin to rise very slowly as in the catalyzed slurry case, due to ignition of the carbon by the hot gases produced by the envelope flame. As the carbon particle heats up, the rate of reaction increases. At sufficiently high temperatures, the surface layer of the carbon agglomerate vigorously combusts which causes the diameter of the particle to decrease. As the process continues, the particle will either become small enough to be extinguished by natural convection effects, or will burn until there is no carbon remaining on the support probe.

1.3 Previous Related Studies

The preliminary tests suggested that the life-history of a combusting slurry droplet could be divided into two separate phases, the liquid heat-up and evaporation phase, followed by the agglomerate heat-up and reaction phase. Therefore, it appears logical to model the slurry droplet combustion process as two independent stages. The review of previous related studies is separated in the same manner.

1.3.1 Evaporation of Liquid Droplets

Drop-life-histories must be calculated in order to determine interphase heat, mass and momentum transfer. In determining the drop-life history, the drop configuration, convection effects, transient effects, fluid properties, interface effects, radial pressure gradient, radiation effects, constitutive relations for fluxes, and whether the droplet is evaporating or combusting all play a significant role. A recent review of drop-life-history assumptions and models is presented by Faeth [11].

Most studies have considered a drop to be a smooth sphere although deformation of the drop into a flattened elliptical shape occurs at higher Reynolds numbers [12,13].

The spherical case itself presents substantial analytical difficulties since the presence of convection requires numerical solutions, except at the limit of low Reynolds numbers. Results are available, for low Reynolds numbers flow over a rigid sphere [14,15], and some studies have considered higher Reynolds numbers and circulating liquid drops [16-13].

Complete solutions for drop characteristics are of value to check more approximate methods, but they are too complex to be useful for drop-life-history analysis at this time. The general approach has been to model the drops as a spherically symmetric flow field, and then employ an empirical correction for convection [19-26]. This procedure frequently involves the use of film theory, where the transport process is analyzed in a spherically symmetric layer about the droplet. Only the radial motion due to mass transfer is considered; convection is handled by selecting the film thickness to yield the correct heat or mass transfer rate, at a given Reynolds number, at the limit of low mass-transfer rates [11].

During its lifetime a droplet is heating up; its radius is changing; due to drag, its relative velocity is changing; and the ambient conditions may be changing as the droplet travels through the flow field. Therefore, both gas- and liquid-phase transient effects must be considered for exact analysis. However, just as in the case of convection for a sphere, a complete transient solution is too unwieldy to be of value in drop-life-history analysis, and simplifications must be sought.

At high Reynolds number, or at low Reynolds numbers and moderate pressures where the thermal diffusivity of the gas phase is two to three orders of magnitude larger than the thermal diffusivity of liquid phase, the gas-phase transient time is much smaller than the liquid-phase transient time [11]. Thus, it is reasonable to assume a quasisteady gas phase where the boundary layer around the droplet has

the same properties as a steady boundary layer for the same conditions of droplet size, velocity, surface and ambient temperatures, etc.; and the effect of the radial velocity of the liquid surface can be neglected.

Comparison between detailed numerical calculations of the transient evaporation process and the quasisteady gas-phase model have been completed by Hubbard, Denny, and Mills [27]. The calculations demonstrate that the quasisteady gas-phase approximation yields small errors, at least for pressures below 10 bar. Bellan and Summerfield [28] present some simplified rules for determining the region where the quasisteady approximation is valid, concluding that transient gas-phase effects are small at low pressures. Several other investigators also present discussions on various aspects of the quasisteady gas-phase assumptions with generally similar conclusions [25,26,29].

For volatile fuels at low pressures, the wet-bulb temperature is close to typical injection temperatures, and liquid-phase properties can be assumed to be constant. At higher pressures, however, reduced liquid densities cause the droplet to swell, and variable properties must be considered for accurate work [30].

A number of analyses have been conducted for variable gas-phase property effects on the evaporation process [27,31,32]. While early variable property studies only considered variable temperature effects, recent work has also treated variable concentration effects, since the effect of species concentrations can be appreciable [27].

Conditions at the droplet surface must also be specified; the formulation requires an estimation of the radial mass flux of the ambient gas at this position, as well as a relationship between the temperature of the liquid surface and the concentration of the fuel in the gas phase adjacent to the surface. At moderate pressures, where the quasisteady gas-phase assumption is valid, liquid fuels have low solubilities for the nonfuel portion of the ambient gas. Therefore, Spalding's [33] insolubility condition is most often employed as a boundary condition, and the mass flux of the ambient gas is taken to be zero at the liquid surface.

The relationship between the liquid temperature and the gas-phase fuel concentration at the liquid surface is usually obtained from the equilibrium vapor pressure of the pure fuel as a function of temperature. Vapor-pressure data can be correlated with the Clausius-Clapeyron equation. The assumption implied by the use of pure-vapor-pressure data is that the presence of other gases at the surface does not affect the equilibrium vapor pressure. This is adequate as long as the liquid-phase solubilities of the ambient gases are low and pressure levels are moderate, i.e., in the range where an ideal gas model is valid near the liquid surface.

Models of spherically symmetric evaporation usually ignore the radial momentum equation and assume that the pressure is uniform. The bulk radial flow, however, causes a radial pressure gradient since the mean radial velocity decreases with increasing radial distance. The worst condition occurs during the steady evaporation period, when

radial velocities are largest. However, the pressure can be assumed to be nearly constant, except for drops on the order of 1 μm or less, at pressures above atmosphere pressure [11]. Further discussion of radial pressure gradient can be found in Reference 27.

Previous studies of burning drops have indicated that radiative heating is relatively unimportant for drop sizes representative of most sprays [34-38]. Berlad and Hibbard [36] compared the measured absorption spectrum of 113 μm thick layers of typical hydrocarbon fuels, iso-octane, cyclohexane, toluene, hexene, and JP-4, with measured emission spectra of "luminous and nonluminous" burner flames. The fuels generally absorb radiation near 3.5 m, where flame emission was low in both cases. They conclude that these fuels absorb little radiative energy from the combustion regions of gas turbine combustors.

Droplet evaporation involves heat and mass transfer in the presence of temperature gradients and multi-component mixtures. The appropriate expressions for mass and heat transfer flux are discussed by Lees [39], Bird, Stewart and Lightfoot [40], and Williams [25]. The mass transfer flux contains concentration, thermal, pressure and forced diffusion terms. Forced diffusion occurs only for charged species in the presence of an electrical field and does not have to be considered [40]. Pressure diffusion is usually small for typical flow conditions [40], and is absent in the constant-pressure field of a spherically symmetric evaporating drop. Thermal diffusion is more important; however, the contribution of the thermal-diffusion term is

still generally less than 10%, when compared with concentration diffusion [39]. This leaves concentration diffusion as the major driving potential of the mass flux. Rather than solve the multi-component diffusion equations, most analyses assume an effective binary diffusion expression--Fick's Law [25]. This approximation is adequate when the binary diffusivity of all species is the the same, or when all species, but one, are moving at the same velocity [40]. For drop evaporation where the insolubility condition is satisfied, only the fuel has a non-zero velocity and the condition is met even for fuels with large molecular weights in comparison with the ambient gas.

The energy flux contains the conductive flux as well as contributions from interdiffusing species and the Dufour effect [40]. The Dufour effect is related to thermodiffusion and is small even when thermodiffusion must be considered [25]. The interdiffusion term is generally considered, although the equations assume a particularly simple form when the Lewis number is unity and this approximation is frequently made [25,39]. Even when the Lewis number is not unity, if only the fuel has a net mass flux, only energy transported by fuel transport must be considered.

When a drop is surrounded by a hot oxidizing medium, it can ignite, giving rise to a reaction zone in its immediate vicinity. For fast rates of reaction, the flame zone is very thin and surrounds the drop. In this case, the process is diffusion controlled and bears many similarities to drop evaporation without combustion. New

difficulties involve more extreme property variations, and the need to determine the point of ignition. Criteria are also needed to determine when the flame zone is thin enough for the diffusion flame approximation to be valid and when a stable flame is established around the drop.

Many investigators [19-23,34,41-47] have been able to correlate measurements of droplet gasification rates with diffusion flame models. This suggests that either the gasification rate itself is relatively insensitive to the details of the flame structure, or that property uncertainties are masking significant effects. (Predicted burning rates can be modified within an order of magnitude while still making reasonable choices for "average" properties; even variable property models provide considerable latitude due to the uncertainties of concentration effects and convection correlations.)

More sophisticated droplet combustion models allowing for variable property effects and employing the diffusion-flame approximation may be found in the literature. Law and Law [48] present a rather complete version for a pure fuel at its wet-bulb state, which allows for both concentration and temperature effects. These authors also review a number of the common variable-property models which only allow for variations with temperature.

1.3.2 Combustion of Carbon

Carbon-slurry combustion is complex since the combustion of gaseous or liquid fuels is superimposed on the heterogeneous oxidation of carbon particles. To gain some insight into the carbon-agglomerate

combustion process of a combusting-slurry droplet, a review will be made of the combustion of coal and carbon particles, carbon--gas-phase reaction mechanisms, and carbon structure.

1.3.2.1 Combustion of Particles

While in comparison with carbon combustion, the presence of ash and volatile material in coal modifies the combustion process, past observations of coal-particle combustion afford useful background information for the present investigation. Therefore, earlier studies of both carbon and coal particles combustion are discussed in this section.

1.3.2.1.1 Suspended Coal Particles

There have been surprisingly few studies of single coal-particle combustion. Important among the earlier studies was the work of Tu, Davis and Hottel [49], where carbon spheres approximately 25 mm in diameter were burned within a furnace. Burning rates and surface temperatures were measured for various furnace temperatures, ambient gas compositions and gas velocities. A low-temperature regime where kinetics dominates, and a high-temperature region where diffusion dominates were delineated and interpreted using a film theory model. Later, this data was reinterpreted in terms of a combined absorption, desorption and diffusion mechanism [50].

Following this initial work there have been a number of studies of the combustion characteristics of carbon, coke and char [7,51-60]; reviews of this work may be found in References 7, 8 and 10. This

area has received attention since carbon and chars are reasonably well-defined materials, without the complication of a devolatilization process. The chars most often have been formed by slow heating in order to preserve the structure of the material. For overall furnace analysis, the carbon-combustion process is also much longer than major devolatilization processes, making this aspect more critical in the determination of performance and heat loading. Questions remain, however, concerning whether these structures are at all typical of materials subjected to rapid devolatilization in a furnace.

Many of these studies have involved determination of the rate of reaction by continuously weighing a particle supported within a furnace [49,51,54-60]. The structural characteristics of the solid have also received some attention. Orenbakh [55,56] employed mercury porousimetry to estimate pore-size distributions during burnout; others have determined density distributions by progressively grinding away the surface and reweighing the sample [37]. Kurylko and Essenhigh [58,60] obtained information on the temperature distribution within the particle using embedded thermocouples. By combining photographic size determinations with continuous weighing, it also has been possible to determine the average density variation of the particle during burnout [57,58,60].

The gas phase around a burning carbon particle has not received much attention. Kurylko [58] made qualitative measurements around a sphere. Quantitative measurements were completed in the boundary layer of a carbon cylinder burning in oxygen by Wicke et al. [52,53].

In general, however, the role of carbon monoxide combustion in the gas phase around a burning carbon particle is not well understood, particularly in the presence of hydrocarbon compounds and their combustion products [7]. This uncertainty in the ratio of CO_2 and CO production at the solid surface has led to considerable vagueness in the interpretation of experimental results, even at the diffusional limit [7].

Fewer studies have been made of captive coal particles containing volatiles. Essenhigh and Thring [61] studied the combustion of individual captive coal particles having sizes greater than 1000 μm. Flame observations indicated evolution, ignition and gas-phase combustion of volatiles as a first step in the process. The last stage involved collapse of the gas-phase flame, followed by combustion of the solid residue. The times of these two stages were proportional to the square of the initial particle diameter, with the first stage approximately an order of magnitude shorter than the second. Later work by Essenhigh and coworkers [62,63] considered the constants of proportionality for the time of these two processes for various coal ranks and oxygen concentrations. Measurements were also made of the influence of swelling and shape on the combustion rate of single particles [14].

Anson et al. [65] considered supported coal particles heated radiatively with projector lamps in a cold-air environment. Particle size was on the order of 300 μm, with both low- and medium-rank coals being considered. The expulsion of volatiles exposed to high

radiation fluxes caused swelling and the formation of hollow spheres, most often with a lacy internal structure. The authors argue that combustion proceeds externally and internally at constant diameter until at an advanced stage the particles fragment. The ash was not observed to participate in the process, or to wet the surface, thereby reducing oxidizer access to the combustible material. The findings of this investigation emphasize the need for considering materials prepared at heating rates typical of operating conditions if the results are to be relevant to actual combustion systems.

1.3.2.1.2 Free Coal Particles

Following its introduction by Orning [66], the gas swept drop tube, or one-dimensional laminar-suspension flow furnace, has been a major tool in research on the combustion of small coal particles. With the exception of a study by Saji [67], who considered some of the overall characteristics of pulverized coal flames, the bulk of this work has dealt with devolatilized materials, or materials of low volatility. Early work, represented by References 67-71, employed pure carbons to eliminate complications due to the presence of both volatiles and ash. Reviews of much of this work may be found in References 7, 8 and 10. More recent use of this technique by workers at BCURA and CSIRO [72-77] has primarily considered prepared chars of relatively low volatile content.

The technique has been to introduce the particles into a preheated stream of gas, and then allow them to flow through a furnace at low loading so that temperatures (except particle temperature) are

primarily fixed by the furnace temperature. Since the characteristics of the particle are influenced by its heating rate during volatilization, in the most recent work [72-77], chars are prepared in a similar furnace arrangement to achieve initial heating rates characteristic of furnace applications, (10^4 K/s).

With the laminar-suspension flow-furnace technique, burning rate measurements are made by sampling the particles after various times of exposure in the furnace. Major variables considered have been particle size, feed rate, coal type, gas velocity, gas composition (oxygen concentration, etc.) and furnace temperature. Burning rates are measured both gravimetrically and by the appearance of CO and CO_2 in the gas stream. Particle-density variation has been determined by weighing and sizing particles at various sampling stations.

Using a similar apparatus in tests of bituminous coal, Anson et al. [65] determined surface area through BET techniques. Guerin et al. [78] employed similar methods to infer the characteristics of the pore structure of a pulverized coal char contained in a combustion boat within a furnace (non-flowing).

The one-dimensional furnace has successfully been used for studying the entire combustion process of coal by Howard [79] and Howard and Essenhigh [30,81]. Samples withdrawn from the furnace were analyzed in order to determine the variation of volatile matter, ash and fixed carbon content of the particles. Temperature and gas-composition measurements were also made in the furnace. In order to simulate combustion at elevated pressures, where heating rates of the

particles are even higher than at atmospheric pressure, a few studies have been conducted in shock tubes [82].

There is general recognition that pulverized-coal combustion is so complicated that there is little likelihood of formulating valid and accurate analytical combustion models unless they are based on thorough experimental delineation of key processes. For that reason, current coal-particle combustion models are oversimplified, simply because the available experimental data cannot support a higher degree of sophistication. Of course, the degree of oversimplification depends upon the user's viewpoint; if the burning rates are of primary interest, the present models give credible predictions since that is the principal kind of experimental data upon which they are based.

The most extensive models consider devolatized materials. All employ conventional spherically symmetric film theory for mass transfer to a solid sphere, with consideration of some type of reaction at the surface [10,61-78]; although just what is diffusing is not clear in all cases due to competing processes of CO and CO_2 formation. Some models allow for diffusion through an ash layer [10,69]; in some cases, diffusion in the carbon pore structure is considered [8,57,58,60], and gas-phase reaction has been treated for cylindrical geometries [52]. Most often, however, gas-phase reaction is neglected, the particle is assumed to burn over its outer surface, and the actual products of combustion are assumed [10,72-78].

1.3.2.1.3 Theoretical Models

In most theoretical studies of burning carbon particles, only radial-diffusive transport in the gas phase and the heterogeneous reactions are considered to influence the overall reaction rate. In early work, Spalding [83] and Avedesian and Davidson [84] included gas-phase chemistry through a flame sheet which stands off the surface of the particle where CO was oxidized. However, these analyses are limited by the assumption of negligible radial convection; furthermore, the heterogeneous reactions are assumed to be fast enough so that the carbon consumption is diffusion dominated. The theoretical work of Ubhayakar and Williams [85], which included the influence of radial convection in the gas phase, supports their experimental results. In this case the authors assumed that the gas-phase chemistry is frozen and that only the carbon-oxygen reaction is operative.

Studies by Amundson and coworkers [86,87] considered burning of spherical carbon particles surrounded by finite, quiescent gas films. Caram and Amundson [86] also provide an extensive review of single-particle carbon combustion studies, including information on the various fluid-mechanical and chemical models used in each. The emphasis in both Caram and Amundson [86] and Mon and Amundson [87] is on the gas phase alone.

Libby and Blake [88] studied the particle-life history of a single-carbon particle in a hot oxidizing ambient environment. Their theoretical model was based on a uniform-temperature, constant-

density, spherical particle of carbon surrounded by a quiescent gas phase having constant transport and thermophysical properties. The direct oxidation of carbon with oxygen and the indirect oxidation via carbon dioxide were taken into account. While both mechanisms influenced the dynamic behavior of carbon particles, mass loss by oxygen dominated the process. Theoretical results of Libby and Blake [88] indicate that particle consumption involves complex interactions of convective, diffusional and thermochemical effects. In a later paper, Libby and Blake [89] extended their model to include the effects of water vapor and hydrogen. Their prediction of rates of particle mass loss for specified ambient conditions and particle temperature and size suggest that in the high temperature or the diffusion limit, the influence of water vapor and oxygen on particle-mass loss are approximately equivalent. However, at the kinetic limit, oxygen yields higher rates of mass loss.

Combustion of carbon particles in an oxidizing atmosphere was also studied by Matalon [90]. In this investigation the author describes the departure from an equilibrium gas-phase behavior for a pure carbon particle immersed in an oxidizing atmosphere over a wide range of particle sizes and pressures. Matalon [90] determined that the oxidation of the carbon particle depended on both direct oxidation by oxygen and indirect oxidation by carbon dioxide. The latter mechanism was modeled as a CO flame sheet surrounding the particle.

1.3.2.2 Gas-Solid Reaction Mechanisms

From the material reviewed in the previous section, it is apparent that accurate predictions of the reaction rate of carbon in a hot oxidizing environment requires a thorough understanding of the gas-solid reaction mechanisms. Therefore, this section provides a review of the mechanisms which are pertinent for carbon reaction.

It is generally accepted that there are three principal global reactions of carbon which are of major interest in the carbon-particle combustion process:

$$C_s + O_2 \rightarrow CO_2 \, , \, CO$$

$$C_s + CO_2 \rightarrow 2 \, CO \qquad\qquad (1.2)$$

$$C_s + H_2O \rightarrow CO + H_2$$
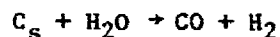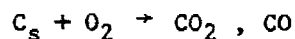
The reactions are, of course, much more complex than is indicated by the simple schemes shown; a common feature is that they are all accompanied by the formation of surface complexes. Also, the behavior of these surface complexes is determined, in part, by the properties of the carbon surface. This reaction surface cannot be defined adequately, and according to the circumstances in which the reaction takes place, both the internal and external surface of the carbon particle may be involved in the reaction. In the following, each of the reactions described in Equation (1.2) will be discussed.

The chemical reaction of oxygen with solid carbon is generally agreed to occur by the processes of adsorption and desorption [7]. Although there is some difference of opinion concerning the detailed steps by which these processes occur, a relatively simple adsorption-desorption model was developed by Lewis and Simons [91] as follows:

$$C_s + O_2 \rightleftharpoons C(O_2)$$

(1.3)

$$C_s + C(O_2) \rightarrow 2 \ CO$$
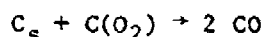
where $C(O_2)$ is an O_2 molecule adsorbed on the carbon surface. Other investigators [8,9,72] prefer a more direct oxidation of carbon by oxygen mechanism as expressed in Equation (1.2). However, there is a great deal of controversy concerning the interpretation of existing data which has led to a wide range of activation energy and reaction orders for even this well-documented reaction [8,9,72]. For example, data on pulverized coal and carbon combustion for temperatures greater than 1200 K given by Field [72,73], Mulcahy and Smith [7], Khitrin and Golovina [92], and Smith [74,75] indicate the reaction to be first order in the partial pressure of oxygen with an apparent activation energy of 20 to 40 kcal/mole. Such behavior is in accord with the accepted heuristic consideration, although the observed activation energy appears to be large.

The principal mechanistic studies of the carbon–carbon dioxide reaction have been reported by Gadsby et al. [93], Ergun et al. [94–96], Walker et al. [97,98], von Fredersdorff and Elliott [99], Lewis et al. [100], and Reif [101]. In each case, the authors suggest the following oxygen–exchange mechanism:

$$C_s + CO_2 \rightleftharpoons CO + C(O)$$

(1.4)

$$C(O) \rightleftharpoons CO$$
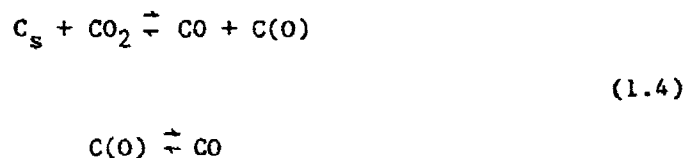
This mechanism is the most widely accepted explanation of the course of the CO_2 reaction below or near atmospheric pressure [99]; however, the other investigators [101,102] support a mechanism with unidirectional oxygen exchange at the surface.

Gadsby et al. [102] supported the second carbon dioxide mechanism on the basis of charcoal chemisorption experiments at $750^{\circ}C$ and about 300 to 400 mm Hg total pressure, which indicated that variations in CO_2 partial pressures corresponded more closely to variations in CO partial pressure than to changes in amount of oxygen complex absorbed. In addition, the quantity of oxygen complex remained relatively constant with variation in CO partial pressure at constant CO_2 partial pressure. This was taken as evidence that the rate of inhibition must have been set by CO chemisorption, not by the reverse oxygen exchange reaction of Equation (1.4).

In addition to the uncertainty about which mechanism correctly predicts the oxidation of carbon by carbon dioxide, once a mechanism is chosen there is a wide range of reported activation energies and reaction orders [99]. As in the case of oxygen reaction, the activation energy varies by a factor of two, from 30 to 60 kcal/mole [100-102].

The kinetics of the carbon-steam reaction is in many respects analogous to the CO_2 reaction. A unified theory of the course of gas reactions of carbon, where the reactants are oxidizing, holds that their mechanisms or elementary steps should be similar. However, the $C-CO_2$ system comprises only two constituents--carbon and oxygen--allowing less uncertainty about the choice of its limited number of possible mechanisms. The carbon-steam system, on the other hand, poses the added complexity contributed through possible roles of hydrogen and/or other intermediate dissociation products of water vapor. Furthermore, the carbon dioxide reaction with carbon is occurring simultaneously.

The principal mechanistic studies of the carbon-steam reaction have been reported by Gadsby et al. [102], Johnstone et al. [103], von Fredersdorff and Elliott [99], Long and Sykes [104], Strickland-Constable [105], Wicke and Rossberg [106], Binford and Eyring [107] and Eurgun [95]. In each case, the authors recommend the following oxygen exchange mechanism:

$$C_s + H_2O \leftrightarrows H_2 + C(O)$$

(1.5)

$$C(O) \leftrightarrows CO$$
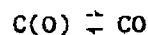
There seems to be general agreement that the primary products of the steam reaction with relatively pure carbons at atmospheric or lower pressures are carbon monoxide and hydrogen, whereas CO_2 is a secondary product arising through the water-gas shift reaction which is known to be catalyzed by carbon surfaces [93,108].

Similar to the carbon-carbon dioxide mechanisms, there are several other proposed carbon-steam mechanisms and a wide range of reported activation energies and reaction orders [99]. Activation energy for the carbon-steam reaction has been reported from 10 to 65 kcal/mole [99]. In addition, the reaction rate of water vapor and carbon is complicated by oxygen and carbon dioxide all competing for the same active sites.

In addition to the reaction mechanism which investigators have suggested for the reaction of carbon or coal, oth investigators [109-121] have determined separate reaction rat mechanisms for graphite, soot and carbon black. Nagle and Strickland-Constable [109] formulated a semi-empirical formula based on reaction of oxygen with pyrolytic graphite. Rosner and Allendorf [110] have determined that for pyrolytic graphite monatomic-oxygen atoms tend to be more reactive than diatomic oxygen . Wright [111] has also correlated the reaction rate of soot and pyrolytic graphite with monatomic oxygen as the

oxidant. Otterbein and Bonnetain [112] and Appleton et al. [115,116] compared the rates of soot oxidation in flames [117-119], pyrolytic graphite oxidation using oxygen [110,113] and carbon black oxidation in a shock tube [120], with the rates predicted by the Nagle and Strickland-Constable formula [109]. They concluded that the magnitude of most of the soot and pyrolytic-graphite oxidation rates can be adequately correlated by the Nagle and Strickland-Constable formula.

Although the Nagle and Strickland-Constable formula seems adequate for predicting oxidation rates of soot and pyrolytic graphite by oxygen, there is a lack of evidence that this formula will correctly predict soot oxidation rates in flames where there are more than one potential oxidant. In fuel-rich flames the O_2 concentration can be comparable to the O concentration and also can be much less than the OH concentration. The reaction probability of soot with O and OH can be expected to be higher than with O_2. Neoh, Howard and Sarofim [121] determined that at high temperature and fuel-rich conditions, the OH radical was the principal oxidant, with oxygen dominating only in the lower-temperature and fuel-lean conditions.

1.3.2.3 Carbon Structure

The chemistry and fluid mechanics of the combustion and gasification of porous carbon char have been studied by numerous researchers and summarized in two extensive review articles, one by Walker et al. [8] one by and Mulcahy and Smith [7]. It is known that the gasification process can depend upon the gaseous environment and porous structure, and is either diffusion limited or kinetically

limited. The diffusion process may be controlled by Knudsen diffusion within the pores, or by continuum diffusion either within the pores or in the boundary layer surrounding the particle. In addition, the heterogeneous rate constant may be limited by either the adsorption or the desorption process. The complications introduced by the presence of many limiting processes are compounded by lack of a complete description of the porous structure. Recognizing these difficulties, transport processes have been modeled in highly idealized situations. Thiele [122] described the diffusion and heterogeneous chemistry occurring within a single isolated cylindrical pore and determined that the diffusion limited gasification process scales as the square root of the kinetic rate. Wheeler [123] applied the Thiele solution to a pore structure which consisted of a large number of identical parallel pores. He demonstrated that the gasification process, when limited by Knudsen diffusion, scaled as the porosity over the square root of the kinetic rate.

While the works of Thiele and Wheeler have yielded a better understanding of the gasification process, the models are rigorously valid only in extreme limits, since they do not include a realistic pore size distribution or a description of pore branching and pore combination. These effects have been incorporated by Hashimoto and Silverston [124,125] using an integral technique with adjustable empirical parameters to close the mathematical system. A qualitative description of the pore-distribution function, pore branching and pore combination was not developed, and the adjustable parameters handled

this part of the model. A model proposed by Kriegbaum and Laurendeau [126] considers the gasification of pulverized or crushed coal char particles. This model characterizes the porous solid reactant as a system of individual pores. A pore is assumed to consist of a tubular capillary bounded radially by a nonporous carbon sheath. This carbon sheath is assumed to be bounded radially by nonporous ash. The ash serves to limit the radial growth of the pore. The model combines Knudsen capillary-flow theory with standard molecular-diffusion theory. The resulting diffusion coefficient accounts for effects of pore growth on diffusion since it is a function of pore radius. The model also uses Langmuir-Hinshelwood kinetics to model the surface reaction. Analysis of the simultaneous mass transport plus reaction within the individual pores yields burnoff data for the entire particle. The model, however, is incapable of predicting pore structure development with burnoff, since pore interactions are not considered.

Beshty [127] developed a mathematical model to analyze the internal combustion of a porous carbon sphere with uniform spherical pores arranged on a simple cubic lattice extending through the particle volume. Beshty assumed that as the reaction proceeded the pores enlarged and eventually merged, causing the partial collapse of the particle. The model was used to examine the effect of particle size, temperature and extent of burnoff on the rate of combustion and the change in internal specific surface area. Three combustion regimes were predicted by the model: chemically controlled uniform

burning, joint chemically and pore-diffusion controlled combustion, and a pore-diffusion region leading to nonuniform burning. As the temperature of the particle and particle size increases, the effects of pore diffusion becomes more significant. Although temperature and particle size determine the initial combustion region, as burnoff progresses, transition to the chemically controlled region gradually occurs. Beshty [127] determined that this is a result of the diminishing effect of pore diffusion as combustion progresses and pores develop.

Simons et al. [92,128-130] developed a model to describe the mass transport and heterogeneous chemistry which occurs during the combustion and/or gasification of porous coal char. The authors develop a semi-empirical model to describe the porous coal char structure. The pores were assumed to be cylindrical tubes connnected to other pores of the same shape to form pore-tree structures. Data suggest that the distribution of pore number density is inversely proportional to the pore radius cubed. Simons and Finson [128] determined that the smaller pore trees were kinetically limited while the larger trees were diffusion limited. This is the opposite to that which one would conclude from the Thiele-Wheeler [122,123] approach, which does not include pore branching or the concept of a pore tree.

Simons [129] developed a mechanistic model which describes pore combination during char gasification by expressing a general population balance for a given pore size which includes pore growth and pore engulfment. The engulfment of the smaller pores by the

larger ones was responsible for the relative depletion of the small pores and enhanced growth of the larger pores. Simons also concluded that the influence of the parent coal and effects of pyrolysis and pore growth during gasification are as significant as the effect of pore combination and must be considered before the time history of the pore distribution may be accurately predicted.

The effects of Knudsen diffusion, continuum diffusion, and both adsorption and desorption kinetics were considered by Simons [129]. He concluded that each physical mechanism may limit the gasification rate within some range of pore size, particle size, gas temperature and gas pressure. In general, however, no single mechanism controls the entire gasification process.

Although there are several models which can predict the pore structure of coals and chars reasonably well, no models considering agglomerate pore structure were found in the literature.

1.3.3 Combustion of Slurry Droplets

The combustion of a pure-component fuel droplet can be considered to be reasonably well understood [11], and its burning rate can be predicted quite accurately by applying the classical d^2-Law [131]. This law assumes a constant droplet temperature when the process of droplet heating is taken into account [131,132]. A short period spanning about 10% of the initial droplet lifetime, at low pressures, exists during which the droplet is actively heated up and the burning rate is very slow. It was further shown that the bulk droplet combustion characteristics depend only minimally on the

detailed description of the heat transport mechanism within the droplet interior [132].

However, studies [133-135] on miscible multi-component droplets show that their combustion behavior depends critically on the liquid-phase heat and mass transport processes. In particular, two limiting cases have been identified. In the diffusion limit [133], the external gas motion, which exerts shear stress at the droplet surface, produces essentially no motion within the droplet interior because of the small droplet size and high liquid viscosity. In the convective limit, the internal states of the droplet are assumed to be maintained as perpetually uniform since the rate of internal circulation, and therefore the rate of convective transport, is fast.

Recently, the above concepts have been extended to systems involving more than one liquid phase. The use of emulsions of water in oil has attracted considerable attention as a means of reducing emissions of particulate solids and saving fuel because of the reduction in combustion air that can be achieved [136-143]. The addition of small quantities of water significantly enhances the potential and intensity of droplet explosion [144].

In the combustion of the carbon-oil mixtures, the oil is much more volatile than the carbon particles. Therefore, it is reasonable to expect that the oil will be vaporized first and that a large carbon particle agglomerate will be left behind. This possible agglomeration implies that the sizes of the carbon particles which actually undergo combustion in the form of agglomerates are determined by the initial

concentrations of the carbon particles and the initial droplet sizes, but not by the sizes of the individual carbon particles. Therefore, it is probably not necessary to use extremely fine carbon powders in the preparation of slurries [142], at least from the combustion standpoint. These agglomerates will also affect the rate of radiation transfer, which is an important heat-transfer mechanism within furnaces and boilers. Also, the large agglomerate size and non-volatile nature of the carbon may lead to incomplete combustion [142].

On the other hand, it has also been suggested by Law et al. [144] that agglomeration may be either prevented or minimized through the bubbling of some volatile component trapped within the droplet interior. The resultant internal pressure buildup will shatter the agglomerate into much smaller pieces. This so-called "micro-explosion" event has been theoretically predicted by Law [134,135] and experimentally verified by Lasheras et al. [145-147] for miscible and immiscible liquid mixtures consisting of oil, water and alcohol.

A preliminary experiment was conducted by Law et al. [142] at room temperature air on the burning of a single coal-oil mixture droplet suspended at the end of a quartz fiber. A mixed behavior was observed showing the occasional ejection of small masses from the droplet and the eventual formation of an irregularly shaped coal-particle agglomerate. The agglomerate was formed when burning was terminated upon complete depletion of the oil component. Addition of small quantities of water intensified the fragmentation.

Law [148] also studied free-falling droplets in a hot environment
simulating the furnace interior. The use of free-falling droplets
allowed the agglomerates to be formed without uncertainties due to the
presence of the suspension fiber. It was determined [148] that the
coal burns in the form of agglomerates instead of individual
particles. Therefore, from combustion considerations it is
unnecessary to fine-crush the coal unless the particles can be reduced
to micron-size. Law [148] also determined that attempts to make the
coal-oil mixtuie more volatile in the hope of facilitating combustion
may in fact prolong the total burning time, since a more volatile oil
produces delays in agglomeration, heat-up and ignition of the
agglomerate.

1.4 Specific Objectives of the Study

As discussed in the last section, many investigators have studied
the combustion process of both single-suspended and free-flowing
carbon particles. Combustion of coal-slurry droplets has also been
observed. However, no method has been demonstrated which can provide
predictions of carbon-slurry combustion properties under typical
combustion-chamber conditions. The main objective cf this
investigation was to develop a comprehensive theory for the combustion
of carbon-slurry drops and to evaluate the theory by comparison with
measurements.

The experimental portion of this investigation involved observing
the combustion of slurry drops supported in a turbulent-diffusion
flame and free drops in the post-flame region of a flat-flame burner.

These test conditions were examined in order to simulate the local environment of drops within a combustion chamber. In order to study the nature of agglomeration of the carbon particles, slurry droplets were extinguished at various stages in its combustion process. The resulting agglomerate structure was studied using a scanning electron microscope.

The specific objectives of each experimental test apparatus is discussed in the following sections.

1.4.1 Combustion of Large, Suspended Slurry Droplets in a Turbulent-Diffusion Flame

The specific objectives of the combustion tests of large, suspended slurry droplets in a turbulent-diffusion flame can be summarized as follows:

1. Identify the conditions under which a slurry droplet will ignite and completely burn.

2. Determine if carbon particles are ejected from the carbon-slurry droplet during the liquid-evaporation stage as has been observed for coal-slurry-droplet combustion.

3. Determine the effect of a catalyst on the carbon slurry droplet combustion process.

4. Examine the structure of the carbon residue at various times during the combustion process.

5. Determine the different stages of the combustion process of a slurry droplet and their relative duration.

6. Develop and evaluate a liquid-evaporation model to predict the heat-up and evaporation of the liquid phase of a slurry droplet. The model should be able to accurately predict the droplet diameter and temperature during the liquid evaporation process.

7. Develop and evaluate a carbon agglomerate combustion model to predict the heat-up and combustion of the particle. The model should be able to accurately predict the particle diameter and temperature during the combustion process.

8. Determine which gas species most readily reacts with carbon.

1.4.2 Combustion of Small, Free-Falling Carbon Particles in a Laminar-Premixed Flame

The specific objectives of the combustion tests of small, free-falling carbon particles in a laminar-premixed flat-flame burner can be summarized as follows:

1. Study the combustion process of carbon particles typical of the size that would be encountered in a combustion chamber.

2. Develop an experimental apparatus which eliminates the effect of the support probe from the carbon-particle combustion process.

3. Study the effect of different equivalence ratios of the flame gas at constant temperature, and different temperature levels for a given equivalence ratio.

4. Identify the conditions which lead to the combustion of the carbon particle by either diffusion-controlled combustion or

kinetically controlled combustion. Most of the regions of the turbulent-diffusion flame test approached the diffusionally-controlled limit or the quenching limit, which reduced the sensitivity of the reaction rate evaluation. Therefore, more kinetically controlled test conditions will be studied.

5. Examine the variation of particle density during the agglomerate combustion process, by measuring particle mass as well as particle diameter.

6. Evaluate the theoretical model for these test conditions.

CHAPTER II

EXPERIMENTAL APPARATUS AND PROCEDURES

2.1 Introduction

The first experimental arrangement involved a single slurry droplet suspended from a thermocouple probe in an atmospheric pressure, turbulent-diffusion flame. This arrangement was considered since slurry drops placed at various locations in the flame would experience conditions similar to those in a combustion chamber. By mounting the droplet on a thermocouple, the apparatus also afforded an opportunity to measure the temperature of the carbon-slurry droplet during combustion.

The second experimental apparatus involved injecting slurry droplets through a laminar-premixed flame. This arrangement provided a means of observing the combustion of very small slurry droplets, while maintaining control of the surroundings of the drops, and eliminating any effects due to the presence of a support probe.

Both apparatus are discussed in detail in the remainder of this chapter.

2.2 Turbulent Diffusion Flame Apparatus

2.2.1 Test Apparatus

The test apparatus involved a modification of an earlier arrangement employed for a study of a gaseous turbulent-diffusion flame [149,150,151]. A sketch of the apparatus appears in Figure 6.
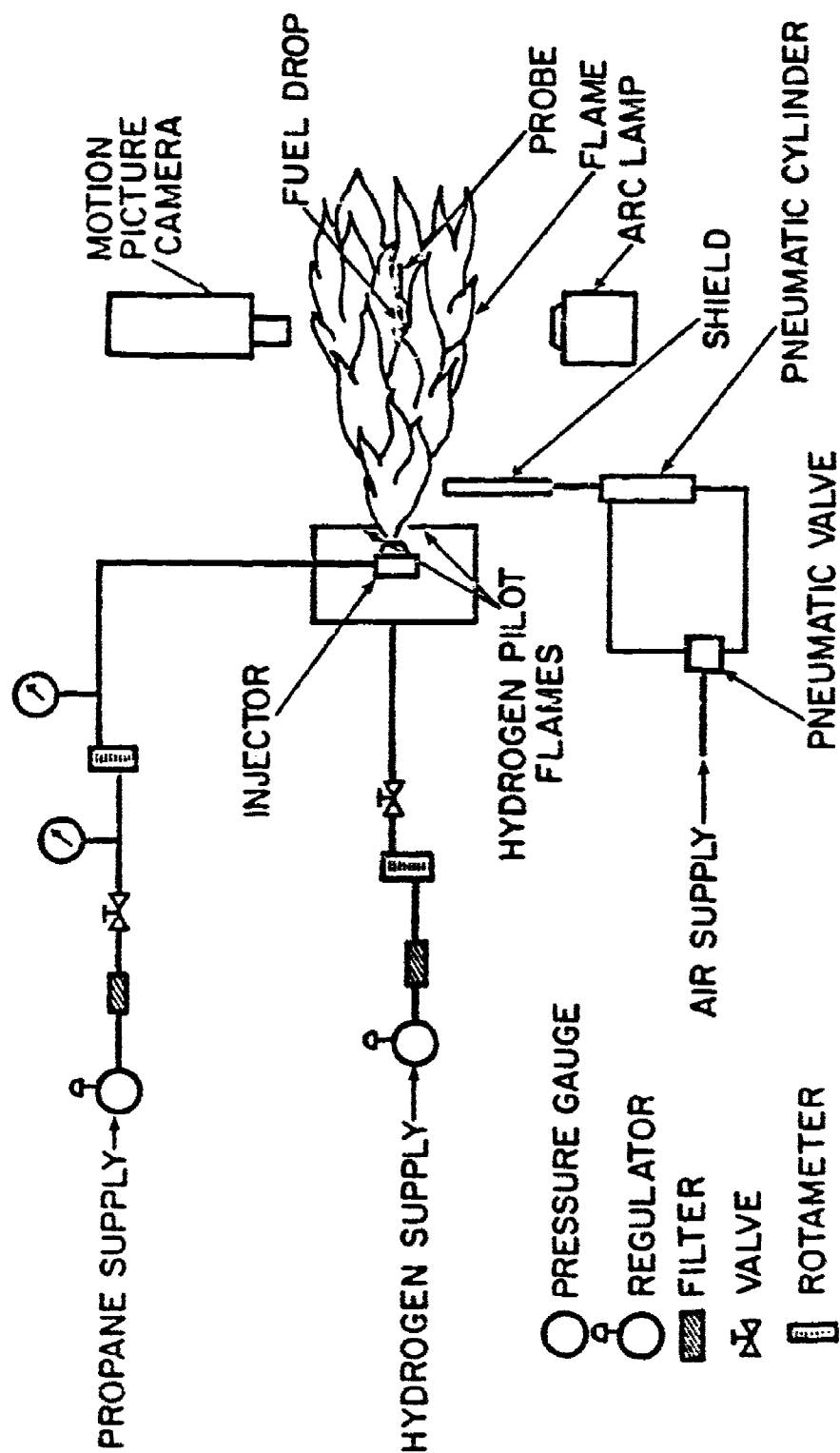
Figure 6. Schematic diagram of the turbulent diffusion flame apparatus.

The arrangement consists of an injector flowing propane gas, which is burned as a diffusion flame in stagnant room air. The carbon agglomerate was supported from a fine-wire thermocouple probe at various locations in the flame, photographed with a motion-picture camera, and the particle temperature was recorded with an analog-to-digital signal converter.

The gas injector was positioned near the bottom of the test stand and oriented vertically upward. The test stand was an area 1.2 m square and 3 m high enclosed with a single thickness of 16 mesh screen. The test stand was located within a room having dimensions 4 m x 7 m x 4 m high. Combustion products were removed through an exhaust fan located near the ceiling of the test cell. The injector was mounted on a support which allowed a vertical movement of 1.2 m. Two traversing mechanisms were used to position the nozzle in the horizontal plane.

The nozzle was a full-cone air-atomizing injector, with no swirl, manufactured by the Spraying Systems Company (model 1/4 J 2050 fluid nozzle and model 67147 air nozzle). The outlet diameter of the nozzle was 1.194 mm.

The gas flame was stabilized near the exit of the injector by employing an array of four hydrogen capillary flames. The flame tubes were mounted in a symmetrically opposed pattern injecting toward the centerline of the injector passage. The flow passages for the hydrogen were slots 0.4 mm wide and 2 mm long, with the long axis parallel to the injector centerline. The lower edges of the slots

were 1.8 mm above the face of the injector. The exit planes of the slots were 6.4 mm apart.

The propane gas flow rate was metered with a Matheson model 604 rotameter, and the pressure was controlled by a Harris model 2515 pressure regulator with an output capacity of 0.069 MPa. The pressure upstream of the rotameter was monitored with a Heise absolute-pressure gauge with a range of 0.0-2.07 MPa, and the downstream pressure was monitored with a Heise absolute-pressure gauge with a range of 0.0-0.41 MPa. The flow rate of the hydrogen gas was metered with a Matheson model 601 rotameter, and the pressure was controlled with a Matheson model 1H pressure regulator having a 0.138 MPa output capacity. The rotameters for both the propane and hydrogen flows were calibrated with a Precision Scientific Company wet-test meter (283 ml/rev).

Slurry droplets were mounted on fine-wire platinum/platinum-10% rhodium thermocouple with a 50 μm wire diameter. The thermocouple junction was encased in a 400 μm bead of Sauereisen cement to help support the drop. The thermocouple was mounted, in turn, on a metal bracket which extended into the flame.

A hypodermic syringe was employed to mount the slurry droplets on the thermocouple probe. The syringe was capable of producing drops in the 500-5000 μm diameter range. The flame was deflected from the mount region until the droplet was in place. The deflector was constructed from a 200 x 305 mm sheet of stainless steel 3 mm thick. The carbon-particle combustion process was initiated by removing the deflector with a pneumatic-cylinder arrangement.

2.2.2 Instrumentation

2.2.2.1 Drop Environment Measurements

The drop environment at each test location within the flame was characterized in previous studies [149,150,151]. These studies involved measurements of mean velocity, temperature and concentration.

2.2.2.1.1 Velocity Measurements

Velocity measurements along the centerline of the propane flame were conducted with a single-channel laser-Doppler anemometer (LDA). An equipment list for the LDA is supplied in Table 1. A schematic of the LDA arrangement is shown in Figure 7. This unit employed a helium-neon laser operating in the dual-beam, forward-scatter mode. The laser power was 50 mW. The sending and receiving optics had a focal length of 241 mm with an 11.6° angle between the beams. The aperture diameter of the photodetector was 0.256 mm. The signal was focused on the photodetector with a 200 mm lens. This produced an ellipsoidal measuring volume 3.0 mm in length with a diameter of 0.31 mm. A frequency shifter was used so that flow reversals could be detected. Interference of the light from the flame was eliminated with a band-pass filter.

The LDA actually measures the velocity of small seeding particles in the flow. The soot that formed in the flames provided a portion of the seeding particles in the region of combustion. In order to avoid biasing the signal, seeding was also added to the surrounding air in the region where measurements were being made. These seeding

Table 1.   LDA Equipment List

Component	Manufacturer	Model
Helium-Neon Laser	Spectra Physics	125A
Integrated Optics	Thermo-Systems	900
Frequency Shifter	Thermo-Systems	980
Photodetector	Thermo-Systems	960
Tracker	Thermo-Systems	1090
RMS Voltmeter	Thermo-Systems	1076
Dual Beam Oscilloscope	Tektronix	912
Integrating Voltmeter	Hewlett-Packard	240IC
Bandpass Filter	Thermo-Systems	957
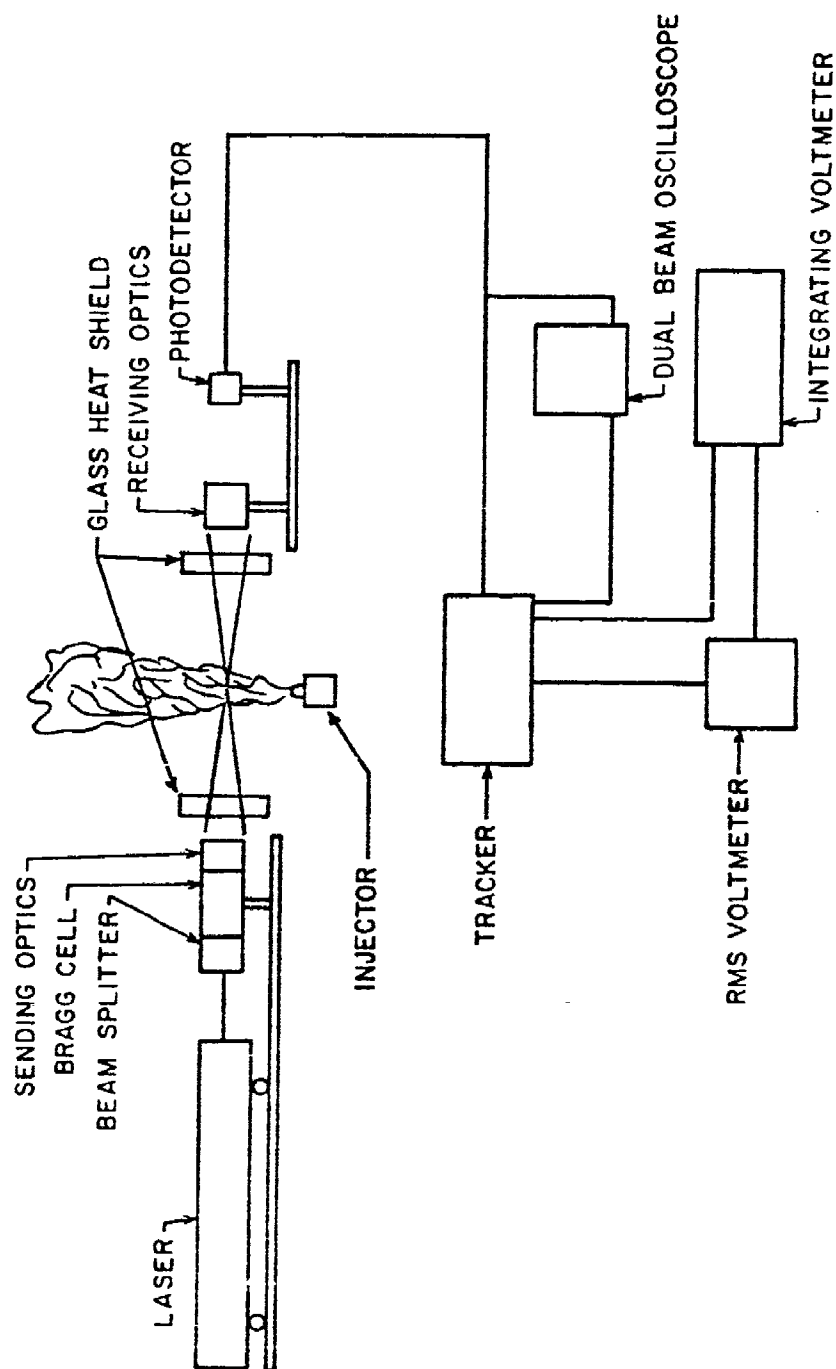
Figure 7. Schematic Diagram of the LDA System.

particles were produced as oil vapor condensed in an air stream passing through an oil heater. The seeding rate was controlled by varying the heat flux and air flow rate. The air-vaporized oil mixture was passed through a condenser tube upon leaving the oil heater. The length of the condenser tube could be varied so that the air-oil droplet mixture entered the test air at approximately the ambient temperature. The oil heater-condenser tube apparatus was positioned so that the particles approached the combusting jet at the approximate entrainment velocity.

As the seeding particles pass through the measuring volume they scatter light. The photomultiplier picks up signals and transfers them to the frequency shifter (which also supplies power for the Bragg cell) and then to the tracker. The tracker process and analyzes the signals and then sends the verified signals to the integrating digital voltmeter, the true RMS meter, and the oscilloscope (which monitors the quality of signals).

The frequency tracker provides a signal proportional to the instantaneous flow velocity in the measuring volume. This signal can be processed similar to a hot-wire detector signal. Mean velocities were found by integrating the signal, fluctuating velocities could be found with a true RMS meter. Various velocity components and the Reynolds stress could be found by rotating the plane of the laser beams. The data reported at each location was the average of at least three measurements each integrated over a period of one minute. At axial locations close to the injector, the tracking signals were too

infrequent to maintain a continuous signal. The occurrence of this discontinuous signal ruled out the use of the integrating voltmeter. Therefore, 150 individual signals were recorded from the tracker and their average was used to determine the velocity quantities.

2.2.2.1.2 Temperature Measurements

The mean gas temperatures along the centerline of the turbulent-diffusion flame were measured using the thermocouple probe illustrated in Figure 8. The temperature probe was constructed from 25 µm diameter platinum/platinum-10% rhodium wires which were spot-welded onto 750 µm diameter lead wires of the same material. The fine-wire thermocouples were manufactured by Omega Engineering, Incorporated. The 25 µm thermocouple wire was used when possible; however, at positions close to the injector, the temperature was high enough to cause the thermocouple probe to fail. When this occurred, thermocouple wire with a 50 µm diameter was used.

The maximum radiation correction for this temperature probe was less than 35°C over the test range. The reference junction was at the ambient temperature, shielded from the flame. An integrating digital voltmeter was used to average the signal over a two-minute time period.

2.2.2.1.3 Concentration Measurements

Mean concentration measurements were conducted along the centerline of the turbulent-diffusion flame. The gas samples were

extracted from the flow at nearly isokinetic conditions using the water-cooled probe illustrated in Figure 9. Both the inside and the outside tubes were stainless steel, and the inside tube had a 2 mm internal bore. The tip of the probe tapered back from 3 mm to 6 mm in external diameter over a distance of about 10 mm. The internal tube was cooled by water which gave substantial cooling within 2 mm of the tip. The temperature of the cooling water was maintained constant at about 339 K ($\pm$ 3 K) in order to avoid condensation of fuel and water vapor in the probe. The flows were isokinetically sampled by applying a suction to the sampling probe and measuring the sampling flow rate. The flow rate through the sampling probe was adjusted to match the local flow rate determined from the velocity measurements. The sampling flow rate was measured with a Precision Scientific wet-test meter (28.3 ml/rev.).

The samples were analyzed with a Perkin Elmer, Model 880, gas chromatograph using a hot-wire detector. A 1.0 ml gas-tight syringe was used to transfer the sample from the sampling port to the gas chromatograph. The response of the hot-wire thermal-conductivity detector was recorded with a Leeds and Northrup Speedomax Strip Chart Recorder.

A Carbosieve, type B, 60-80 mesh column was used to measure the propane concentration in the combusting-gas jet. The column was .92 m x 3.2 mm O.D. stainless steel and was manufactured by Supelco, Incorporated. The flow rate of the carrier gas, helium, was maintained at 50 ml/min. The column temperature was varied from

LEAD WIRE
0.75mm DIA

0.8m

STAINLESS STEEL
SUPPORT ROD

CERAMIC INSULATOR

9.5mm

THERMOCOUPLE WIRE
0.025mm or 0.050mm DIA
PT/PT-10% RH
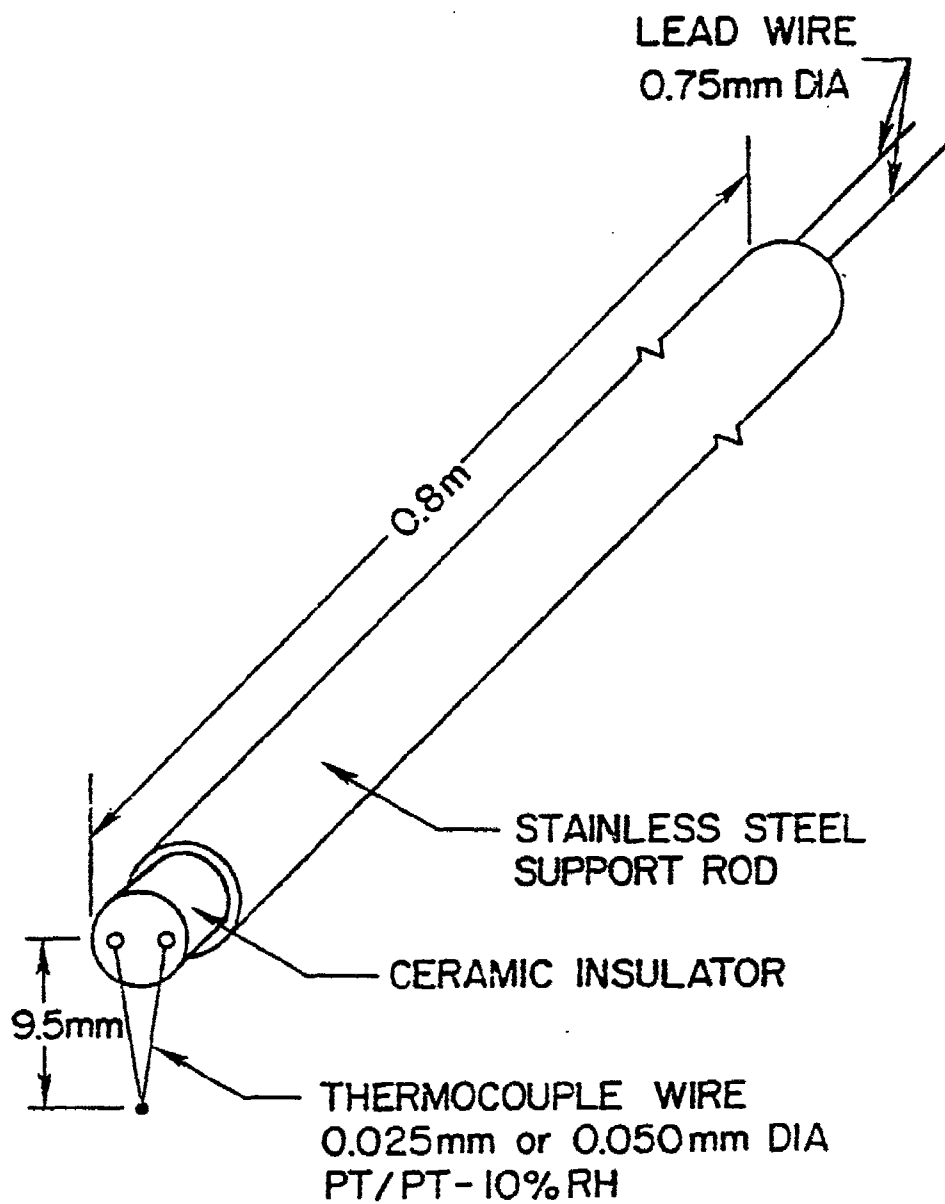
Figure 8.   Sketch of the turbulent diffusion-flame gas-temperature probe.
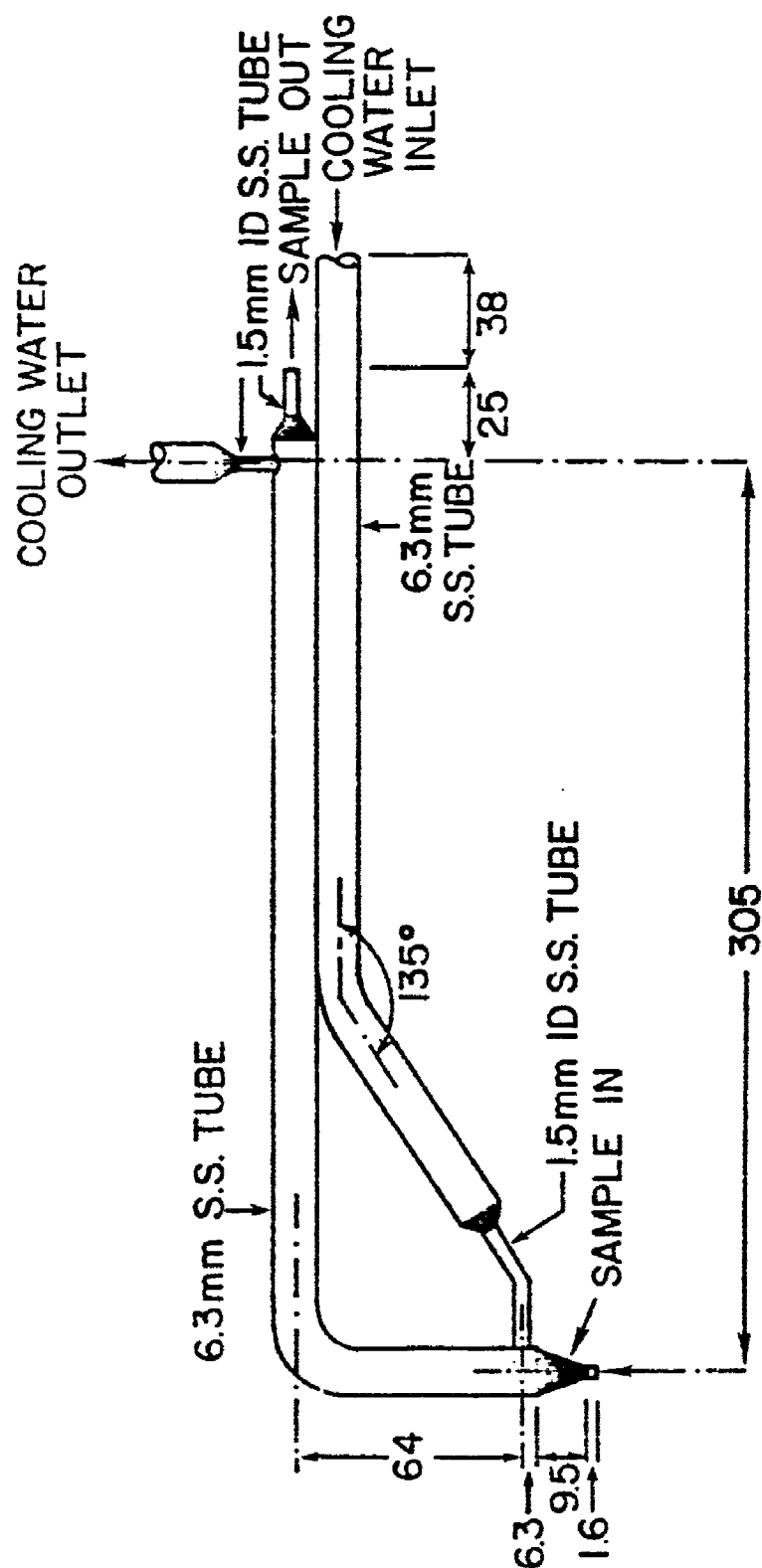
DIMENSIONS IN mm

Figure 9. Sketch of the probe used for gas-concentration measurements in the turbulent diffusion-flame test.

175°C to 225°C with temperature programming at 30°C/min. The column was calibrated using calibration gases manufactured by the Scott Company. The sample size used for the propane concentration measurements was 0.5 ml.

The permanent gases (oxygen, nitrogen, carbon monoxide, carbon dioxide, hydrogen and water vapor) were analyzed using a Carbosieve, type S, 100-120 mesh, 2.1 m x 3.2 mm O.D. stainless-steel column. The gas chromatograph was programmed for a four minute hold at 30°C, followed by temperature programming from 35°C to 175°C at 24°C/min. Helium was used as the carrier gas at a flow rate of 25 ml/min. The column was calibrated for oxygen, nitrogen, carbon monoxide and carbon dioxide using calibration gases manufactured by the Scott Company. The column was calibrated for water vapor by extracting samples over a liquid water surface maintained at a constant temperature at atmospheric pressure. The saturation pressure corresponding to the liquid temperature provided the mole fraction of water vapor in the air-vapor mixture. The column was calibrated for hydrogen by preparing samples of hydrogen and air whose composition was known on a volume basis. In each case, the sample size used was 0.5 ml.

2.2.2.2 Drop Measurements

Two slurry fuels, provided by Suntech Group, were examined during the tests. The fuels consisted of a medium-thermal carbon black having an ultimate particle size of 0.3 μm, with JP-10 as the liquid fuel, c.f., Reference 2 for more complete specifications. The bulk of the testing was conducted with a noncatalyzed slurry with

50.4% dispersed carbon by weight. A catalyzed slurry, which had 49.2% dispersed carbon by weight which contained a proprietary lead compound as a catalyst, was also considered. The properties of the carbon slurry fuels are summarized in Table 2. While these fuels are representative of carbon slurries, fuel development efforts are continuing and they do not necessarily represent the most attractive formulations.

Samples of the carbon agglomerates were obtained by quenching the process by redeflecting the flame. Carbon residue left on the probe after combustion was examined with a scanning electron microscope, International Scientific Instruments, model M-7. Permanent records of appearance of the residue were obtained with Polaroid, type 52, fine-grain film.

2.2.2.2.1 Diameter Measurements

The drop combustion process was observed with a 16 mm, Photosonics, model 16-B, motion-picture camera. The camera was powered by a Kepco, SM 36-5 AM D.C. power supply. The film speed was indicated with a timing light on the camera, activated with an Adtrol Electronic pulse generator, model 501. Kodak Plus-X reversal film was used for all tests.

Backlighting for shadowgraph measurements was provided by a Pek, model 401A, 75W mercury arc lamp. The light from the arc was collimated and directed toward the drop location. A diffuser screen was employed behind the drop to equalize the light intensity of the background. The background intensity was adjusted so that envelope flames around the drop could be observed.

Table 2. Properties of the Carbon Slurry Fuels[a]

	Noncatalyzed	Catalyzed[b]
Designation	790-928	790-942
Liquid	JP-10	JP-10
Dispersed Carbon[c] (wt %)	50.4	49.2

[a]Fuels supplied by R. S. Stearns, Suntech, Inc.,
P. O. Box 1135, Marcus Hook, PA 19061.

[b]The catalyst is a proprietary lead compound [2].

[c]The dispersed carbon is a medium thermal carbon (carbon
black) having an ultimate particle size of 0.3 μm.
Further properties of this material are provided in
Reference 2.

The film records were analyzed on a frame-by-frame basis, with a Vanguard motion picture analyzer. Photographs of objects of known size at the drop location provided a calibration of distances on the film.

2.2.2.2.2 Temperature Measurements

The carbon-agglomerate temperature was measured during the combustion process with the thermocouple temperature probe discussed in the previous section and a Nicolet, model 206, analog-to-digital recording oscilloscope. The Nicolet has a memory capacity of 4096 data points. The combustion process of a large carbon agglomerate was completed within 10 seconds. This gave a time between samples less than 2.5 milliseconds which proved to be more than adequate to record any temperature variation of the carbon particle during the combustion process.

2.2.3 Experimental Conditions

The bulk of the testing was undertaken at locations along the centerline of the gaseous propane diffusion flame, between 75 and 600 injector diameters from the injector. No external ignition source was employed for these tests. A single operating condition was employed for all tests and is summarized in Table 3. A photograph of the flame appears in Figure 10.

A summary of mean velocities, temperatures and compositions in the flow is presented in Figure 11. A complete analysis of this flame

Table 3.   Turbulent Diffusion-Flame Characteristics[a]

Fuel:	propane
Fuel flow rate:	176 mg/s
Initial fuel jet velocity	88.7 m/s
Initial fuel jet diameter:	1.194 mm
Jet Reynolds number:	23600
Orientation:	vertical (upward)
Flame Height:	460 mm (visual)
Injector Thrust:	15.6 mN
Hydrogen flow rate:	0.126 mg/s
Ambient and injector inlet temperature:	296 K
Ambient pressure:	97 kPa

[a]The nozzle is Spraying Systems Company model 1/4J 2050 fluid nozzle and a model 67147 air nozzle, air atomizing injector.

Figure 10. Photograph of the turbulent gas-diffusion flame.
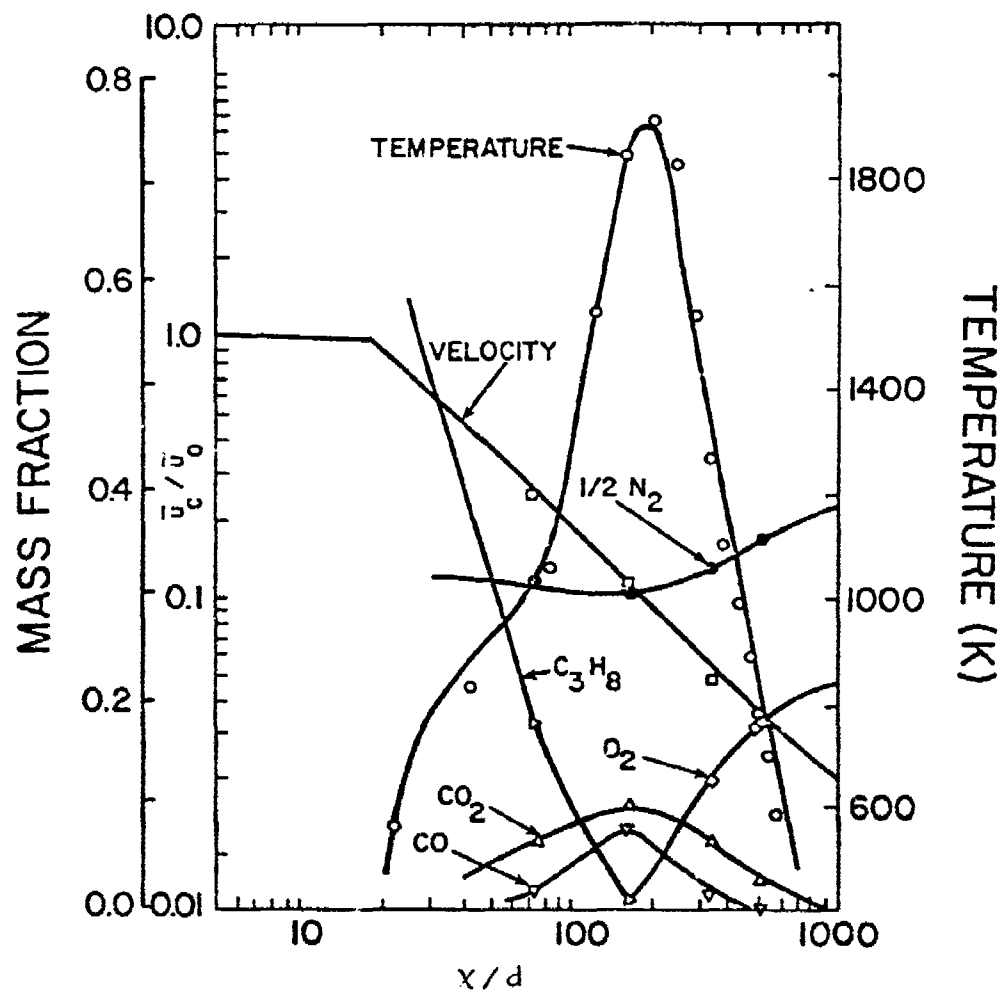
Figure 11. Flow properties of the turbulent propane diffusion flame. Note: x/d indicates injector diameters downstream from injector, and $\bar{u}_c/\bar{u}_o$ indicates centerline velocity normalized by injector velocity.

appears elsewhere [149,150,151]. The chosen operating condition gave a variation of equivalence ratio of approximately 0.2 to 1.4, and a temperature range of approximately 600 to 1900 K along the flame centerline. Initial slurry-drop sizes were in the range of 500-1500 μm.

2.3 Laminar Premixed Flame Apparatus

2.3.1 Test Apparatus

A sketch of the laminar-premixed flame apparatus appears in Figure 12. The arrangement basically consists of a slurry-droplet generator, a convergent-flow section, a liquid evaporation section, and a flat-flame burner. The monodispersed drops produced in the drop generator are accelerated in the convergent-flow section, and the liquid fuel evaporated from the drop in the heated section leaving behind an agglomerate of solid-carbon particles. The carbon agglomerates then passed through a flat flame where they reacted. A sampling probe placed above the flat-flame burner collected the carbon agglomerates for further analysis.

The laminar-premixed flat flame was fueled with a mixture of gaseous nitrogen, oxygen, carbon dioxide, carbon monoxide, methane and hydrogen using rotometers to blend in the desired amount of a specific gas. The mixing pressure was monitored with a Heise absolute-pressure gauge having a pressure range of 0.0-0.41 MPa.

A Matheson rotameter, model 605, was used to meter the nitrogen flow rate. The oxygen, carbon dioxide and methane gas flow rates were
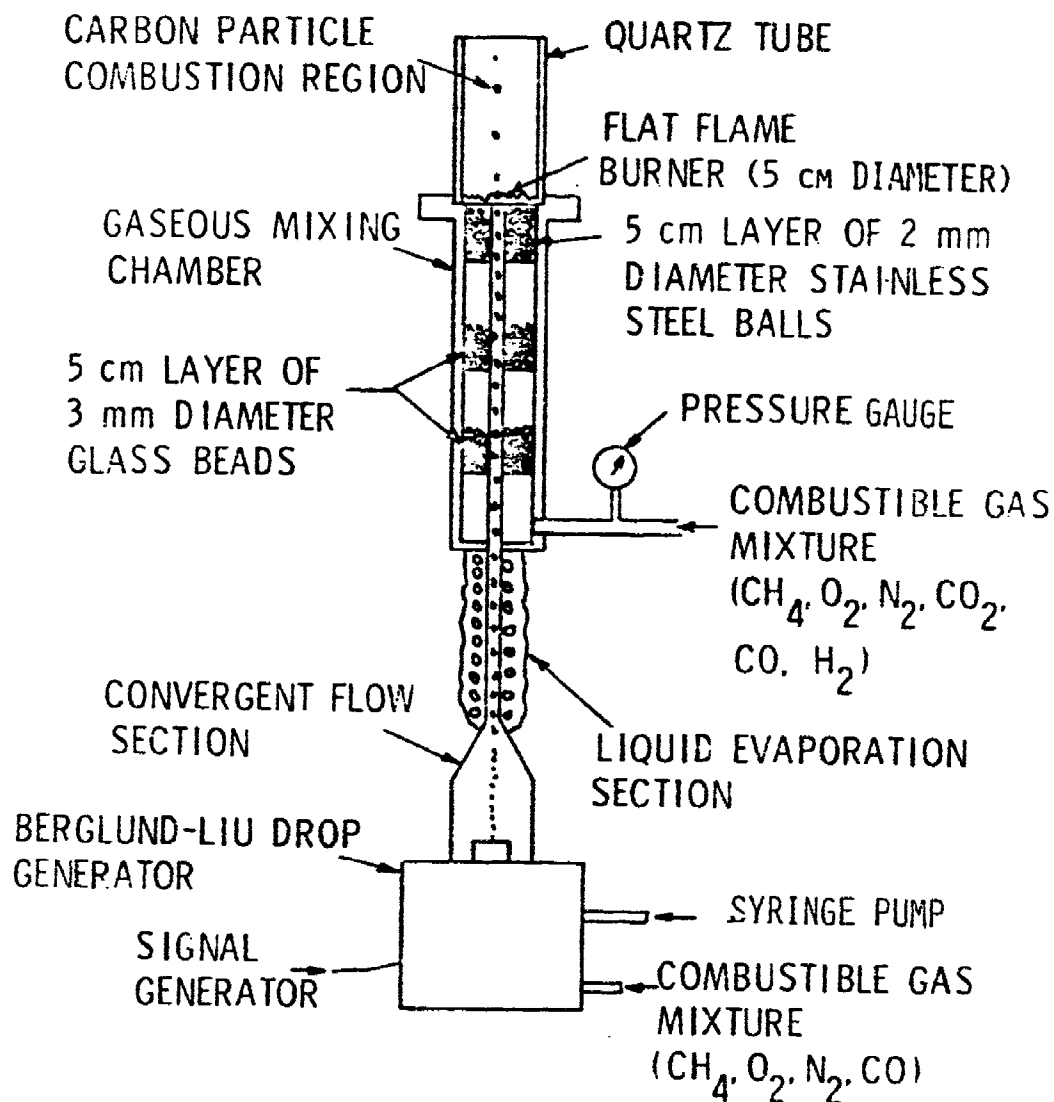
Figure 12.   Schematic diagram of the particle generator
and laminar premixed flame apparatus.

all metered with Matheson model 604 rotameters, while carbon monoxide and hydrogen were metered with a Matheson model 603 rotameter. All of the rotameters were calibrated with a 283 ml/rev Precision Scientific Company wet-test meter.

The pressures of the gases entering the rotameters were controlled using model 8H Matheson two-stage pressure regulators for nitrogen, carbon monoxide, methane and hydrogen. The oxygen pressure was controlled using a model 92-100 Harris two-stage regulator, and the carbon dioxide pressure was controlled using a model 1H Matheson two-stage regulator. Each pressure regulator had an output pressure capacity of 0-1400 kPa.

Gas mixing was aided by flowing the gases through a length of 10 mm I.D. tubing equal to approximately 150 tube diameters. The gas mixture then entered the mixing chamber through a 6.4 mm diameter inlet on the side of the mixing chamber 25 mm from the bottom. The gaseous mixing chamber was constructed from a 51 mm nominal diameter schedule 40 stainless-steel welded pipe and had a length of 300 mm. An endcap over the lower opening and a 152 mm diameter flange around the upper opening were constructed from 13 mm thick stainless-steel plates.

To provide a thoroughly mixed fuel gas with a uniform-velocity profile, several layers of small beads separated by a void space were provided in the gaseous mixing chamber. Upon entering the mixing chamber, the gas encountered a 50 mm high void space followed by a 50 mm layer of 3 mm diameter solid spherical glass beads. The gas

mixture then encountered another 50 mm high void space, another 50 mm layer of the same type of glass bead, and another 50 mm high void space. Finally the gas encountered a 50 mm layer of 2 mm diameter stainless-steel balls. The two layers of glass beads and the layer of stainless-steel balls were supported by a 20 mesh size stainless-steel screen which was spot-welded to the sides of the mixing chamber. A much finer stainless steel screen with a mesh size of 100 was placed immediately on top of the 20 mesh size screen. The glass beads or stainless steel balls were then in turn placed upon the 100 mesh size screen.

After passing through the stainless-steel balls, the fuel gas was ignited and a flat flame was stabilized near the top surface of the balls. The flat flame was measured to be approximately 1-2 mm thick. The flame appeared completely uniform, and was stable at all operating conditions.

The ability of mixing the fuel gases together in any combination enables the system to operate under a wide range of conditions. Equivalence ratios between 0.2 and 1.4 were obtained during the tests. The temperatures of these flames could be varied between 1600 K and the softening temperature of stainless steel. By adding either carbon monoxide and carbon dioxide, or hydrogen along with the methane, the C/H ratio can be varied over a very wide range. Finally, the stainless-steel balls inhibit flash-back and aid in flame attachment such that the gas velocity above the flat-flame burner can be varied between 0.5 and 3.0 m/s.

An ignitor was constructed over the flat-flame burner from 0.25 mm diameter nicrome heating wire. The heating wire was powered from an Ohmite 120 volt, 4.75 amp. Variac; and a 12.6 volt, 3 amp. transformer. Once the flame was ignited, a 53 mm I.D. quartz tube was placed on the burner surface using asbestos coated forceps. The quartz tube surrounded the flame to prohibit entrained air.from mixing with the products of combustion and lowering the flame temperature. The quartz tube also helped maintain a uniform high temperature of the products of combustion far above the burner. The quartz tube was cut into sizes ranging from 50 mm to 200 mm in 50 mm increments to facilitate the access of measuring probes to various locations above the flat flame.

The droplet generator consisted of a TSI model 3050 Berglund-Liu vibrating-orifice monodisperse-aerosol generator, a Sage model 355 continuously-variable syringe pump, and a Hewlett-Packard model 3310B function generator. Three different orifices were used in the Berglund-Liu drop generator: a TSI model 10356 100 μm orifice, a TSI model 10355 50 μm orifice and a TSI model 10353 20 μm orifice. Both a 10 and 50 ml reusable multifit syringe with metal luer tips were used with the syringe pump.

A mixture of methane, oxygen, carbon monoxide and nitrogen was used in the Berglund-Liu droplet generator as the dilution and dispersion flows. The fuels were mixed in proportions to yield the same equivalence ratio and C/H ratio as the fuel mixture in the flat-flame burner assembly. The dispersion flow separates the droplets as

they are formed and transports them away from the orifice to prevent clogging. The dilution flow is used to vary the droplet concentration. The dispersion flow makes up a very small fraction of the total flow and the dilution flow the majority of the total flow. The flow rates of the methane, oxygen, carbon monoxide and nitrogen were all metered with Matheson, model 602, rotameters, which were calibrated using a Precision Scientific Company wet-test meter (28.3 ml/rev). The pressures of the methane, carbon monoxide and nitrogen flows were controlled with Matheson, model 8H, two-stage pressure regulators. The oxygen flow pressure was controlled with a Harris, model 92-100, two-stage pressure regulator.

Only the noncatalyzed slurry with 50.4% dispersed carbon by weight in JP-10 liquid fuel was used for laminar-premixed flame tests. In order to generate slurry droplets with the Berglund-Liu droplet generator without clogging the orifice, the slurry had to be thinned. N-pentane was mixed with the slurry fuel, and it was determined that the carbon particles remained suspended in the mixture for several hours. Thus, mixtures of carbon slurry and n-pentane ranging from one to five parts n-pentane per part of volume of slurry were used in the droplet generating system.

The syringe pump was adjusted to the minimum velocity necessary to establish a liquid jet emerging from the orifice in the Berglund-Liu droplet generator. The frequency of the signal generator was set at a value between 1000 and 4000 Hz. Thus, between 1000 and 4000 drops per second were formed ranging in initial diameter between 24

and 270 μm.   Using the 50 ml syringe allowed continuous operation for up to 3.5 hours.

The Berglund-Liu droplet generator exhausted the slurry droplets into a 50 mm length of a 115 mm diameter plexiglass tube.   The plexiglass tube was connected to a stainless-steel 45° convergent cone, which was attached to the plexiglass with silicon sealant.   The cone was 40 mm high, had a 115 mm diameter opening at the base and a 3.4 mm diameter opening at its tip. The outlet of the cone was welded to a tube having an inner diameter of 3.4 mm and a length of 610 mm. The top end of this tube was welded to a tube with a 1.8 mm inner diameter and a length of 460 mm.   This tube passed through a Conax Corporation thermocouple sliding seal at the bottom of the mixing chamber.   The top end of the 1.8 mm diameter tube was flush with the surface of the flat-flame burner.   Great care was taken in the construction of the droplet guide to assure a smooth flow transition between the individual components.

Nichrome heater wire and fiberfrax ceramic insulation were wrapped around the outside of the 3.4 mm diameter section. Thus, when a particle left the Berglund-Liu droplet generator it was accelerated through the convergent core section of the droplet guide.   Next, the droplet entered the 3.4 mm diameter section which was heated to 600 K by the nichrome heating wire and a 120 volt, 4.75 amp. Ohmite variac. In this region the liquid fuel evaporated leaving behind an agglomerate of solid-carbon particles. The evaporating liquid also served to further accelerate the agglomerate. When the gas flow

emerged from top of the 1.8 mm diameter tube it had the same equivalence ratio, CH ratio and velocity as the surrounding gas of the flat-flame burner. The particle velocity was somewhat lower than the flow velocity due to the gravity effects on the particle. The initial size of the carbon agglomerates leaving the 1.8 mm diameter tube ranged between 10 and 140 m. The particles continued to flow up through the quartz tube as they reacted.

Figure 13 is a time exposure photograph of the carbon agglomerates passing through the flat-flame burner and reacting. The quartz tube described as shown in Figure 12 was not in place for this photograph, and as a result the particles began to cool upon exiting the hot potential core of the flame. Although the particles do disperse somewhat, the photograph show that the particles travel in a straight line producing a streak approximately 3 mm wide at the base for an initial particle diameter of 73.4 m.

2.3.2 Instrumentation

2.3.2.1 Particle Environment Measurements

The particle environment was characterized by measuring the velocity, temperature and concentration of the gas along the centerline of the laminar-premixed flame.

2.3.2.1.1 Velocity Measurements

Velocity measurements were made along the centerline of the laminar-premixed flat flame with basically the same laser-Doppler anemometer as for the turbulent-diffusion flame velocity measurements.
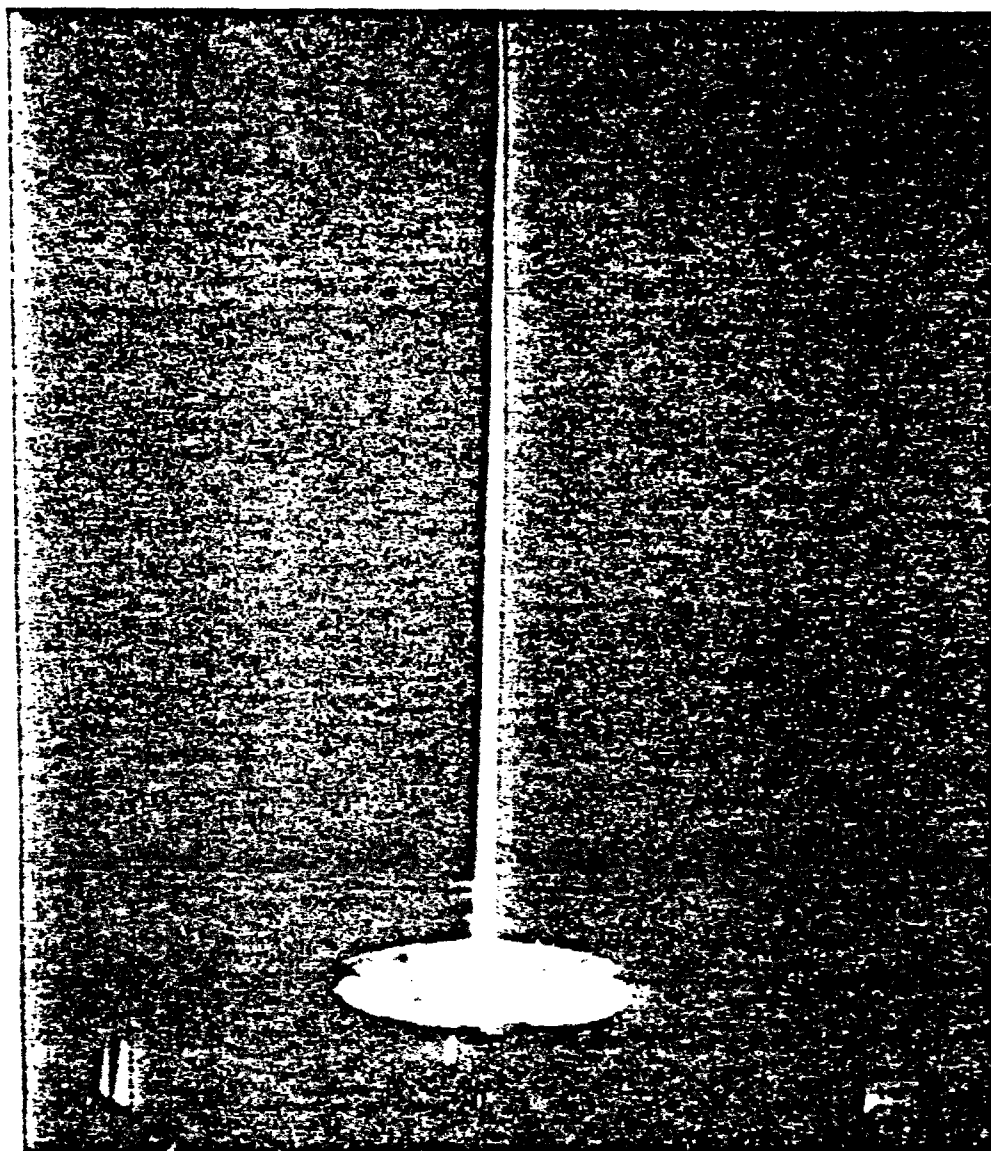
Figure 13. Time exposure photograph of the particles reacting above the flat-flame burner.

However, for the velocity measurements of the laminar-premixed flame a smaller laser was employed (Spectra-Physics Helium-Neon laser, model 120, with a power output of 5.0 mW), the laser was operated in the back-scatter mode, and the tracker was replaced by a burst-counter (TSI model 1984 input conditioner, TSI model 1985 timer, TSI model 1942 readout and TSI model 1988 analog output).

The laminar-premixed flame did not provide a sufficient seeding particle density for the LDA to give gas velocity measurements. In order to increase the seeding concentration of the flow, a particle generator based on a reversed-cyclone separator described by Glass and Kennedy [152] was constructed. Micron-sized aluminum-oxide particle (TSI model 10083) were generated since they have acceptable refractory properties to permit their use in combusting flows.

The reverse-cyclone separator particle generator employed in this investigation is illustrated in Figure 14. The overall height of the seeder was 380 mm. During the particle generator operation a 30-60 mm layer of aluminum-oxide seeding particles were stored at the bottom of the particle generator. The dry filtered gas mixture entered the seeder horizontally and tangentially through a 5 mm diameter stainless-steel tube 280 mm from the bottom of the particle generator. The gas traveled tangentially around the particle generator and mixed with the seeding particles. The air stream and entrained particles then left the particle generator through a 20 mm inner diameter plexiglass tube located at the top of the particle generator. The entrance to the seeding particle guide was at the same height as the tangential gas inlet.

SEEDING PARTICLE GUIDE
20 mm DIAMETER
PLEXIGLASS TUBE

76 mm I.D.
PLEXIGLASS TUBE

TANGENTIAL GAS
INLET
5 mm DIAMETER
TUBE

FLOW
STREAM
LINE

380 mm

280 mm

ALUMINUM
OXIDE
SEEDING
PARTICLES
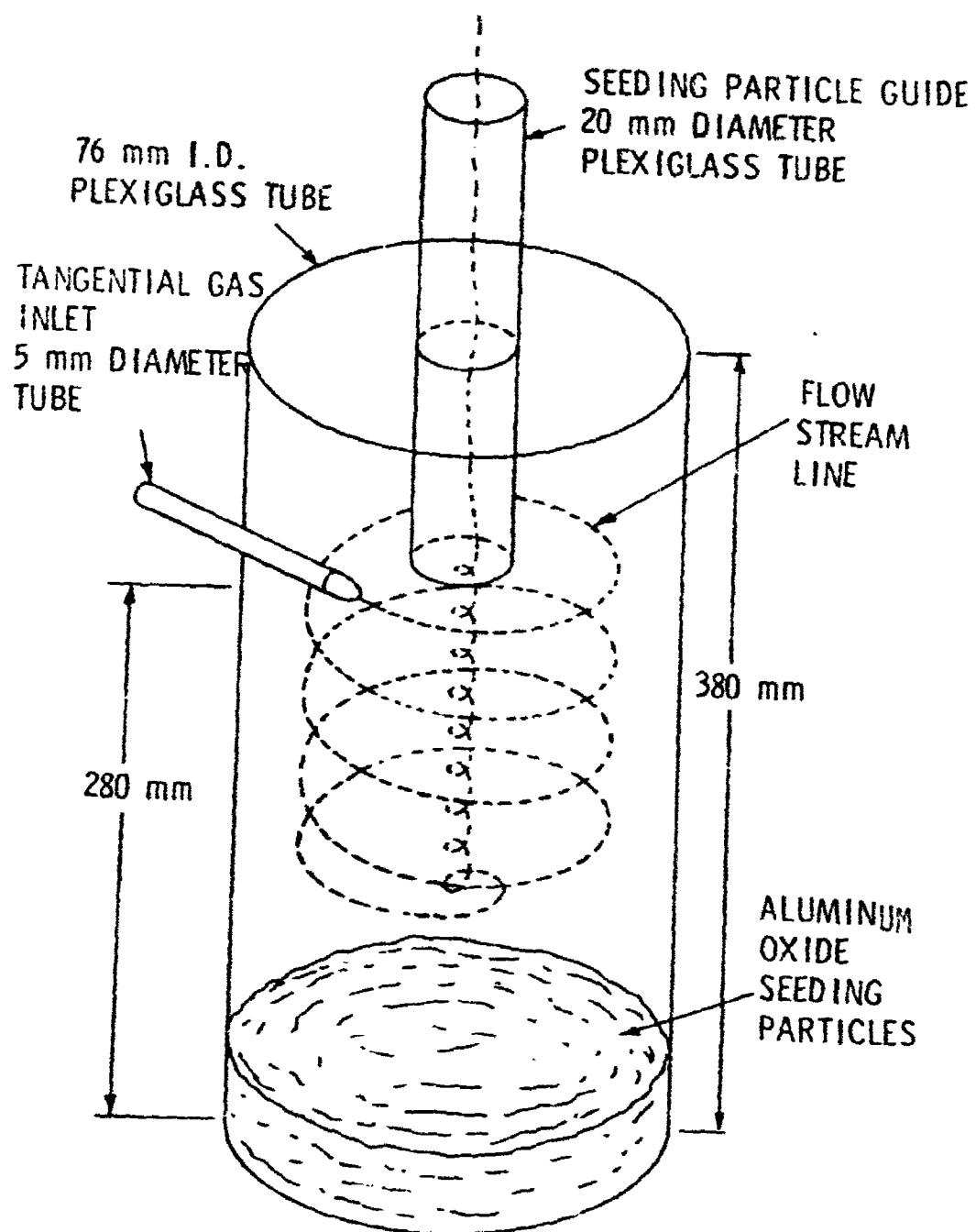
Figure 14.   Schematic diagram of reverse-cyclone-separator
combustion-flame particle seeder.

The reverse-flow cyclone particle seeder was operated with an air flow rate of 540 cm^3/s, which gave a seeding rate of 1.1×10^9 particles/m^3. Between 3.5 and 5.0 cm^3/s of the seeded flow was bled from the main flow and injected through a 1.8 mm inner diameter tube to the centerline of the flat-flame burner. The exit velocity, C/H ratio and the equivalence ratio of the flow was matched to the fuel-gas flow entering into the flat-flame burner. The remaining portion of the seeded flow was routed to a collection chamber with a filter to salvage the unused aluminum-oxide particles.

2.3.2.1.2 Temperature Measurements

The gas temperature along the centerline of the laminar-premixed flat flame were measured using the thermocouple probe illustrated in Figure 15. The temperature probe was constructed from 25 µm diameter platinum/platinum-10% rhodium wires which were spot-welded onto 50 µm diameter lead wires of the same material. The thermocouple wires were manufactured by Omega Engineering, Incorporated. The temperature probe was mounted on a 320 mm Unislide traversing mechanism which allowed the probe to be positioned at various locations along the centerline of the laminar-premixed flat flame.

The emissivity of the thermocouple was maintained at a low level of approximately 0.22 $\pm$ 0.02 by coating the thermocouple with a layer of silica [153]. This was accomplished by flowing the silicon oil ladened exhaust of a model 1402 Sargent-Welch Scientific Company duo-seal vacuum pump over the thermocouple while the thermocouple at

TO INTEGRATING
VOLTMETER

50 μm DIAMETER PLATINUM/
PLATINUM—10% RHODIUM THERMO-
COUPLE LEAD WIRE

6.4 mm O.D. TUBE,
SILVER SOLDERED TOGETHER

500 mm

TWO-HOLE CERAMIC INSULATOR

SAUEREISEN CEMENT

13 mm

25 μm DIAMETER PLATINUM/PLATINUM—
10% RHODIUM THERMOCOUPLE
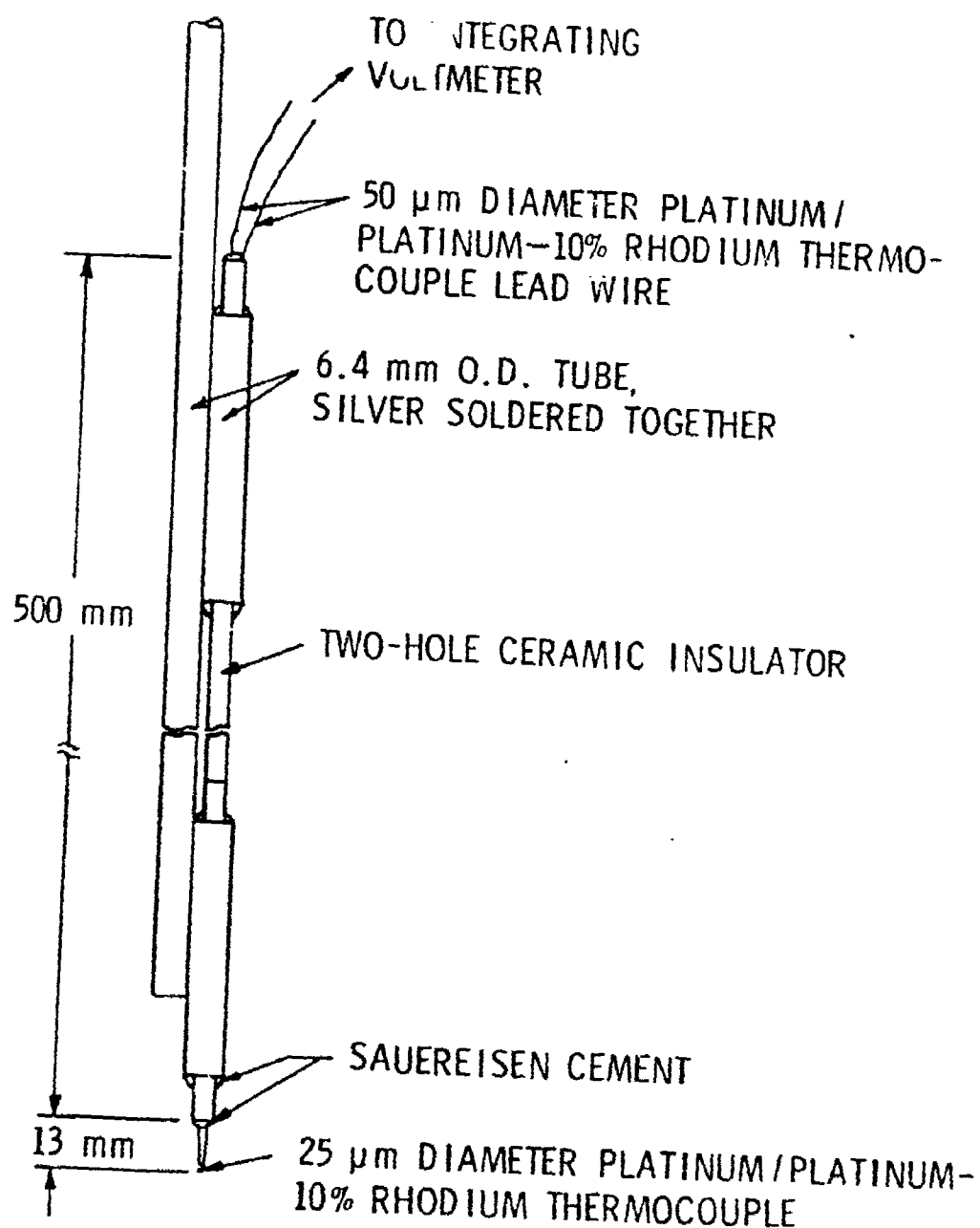
Figure 15.   Sketch of the temperature probe used in
the laminar premixed flame apparatus.

1800 K was protruding from a 1.8 mm diameter tube into the flat-flame burner. A silica layer with a thickness of approximately 3 μm was coated onto the thermocouple junction. The silica layer also eliminates the catalytic decomposition heating of the platinum thermocouple [153].

The platinum/platinum-10% rhodium thermocouple ·probe was calibrated with a 50 μm chromel/alumel thermocouple in a furnace environment where the radiation error would be minimized. The furnace was a Lindberg "Hevi-Duty", ype 54032-A, furnace with a power capacity of 960 watts. The furnace was powered by a Lindberg, type 59445 power supply. Both thermocouples agreed to within 6°C of each other up to a temperature of 1500 K, which was the maximum temperature of the furnace.

The maximum radiation correction for this temperature probe was 39°C over the test range. The reference junction was at the ambient temperature, shielded from the flame. A Hewlett-Packard, model 240IC, integrating digital voltmeter was used to average the signal over a two-minute period.

2.3.2.1.3 Concentration Measurements

The concentration measurements were made using a gas chromatograph (Varian model 3720, incorporating a thermal-conductivity detector). The gas samples were extracted from the flow at nearly isokinetic conditions using a small diameter probe shown in Figure 16. Both the inside and the outside tubes were stainless steel, and the inside tube had a 1 mm internal bore. The tip of the probe tapered
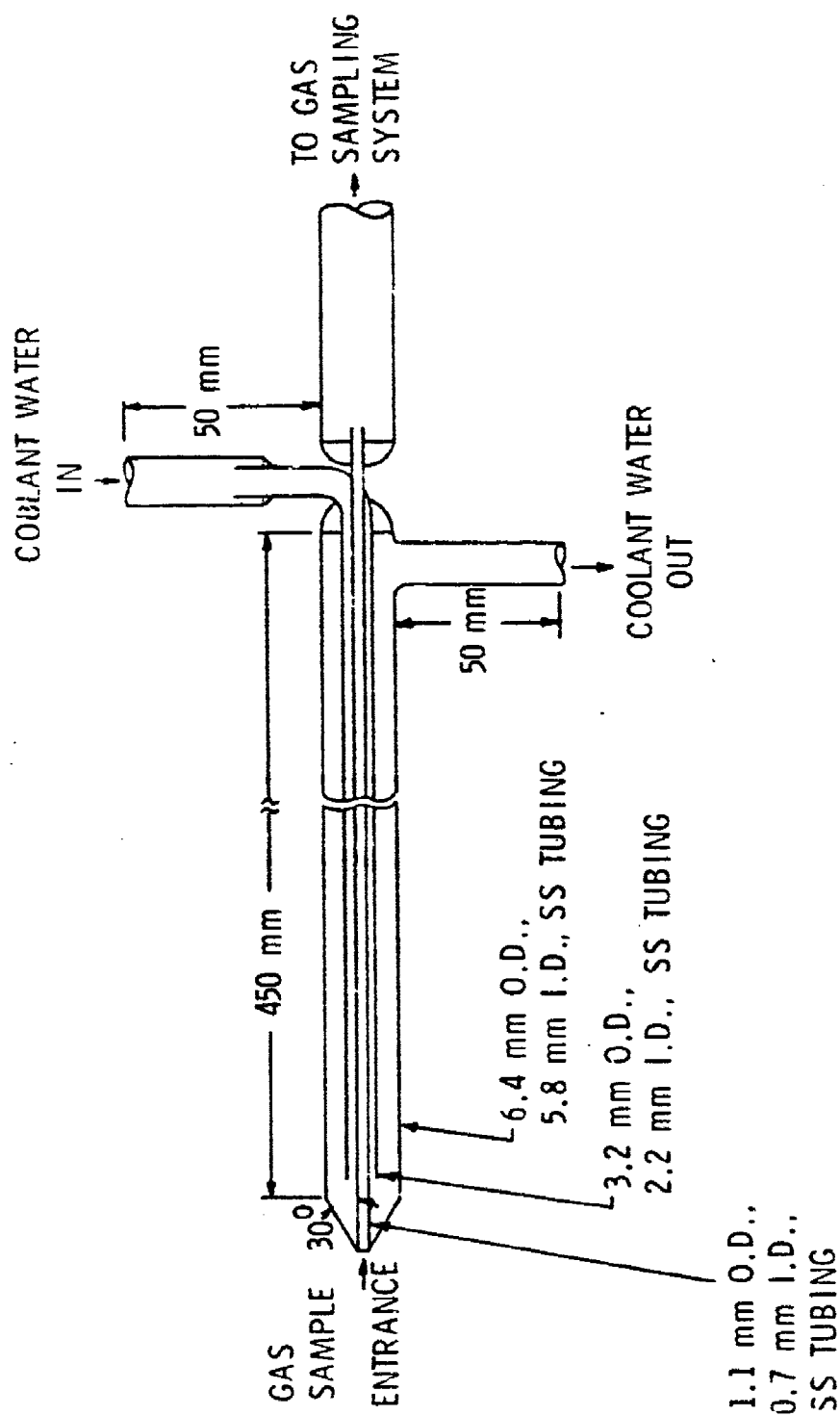
Figure 16. Sketch of the water cooled gas sampling probe used to measure the concentration of species above the laminar premixed flame apparatus.

back from 2 mm to 6 mm in external diameter over about 5 mm. The internal tube was cooled by water which gave substantial cooling within 2 mm of the tip. The temperature of the cooling water was maintained constant about 338 K ($\pm$ 2 K) to avoid the condensation of fuel and water vapor in the probe prior to the sampling point.

The samples were analyzed using a carbosieve column (Supelco, Carbosieve, type S, 100/120 mesh, 2.1 m x 3.2 mm stainless steel; 4 min. hold at 35°C; programming, 25°C to 175°C at 25°C/min.) for the analysis of hydrogen, oxygen, nitrogen, carbon monoxide, carbon dioxide and methane. The concentration of water vapor was obtained by a conservation of element analysis. Helium at a flow rate of 30 ml/min. was used as carrier gas. The output of the hot-wire thermal-conductivity detector was recorded with a Varian strip chart recorder.

The Carbosieve column was calibrated for hydrogen, oxygen, nitrogen, carbon monoxide, carbon dioxide and methane using calibrated gases manufactured by the Scott Company. The sample size used for the laminar-premixed flat flame composition measurements was 0.5 ml.

Since the products of combustion from a premixed methane flame contain a large mole fraction of water, the water must be condensed prior to gas analysis to avoid damaging the thermal-conductivity detectors in the gas chromatograph. The sampling system that accomplished this water condensation process is illustrated in Figure 17. The water-cooled gas-sampling probe is shown in position above the flat-flame burner. The gas-sampling probe was mounted on a 320 mm
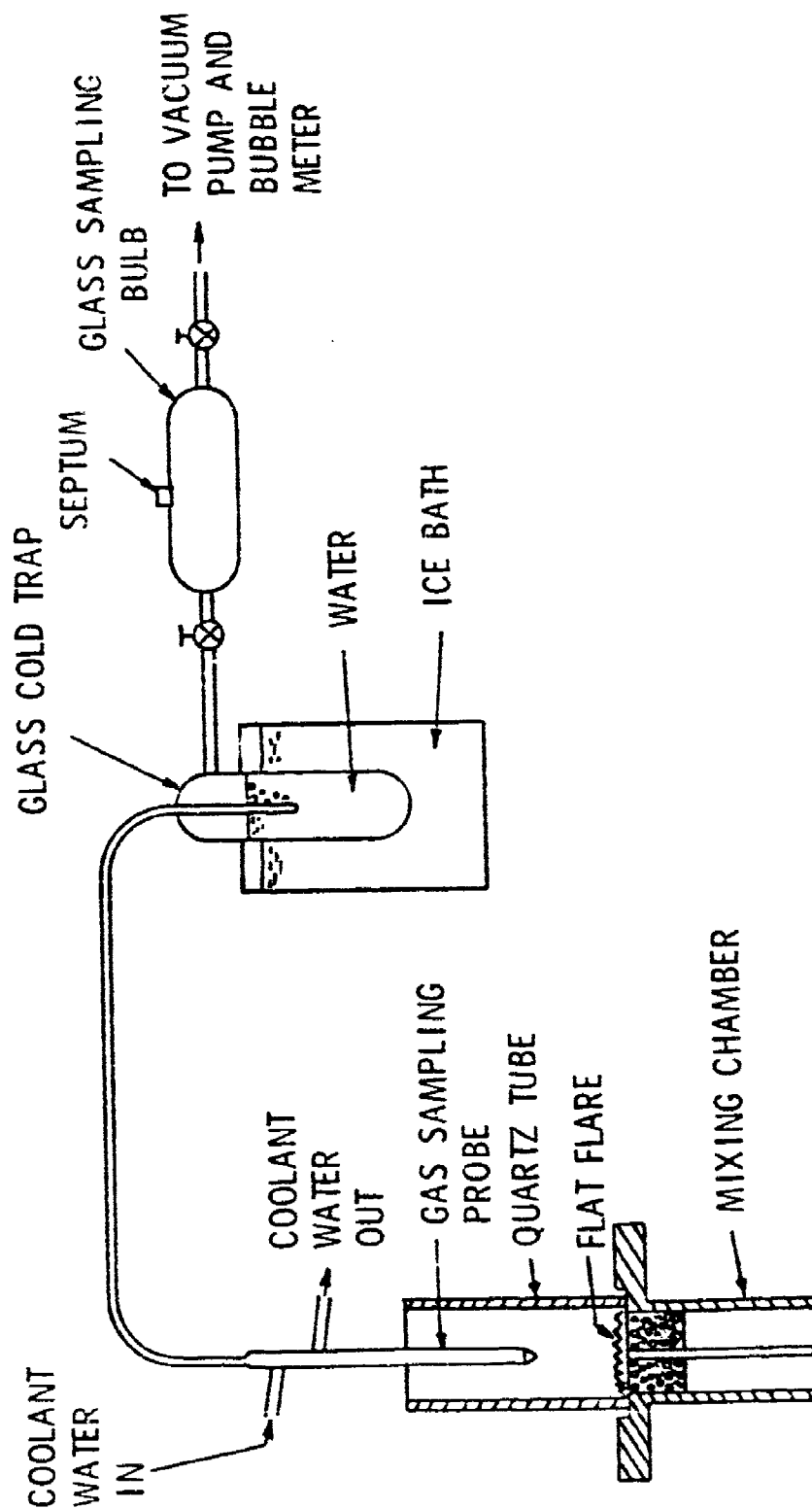
Figure 17. Sketch of the gas-sampling system of the laminar premixed flame apparatus.

Unislide traversing mechanism which allowed the probe to be positioned at various locations along the centerline of the laminar-premixed flat flame. The sample entered the probe where the temperature was approximately 338 K and the pressure 60.8 kPa, both of which help to quench any further gas reactions. The exhaust from the gas sampling-probe was directed to a glass cold trap (Supelco, model 2-2422) to condense a portion of the water vapor from the gas flow. The flow was then directed to a 125 ml glass sampling bulb (Supelco, model 2-2161). The sampling bulb was then connected to a Sargent-Welch Scientific Company duo-seal vacuum pump, model 1402. The flow rate was controlled with a Whitey forged-body regulating valve, model SS-1RS4, and metered with a Varian aerograph bubble meter.

The sampling procedure was to match the gas velocity at the sampling-probe inlet with the velocity of the the surrounding flow. After allowing the system to operate for approximately 5 minutes to purge the system, the stopcock on the downstream end of the glass sampling bulb was closed. After a few seconds the system reached pressure equilibrium, and the stopcock on the upstream end of the sampling bulb was closed. A 5 ml sample was then drawn from the septum on the glass sampling bulb with a 0-1.0 ml pressure-lok series "c" gas syringe, model 030033. The gas sample was then immediately taken to the gas chromatograph for analysis.

2.3.2.2 Particle Measurements

2.3.2.2.1 Temperature and Velocity Measurements

The temperature of the carbon particles as they reacted above the flat-flame burner assembly was measured using an optical pyrometer. The pyrometer used was a Leeds and Northrup, model 8622, with a temperature range of 1000-3150 K. The optical pyrometer was calibrated using the platinum/platinum-10% rhodium thermocouple temperature probe illustrated in Figure 15.

Still photographs of the reacting carbon particles were taken with a Graflex Optar f/7.5, 203 mm camera, model N-C55586. Polaroid high-speed instant film, type 57, was used. The camera lens was placed 1.6 m from the film face which gave a magnification of 7.5 to 1.

In order to obtain the still photographs, a monodispersed aerosol was established at the flat-flame burner face in a completely dark environment. The aperture on the camera optics was held open while a light pulse illuminated the particles. The light pulse was generated by a General Radio strobotac, model 1538-A. The photograph was then analyzed on a Spencer microscope, manufactured by the American Optical Company, to observe particle spacing and carbon-reaction characteristics.

The particle velocity measurements were made with the LDA system used to measure the velocity of the gas above the flat-flame burner. The particle spacing was also measured with the LDA system. A Nicolet, model 206, analog-to-digital recording oscilloscope was

employed to measure the time between the pedestal signals generated by individual particles. Since the particle velocity was known, the distance between particles could be determined.

2.3.2.2.2 Diameter Measurements

The probe used to collect the carbon-agglomerated particles for analysis is shown in Figure 18. The probe was positioned along the flame centerline at various locations above the flat-flame burner with a 320 mm Unislide traversing mechanism. The collection filter was constructed by modifying a Gelman, model 2220, stainless-steel in-line filter holder. The upstream end of the filter holder was modified to include two concentric stainless-steel cones which were silver soldered to the upstream face of the filter holder. The inner cone had a 6.4 mm inlet, a 15° angle, and a length of 23.7 mm. The outer cone had a 12.7 mm inlet, a 30° angle, and a length of 30.5 mm. Both cones had an approximate thickness of 1.6 mm. A stainless-steel tip was silver soldered to the outer core. The tip was 12.7 mm in diameter, 6.4 mm in length and tapered to a 4.7 mm inlet with an angle of 45°.

A nitrogen-quenching flow passed through the outer core of the filter holder from a 6.4 mm diameter tube. The nitrogen flowed between the two concentric cones to the inlet of the collection probe to quench the reacting particles as they entered the probe. The particles then were collected on 47 mm diameter Alpha metricel, grade Alpha-200, Gelman membrane filters, model 60585. These filters have a pore size of 0.2 μm, a thickness of 65 μm, a very high chemical resistance, and a maximum operating temperature of 450 K.

TO VACUUM PUMP
AND BUBBLE METER

NITROGEN
QUENCH

6.4 mm O.D. TUBING
SUPPORTED BY UNISLIDE
TRAVERSING
MECHANISM

FILTER SHEET

GELMAN FILTER
HOLDER

30.5 mm

30°

23.7 mm

15°

45°

4.7 mm

6.4 mm

12.7 mm
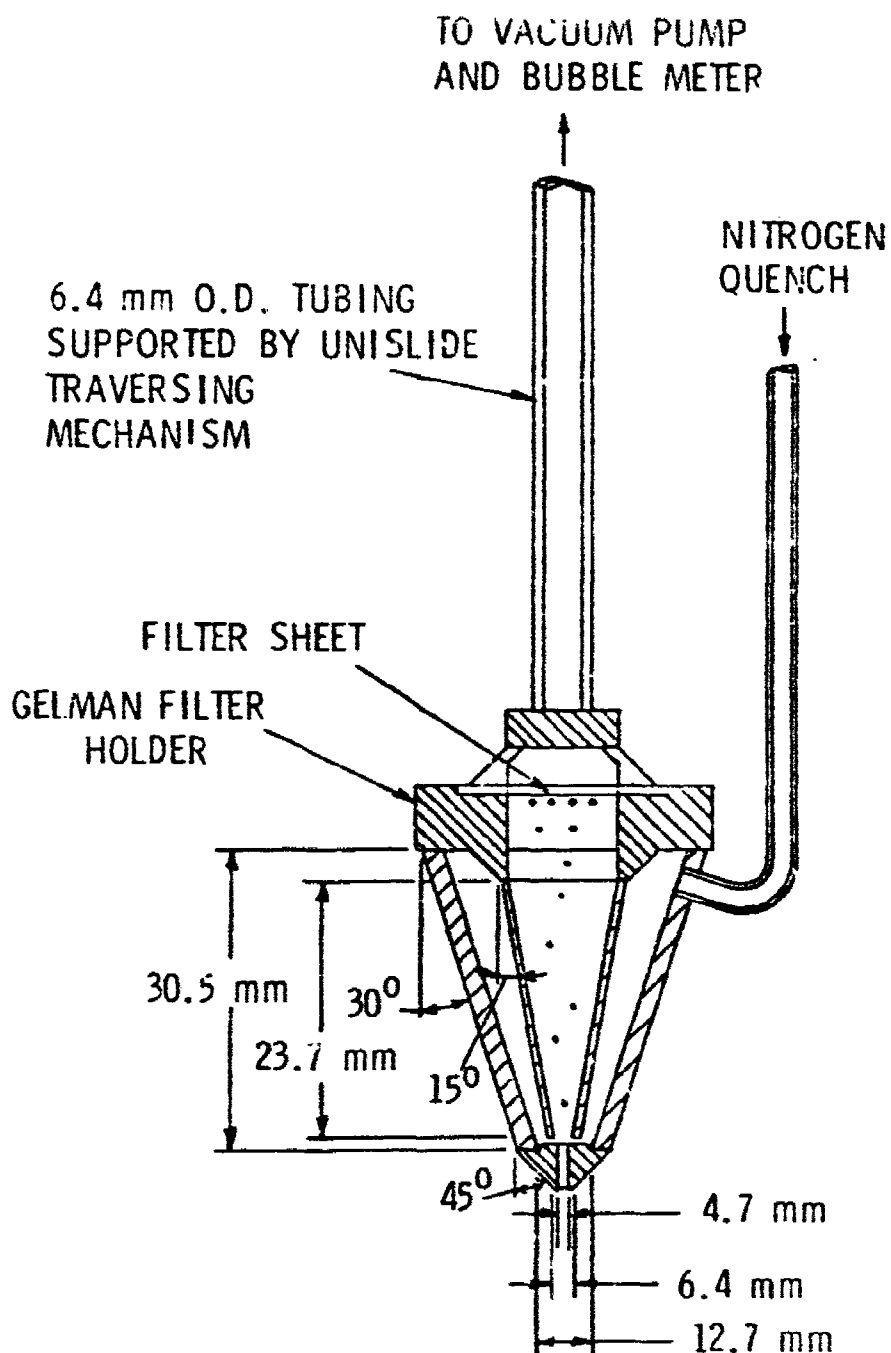
Figure 18.   Sketch of the filter system used to collect agglomerated-
             carbon particles above the laminar premixed flame apparatus.

The particle collection probe was then connected to a Sargent-Welc, Scientific Company duo-seal vacuum pump, model 1402. The velocity at the inlet to the collection probe was matched with the gas velocity at the sampling location. The flow rate was controlled with a Whitey forged body regulating valve, model SS-1RS4, and metered with a Varian aerograph bubble meter. A sufficient amount of nitrogen gas was mixed in the collection filter to lower the gas temperature to 400 K and quench the reacting carbon particles. The nitrogen was metered with a Matheson 603 rotometer, and the pressure was controlled with a Matheson, model 8H, two-stage pressure regulator with an output capacity of 0-1400 kPa. The operating pressure in the filter was subatmospheric with a value of approximately 71 kPa which also tended to help quench the reacting carbon particles.

A Nupro BKT series quick response toggle operated bellows valve was placed in the flow line between the collection probe and the vacuum pump in order to be able to operate the collection filter for a short time period of a few seconds. This small sampling time resulted in widely spaced single particles on the collection filter. After the sample was collected the filter medium was removed and the sizes of the particles collected were analyzed on a scanning electron microscope, International Scientific Instruments, model Super III-A. Permanent records of the particle sizes were recorded with fine-grain Polaroid film, type 52.

The diameter quoted is the arithmatic average of six diameter measurements per particle each spaced 30° apart and passing through the center of the particle. At least eight particles were examined in order to obtain an average particle size.

2.3.2.2.3 Mass Measurements

The filter collection probe illustrated in Figure 18 was also employed to collect particles for particle mass measurements. However, the sampling period for the mass measurements was increased to between 10 seconds and 2 hours, and a stainless-steel filter medium was substituted for the Alpha metricel filter described earlier. The stainless-steel filter was a Dynalloy filter, model X4, manufactured by the Fluid Dynamics Branch of Brunswick Technetics. The filters had a diameter of 47 mm, a thickness of 300 μm, and a pore size of 3 μm. The filters were preconditioned by baking them for three hours at a temperature in excess of 1000 K to burn off any contaminants which may have adhered to the filter.

After the carbon particles were collected, the filter was removed and placed in an evacuated reaction chamber. The temperature was elevated to 500 K, and the pressure lowered to less than 4000 Pa. These conditions were maintained for several hours to remove any condensibles entrapped within the particles. The dried carbon particles were then exposed to an oxygen and hydrogen environment. The temperature was elevated above 1000 K and the pressure increased to 85 kPa. These conditions were maintained for several hours until all of the carbon was reacted. By measuring the carbon dioxide and

carbon monoxide concentrations in the reaction chamber, the mass of carbon initially present on the filter was determined. Knowing the total number of particles collected during the collection period (from the droplet production frequency) gave the mass of carbon per particle. The pressure of the reaction chamber was kept subatmospheric to monitor whether the system developed leaks, since nitrogen would show up in the gas analysis of the reacted gas if a leak was present.

The carbon slurry mixture incorporated several additives to assure stability. In order to determine whether these additives altered the carbon mass measurement, a slurry mixture consisting of the same ultimate sized carbon particles (0.35 m) and nearly pure JP-10 (greater than 99.95%) was prepared in this laboratory. The resulting slurry was then injected through the flat-flame burner and combusted. Particles were collected at various axial locations for several operating conditions, and their mass analyzed. The mass measurements of the carbon agglomerate with and without the additives present were found to agree well within the experimental accuracy. It is therefore assumed in the analysis that the additives did not significantly alter the mass measurements.

A diagram of the particle dryer and reaction chamber system is shown in Figure 19. The reaction chamber was constructed from a 95 cc clear fused quartz test tube with an I.D. of 25 mm. The lower 120 mm of the test tube was wrapped with nicrome heating wire and high temperature fiberfrax ceramic fiber insulation. The upper 80 mm of
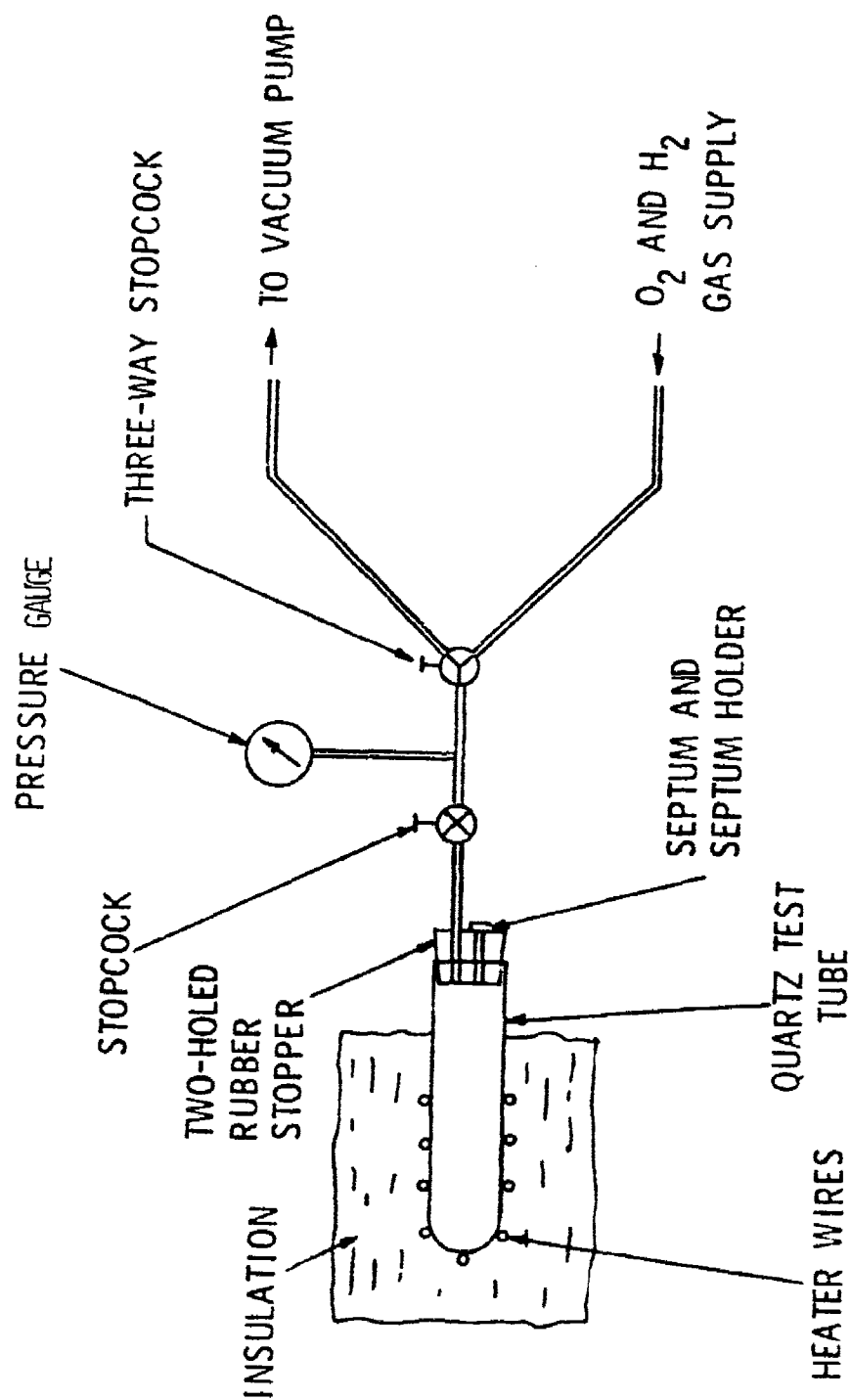
Figure 19. Schematic diagram of the particle-dryer reaction-chamber system.

the test tube was not insulated which kept it at a lower temperature. The tube was capped with a two-hole size No. 5 rubber stopper. A septum holder and septum were connected to one of the holes in the rubber stopper. The other hole was connected to a three-way stopcock which allowed the test tube to be connected to either a vacuum pump or an oxygen and hydrogen supply. The vacuum pump was a Sargent-Welch Scientific Company duo-seal vacuum pump, model 1402. The oxygen pressure was controlled with a Harris two-stage regulator, model 92-100; and the hydrogen pressure was controlled with a Matheson two-stage pressure regulator, model 8H.

A pressure gauge was also incorporated into the particle dryer-reaction chamber system. The pressure gauge was a Wallace and Tiernan absolute-pressure gauge, model FA129, with a range of 0 to 339 kPa. After the particles were dried, as described earlier, the system was evacuated. Then oxygen was added until the pressure reached 83 kPa, hydrogen was then added until the pressure reached 85 kPa. The reaction chamber temperature was elevated above 1000 K, and after all of the carbon reacted (approximately two hours), the temperature was reduced to 300 K. A 5 ml sample was extracted from the reaction chamber through the septum with a 0-1.0 ml Pressure-Lok, series "c", gas syringe, model 030033. The gas sample was then analyzed using a Varian, model 3700, gas chromatograph.

2.3.3 Experimental Conditions

The experimental conditions for the laminar flat-flame burner tests are summarized in Table 4. Four equivalence ratio conditions

Table 4. Summary of Test Conditions for the Laminar Flat-Flame Burner Tests

ϕ	T_f (K)	d_{p_o} (μm)	u_∞^a (m/s)	Mass Fraction						
				O_2	N_2	CO_2	CO	H_2	H_2O^b	OH^c
0.2	1667	73.4	1.47	0.569	0.252	0.098	--	--	0.080	--
0.6	1663	73.4	1.52	0.098	0.719	0.101	--	--	0.083	--
	1814	73.4	1.54	0.111	0.681	0.114	--	--	0.094	--
	1953	73.4	1.49	0.125	0.640	0.129	--	--	0.105	0.001
1.0	1683	10.5-73.4	1.50	--	0.813	0.102	--	--	0.084	--
	1819	73.4	1.52	0.001	0.789	0.115	0.001	--	0.095	--
	1952	10.2-73.4	1.53	0.002	0.761	0.128	0.002	--	0.107	--
1.4	1624	73.4	1.52	--	0.767	0.077	0.059	0.004	0.098	--

[a] Ambient velocity at injector exit.

[b] H_2O mole fraction was obtained from H and O element balances.

[c] OH mole fraction was obtained from CEC-72 equilibrium calculations.

were examined: ϕ = 0.2, 0.6, 1.0 and 1.4. Three temperature ranges were also studied: a low temperature range, T_f = 1660 K; an intermediate temperature range, T_f = 1815 K; and a high temperature range, T_f = 1950 K. The temperature at a given equivalence ratio was increased by replacing a portion of the combustible mixture with additional nitrogen. This substitution provided an increase in flame temperature without additional thermal decomposition of nitrogen [154].

The 73.4 μm particles burning in the ϕ = 0.2 and 0.6 conditions were completely burned within the 200 mm axial length limit of the quartz tube. However, burning was incomplete for the ϕ = 1.0 and 1.4 conditions. Thus, particles with smaller initial diameters were tested at the ϕ = 1.0 test condition in order to examine variation of the combustion process with particle diameter.

CHAPTER III

THEORETICAL CONSIDERATIONS

The life history of a single slurry droplet reacting in a combusting environment was modeled during the present investigation. As pointed out in the first chapter, the liquid fuel in a slurry droplet is much more volatile than the suspended carbon particles. Therefore, it is reasonable to expect that the liquid fuel will be vaporized first and that a single carbon-agglomerated particle will be left behind. Thus, the slurry-combustion process will be modeled as two separate stages: (1) the heat-up and gasification of the liquid fuel, and (2) the heat-up and reaction of the carbon agglomerate. The discussion will begin with the liquid-gasification theory and its evaluation since this analysis is relatively simple and the results serve to establish methods for specifying flow properties for the more complex agglomerate-reaction model.

3.1 Liquid Drop-Life-History Model

The objective of the liquid-gasification analysis is to predict the variation of the drop temperature, the mass of the liquid and the drop diameter as a function of time for the period where liquid is present in the slurry. The analysis was relatively conventional since the carbon particles remained within the liquid droplet. The approach generally follows methods developed during earlier work on modeling drop gasification in this laboratory [11,150,155,156].

3.1.1 Assumptions

Present test conditions were considered involving spherical particles with no particle interaction. An illustration of the liquid gasification model is presented in Figure 20.

The following assumptions were employed for the analysis of gas-phase transport:

1. The flow field around the drop was assumed to be quasisteady, i.e., at each instant of time the flow is equivalent to a steady flow for the same boundary conditions, and the velocity of the surface was neglected. Ambient properties were taken to be local-mean properties ignoring turbulent fluctuations.

2. Predicting flow around spheres exactly is impractical for use in modeling sprays; therefore, the conventional film theory approximation was employed to treat convection [150]. This implies that gas-phase transport can be represented as a stagnant, spherically-symmetric layer whose outer radius is determined from empirical-convection correlations for spheres.

3. Only diffusion of mass by concentration gradients was considered, employing an effective-binary diffusivity. All species were assumed to have equal molecular weights and specific heats, and constant average gas-phase properties were computed at a mean state defined as follows:

$$\phi_{avg} = \alpha \, \phi_p + (1-\alpha) \, \phi_\infty \tag{3.1}$$
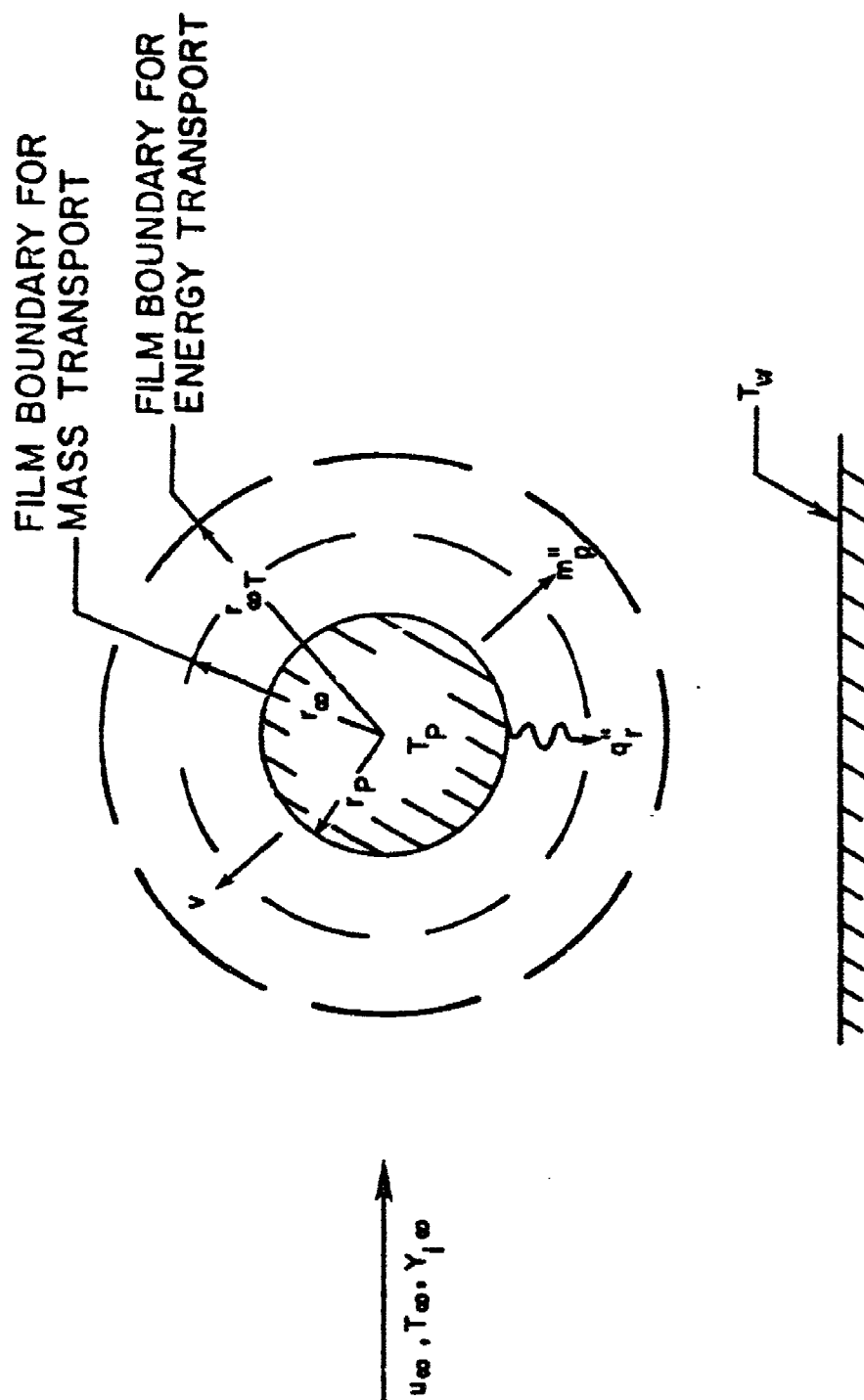
Figure 20. Illustration of transport terms used in the theoretical model.

where φ represents both temperature and species mass fractions. Predictions vary significantly as α is changed; a single value was chosen to provide best agreement between predictions and measurements over the test range. Methods developed during past work were employed to compute properties [11,150,155,156]. A summary of the property evaluation method is given in Appendix A.

4. The liquid was assumed to evaporate without the presence of an envelope flame since this condition is most representative of drops in combusting sprays [11,150,155,156]. Thus, reaction effects, such as fuel decomposition or oxidation, were neglected.

5. The gas phase was assumed to be transparent to radiation, and radiation from the drop to the surroundings was neglected due to the relatively low temperature of the drop liquid.

6. The liquid surface was assumed to be in thermodynamic equilibrium, with the Clausius-Clapeyron equation providing the relationship between liquid-surface temperature and the concentration of vapor at the surface.

7. The solubility of gases in the liquid was neglected since this effect is small at atmospheric pressure [156]. JP-10 is a pure hydrocarbon; therefore, the analysis only considers the evaporation of a single component. Only the fuel was considered to diffuse in the gas phase.

8. Radial motion of the liquid surface was neglected.

9. The pressure of the flow field surrounding the drop was constant.

10. Dufour and Soret effects were neglected.

These assumptions are generally similar to those employed for drop-transport analysis. Their justifications are discussed more completely in Chapter I and elsewhere [11,157].

3.1.2 Vapor-Phase Conservation Equations

Employing the assumptions listed in the previous section, the gas-phase conservation equations are as follows [11,150]:

Conservation of Mass

$$\frac{d}{dr} \ (\rho r^2 v) = 0 \tag{3.2}$$

Conservation of Species

$$\frac{d}{dr} \ (\rho r^2 (v Y_F - D\frac{dY_F}{dr})) = 0 \tag{3.3}$$

Conservation of Energy

$$\frac{d}{dr} \ (r^2(\rho v C_p(T - T_p) - \lambda\frac{dT}{dr})) = 0 \tag{3.4}$$

The boundary conditions for these equations are as follows:

$$r = d_p/2, \quad Y_F = Y_{Fg_p}, \quad T = T_p, \quad \rho v = \dot{m}_F'' \tag{3.5}$$

$$r = d_p/2, \quad \rho v(1 - Y_{Fg_p}) + \rho D(\frac{dY_{Fg}}{dr})_p = 0 \tag{3.6}$$

$$r = r_\infty, \quad Y_F = Y_{Fg}; \quad r = r_{\infty T}, \quad T = T_\infty \tag{3.7}$$

where

$$\frac{r_\infty}{r_p} = \frac{Sh}{Sh-2} \tag{3.8}$$

$$\frac{r_{\infty}}{r_p} = \frac{Nu}{Nu-2} \tag{3.9}$$

$$Nu \text{ or } Sh = 2 + \frac{[0.552 \ Re^{1/2} \ (Pr \text{ or } Sc)^{1/3}]}{[1 + 1.232/(Re \ (Pr \text{ or } Sc)^{4/3})]^{1/2}} \tag{3.10}$$

and

$$Re = d_p |u_\infty - u_p| \rho/\mu. \tag{3.11}$$

The terms given in Equations (3.8) to (3.11) are incorporated to account for convection effects. These expressions were obtained by Faeth and Lazar [41] and are cited in References 11 and 157.

The boundary condition of Equation (3.6) follows from the fact that the nonfuel gases are assumed to be insoluble in the liquid phase. A conventional heat-transfer coefficient is also defined, as follows:

$$\lambda \left(\frac{dT}{dr}\right)_p = h \ (T_\infty - T_p). \tag{3.12}$$

Integrating Equation (3.2) and applying Equation (3.5) yields

$$\rho r^2 v = \text{constant} = d_p^2 \dot{m}_f''/4. \tag{3.13}$$

Integrating Equation (3.3) and applying the boundary conditions yields

$$\dot{m}_f'' \, d_p/\rho D = \text{Sh} \ln (1 + B) \tag{3.14}$$

where

$$B = \frac{(Y_{Fg_p} - Y_{Fg})}{(1 - Y_{Fg_p})} = \frac{Y_{Fg_p}}{(1 - Y_{Fg_p})} \quad . \tag{3.15}$$

Integrating Equation (3.4) in a similar manner results in

$$\frac{hd_p}{\lambda} = \frac{\text{Nu} \ln [(1 + B)^{Le^{-1}}]}{[(1 + B)^{Le^{-1}} - 1]} \quad , \tag{3.16}$$

where the Lewis number, Le, is based only on the specific heat of the gaseous fuel, since only the gaseous fuel diffuses away from the particle.

Equations (3.14) and (3.16) provide the basic relationships for mass and heat transfer in the presence of mass diffusion from the drop. These equations are limited to spherically-symmetric flow and the effect of convection is handled by the terms Nu and Sh.

3.1.3 Droplet Evaporation Model

The conservation equations for the drop are obtained under the assumptions that all drop properties are uniform at each instant of time. Dufour and Soret effects are also neglected. With these assumptions, the conservation equations are as follows [11]:

$$\frac{dm_f}{dt} = \frac{d}{dt}(\rho \, \tfrac{\pi}{6} d_p^3) = - \pi d_p^2 \, \dot{m}_f'' \tag{3.17}$$

$$\frac{\pi}{6} \, \bar{\rho} \, \bar{C}_p \, d_p^3 \, \frac{dT_p}{dt} = \pi d_p^2 [h(T_\infty - T_p) - \dot{m}_f'' \, i_{fg}] \tag{3.18}$$

$$\frac{\pi}{6} \, \bar{\rho} \, d_p^3 \, \frac{du_p}{dt} = - \frac{\pi}{8} \, d_p^2 \, \rho \, C_D \, (u_p - u_\infty) \, |u_p - u_\infty| - \frac{\pi}{6} \, d_p^3 \, g \, (\bar{\rho} - \rho_\infty) \tag{3.19}$$

$$\frac{dx_p}{dt} = u_p \tag{3.20}$$

where the drag coefficient is given by White [158] as:

$$C_D = \frac{24}{Re} + \frac{6}{1 + \sqrt{Re}} + 0.4 \tag{3.21}$$

which is valid up to a Reynolds number of 200,000.

The terms $\bar{\rho}$ and $\bar{C}_p$ are average-droplet density and average-droplet specific heat, respectively, and include contributions of liquid fuel, solid carbon, and the support probe.

The average-droplet density is defined as:

$$\bar{\rho} = (\frac{Y_f}{\rho_f} + \frac{Y_c}{\rho_c} + \frac{Y_s}{\rho_s})^{-1}, \tag{3.22}$$

and the average-droplet specific heat is defined as:

$$\bar{C}_p = Y_f C_{p_f} + Y_c C_{p_c} + Y_s C_{p_s} . \tag{3.23}$$

By employing the equation for the average-droplet density (Equation 3.22), the droplet diameter is given as:

$$d_p = [\frac{6}{\pi \bar{\rho}}(m_f + m_c + m_s)]^{1/3} . \tag{3.24}$$

The carbon particles are assumed to remain suspended in the liquid fuel, becoming agglomerated as the liquid evaporates and the droplet diameter becomes smaller. When the solid-carbon particle forms an agglomerate which is as tightly packed as possible, the liquid continues to evaporate through the agglomerate pore structure until all of the liquid has evaporated.

A uniform temperature at each instant of time was assumed for the liquid droplet. The mass fraction of the liquid fuel was also assumed to be uniform throughout the droplet interior. The temperature and concentration profiles assumed by the model are sketched in Figure 21.

3.1.4 Calculation Procedure

The drop-life-history calculations were begun by initializing the particle displacement, velocity, temperature, diameter and carbon mass fractions. The ambient-gas mass fractions, temperature and velocity were also initialized at this point. Time was set equal to zero, and the specific heats for the carbon and liquid fuel and the liquid-fuel density were calculated for the particle temperature. Employing both the particle and ambient temperature, the gas-phase thermophysical and transport properties were calculated as discussed in Appendix A. A group of non-dimensional parameters were then calculated from the gas-phase properties; they included: the Prandtl number, the Lewis number (based on the vaporized liquid-fuel specific heat), the Schmidt number, the Reynolds number from Equation (3.11), the Nusselt and Sherwood numbers from Equation (3.10), and the drag coefficient from Equation (3.21).

EVAPORATION
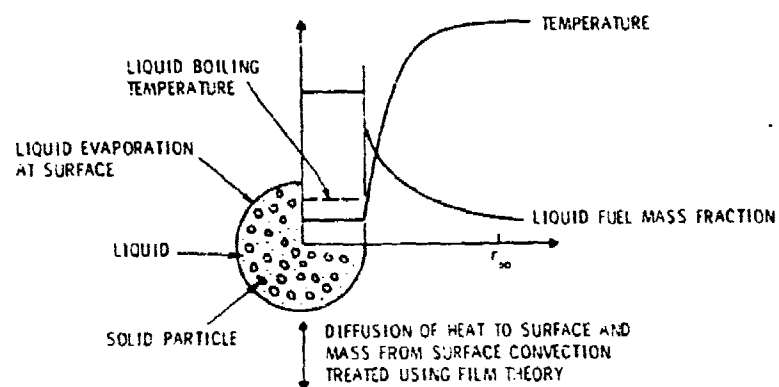
COMBUSTION
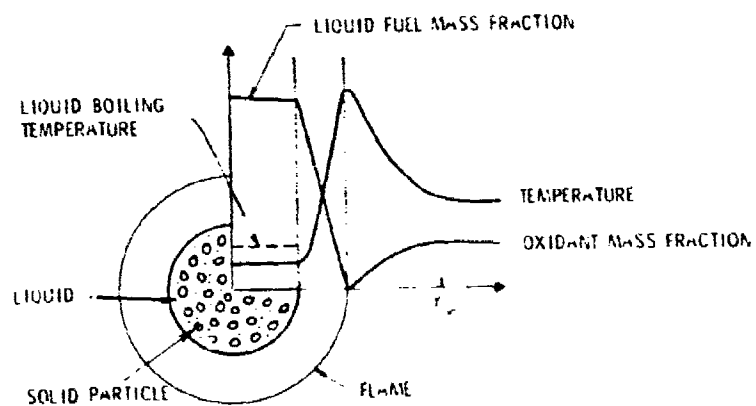
Figure 21. Liquid gasification and combustion models.

The droplet mass fraction for the liquid fuel, solid carbon, and support probe were then calculated. Next, the average-droplet density and specific heat and the droplet diameter were calculated from Equations (3.22), (3.23) and (3.24), respectively. The mass transfer driving potential was obtained from Equation (3.15), and the mass flux of liquid from the drop surface was obtained from Equation (3.14). The convective heat-transfer coefficient was then calculated from Equation (3.16). Finally, the time derivatives of the particle mass, temperature, velocity and displacement were obtained from Equations (3.17) through (3.20).

The minimum-droplet diameter (i.e., the droplet diameter when the carbon particles are packed around the support probe as tightly together as possible) was computed with the carbon agglomerate packed density quoted by Bruce et al. [2]. If the current droplet diameter was smaller than this computed minimum diameter, the droplet diameter was set equal to this minimum diameter. It must be pointed out that even though the minimum diameter has been reached, there still may be liquid fuel present in the space between the individual carbon particles.

If the mass of liquid remaining in the droplet is greater than zero, time is given an incremental step and the entire calculation procedure was repeated. Gear's method of integration was employed to estimate the new values for particle mass, temperature, velocity and location. In the case of a suspended drop the particle location would be fixed and the particle absolute velocity would be zero which means

that Equations (3.19) and (3.20) may be eliminated from the analysis. For a free-flowing drop, the support-probe mass becomes zero and the terms Y_s and m_s would be excluded from the analysis.

3.1.5 Droplet Combustion Model

Drop transport in the presence of envelope flames has been the subject of numerous investigations. In the following, a brief account of envelope-flame theory will be presented and the results will be employed to indicate the effect of envelope flames on drop-transport rates within a turbulent-diffusion flame environment. Further discussion of the properties of envelope flames can be found in recent articles [11,48].

The analysis of envelope flames will employ the same assumptions as the drop-evaporation analysis of Section 3.2.3, except as noted in the following. It was assumed that fuel and oxidizer react in stoichiometric proportions within an infinitely thin flame sheet which completely surrounds the drop. Reaction rates within the flame sheet are assumed to be infinitely large, so that the concentrations of fuel and oxidant are zero at the flame. In order to reduce the complexity of the transport equations, the same average properties are employed on both sides of the flame sheet and the Lewis number is taken to be unity. These approximations are typical of most models of envelope flames [11,48]. The property assumptions are easily removed if required.

The structure of the gas phase near evaporating and combusting drops, under present assumptions, is sketched in Figure 21. The same

surface and ambient conditions are shown for the two cases. It is evident that the presence of an envelope flame increases temperature and concentration gradients at the drop surface, enhancing drop-transport rates. The objective of the analysis is to provide drop heat- and mass-transfer rates given conditions at the drop surface and in the surrounding gas. These results can then be incorporated in drop-life-history computations.

Following Law et al. [48], the overall stoichiometry for a single-component liquid fuel was taken to be

$$\varepsilon_f[F_f] + (\varepsilon_f/\nu_f{}^o)[0] \rightarrow \text{Products} \tag{3.25}$$
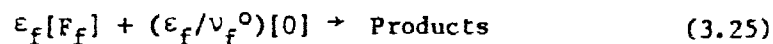
where ε_f is the mass-flux fraction the liquid phase, defined as:

$$\varepsilon_f = \frac{\dot{m}_f}{\dot{m}_t} = \frac{Y_{fs}(1 + B_{Yc})}{B_Y} . \tag{3.26}$$

In these equations, f refers to the liquid-phase fuel evaporating from the drop, which also contains carbon particles and the support probe.

The quasisteady-transport equations can be solved using the film theory approximation, to yield:

$$\frac{\dot{m}_f'' \, d_p}{\rho D} = \frac{\dot{m}_f'' \, C_p}{\lambda} = \text{Sh} \ln \left[(1 + B_Y)(1 + B_0)\right] \tag{3.27}$$

where

$$B_Y = (1 - Y_{as})/Y_{as} \tag{3.28}$$

$$B_0 = Y_{0_\infty}/(\varepsilon_f/\nu_f^0) \qquad (3.29)$$

$$\varepsilon_f = Y_{fs} (1 + B_Y)/B_Y . \qquad (3.30)$$

The quantity Y_{as} is the mass fraction of nonfuel species at the drop surface. This quantity is obtained from the equation of state for liquid-vapor equilibrium; knowing the liquid temperature and composition, and the ambient pressure. Basing the heat-transfer coefficient on the flame temperature,

$$h = \lambda(\frac{dT}{dr})_s/(T_c - T_s) , \qquad (3.31)$$

solution of the transport equations yields

$$\frac{h \, d_p}{\lambda} = \frac{Nu}{B_Y} \ln [(1 + B_Y)(1 + B_0)] . \qquad (3.32)$$

Neglecting dissociation, the flame temperature is

$$\frac{T_f - T_s}{T_\infty - T_s} = \left[\frac{Y_0 \, Q_r}{C_p(T - T_s)} + 1\right] \bigg/ \left[1 + \frac{B_0}{B_Y}(B_Y + B_0)\right] \qquad (3.33)$$

where Q_r is the heat released per unit mass of oxidizer consumed at the flame front

$$Q_r = \varepsilon_f \, Q_f/(\varepsilon_f/\nu_f^0) . \qquad (3.34)$$

If an envelope flame is present, Equations (3.27) to (3.34) replace Equations (3.14) and (3.16) when determining drop heat- and mass-transfer rates. Otherwise, the computation of drop-life

histories is the same as for evaporating drops. In cases where the surroundings of a drop contain oxygen, but a stable envelope flame is not present, drop transport rates can be approximated by setting $Y_{0\infty} = 0$ in Equations (3.27) to (3.34) which retrieves the formulation for an evaporating drop.

At moderate pressures, single-component drops in a fixed surroundings reach a steady wet-bulb temperature (aside from minor effects of non-unity Lewis number which have been ignored in this analysis). In this circumstance, the rate of evaporation is given by

$$\frac{\dot{m}''_f C_p}{\lambda} = Sh \ln [1 + (C_p(T - T_s) + Q_r Y_{0\infty})/i_{fg}] \qquad (3.35)$$

where T_s can be approximated by the boiling temperature of the fuel with little error [29].

Numerous comparisons between predictions of envelope-flame models and measurements have been reported [11]. In general, models similar to Equations (3.27) to (3.35) provide a satisfactory method for correlating data once the results are calibrated by selecting a suitable reference state for computing average properties. The present formulation has been tested for pure fuels in combusting gas environments having particular relevance to analysis of drop-life histories in spray flames. This includes measurements for supported drops in laminar and turbulent flames for pressures in the range 0.1-6.8 MPa [11].

3.2 Carbon-Particle Life-History Model

Once all the liquid has evaporated, the carbon agglomerate begins
to heat-up from the liquid wet-bulb temperature.   The objective of
this portion of the analysis is to predict the agglomerate-life
history,   i.e.,   the variation of agglomerate temperature,   mass,
diameter,   velocity and displacement as a function of time.   The
agglomerate reaction analysis follows the general approach developed
during recent studies of carbon-particle combustion [85,88-90], but
differs in some details.   An illustration of the particle-combustion
model is presented in Figure 20.

3.2.1 Assumptions

Assumptions 1-3 were adopted from the liquid-gasification
analysis. Additional assumptions for this portion of the analysis are
as follows:

4. The particle was pure carbon having a uniform temperature at
    each instant of time.   The gas mixture in the flow was
    approximated by O_2, N_2, CO_2, CO, H_2O, H_2 and OH.

5. Carbon reaction was limited to the apparent surface of the
    particle.   The effects of pores (causing reaction within the
    particle), intrinsic variations of carbon-black reactivity
    and   catalysts were   treated   by introducing   empirical
    area/reactivity multiplication factors of the basic carbon
    reaction rate.

6. Agglomerates were observed to react for equivalence ratios
    both greater and less than unity, with the former conditions

involving low oxygen concentrations. Two surface reaction models were examined, both of which attempt to predict reaction rates over the full range of equivalence ratios where agglomerate reaction rates are significant. The first method employed an approach suggested by Neoh et al. [121] where carbon reaction with OH is assumed to dominate the high-equivalence ratio region while reaction with O_2 becomes more significant at low-equivalence ratios. The second procedure adopted the approach used by Libby and Blake [88,89] for reaction of carbon with oxygen and carbon dioxide, and water vapor.

7. The gas phase was assumed to be in thermodynamic equilibrium at the particle surface.

8. As before, the gas phase was assumed to be transparent to radiation; however, since agglomerates reach high temperatures, their radiation to solid surfaces surrounding the flow was considered. Particle to particle interaction, however was ignored. A unity value was used for the emissivity since the emissivity of carbon is fairly large. In addition, the porous structure of the particle would enable the emissivity to approach the black-body emissivity value of unity.

9. The total gas pressure was constant throughout the region surrounding the carbon particle. Faeth [32] has shown that this assumption is valid except for particles much smaller than the ones studied during the present investigation.

These assumptions are generally similar to those employed for transport to particles during combustion processes [11,85-89]. The main distinctions between the present analysis and that of Libby and Blake [88,89] for carbon-particle reaction involves consideration of different reaction mechanisms, allowance for convection effects, and the use of empirical area/reactivity multiplication factors.

3.2.2 Conservation Equations

The governing equations of conservation of mass, conservation of energy and conservation of chemical elements are presented in this section. These equations were obtained from the general equations presented by Williams [25] and are applicable in all regions surrounding the particle. Employing spherical symmetry, these equations are:

Conservation of mass, as given by Equation (3.2) or as:

$$r^2 v = (\rho v)_p r_p^2 = \dot{m}_p'' r_p^2 = \text{constant} \tag{3.36}$$

which indicates that the radial mass flow rate per unit solid $\dot{m}_p$ is a constant.

Conservation of energy:

$$r_p^2 \dot{m}_p'' \frac{di}{dr} = \frac{\lambda}{C_p} \frac{d}{dr}\left(r^2 \frac{di}{dr}\right) \tag{3.37}$$

where

$$i = c_p(T - T_{ref}) + \sum_{i=1}^{7} Y_i \, i_{f_{ref_i}} . \tag{3.38}$$

Conservation of elements:

$$r_p^2 \dot{m}_p'' \frac{d\tilde{Y}_i}{dr} = \rho D \frac{d}{dr}(r^2 \frac{d\tilde{Y}_i}{dr}) , \quad i=1,2...7 . \tag{3.39}$$

The conservation of radial momentum for the gas phase yields the pressure distribution external to the particle and is, therefore, not essential for the present study.

Assuming no gases are absorbed by the carbon particle there is no net mass flux of the elements oxygen, nitrogen and hydrogen at the particle surface. Furthermore, the net mass flux of carbon at the surface is equal to m_p. Therefore, the surface boundary conditions for Equations (3.37) and (3.39) are:

$$r = r_p ; \quad i = i_p$$

$$\rho D(\frac{d\tilde{Y}_1}{dr})_p = - \dot{m}_p'' (1 - \tilde{Y}_{1p}) \tag{3.40}$$

$$\rho D(\frac{d\tilde{Y}_i}{dr})_p = \dot{m}_p'' \tilde{Y}_{ip} , \quad i=2,3,4$$

where carbon is denoted as species 1. The ambient boundary conditions are:

$$r = r_{\infty T} : \quad i = i_\infty , \quad T = T_\infty$$

$$r = r_\infty : \quad \tilde{Y}_i = \tilde{Y}_{i\infty} , \quad i=1,2,3,4 . \tag{3.41}$$

Equations (3.41) treat the general case where the film radii for mass and heat transfer are not the same. These radii are found from the usual correlations of film theory, and are given in Equations (3.8) and (3.9).

The solution of Equation (3.39), subject to the boundary conditions of Equations (3.40) and (3.41) yields:

$$\tilde{Y}_{1_p} = 1 - (1 - \tilde{Y}_{1\infty}) \exp(-2K/Sh) \tag{3.42}$$

$$\tilde{Y}_{i_p} = \tilde{Y}_{i\infty} \exp(-2K/Sh) , \quad i=2,3,4 \tag{3.43}$$

where

$$K = \dot{m}_p'' \, r_p / \rho D \tag{3.44}$$

Employing the sign convention that convection heat transfer from the surface of the particle is positive, we have:

$$q_c'' = -\lambda (\frac{dT}{dr})_p = -\frac{\lambda}{C_p}(\frac{di}{dr})_p \tag{3.45}$$

where the second part of Equation (3.45) follows by neglecting the slight departure of the Lewis number from unity. The solution of Equation (3.37) yields the convective heat flux, as follows:

$$\frac{q_c'' \, C_p}{(i_p - i_\infty)} = \frac{\lambda K / r_p}{1 - \exp(2K/LeNu)} \tag{3.46}$$

3.2.3 Gas-Phase Transport

This portion of the analysis generally follows Libby and Blake [88,89], and will only be briefly described. Since binary

diffusivities are equal, mass transport is conveniently expressed in terms of element mass fractions. Four elements, C, O, N and H, and seven species, O_2, N_2, CO_2, CO, H_2O, H_2 and OH, appear in the analysis. Note that this analysis follows Ubhayakar and Williams [85], Libby and Blake [88,89] and others in neglecting atomic oxygen on the grounds that below 4000 K its concentration will be small, insufficient to contribute significantly to the carbon oxidation.

The element and species mass fraction are related as follows:

$$\tilde{Y}_i = \sum_{j=1}^{7} \mu_{ij} Y_j , \quad i=1,2,3,4 \tag{3.47}$$

where μ_{ij} is the mass fraction of the i'th element in the j'th species. The utilization of the above element mass fractions greatly simplified the theoretical analysis since elements are conserved through the particle boundary layer.

Given the $\tilde{Y}_i$ at a particular location, Equation (3.47) provides four equations to determine the seven unknown Y_i. Three additional equations were obtained from the assumption of thermodynamic equilibrium. The equilibrium relations employed in the analysis were:

$$H_2O \overset{K_{p1}}{\rightleftharpoons} H_2 + 1/2 \ O_2$$

$$H_2O \overset{K_{p2}}{\rightleftharpoons} 1/2 \ H_2 + OH \tag{3.48}$$

$$CO_2 \overset{K_{p3}}{\rightleftharpoons} CO + 1/2 \ O_2$$
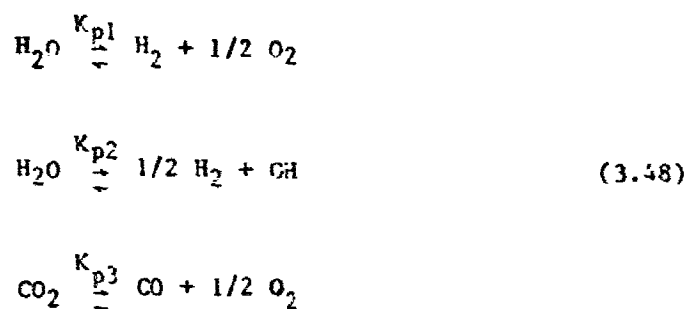
where the equilibrium constants for the above reactions are functions of temperature and given as:

$$K_{p1} = \frac{Y_{H_2} (Y_{O_2})^{1/2}}{Y_{H_2O}} \, p^{1/2}$$

$$K_{p2} = \frac{(Y_{H_2})^{1/2} Y_{OH}}{Y_{H_2O}} \, p^{1/2} \tag{3.49}$$

$$K_{p3} = \frac{Y_{CO} (Y_{O_2})^{1/2}}{Y_{CO_2}} \, p^{1/2} .$$

Where the equilibrium constants K_{pi} are taken from the JANAF Thermochemical Tables [159].

3.2.4 Surface Reactions

There are numerous uncertainties in modeling the reaction of a porous carbon agglomerate in a flame. The flame environment contains several species which are potential oxidants of carbon, e.g., H_2O. CO_2, O, O_2 and OH, and the reaction mechanism is not well established [121]. Since the material is porous, reaction is not limited to the apparent outer surface of the agglomerate [160]. Carbon substances exhibit intrinsic variations in reactivity due to their surface structure [160]. Finally, the presence of a catalyst was found to influence reaction rates.

The effect of various gaseous reactants was treated by considering a mechanism recently proposed by Neoh et al. [121] as well as an extension of an earlier approach employed by Libby and

Blake [88,89]. The effects of pores, surface reactivity and catalysts were treated by identifying empirical area-reactivity multiplication factors, selected to best match the present measurements. (It was found that a fixed value, for a given carbon black and reaction, could correlate the measurements over the range of the data.)

Neoh et al. [121] concluded that OH is the dominant carbon oxidant under fuel-rich conditions; that O is of secondary importance at temperatures below 2000 K; and that O_2 becomes a significant factor for fuel-lean conditions, particularly at lower temperatures. Present test conditions correspond to these circumstances, therefore, carbon reaction with both OH and O_2 was considered, while ignoring the remaining species. Neoh et al. [121] found that reaction of carbon with OH could be represented by assuming a constant collision efficiency, yielding the following reaction rate expression

$$R_1 = K_{r1}P_{OH} .$$
(3.50)

The results of Nagle and Strickland-Constable [109] were employed to determine the rate of reaction of carbon with O_2 These rate expressions are also in reasonable agreement with later measurements by Park and Appleton [120]. The carbon reaction rate is given by

$$R_2 = K_{r2}P_{O_2}X/(1 + K_{r3}P_{O_2}) + K_{r4}P_{O_2}(1 - X)$$
(3.51)

where

$$X = [1 + K_{r5}/(K_{r4}P_{O_2})]^{-1} .$$
(3.52)

The measurements of Neoh et al. [121] suggest that the larger of R_1 or R_2 should represent the reaction rate at any condition. Therefore, the dimensionless mass burning rate was determined from

$$K = (r_p/\rho D) \max [a_1 R_1, a_2 R_2] \qquad (3.53)$$

where the a_i appearing in Equation (3.53) are the empirical area-reactivity multiplication factors.

The carbon-reaction mechanism used by Libby and Blake [88] considers reaction with O_2 and CO_2 employing the following expressions:

$$R_3 = K_{r6} P_{O_2} \qquad (3.54)$$

$$R_4 = K_{r7} P_{CO_2} . \qquad (3.55)$$

This approach was extended during the present study to include the reaction of carbon with H_2O, by employing the results of Johnstone et al. [103]. The reaction rate expression for this case is

$$R_5 = K_{r8} P_{H_2O}/(1 + K_{r9} P_{H_2} + K_{r10} P_{H_2O}) . \qquad (3.56)$$

For this second approach, the total reaction rate of carbon was obtained as the sum of the rates for O_2, CO_2 and H_2O, ignoring potential interactions between reactants. This yields:

$$K = (r_p/\rho D) \sum_{i=3}^{5} a_i R_i . \qquad (3.57)$$

The specific reaction rate parameters used in the computations are summarized in Table 5, where the K_{ri} are assumed to have the following general form

$$K_{ri} = A_i T^{n_i} \exp(-e_i/RT) . \qquad (3.58)$$

In all cases, P_i was found from the mass fractions at the particle surface as follows:

$$P_i = M \, Y_i P/M_i . \qquad (3.59)$$

The area-reactivity multiplication factors which provided the best match of the present data are summarized in Table 6 for the turbulent-diffusion flame tests. Neoh et al. [121] estimate collision efficiencies for OH in the range 0.13-0.28, the latter value was employed for the present estimate of a_i. The area-reactivity multiplication factors for R_4 and R_5 could not be separated for turbulent-diffusion flame test conditions, since the relative proportions of CO_2 and H_2O were roughly the same throughout the flame: therefore, the values were taken to be identical for both reactions. As might be expected, the presence of pores in the agglomerate result in a_i values greater than unity since the actual reaction area is greater than the apparent surface area. The a_i for a catalyzed slurry were only evaluated for the second reaction approximation. The use of a catalyst increases the intrinsic surface reactivity of the carbon, yielding higher a_i than for the noncatalyzed agglomerate.

Table 5. Summary of Reaction Rate Parameters

i	A	n	E (kcal/gmol)
1[a]	361 kg $K^{1/2}/m^2$s atm	$-1/2$	0
2	2400 kg/m^2s atm	0	30.0
3	21.3 atm^{-1}	0	~ 4.1
4	0.535 kg/m^2s atm	0	15.2
5	18.1 x 10^6 kg/m^2s	0	97.0
6	87100 kg/m^2s atm	0	35.8
7	2470 kg/m^2s atm	0	41.9
8[b]	15.15 x 10^{-3} kg/m^2s atm	0	32.7
9	9.42 x 10^{-11} atm^{-1}	0	−60.8
10	7.07 x 10^{-16} atm^{-1}	0	−79.3

[a]Assuming a collision efficiency of 0.28 [121].

[b]Assuming a surface area of reaction of 1.15 m^2/g of carbon, which is the average surface area over the period of reaction [103].

Table 6.   Summary of Area-Reactivity Factors
for Turbulent Diffusion Flame Tests

Reaction	Noncatalyzed	Catalyzed
Neoh, et al., [121] reaction approximation:		
1	54.3	--
2	758.	--
Extended Libby and Blake [88] reaction approximation:		
3	58.2	70.6
4	112.9	140.0
5	112.9	140.0

3.2.5 Particle-Life History

The results of the previous sections will now be applied to determine the particle-life history of a cold particle suddenly immersed in a hot-oxidizing ambient. To simplify the analysis, the particle will be assumed to have a uniform temperature.

Assuming that the density of the particle is a constant, conservation of particle mass yields:

$$\frac{dr_p}{dt} = -\rho DK/\rho_c r_p .$$

(3.60)

Conservation of energy at the particle surface yields:

$$\frac{dT_p}{dt} = (\frac{-3}{\rho_c C_{p_c} r_p})[\dot{m}_p''(i_p - i_c) + q_c'' + q_r'']$$

(3.61)

where q_r is the particle surface heat flux for radiation to the enclosure surrounding the flow:

$$q_r'' = \sigma \epsilon (T_p^4 - T_w^4) .$$

(3.62)

The particle velocity and displacement were obtained by integrating Equations (3.19) and (3.20) after replacing the average droplet density with the carbon density.

The initial conditions for Equations (3.60) and (3.61) were based on conditions at the end of the liquid-vaporization period. At this point, all the carbon initially in the slurry was present in the agglomerate, the agglomerate density is known [2] and the particle was at the wet-bulb temperature for liquid evaporation.

As mentioned earlier, the model assumes a uniform temperature for the carbon particle as illustrated in Figure 22. The temperature profile of the gas phase decreases from the particle temperature at the particle surface; to the ambient temperature, at a radius predicted by the film theory. Figure 22 also illustrates that the oxidant mass fraction decreases and the product species mass fraction exponentially increases from their ambient values to their values at the particle surface.

3.2.6 Calculation Procedure

Initially the time, particle radius, temperature, velocity and displacement were set equal to their values at the end of the liquid-gasification period. The values for the mass fraction at the particle surface are initially set equal to the ambient values. The transport and thermophysical properties of the gas phase surrounding the particle were evaluated, as discussed in Appendix A, considering the mass fraction and temperature of the particle surface and of the surroundings.

The equilibrium constants: K_{p1}, K_{p2} and K_{p3}, from Equations (3.48) and (3.49), were evaluated using the particle temperatures, ambient pressures and regression equations curve fitting the chemical equilibrium data of the JANAF tables [159]. Values for the kinetic rates given in Equation (3.58) were then determined at the particle temperature. The film parameters were determined next from Equations (3.8)-(3.10). The non-dimensional carbon mass-loss parameter was then calculated by employing Equations (3.50)-(3.53) or Equations
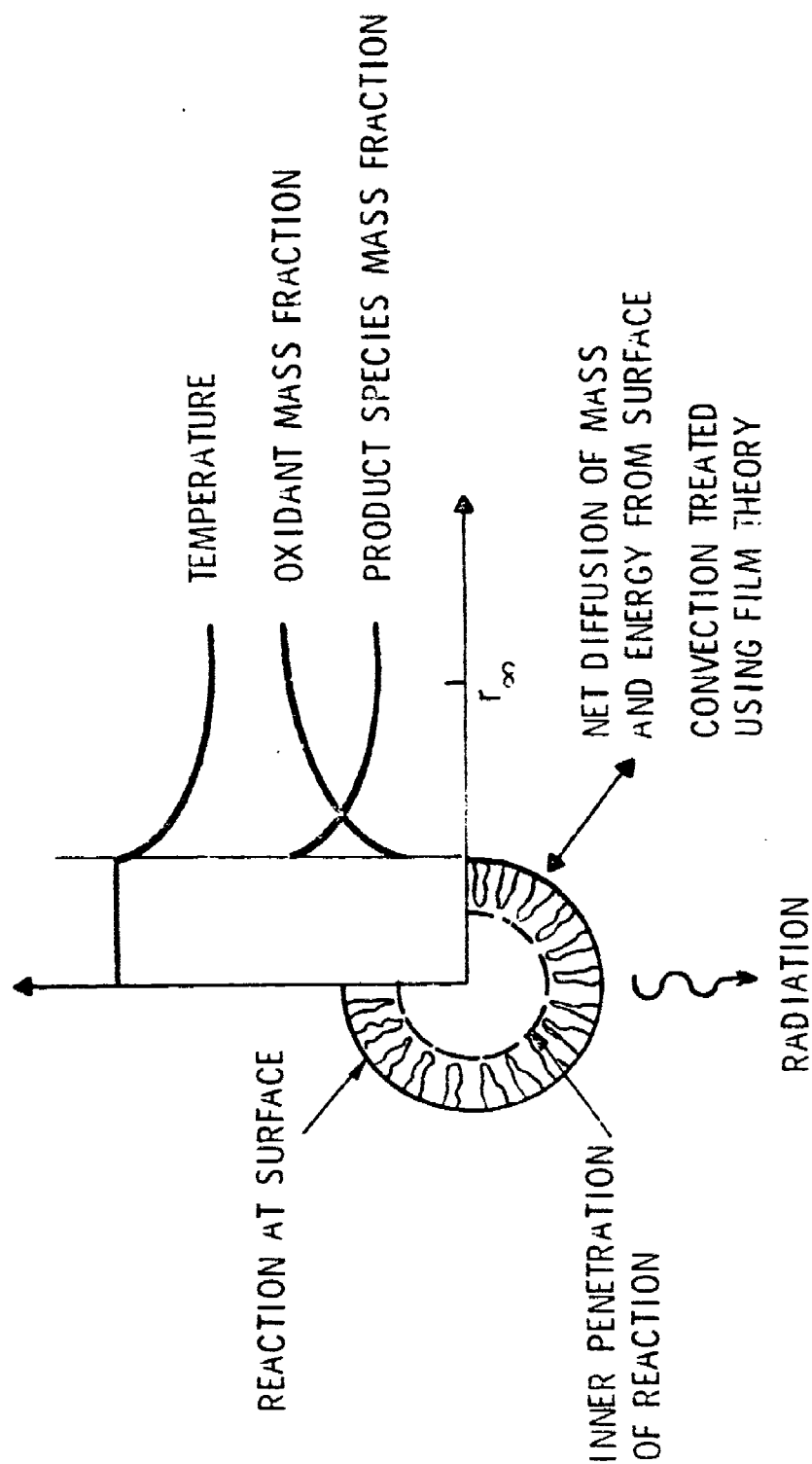
Figure 22. Carbon-agglomerate reaction model.

(3.54)-(3.57), depending upon whether the $OH-O_2$ mechanism or the $O_2-CO_2-H_2O$ mechanism was chosen. Next, the gas-phase mass fractions (O_2, CO_2, CO, H_2, OH, H_2O and N_2) at the particle surface were calculated by simultaneously solving Equations (3.39) and (3.47) by either the Newton-Raphson method, or the interval bisection method. The Newton-Raphson method was normally used, while the interval bisection method was employed for the more unstable cases.

The properties of the gas phase were then reevaluated with the updated mass fractions. The procedure was continued until convergence of the mass fractions was obtained. At this point, Equations (3.20), (3.60) and (3.61) were solved for the values of particle displacement, radius and temperature at the next time increment, using Gear's method of integration. Particle velocity was obtained from experimental measurements. The entire procedure was continued until the particle was consumed or extinguished. If the particle was suspended, the particle location is fixed and Equations (3.19) and (3.20) may be dropped from the analysis.

CHAPTER IV

RESULTS AND DISCUSSION

The main objective of the present study was to compare measurements and predictions for the heat-up and combustion processes of a slurry droplet under conditions which simulate the environment in a combustion chamber. The theoretical model discussed in Chapter III was used to predict the diameter, temperature, mass, velocity and position of a slurry droplet burning in both a turbulent-diffusion flame and a laminar-premixed flat flame.

4.1 Slurry Droplet Combustion in the Turbulent-Diffusion Flame

For the turbulent diffusion flame tests, a slurry droplet was supported on a probe in the flame. The droplets were observed to have various degrees of reaction in the different flame regions. The drop-life-history and the particle-life-history models were employed to predict the heat-up and combustion process of the slurry droplet. Each of these results are discussed in the following sections.

4.1.1 Flame Regions

Figure 23 is an illustration of the variation in mean properties along the centerline of the turbulent flame fueled with gaseous propane. In the region near the nozzle exit, gas velocities and the concentrations of propane are relatively high, while the temperature is low and oxygen is absent. Moving downstream, the gas velocity and concentration of propane decrease monotonically. The
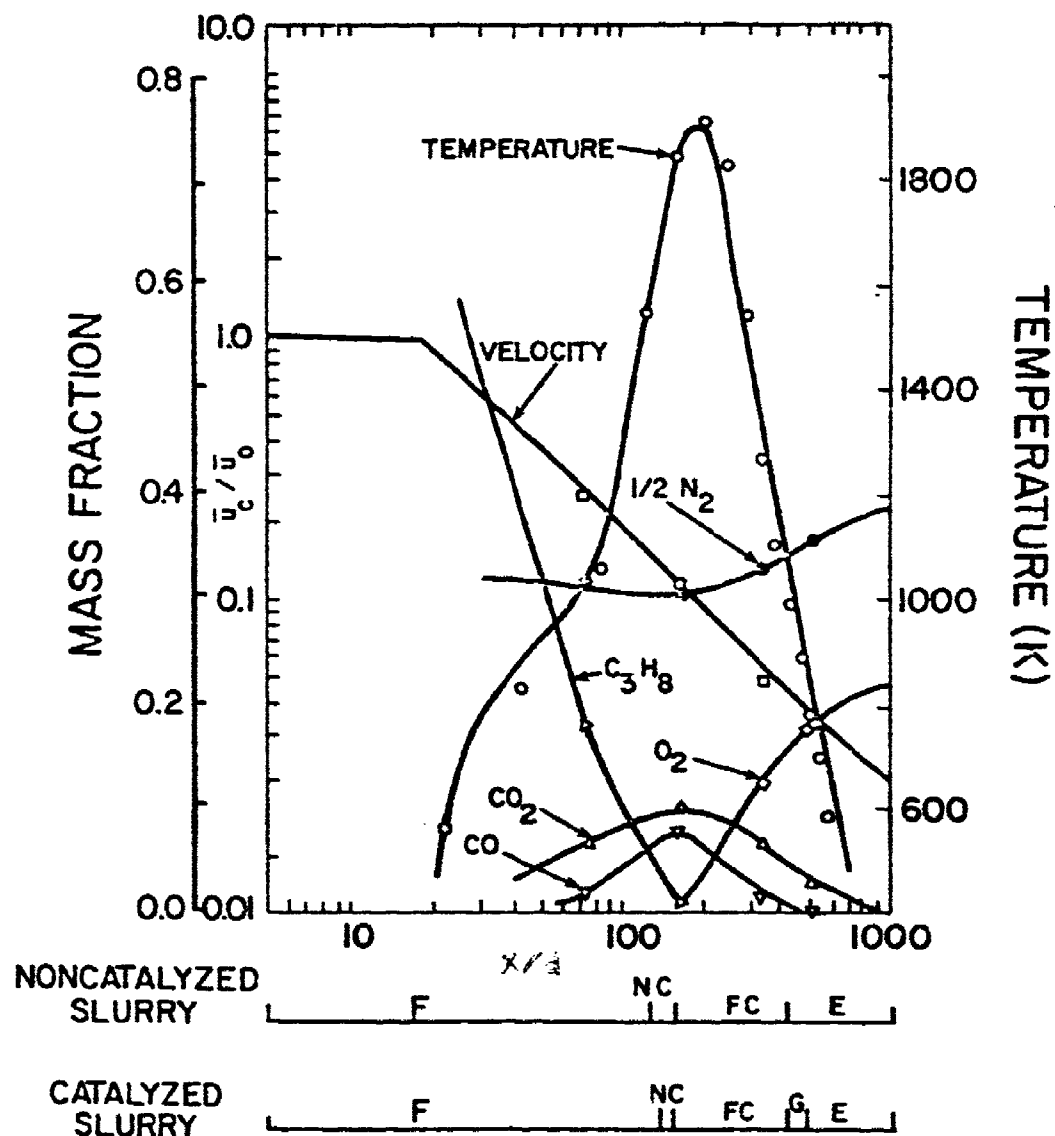
Figure 23. Droplet environment diagram modified to
show the various droplet burning regions.

temperature increases at first, reaching a maximum at the flame tip, where the fuel has disappeared and combustion product concentrations are highest. Beyond the tip of the flame the flow decays with increasing concentrations of oxygen and nitrogen and decreasing temperatures and combustion product concentrations.

The structure of the burner flame used in this study is typical of other gas and spray fueled diffusion flames [11,149-151,157]. The region near the injector is highly fuel rich and has a relatively low temperature. Significant concentrations of oxygen and high temperature levels only appear as the turbulent reaction zone is approached.

Drop behavior varied substantially with position in the flame. Table 7 is a description of the various types of behavior that were observed: fragmentation (F), noncombusting (NC), full combustion (FC), glowing (G), and evaporation (E). The regimes are listed in the order in which they appear with increasing distance from the injector. Table 8 is a summary of the portion of the flame where the various regions were observed, for both the catalyzed and noncatalyzed slurries.

The various drop burning regimes are also indicated on the lower part of Figure 23. The observations in each of these regions will be considered in turn.

Table 7. Description of the Slurry Droplet Combustion Regions in the Turbulent Diffusion Flame

Region[a]	Designation	Description
Fragmentation	F	The liquid fuel evaporated without an envelope flame; however, a diffuse luminous wake was observed. When all the liquid was gone, some of the carbon agglomerate was fragmented into 3-5 large flakes. A carbon agglomerate also remained on the probe.
Noncombusting	NC	The liquid fuel evaporated without an envelope flame; however, a diffuse luminous wake was observed. When all the liquid had evaporated, a luminous wake or reduced intensity was still observed. A carbon agglomerate remained on the probe.
Full Combustion	FC	An envelope flame was observed around the particle until the liquid fuel was consumed. After a dark period, the carbon agglomerate began to glow. Glowing continued until virtually all the carbon was consumed.
Glowing	G	The liquid fuel evaporated with no envelope flame observed. Some time after the liquid was gone (2-15 s for present test conditions), the carbon agglomerate began to glow. Glowing persisted until virtually all the carbon was consumed. This region was only observed for the catalyzed slurry.
Evaporation	E	The liquid fuel evaporated with no envelope flame observed. Glowing of the carbon agglomerate was not observed. No change of the particle size was observed once the liquid was gone for the noncatalyzed slurry. Some reaction of the catalyzed slurry was observed in the upstream end of this zone.

[a]In order of increasing distance from the injector.

Table 8. Summary of the Slurry Droplet Combustion Regions in the Turbulent Diffusion Flame

Region	Designation	Range x/d^a	
		Catalyzed Slurry	Noncatalyzed Slurry
Fragmentation	F	42^b – 138	42^b – 128
Noncombusting	NC	143 – 154	132 – 154
Full Combustion	FC	159 – 404	159 – 383
Glowing	G	409 – 500	----
Evaporation	E	505 – 680^c	404 – 680^c

[a] Gaps in the ranges are due to finite spacing of test locations

[b] Nearest point to injector considered. There was no evidence that closer locations would not be in the blow-off region.

[c] Farthest point from the injector considered. There was no evidence that locations farther downstream would not be in the evaporation region.

4.1.1.1 Fragmentation Region

The fragmentation region is closest to the injector,
involving relatively high gas velocities and propane concentrations,
moderate combustion product concentrations, virtually no oxygen and
temperatures from 300 to roughly 1600 K. In this region, the liquid
fuel evaporated with no envelope flame present. A luminous wake was
visible behind the drop as the liquid evaporated. This behavior is
typical of a liquid fuel evaporating in a high-temperature gas in the
absence of oxygen [11,41]. The liquid drop primarily evaporates
without combustion. As the fuel gases become heated they decomposed
forming soot. When the temperature is high enough, the soot glows
yielding a diffuse-luminous wake.

When the bulk of the liquid had evaporated, most of the carbon
agglomerate was blown off the probe in three to five large flakes.
The mechanical breakdown of the agglomerate results from the
relatively high gas velocities in this region. Figure 24 is a SEM
photograph of the residue remaining of the probe after exposure of a
catalyzed-slurry drop to the fragmentation region of the flame. The
appearance of the residue from the noncatalyzed slurry was similar.
The surface is very irregular with waves frozen into the structure by
the high gas velocity. The surface structure is similar to that
observed when these drops are burned in air, c.f., Figure 3. At
higher magnifications, sub-elements having a size comparable to the
ultimate carbon particle size, 0.3 m, were observed.
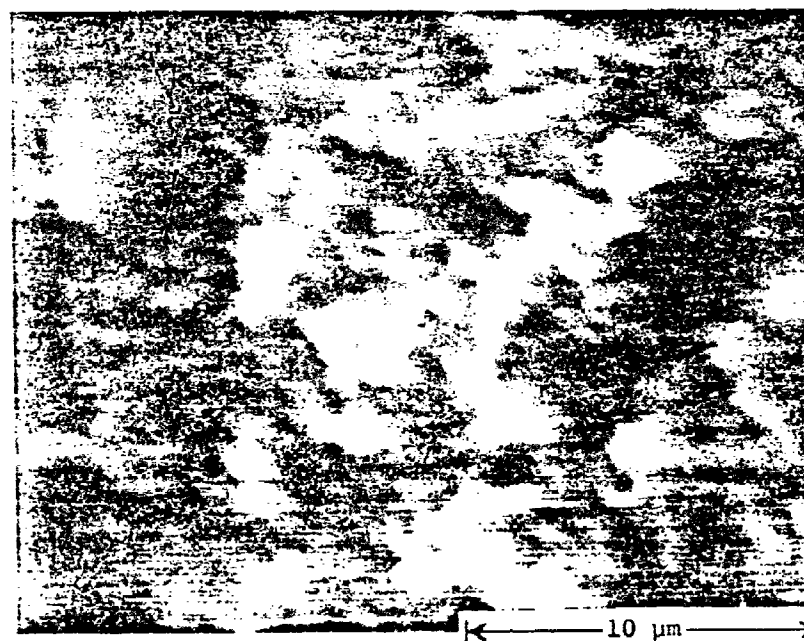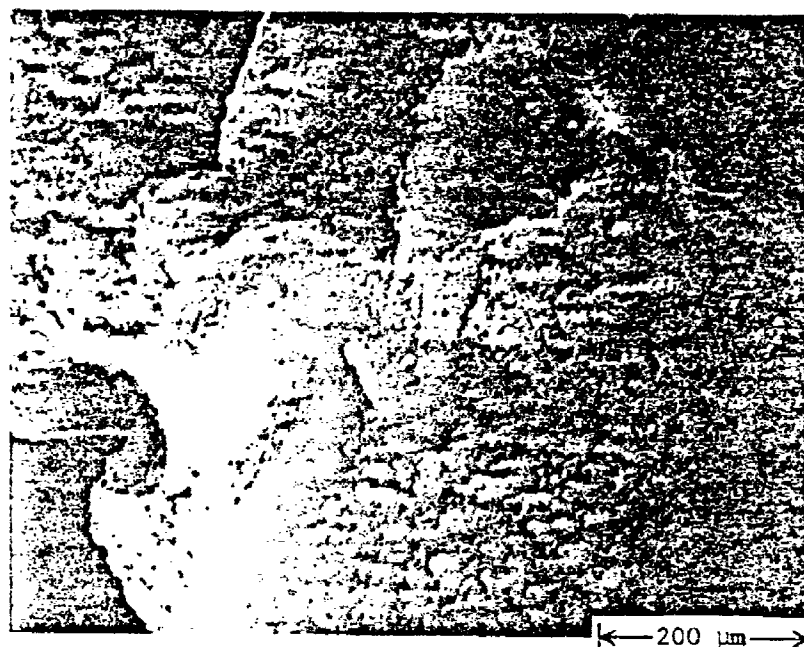
Figure 24. SEM photograph of the carbon residue from a catalyzed slurry droplet in the fragmentation region, x/d = 75.

4.1.1.2 Noncombusting Region

The noncombusting region was relatively narrow for both fuels. It was located on the fuel-rich side of the reaction zone; where velocities and oxygen concentrations were relatively low, while temperatures and product concentrations approached their maximum values. The liquid fuel evaporated without an envelope flame, similar to behavior in the fragmentation region. However, there was little flaking of the residue and greater amounts of carbon remained on the probe. After the liquid had evaporated, a luminous wake of reduced intensity was still observed. This suggests continued shedding of small carbon particles which eventually glowed as they heated (and began to react) in the flow.

Figure 25 is a SEM photograph of the surface of the residue from the noncombusting region. The residue from both nontcatalyzed and catalyzed slurries was similar. The structure is similar to the structure seen in the fragmentation region. The major difference between the two regimes is that the lower velocities do not cause the residue to flake. Rates of carbon reaction are also probably somewhat higher, although the rates are still relatively low. The support of particles is weakened due to reaction, which caused small portions to flake off.

4.1.1.3 Full-Combustion Region

The full-combustion region has low gas velocities, and relatively high temperatures and high concentrations of oxygen and combustion products. An envelope flame was observed around the drop
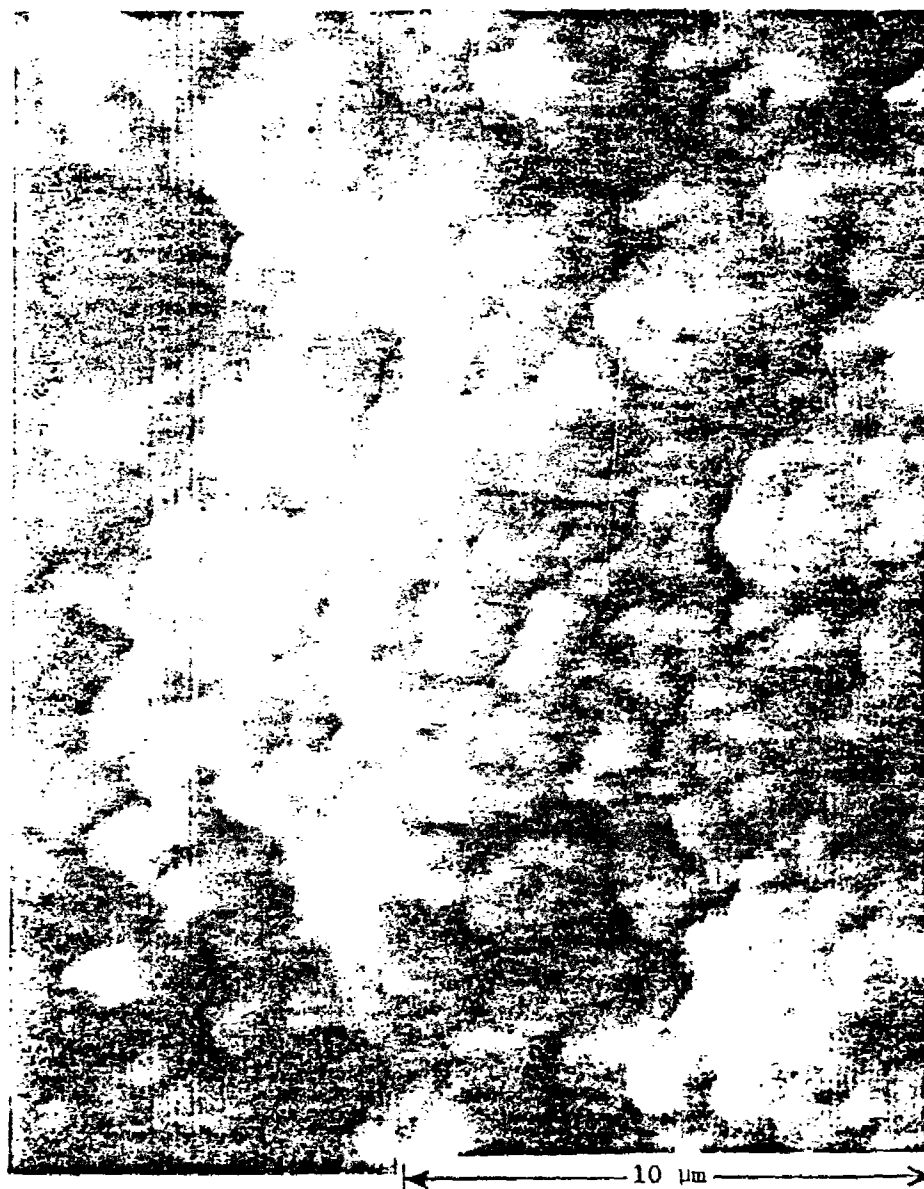
Figure 25. SEM photograph of the carbon residue from a catalyzed slurry droplet in the noncombusting region, x/d = 149.

as the liquid evaporated. Similar to combustion in air, a dark period was observed between the time when the envelope flame was extinguished and the residue began to glow. The dark period involves transient heating of the surface from the low temperature levels characteristic of liquid evaporation to the high temperatures characteristic of carbon reaction. In contrast to combustion in air, both the noncatalyzed- and catalyzed-slurry residues exhibited glowing in the burner flame. The glowing persisted until very little carbon residue remained.

Figure 26 shows two SEM photographs of the residue from a catalyzed-slurry drop in the full-combustion region. The residue from the noncatalyzed slurry was similar. The structure is thin and very porous. In this region, the residue was a cenosphere; which is probably the result of convective and radiative heat losses, which tend to quench the reaction at the outer surface. The shielding effect of the outer structure allows higher-temperature levels in the interior of the residue and the reaction completes the gasification of the solid. The greater extent of reaction on the outer surface results in a structure that is less related to the original slurry particles than was the case for the region nearer to the injector.

4.1.1.4 Glowing Region

The glowing region was only observed for the catalyzed slurry, and is relatively narrow. Oxygen concentrations are high in this region (mass fractions in the range 0.15-0.20) and temperatures
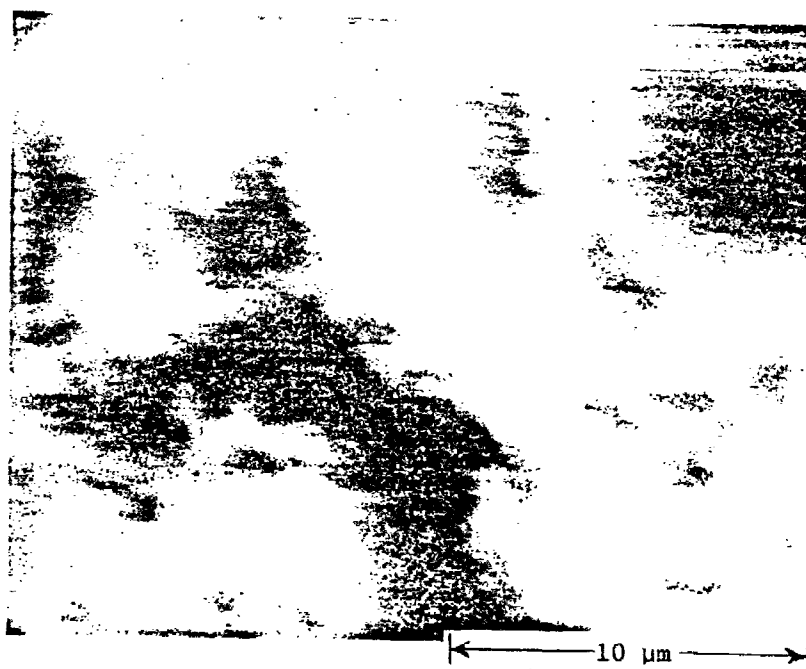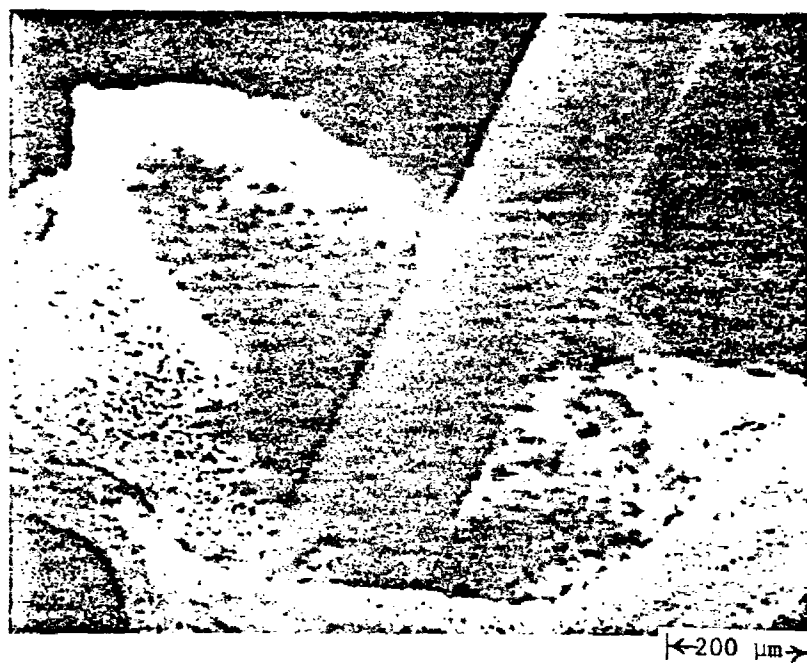
Figure 26.   SEM photograph of the carbon residue from a catalyzed
slurry droplet in the full combustion region, x/d = 340.

are relatively low (800-1000 K). The liquid fuel evaporated with no envelope flame present and no luminous wake. Some time after the liquid had evaporated, 2 to 15 s for present test conditions, the residue began to glow. Glowing persisted until little carbon was left on the probe.

The surface structure of the residue from this region was similar to the full-combustion region. SEM photographs of the surface appear in Figure 27. The structure is very porous.

4.1.1.5 Evaporation Region

The evaporation region was farthest from the injector, where the flow decays to approach the properties of room air. In this region, the liquid evaporated leaving a carbon agglomerate. There was little evidence of subsequent reaction of the agglomerate.

SEM photographs of the residue in this region appear in Figure 28. The surface appears smooth in some regions and coarse in others (due to fracture of the sample). The appearance is generally similar to evaporation in air with little reaction of the agglomerate, c.f., Figures 4 and 5.

4.1.1.6 Effect of Catalyst

The appearance of the residue from both slurry fuels was similar in each region. The main effect of the catalyst was to extend the region where reaction of the residue could be sustained. The noncatalyzed residue reacted in the range $x/d = 159-383$ while the catalyzed residue reacted in the range $x/d = 159-500$. This
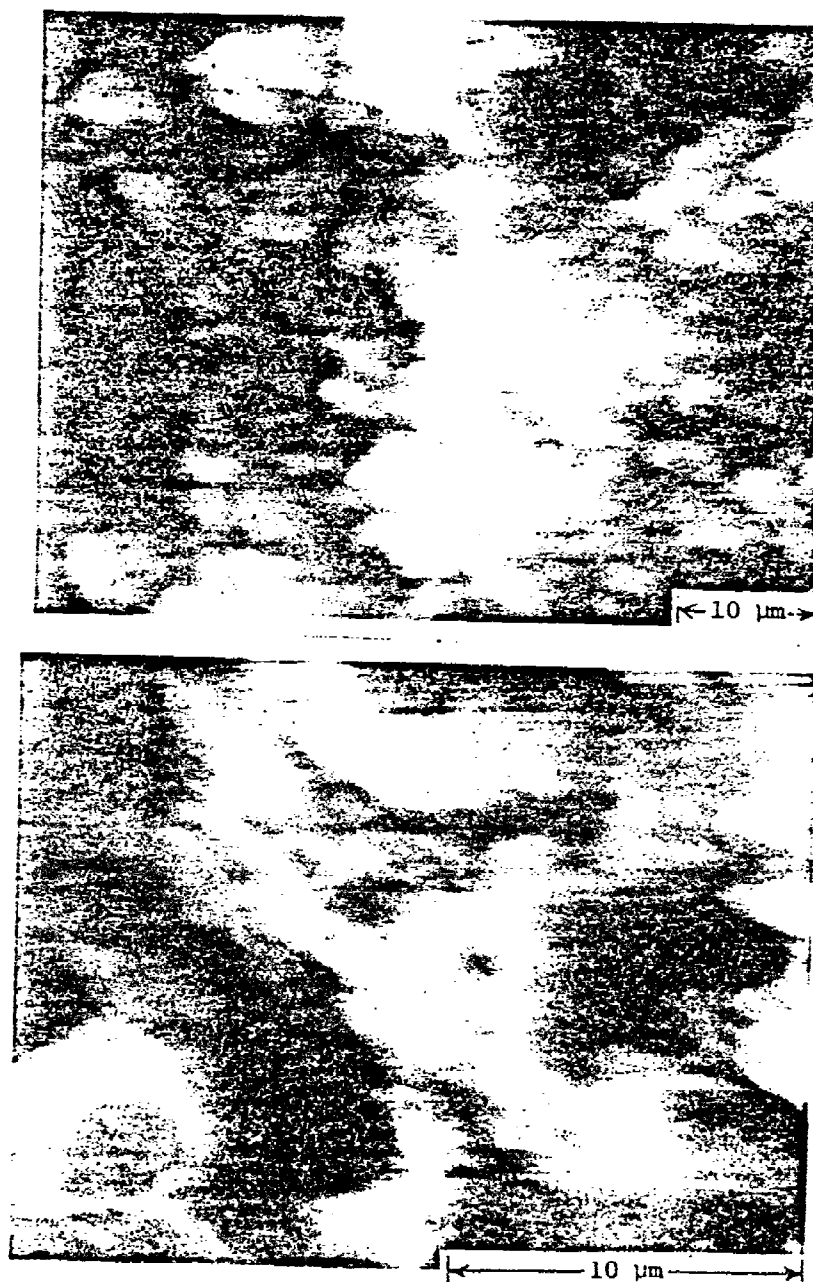
Figure 27. SEM photograph of the carbon residue from a catalyzed slurry droplet from a glowing region, x/d = 489.
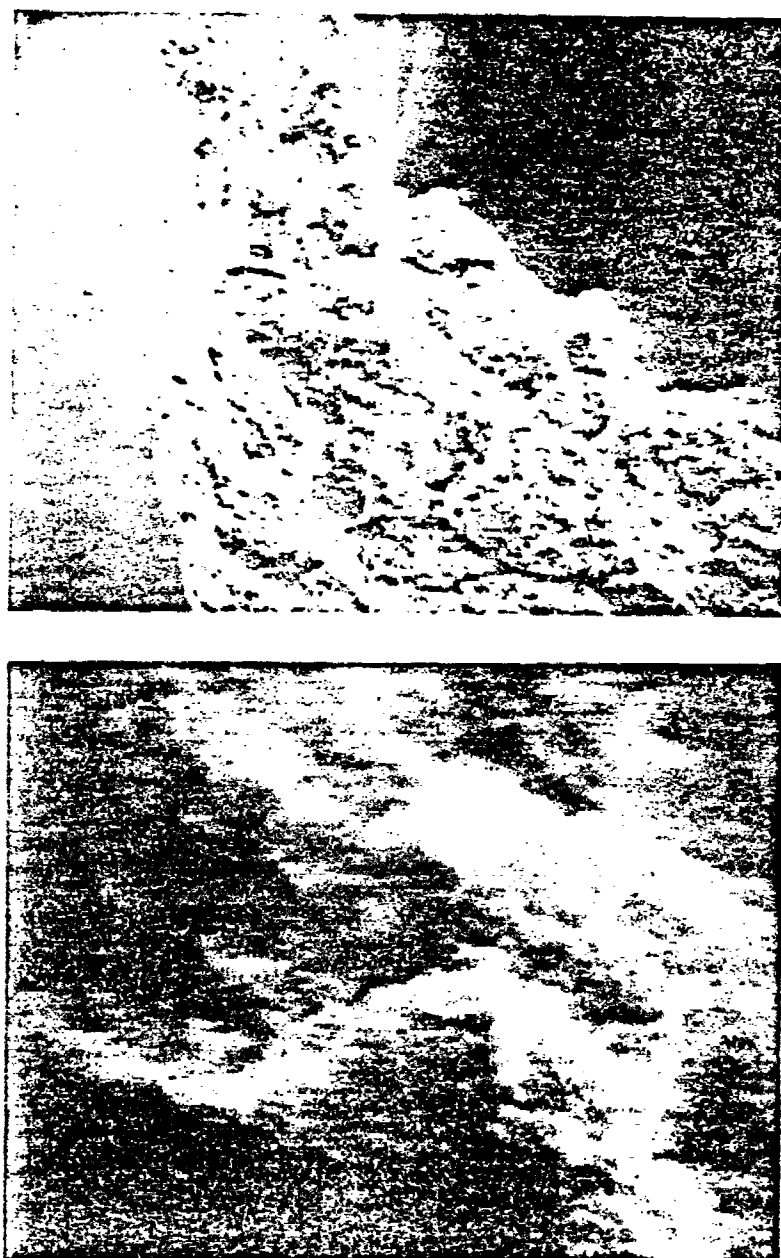
Figure 28. SEM photograph of the carbon residue from a catalyzed
            slurry droplet from the evaporation region, x/d = 510.

substantially increases the residence time where reaction of residue occurs in the flow. For example, if the particles are small enough to move with the gas velocity

$$t_r = \int_{x_i}^{x_e} dx/u \qquad (4.1)$$

where x_i and x_e are the beginning and end of the reaction region, t_r is the residence time in the reaction zone, x is distance from the injector and u is the gas velocity. Completing the integration of Equation (4.1) for present burner conditions yields $t_r = 41$ ms for the noncatalyzed residue and $t_r = 76$ ms for the catalyzed slurry—almost twice as long. Naturally, within an actual combustion chamber, conditions will be different. It seems likely, however, that the catalyzed-slurry residue will react over a greater portion of the flow.

4.1.2 Liquid Evaporation

Results during the steady-evaporation period of the drop were employed for initial evaluation of the liquid-gasification theory. During steady evaporation, with fixed-ambient conditions, the drop was stabilized at its wet-bulb temperature where virtually all the heat transferred to the drop is utilized for the heat of vaporization of the evaporating liquid. Predicted and measured evaporation rate constants, defined as

$$K_e = -\frac{dd_p^2}{dt} \qquad (4.2)$$

were compared. Since K_e varies with drop diameter due to convection, values were compared at various drop sizes.

Predicted and measured evaporation-rate constants for the steady evaporation period, are illustrated in Figure 29. The evaporation-rate constant is plotted as a function of particle diameter with the equivalence ratio of the flame taken as a parameter. The predictions employed $\alpha = 0.9$, which is the value that has generally yielded the best correlation between predictions and measurements during past work in this laboratory [11,150,151,155,156].

Predictions and measurements in Figure 29 are in good agreement, except for results at equivalence ratios of 0.761 and 0.870 where the predictions underestimate the measurements. Envelope flames were observed at these conditions which accounts for the enhancement of evaporation rates over present predictions which ignore envelope flames. Farther downstream, where the equivalence ratio was lower, an envelope flame would cause an even grater enhancement of evaporation rates over present predictions; however, the drops could not sustain stable envelope flames at these positions. At higher equivalence ratios, $\phi = 0.939$ and 1.350, mean oxygen concentrations are finite around the drop (c.f., Figure 12) and envelope flames may also have been present although they could not be observed due to flame luminosity. This would have little consequence, however, since the presence of envelope flames near equivalence ratios of unity does not have a large influence on drop evaporation rates [11]. The model could easily be extended to accommodate envelope flames. However,
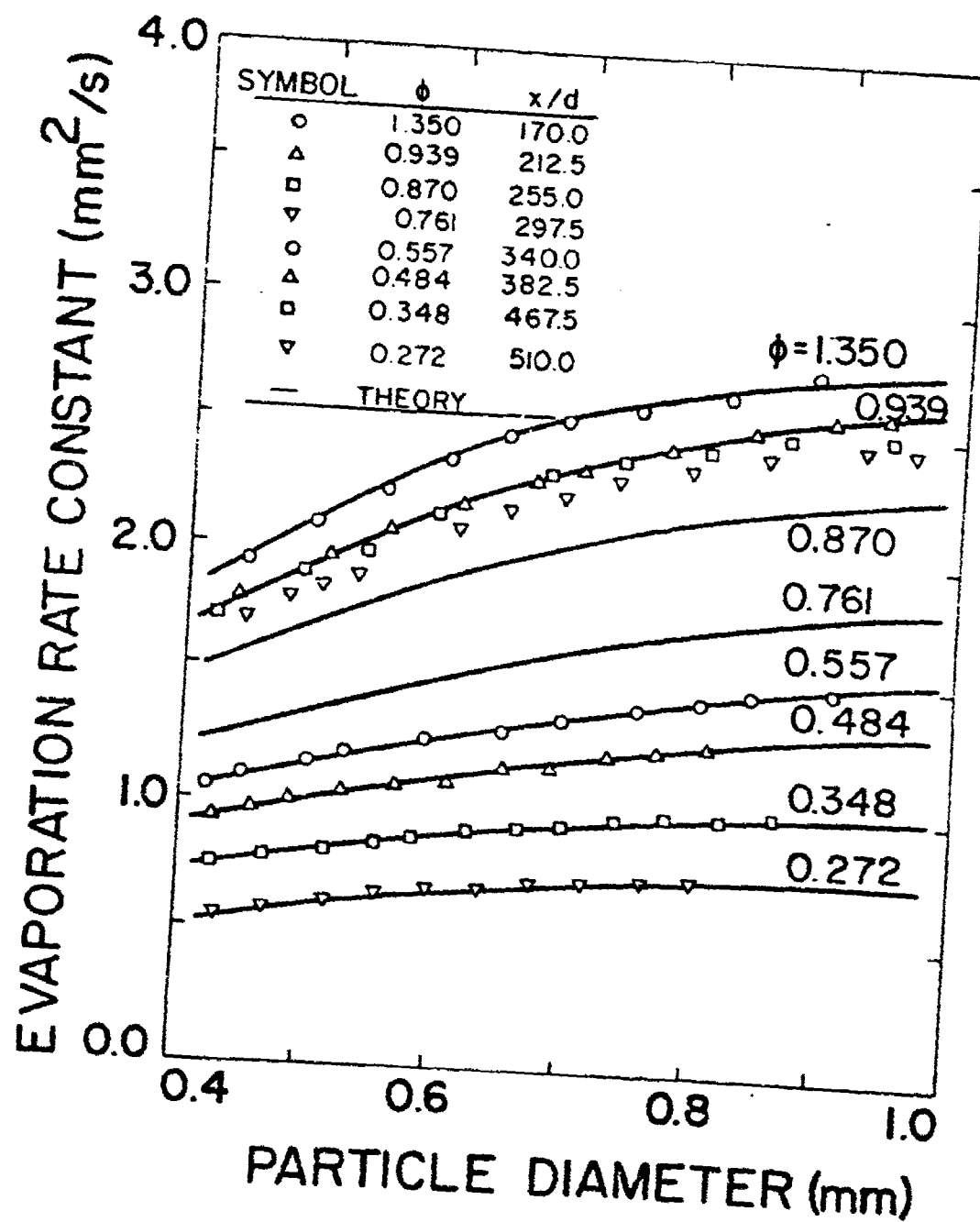
Figure 29. Quasisteady gasification rates for JP-10 droplets.

this was not done here since liquid evaporation in combusting sprays is generally confined to regions where envelope flames are unlikely, even though they were observed when drops were supported in a diffusion flame [11,150,151,155,156].

To illustrate the effect of droplet combustion a simple calculation was performed for a 435 m initial diameter combusting liquid JP-10 droplet over the range of fuel equivalence ratios of the bulk gas. These results are compared to the theoretical prediction for an evaporating droplet, and the experimental measurements in Figure 30 for the same droplet size and conditions. For equivalence ratios greater than unity, the ambient oxygen concentration is small and both theories yield the same burning-rate constant, which is in good agreement with the data. As the equivalence ratio decreases below unity, the theories begin to diverge. In the region where envelope flames were observed the combusting drop model yields best agreement with the data. As the equivalence ratio continues to decrease, however, envelope flames are no longer stable and the measurements shift to the predictions for evaporating drops. The results indicate that the models give reasonable predictions for both evaporating and combusting drops in sprays, as long as the appropriate branch of the solution can be selected for equivalence ratios less than unity.

4.1.3 Carbon Combustion

Equation (3.10) was developed from theoretical and experimental results for smooth spheres and drops and provided a good correlation
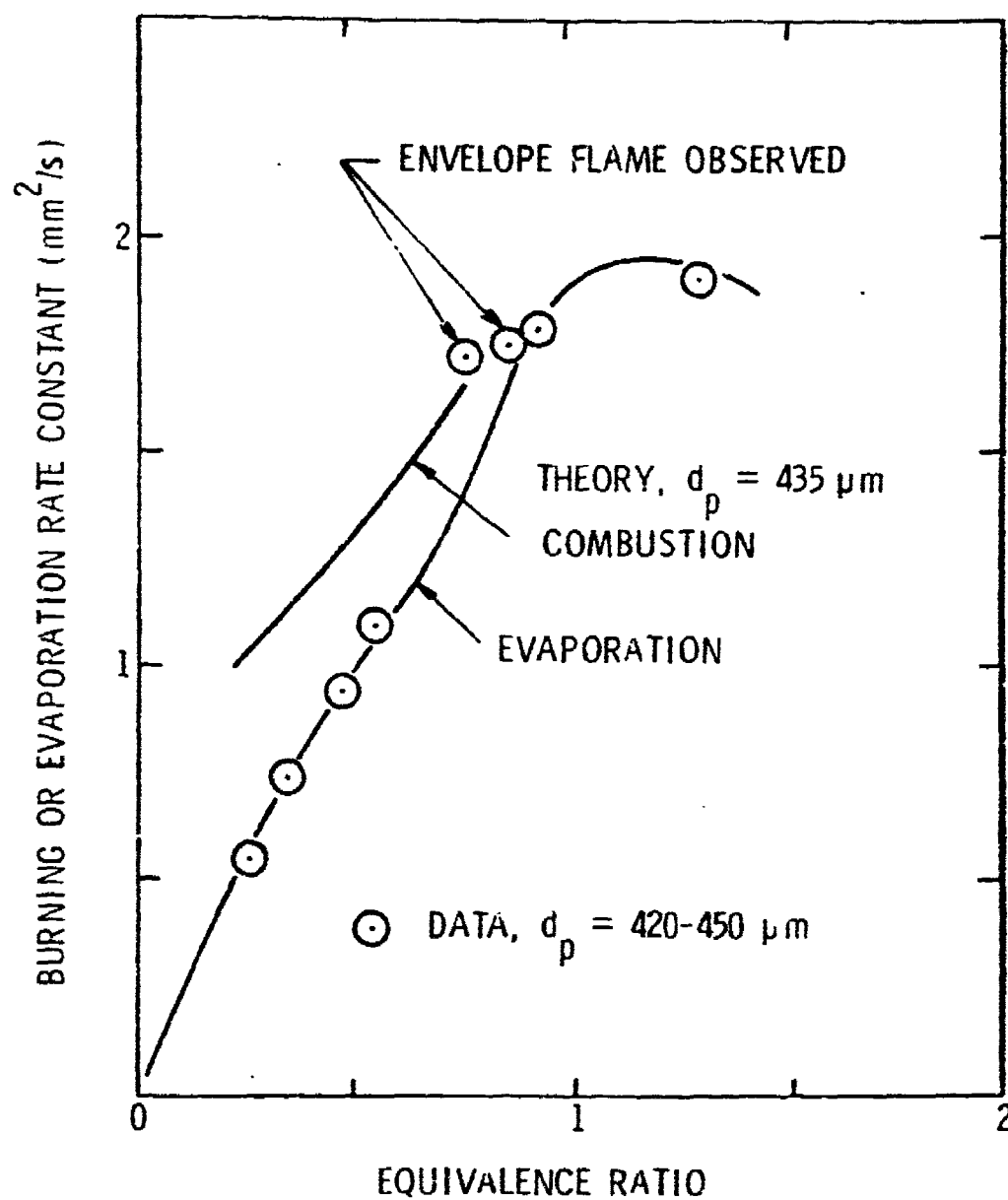
Figure 3C. Comparison of combusting and evaporating drop-life history predictions with experimental results.

of convective effects for drops during this and earlier investigations
[7-11]. The use of this equation, however, underestimated transport
rates of the present agglomerates for all reasonable selections of
physical properties. This behavior was attributed to the fact that
the agglomerates have an open porous structure near the surface
providing roughness effects and allowing the flow to penetrate the
apparent surface to some extent. It was found that this enhancement
of convective transport rates could be accommodated in the model by
multiplying the Nusselt and Sherwood numbers given by Equation (3.10)
by a constant convective enhancement factor of 6.7 throughout the
carbon-combustion analysis for the turbulent-diffusion flame.

Predicted and measured burning rates for noncatalyzed
agglomerates are illustrated in Figures 31 and 32. Burning rate is
plotted as a function of agglomerate diameter with flame position
(equivalence ratio) as a parameter. The data for the turbulent-
diffusion flame tests are tabulated in Appendix B. Equivalence ratios
of 0.870-1.350 are illustrated in Figure 31, while lean conditions,
corresponding to equivalence ratios of 0.272-0.761, are illustrated in
Figure 32. The predictions employ the reaction parameters summarized
in Table 3. For this selection of parameters, the two reaction
approximations gave nearly the same results and both methods can be
represented by a single line. Clearly, the use of a single set of
area-reactivity multiplication factors, a_i, provides a good
representation of the data over the entire range of the tests. The
low reaction rates at low equivalance ratios were also predicted
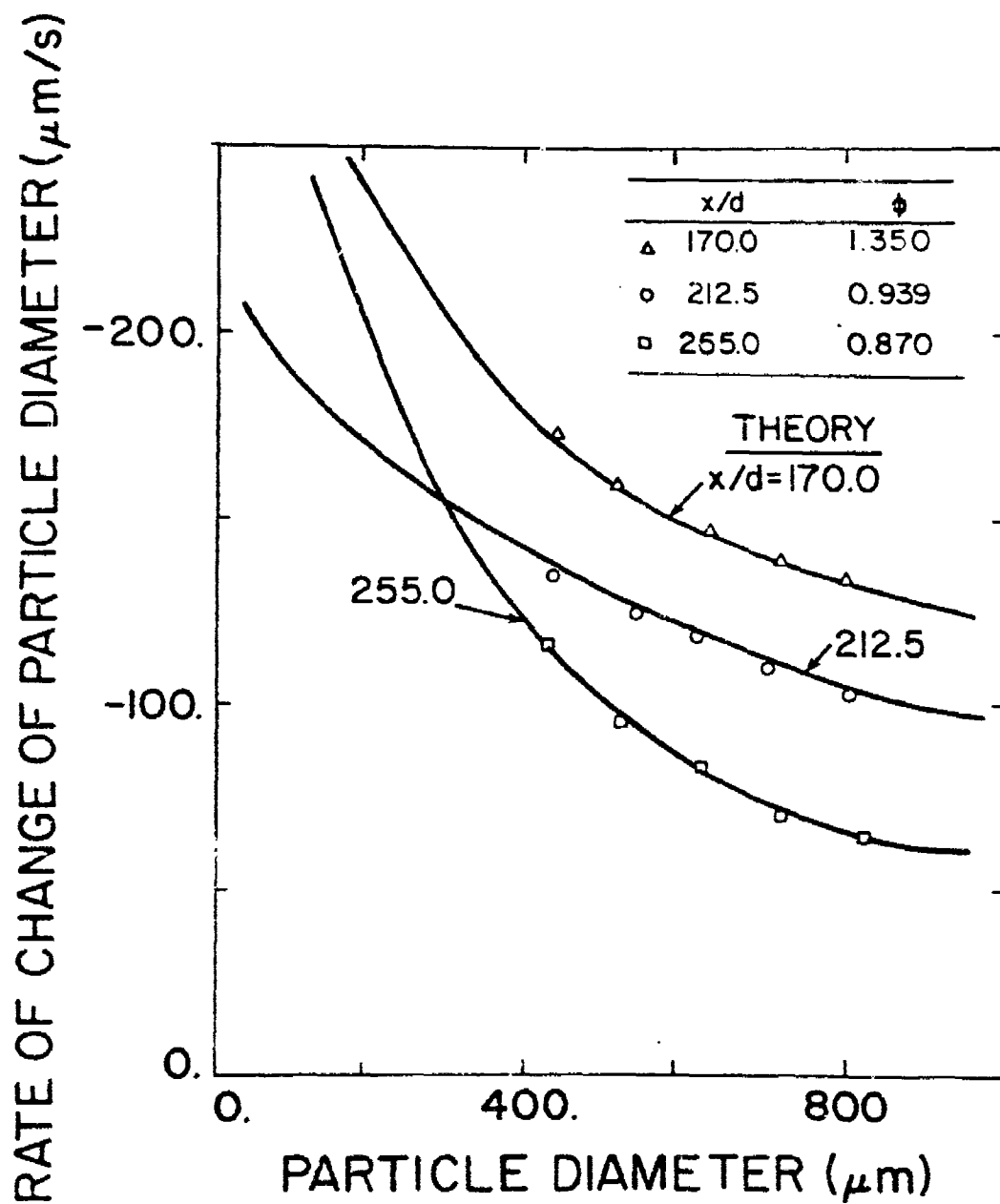
Figure 31. Quasisteady burning rates for noncatalyzed carbon agglomerates at high equivalence ratios.
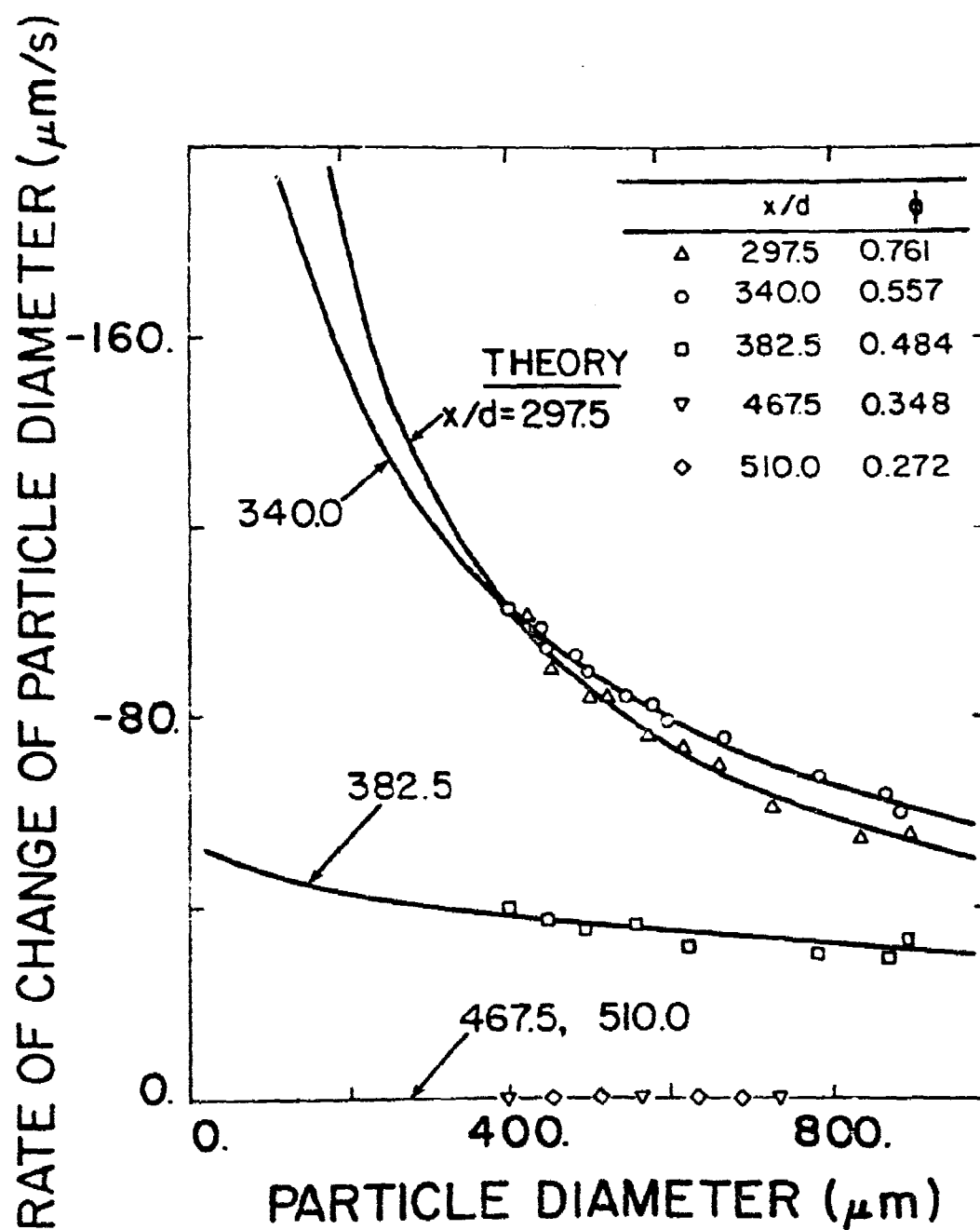
Figure 72. Quasisteady burning rates for noncatalyzed carbon agglomerates at low equivalence ratios.

reasonably well, suggesting that the model has some potential for predicting quenching of the agglomerate reaction.

There are two main combustion limits for carbon agglomerates, the reaction-controlled limit and the diffusion-controlled limit [159]. For reaction control, reaction rates are low in comparison to diffusion rates, and there is no mass transfer limitation on the supply of gaseous reactants to the particle surface. This limit is characterized by the burning rate being relatively independent of particle diameter, e.g., the results for x/d 382.5 in Figure 32 approach the reaction controlled limit.

The diffusion-controlled limit is characterized by high reaction rates in comparison to diffusion rates, leading to small concentrations of reactant gases at the particle surface. In this case, the burning rate is largely determined by the mass-transfer properties of the flow around the particle. The magnitude of the burning rate is then influenced by particle diameter, as follows:

$$\frac{dd_p}{dt} \sim d_p^{-(0.5 \text{ to } 1.0)} \tag{4.3}$$

The power of d_p in Equation (4.3) tends toward -1 as the Reynolds number of the particle decreases. From this argument, it is apparent that results in the range $255.0 \leq x/d \leq 340$, in Figures 31 and 32 are approaching the diffusion-controlled limit. The remainder of the measurements involve both reaction and diffusion effects to some extent. Diffusion rates become large for small particles; therefore,

all regions of the flow would eventually exhibit reaction control for sufficiently small particles.

Figure 33 is an illustration of predicted and measured burning rates for the catalyzed agglomerate. These test results were limited to x/d = 297.5, 340.0 and 382.5 and were analyzed only using the extended Libby and Blake [88,89] reaction mechanism. Reaction of the agglomerate is nearly diffusion controlled at the first two positions, resulting in little change in the burning rate when the catalyst was used. At x/d = 382.5, however, adding catalyst increased the burning rate 20-25%, since the rate of gasification of carbon is nearly reaction controlled at this position. Naturally, the effect of catalyst would be even greater at positions farther downstream, e.g., the presence of catalyst reduced the lean limit for quenching from an equivalence ratio of 0.37 to 0.21.

Another property of catalyzed slurries was their tendency to spontaneously shatter from time-to-time. When observed, shattering occurred after all the liquid had apparently evaporated. This behavior could be influenced by the presence of the drop support, and was not consistently observed. If shattering does persist for small unsupported particles, however, this would provide another (physical) mechanism for the improved combustion properties observed for catalyzed slurries during combustion-chamber tests [2,3]. Tests with unsupported particles, having sizes more typical of sprays, will be required in order to establish the importance of this effect.
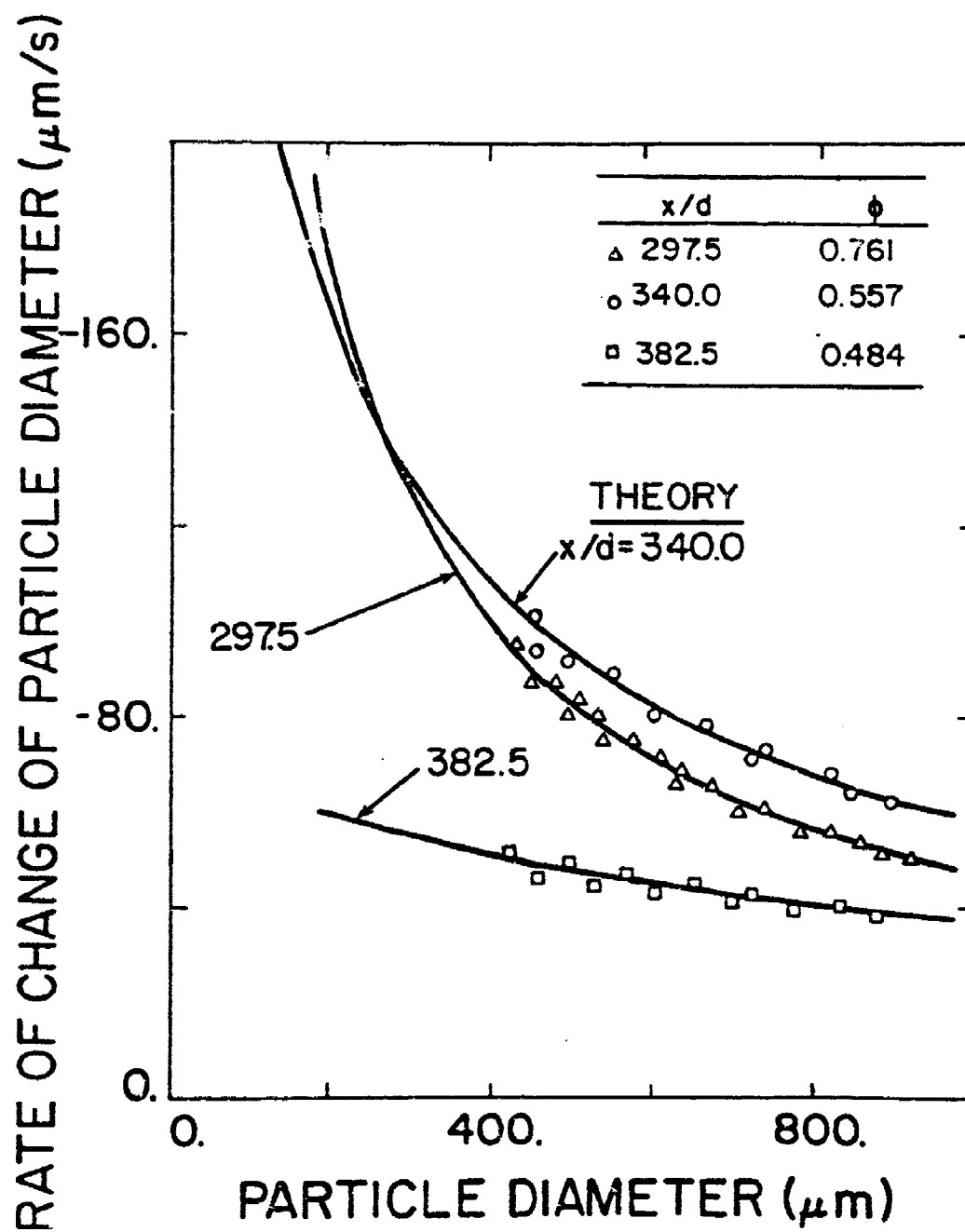
Figure 33. Quasisteady burning rates for catalyzed agglomerates.

The final step in evaluating the model for the turbulent-diffusion flame tests involved comparison of predicted and measured slurry drop-life histories. Life histories were computed for noncatalyzed slurries over the test range. The results are illustrated in Figures 34-41 which covers equivalence ratios of 0.272-1.350. Predicted and measured particle diameters and temperatures are plotted as a function of time, with results illustrated for both reaction approximations. The local temperature of the flow is also shown on each plot, for reference purposes. The time scale of Figures 34-37 has been expanded in the period where liquid is present, since this period is short in comparison to the total lifetime of the slurry drop. The liquid evaporation period is not shown in Figures 38-41.

The two-stage combustion process of slurry drops is quite evident from the results pictured in Figures 34-37. The first stage involves heat-u$_r$ of the particle to the wet-bulb temperature for liquid gasification. Some evaporation occurs throughout this period; however, the rate is highest when the particle is near the wet-bulb temperature. Since JP-10 is a pure hydrocarbon, its wet-bulb temperature is nearly constant at a fixed location in the flame (having a value somewhat below the boiling temperature of the liquid) [11]. The second stage involves heat-up and reaction of the agglomerate, once all the liquid has evaporated. Initially, the variation of agglomerate diameter is relatively slow in this period, until the particle temperature approaches the gas temperature.
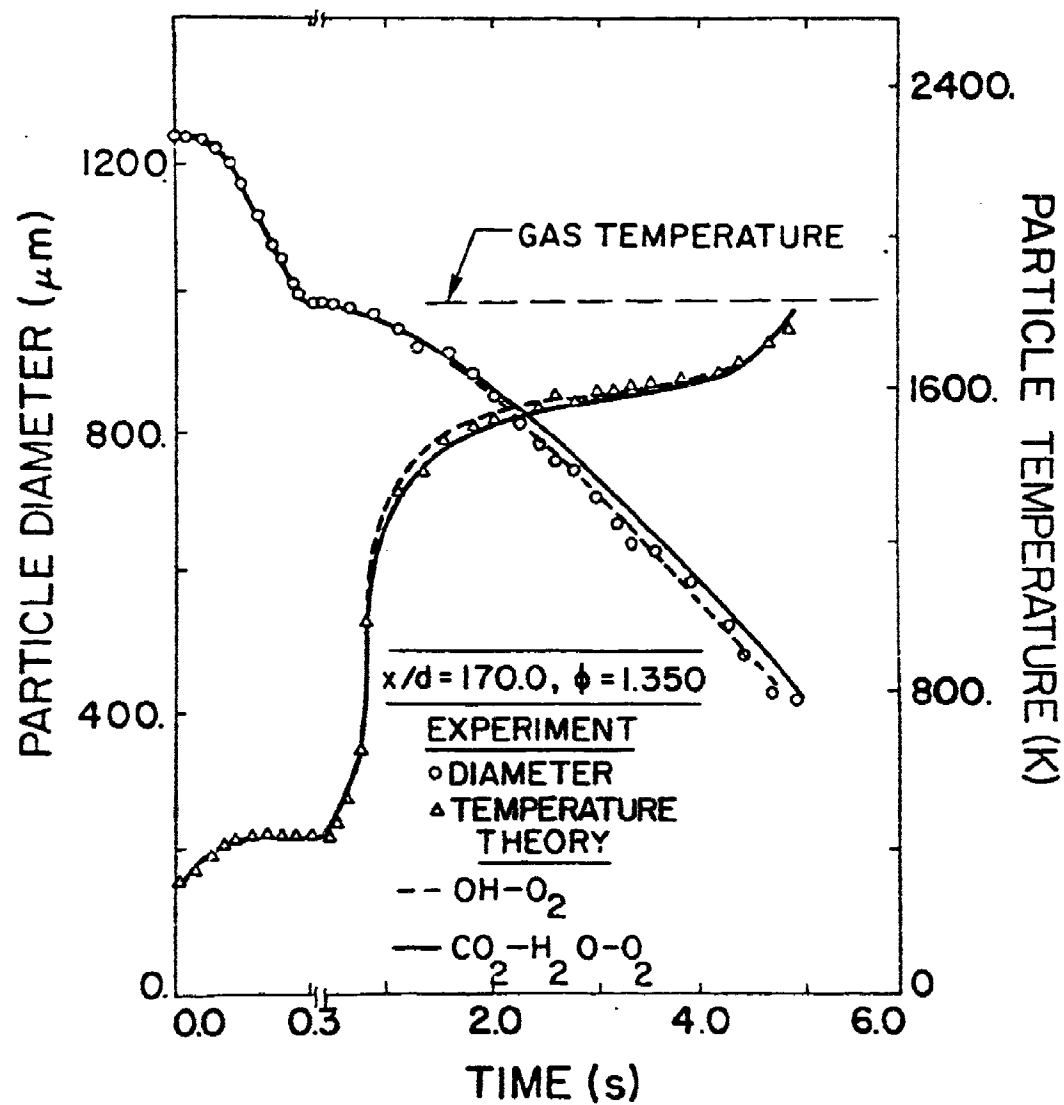
Figure 34. Noncatalyzed slurry drop-life history at x/d = 170.0.
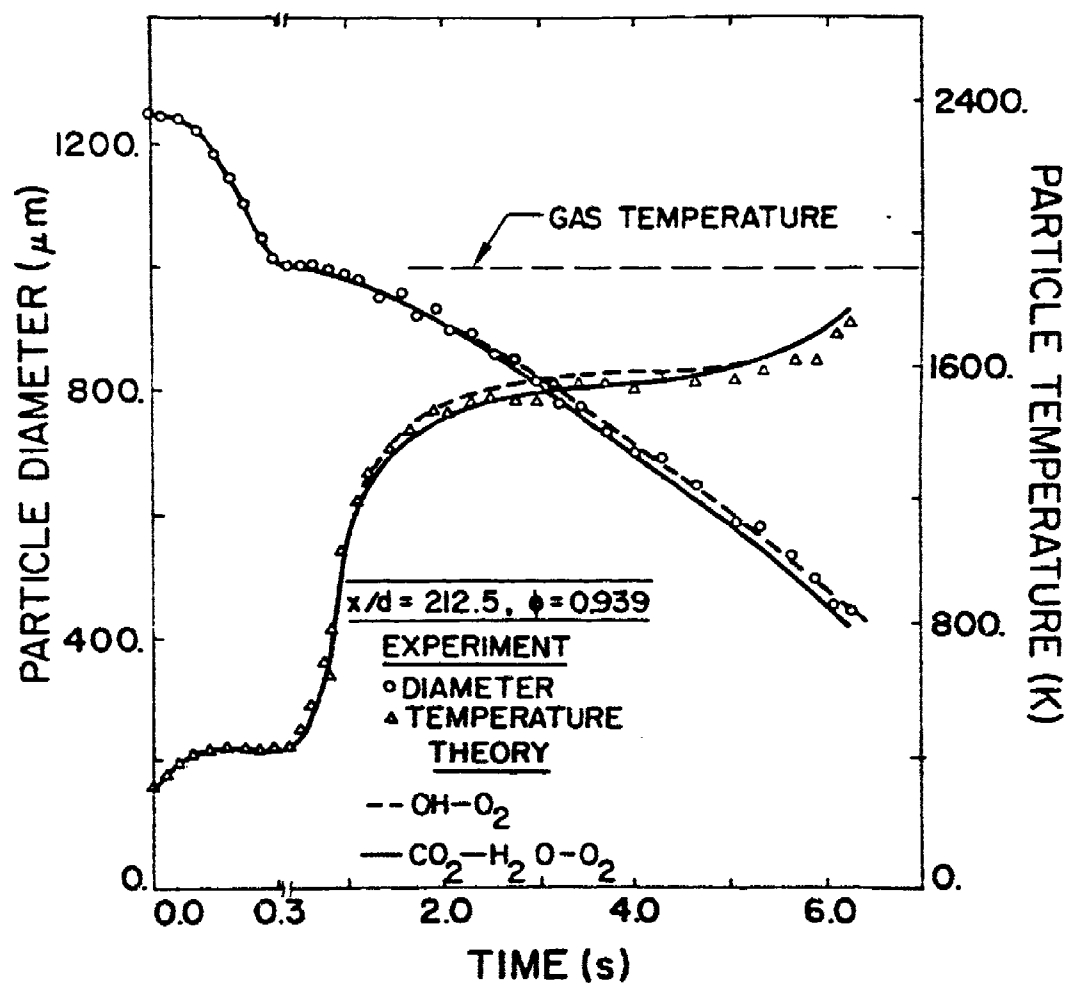
Figure 35. Noncatalyzed slurry drop-life history at x/d = 212.5.
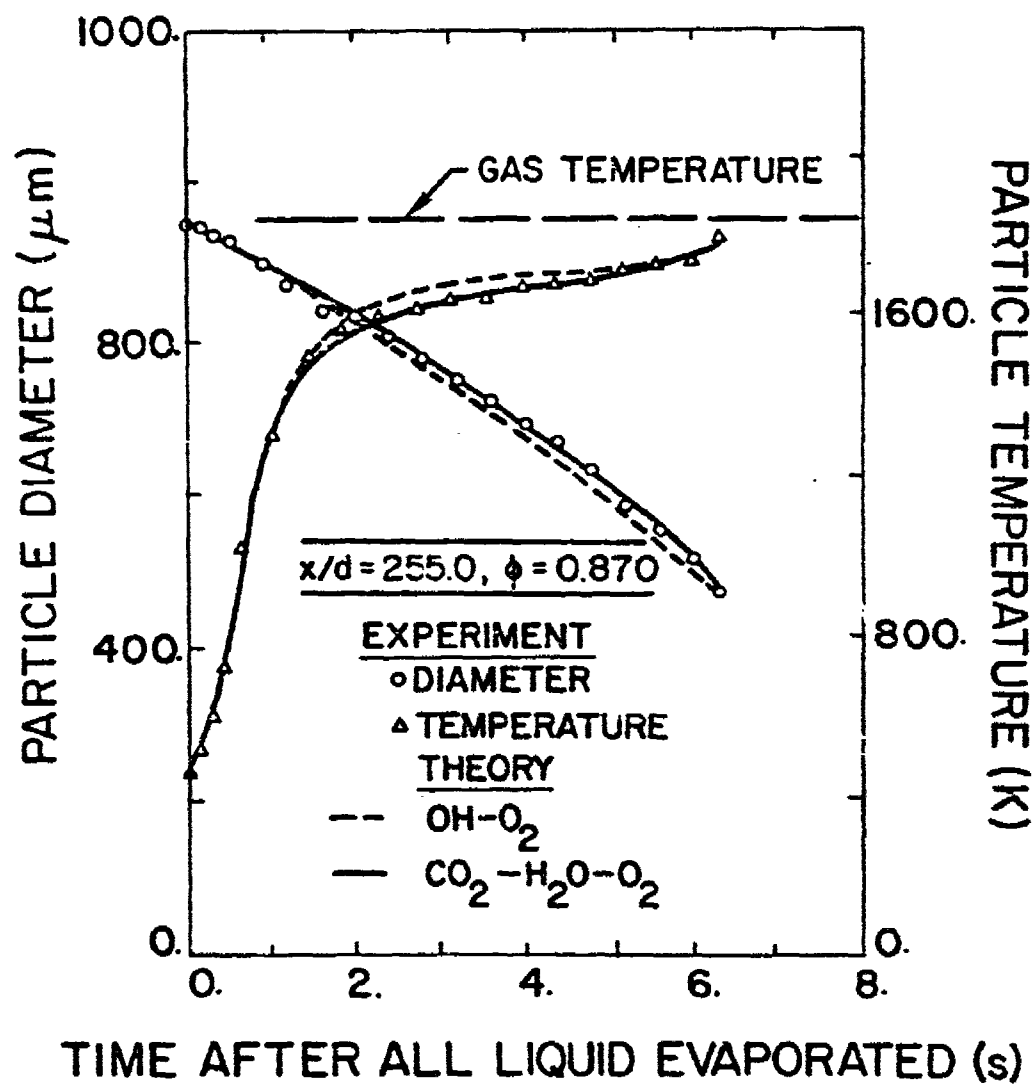
Figure 36. Noncatalyzed slurry drop-life history at x/d = 340.0.
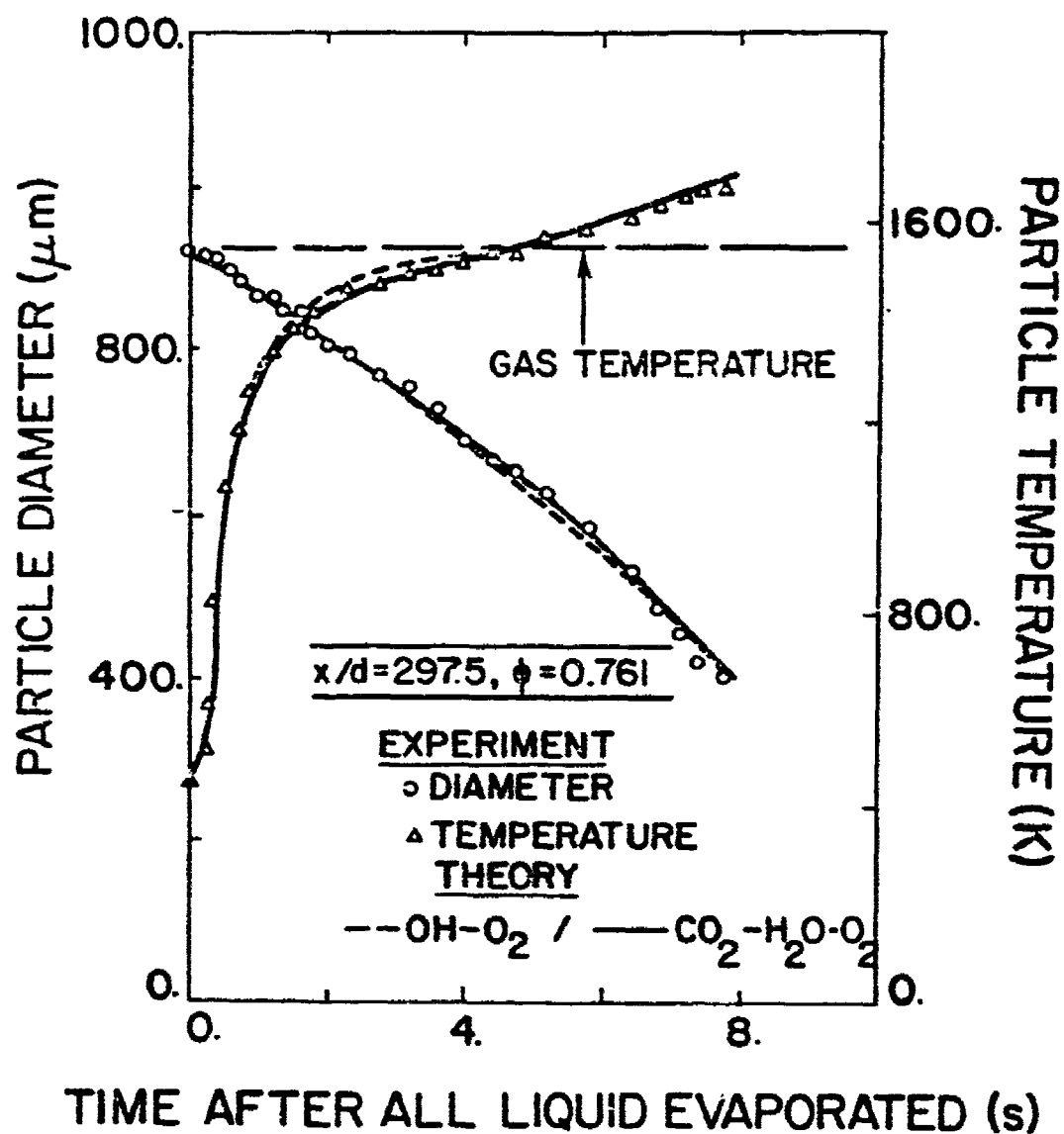
Figure 37. Noncatalyzed slurry drop-life history at x/d = 467.5.
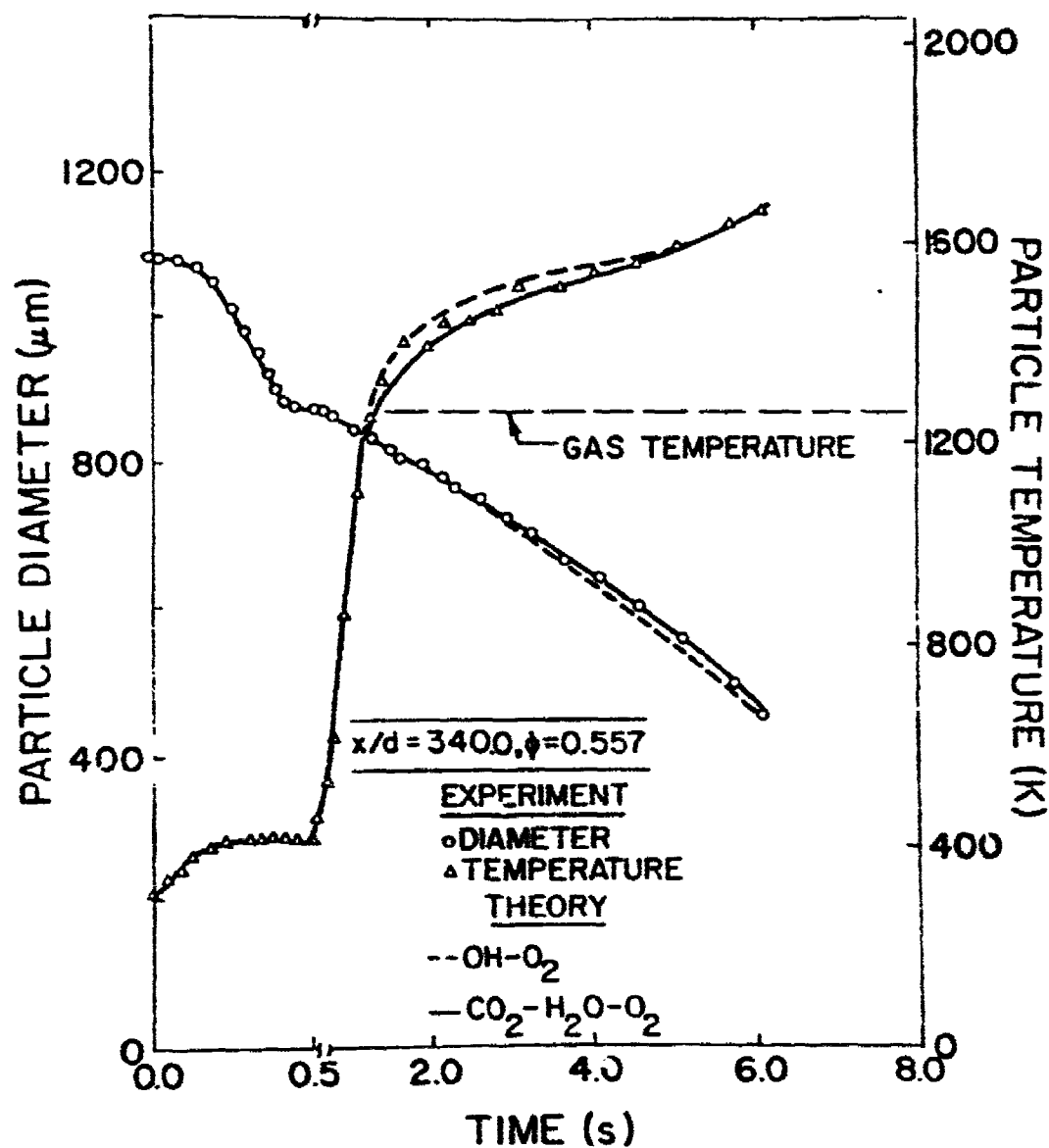
Figure 38. Noncatalyzed slurry drop-life history at x/d = 255.0.
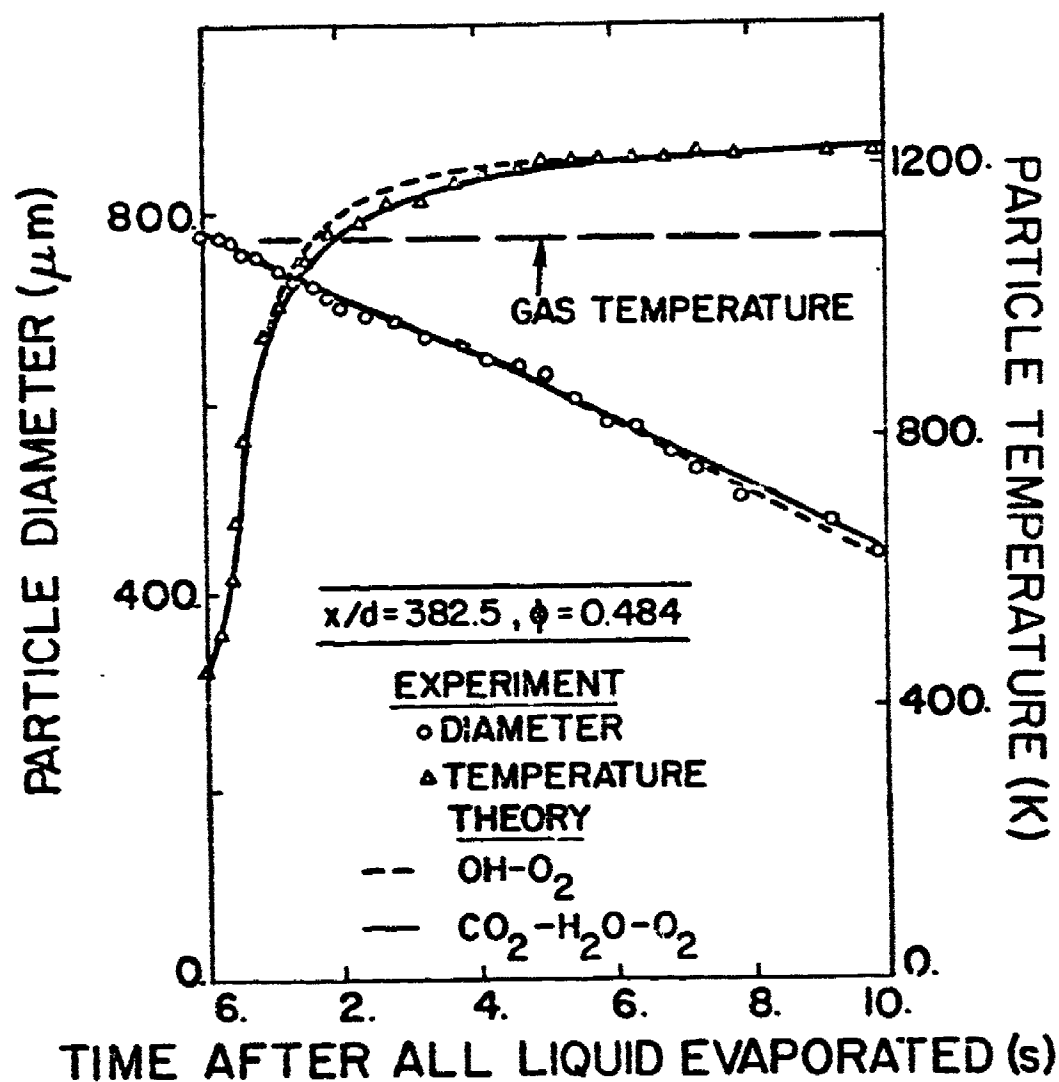
Figure 39.   Noncatalyzed slurry drop-life history at x/d = 297.5.
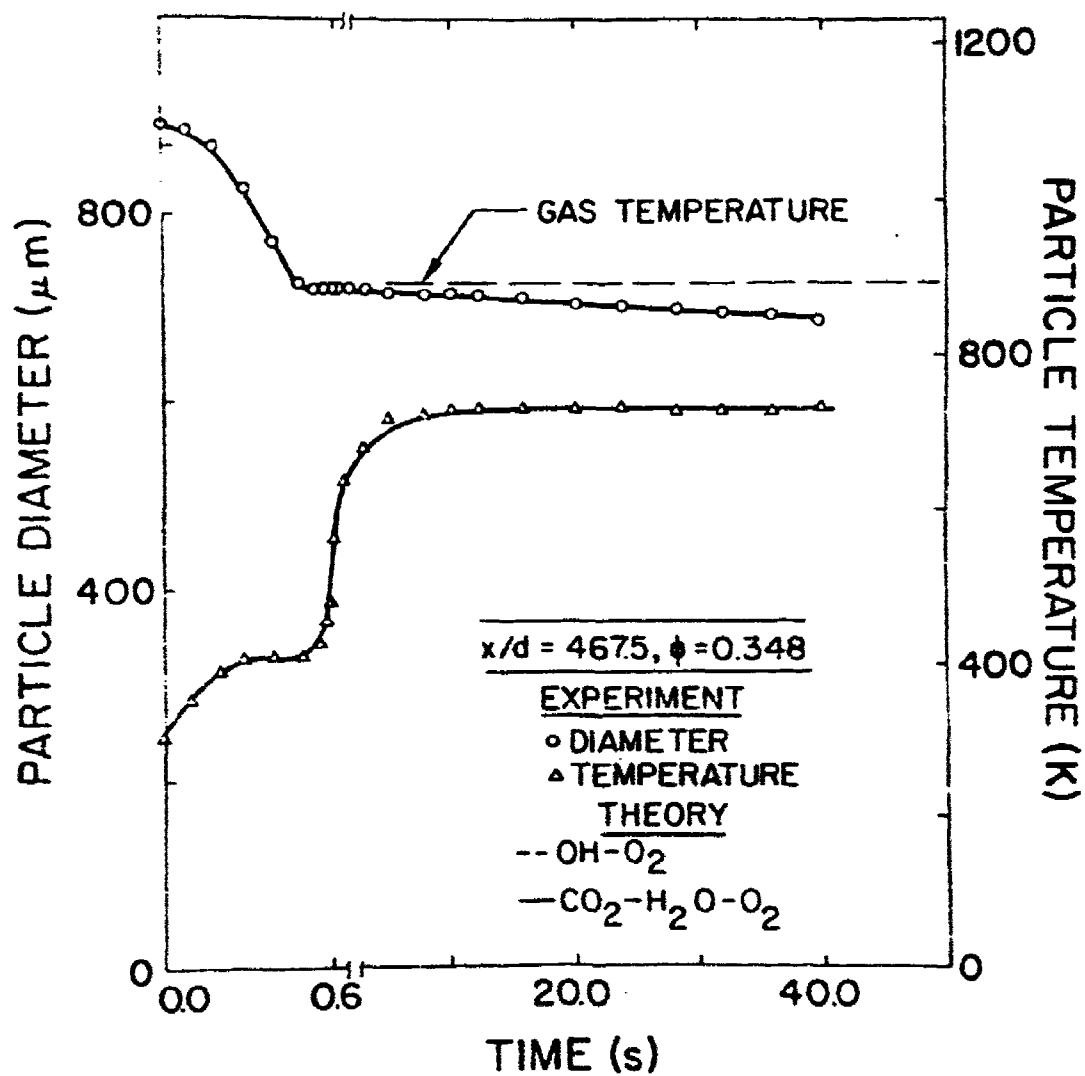
Figure 40. Noncatalyzed slurry drop-life history at x/d = 382.5.
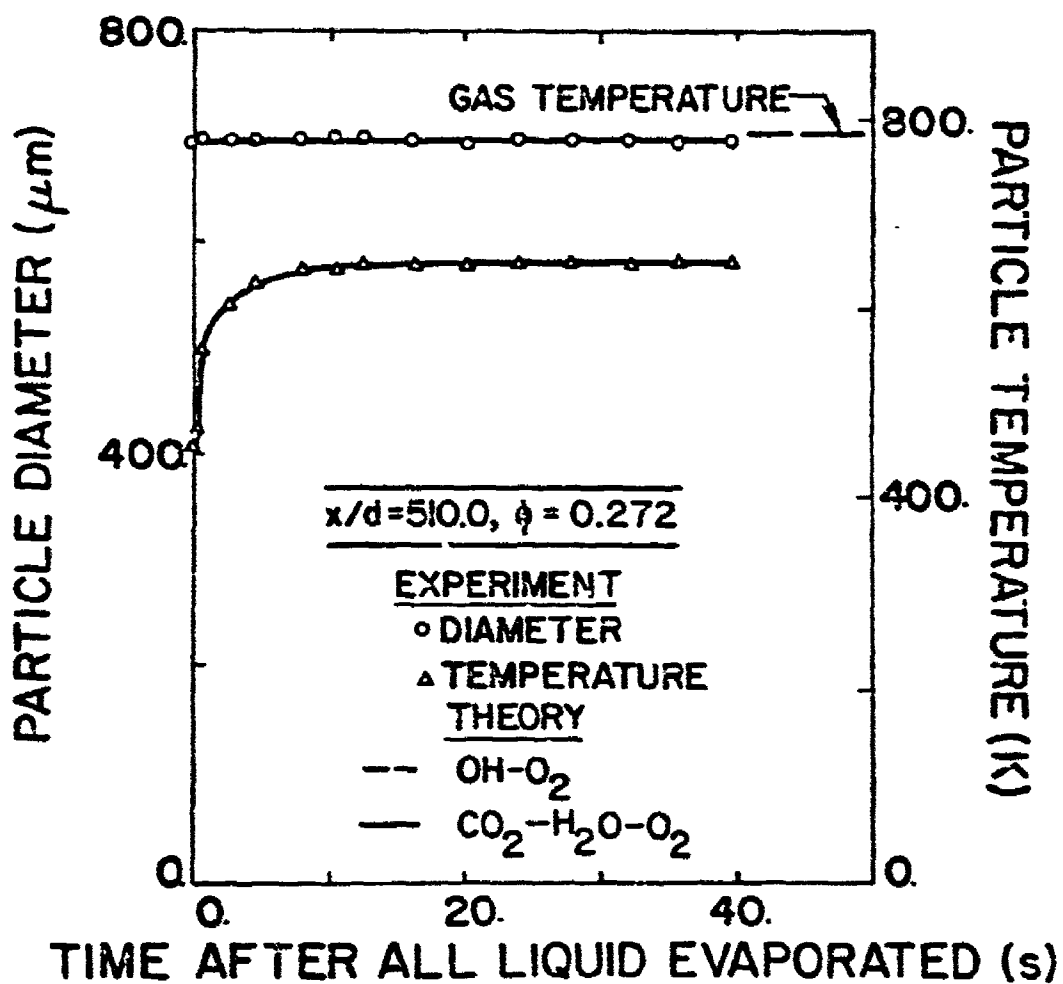
Figure 41. Noncatalyzed slurry drop-life history at x/d = 510.0.

Maximum particle temperatures can be above or below the gas temperature, depending on the energy release by reaction, and heat transport by convection and radiation. Near the lean and rich limits, particle temperatures tend to be below the flame temperature due to radiative heat losses. Intermediate equivalence ratios, e.g., 0.557 for Figure 36, yield relatively high reaction rates and particle temperatures exceed the flame temperature. The relative rates of reaction, convection and radiation, however, vary with particle size. Therefore, there is no fixed particle temperature during the latter part of agglomerate reaction, even at a fixed location in the flame, unlike the liquid evaporation period. As the particle becomes small, however, convection heat transfer rates become large in comparison to reaction and radiation effects, and the particle eventually approaches the local gas temperature. This is not observed in Figures 34-41 due to the finite-sized bead used to mount the slurry drop.

The comparison between the predictions and measurements illustrated in Figures 34-41 is quite good. This is partly expected, since the model was capable of correlating the burning-rate measurements for this range of flame conditions. However, it is encouraging that the model is also capable of predicting heat-up, where reaction effects are small, as well as final temperature levels, where radiation becomes important. There is little difference in the predictions using the two reaction approximations, similar to the agglomerate burning-rate results.

4.2 Carbon-Agglomerate Combustion in the Laminar Premixed Flame

4.2.1 Empirical Parameters

Figure 42 is a scanning electron microscope photograph of four carbon agglomerated particles collected near the injector exit. Since the particles were irregular, the average of at least eight particle diameters is employed for the diameters quoted in the following. The agglomerate diameters of the particles in Figure 42 vary within 15% of each other, which was typical for all of the test conditions.

Figure 43 shows two SEM photographs of particles collected at the same test condition, one just after injection and the second after it had partially reacted by passing 8.1 mm through the burner gases. The nonreacted particle has some irregularities, but is basically spherical in shape and has a relatively smooth surface. After some reaction, however, the particle becomes very porous. There appears to be a less dense pore layer surrounding a more dense central core. This yielded an apparent average density reduction from 1820 kg/m^3 to 1640 kg/m^3. The porous structure allows gas to percolate through the particle and provides substantially more surface area for reaction than the surface area of a smooth sphere having the same outer diameter -- supporting the need for separate convection enhancement factors and area/reactivity factors employed in the present analysis.

The upper photograph of Figure 43 had a reacted mass fraction of 0.0, and the lower photograph had an 0.122 reacted mass fraction. Particles burning in other flame conditions, which had similar reacted mass fraction values, appear analogous to these photographs. The

Figure 42. SEM photograph of four particles collected from
the ϕ = 1.0, T_f = 1683 K, d_{po} = 52.6 μm test
condition at a distance of 1.8 mm from the injector.
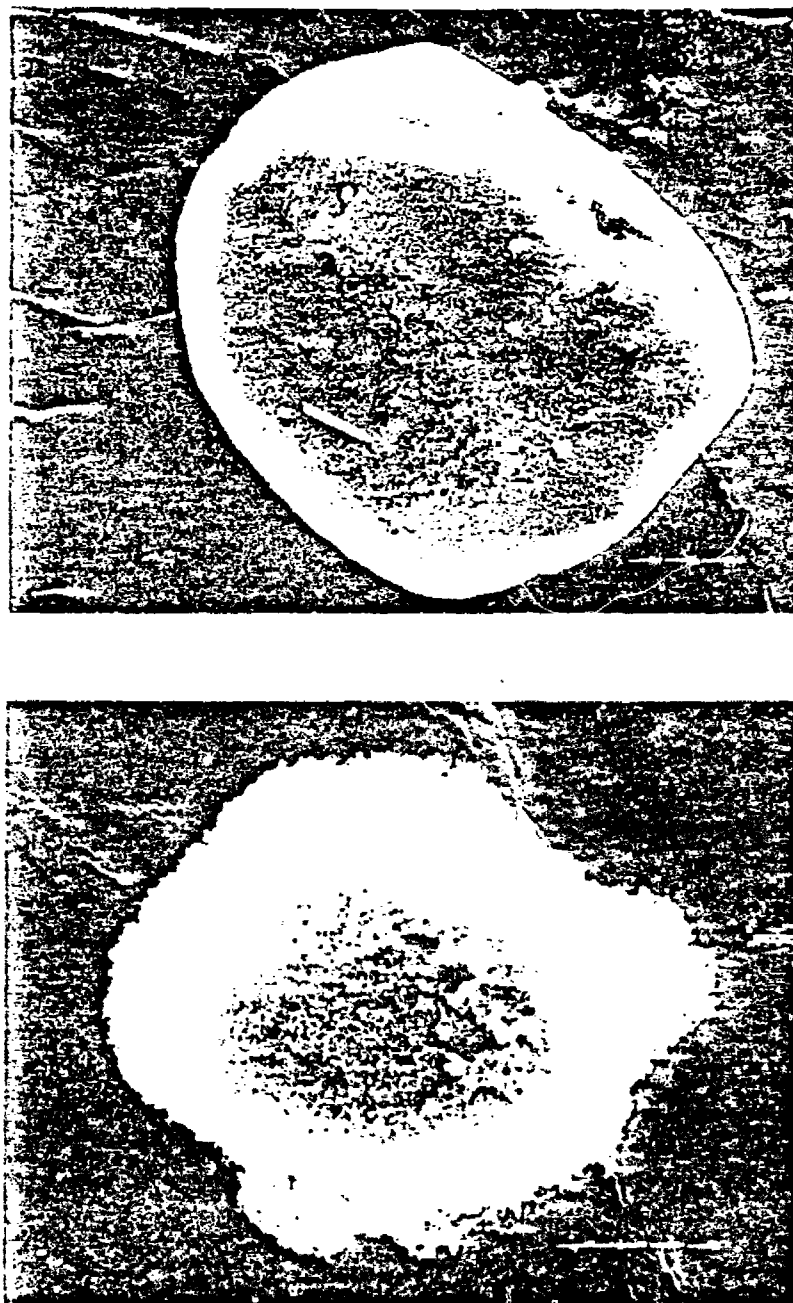
Figure 43. Two SEM photographs of particle a particle collected from
the $\phi = 1.0$, $T_r = 1683$ K, $d_{po} = 71.4$ μm test condition.
The particle shown in the upper photograph has a reacted
mass fraction of 0.0, while the lower has a 0.122 reacted
mass fraction.

upper photograph of Figure 44 had a reacted mass fraction of 0.902 and the lower photograph 0.999. Again particles burned in other flame conditions which had equivalent reacted mass fraction values appeared very much the same as the photographs in Figure 44. From these four photographs, it appears that as the particle burns, a surface pore structure evolves. Initially the central core is unaffected, however, as the pore structure develops even the center of the particle develops void spaces. Near the end of the combustion process, the pore structure has grown to the point where the particle has an almost lacey structure with a near zero apparent density, while still having a substaintial diameter.

Figure 45 is an illustration of the variation of particle density with the extent of reaction, measured for the various flame conditions. The density variation is relatively independent of initial particle diameter and flame conditions yielding the correlation:

$$\rho_p = 1820 \cdot (1 - \varepsilon)^{0.6} \qquad (4.4)$$

where ε is the reacted mass fraction. The greatest discrepancies between Equation (4.4) and the measurements occurred for either the very small diameter cases or the first test case investigated. The small particle test conditions ($d_{po} = 10 \ \mu m$) deviated from the bulk of the data since experimental accuracy has deteriorated. The deviation of the first test condition examined ($\phi = 0.6$, $T_f = 1663$ K, $d_{po} = 73.4 \ \mu m$) from the bulk of the data may possibly be attributed
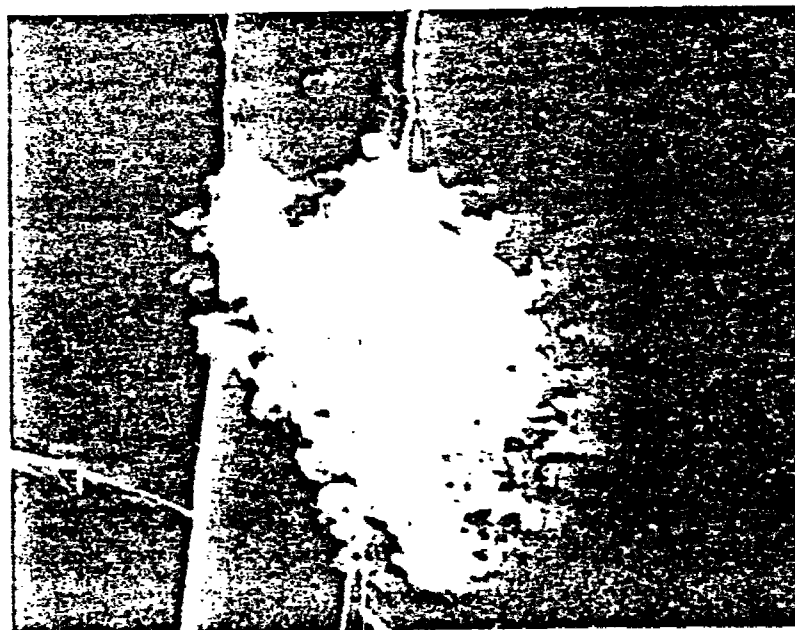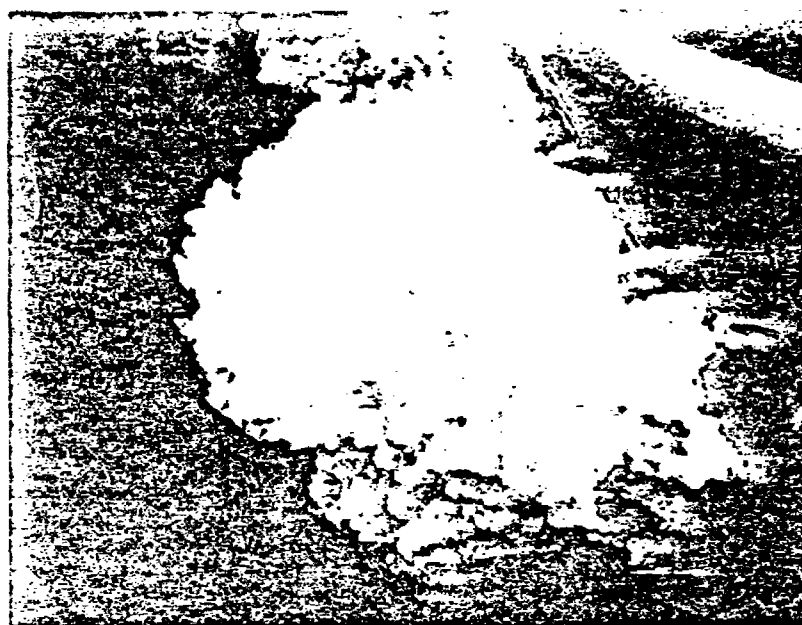
Figure 44. Two SEM photographs of collected carbon agglomerates.
The upper photograph shows a particle with a reacted
mass fraction of 0.902 while the lower has a reacted
mass fraction of 0.999.
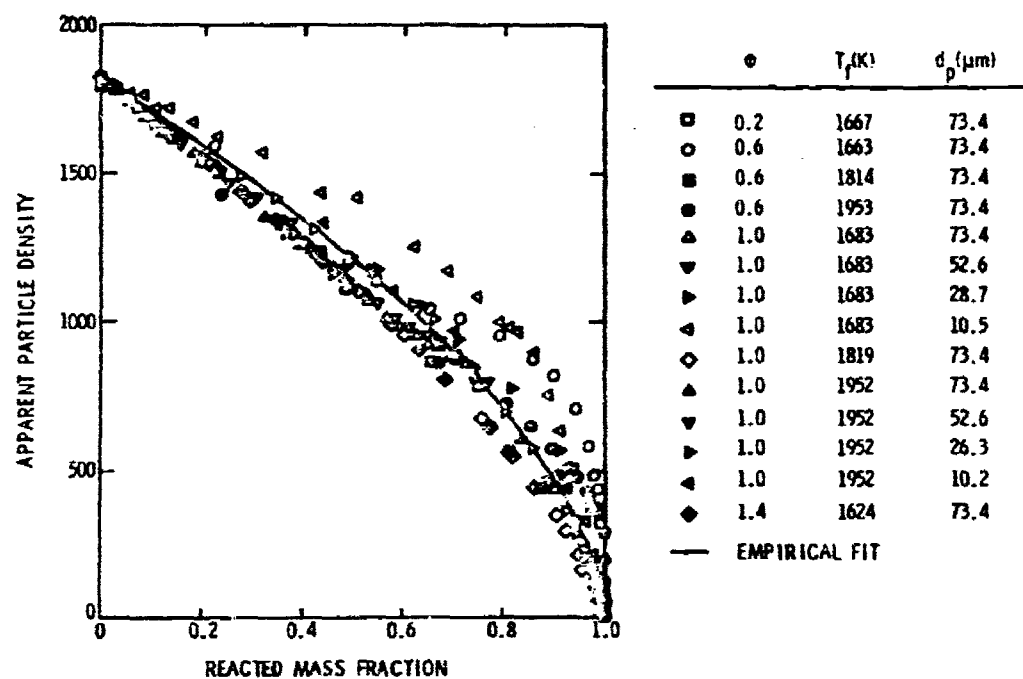
Figure 45. Apparent particle density vs. reacted mass
fraction for all the test conditions examined.

to experimental inaccuracies since the data collection procedure had
not yet been fully developed, and perhaps the required prudence was
not exercised.

In addition to the particle density variation, the pore structure
also gave rise to transport-enhancement factors since the ambient gas
could percolate through the porous particle. The experimental values
of the transport-enhancement factor for each experimental data point
examined is shown in Figure 46.

Also shown in the figure are the transport-enhancement factors
for the large particle test which was taken to be a constant as a
result of insufficient data. In all the test cases, the particle
diameters ranged between 0 and 75 μm. As for the large particle
tests, both the energy and mass transport-enhancement factors were
found to be equal. The empirical curve-fit of the transport-
enhancement factor which best correlated the data is given as a
function of reacted mass fraction and particle diameter:

$$\Psi = -0.00858d_p + 18.3\epsilon - 13.2\epsilon^2 + 2.02 \qquad (4.5)$$

where the particle diameter, d_p, is expressed in microns. Also
plotted in Figure 46 is the transport-enhancement factor empirical
curve-fit for a constant particle diameter of 0 and 75 μm. The
empirical curve-fit for the two-constant particle diameter cases bound
the experimental data.

Note, at the particle injector exit, where the particle is nearly
smooth with a uniform density; a near unity enhancement factor is

	Φ	T_f(K)	d_p(μm)
▫	0.2	1667	73.4
○	0.6	1663	73.4
■	0.6	1814	73.4
●	0.6	1953	73.4
△	1.0	1683	73.4
▼	1.0	1683	52.6
▷	1.0	1683	28.7
◁	1.0	1683	10.5
◇	1.0	1819	73.4
▲	1.0	1952	73.4
▼	1.0	1952	52.6
▶	1.0	1952	26.3
◀	1.0	1952	10.2
◆	1.4	1624	73.4

—— EMPIRICAL FIT

- - - LARGE PARTICLE VALUES
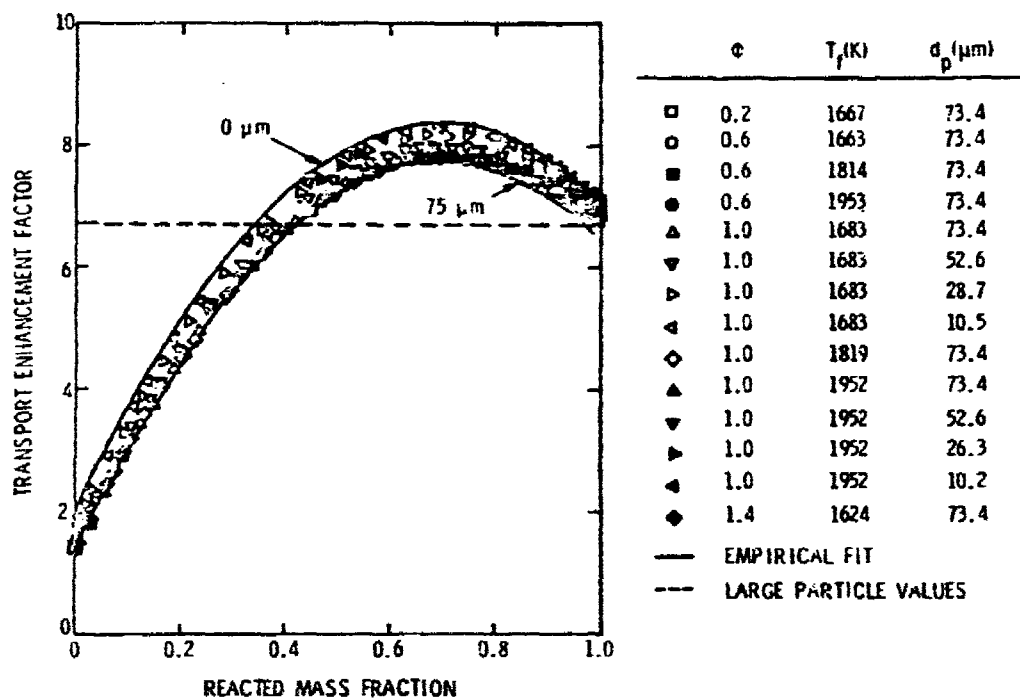
Figure 46. Transport-enhancement factor vs. reacted mass
fraction for all the test conditions examined.

indicated. In addition, during the first 20% of the combustion process where the particle is less porous, a smaller transport-enhancement factor is predicted. Finally, the transport-enhancement correlation based on the small particle test gives a reasonable prediction for the value obtained from the large particle test over the last 80% of the combustion process.

The increase in particle reactivity due to the pore structure is indicated in Figure 47 for the O_2-H_2O-H_2O reaction mechanism. The area-reactivity multiplication factors on a zero suppressed scale are plotted in this figure vs. reacted mass fraction for the oxygen, carbon dioxide and water vapor reaction mechanisms. Again for each experimental test condition the particle diameter ranged between 0 and 75 μm.

The empirical factors were established in the following manner: the values of the transport-enhancement factor were determined first, under the constraint that the mass and energy transport-enhancement factors must be equal. The variation of the transport-enhancement factor with reacted mass fraction was determined by matching the initial temperature increase period as well as conditions where the reaction rate was diffusionally controlled. The results were correlated to give an expression for the transport-enhancement factor based on particle diameter and reacted mass fraction. Once the transport-enhancement factor relationship was determined, an optimization routine was employed which examined each individual data point and determined the appropriate area-reactivity multiplication
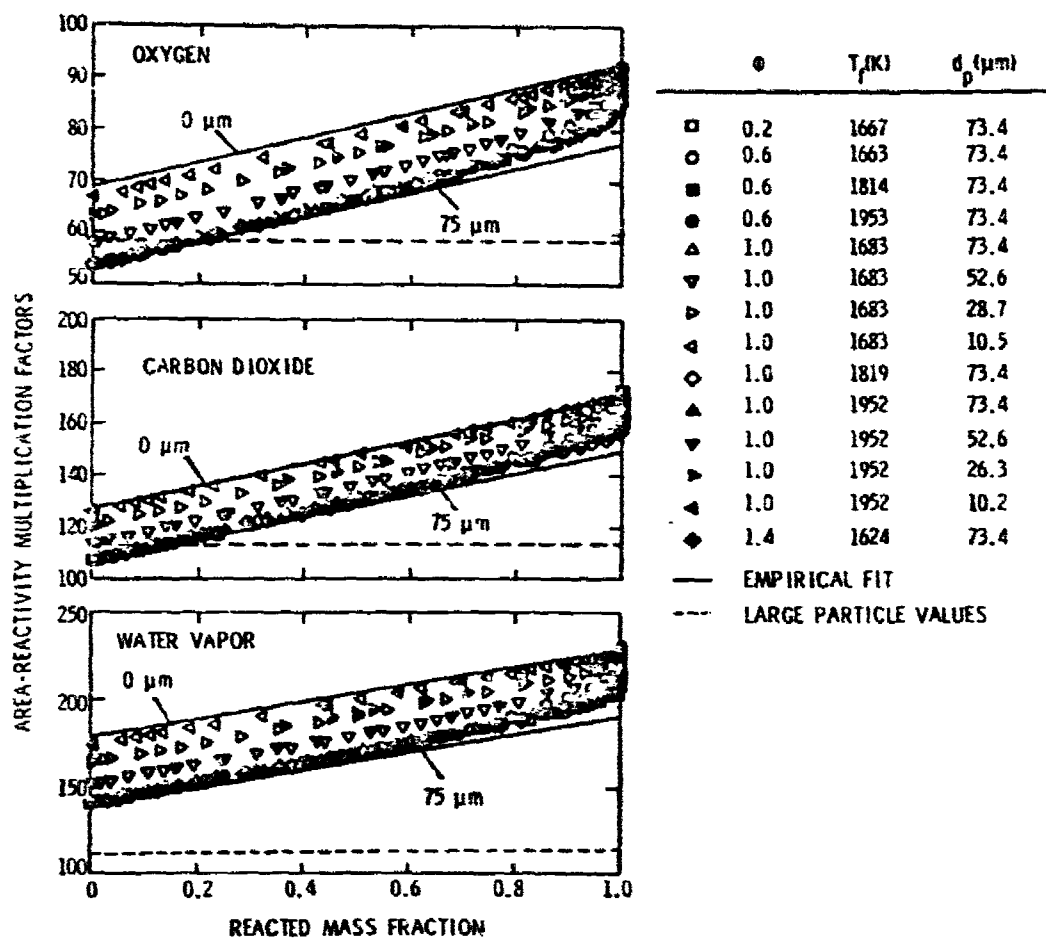
Figure 47. Area-reactivity multiplication factors for the O_2-CO_2-H_2O reaction mechanism, for all the test conditions examined.

factors values to match the rate of change of particle properties. The results were correlated to yield the relationship between the area-reactivity multiplication factor values with particle diameter and reacted mass fraction.

The empirical curve-fits of the area-reactivity multiplication factors for the O_2-CO_2-H_2O reaction mechanismare given as:

$$a_{O_2} = -0.206d_p + 23.7\varepsilon + 68.8$$
$$a_{CO_2} = -0.290d_p + 43.2\varepsilon + 128.1 \qquad (4.6)$$
$$a_{H_2O} = -0.513d_p + 50.1\varepsilon + 178.6$$

where the particle diameter, d_p, is expressed in microns. The empirical curve-fits for the multiplication factors are plotted for each reaction mechanism for a particle diameter of 0 and 75 μm. The empirical curve-fits bound the experimental data for all three reaction mechanisms.

Also shown in Figure 47 are the large particle values used for the area-reactivity multiplication factors. The large particle test did not afford sufficient data to examine the multiplication factors' dependence on particle diameter or fraction of original mass consumed, therefore, constant valued multiplication factors were used. For each reaction mechanism, the area-reactivity multiplication factors for the smaller particle test show an overall increase of at least 20% above the large particle values.
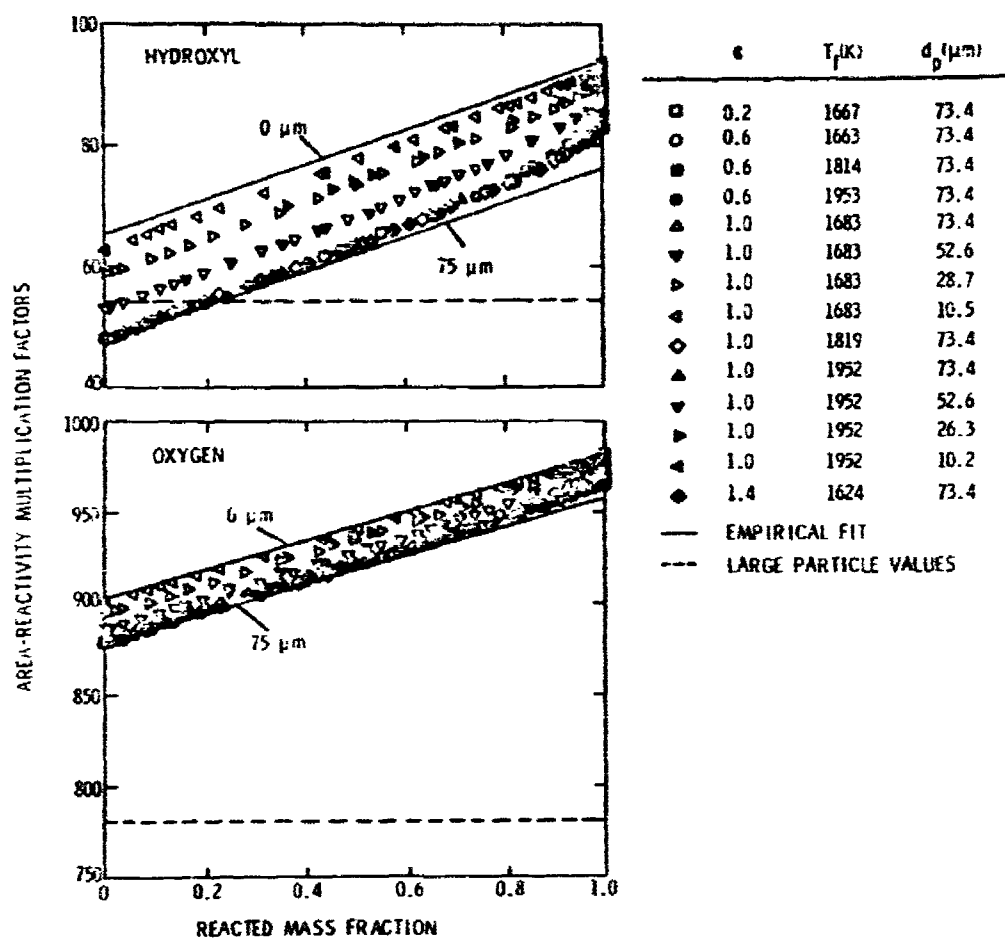
Figure 4S. Area-reactivity multiplication factors for the OH-O$_2$ reaction mechanism, for all the test conditions examined.

Figure 48 plots the area-reactivity multiplication factors vs. reacted mass fraction on a zero suppressed scale for the $OH-O_2$ reaction mechanism. As before, the particle diameter in each experimental test condition ranged between 0 and 75 µm.

The empirical curve-fits of the area-rectivity multiplication factor for the hydroxyl-oxygen reaction mechanism have a form similar to the multiplication factors for the oxygen-carbon dioxide-water vapor reaction mechanism:

$$a_{OH} = -0.234d_p + 28.2\varepsilon + 65.3$$

$$a_{O_2} = -0.307d_p + 79.3\varepsilon + 902.3 \tag{4.7}$$

where the particle diameter is again expressed in microns. As before, the multiplication factor empirical curve-fit for a constant diameter of 0 and 75 µm bound the experimental data. Upon examining the multiplication factor values for both sets of reaction mechanisms for each test condition studied, there does not appear to be a relationship between the multiplication factor and either the flame equivalence ratio or flame temperture.

As earlier, Figure 48 also plots the large particle area-reactivity multiplication factor for both the OH and O_2 reaction mechanisms. Again the large particle values were chosen to be a constant due to lack of experimental data. As before, the small particle multiplication values exhibit an overall increase of at least 20% above the constant large particle values.

4.2.2 Carbon Agglomerate Combustion

Predicted and measured burning rates for the noncatalyzed agglomerate are illustrated in Figures 49-53. In these figures particle burning rate (based on rate of change of the particle diameter with time) is plotted as a function of particle diameter with either flame temperature, equivalence ratio or initial particle diameter taken as a parameter. The data for these tests are tabulated in Appendix B. For these tests, the burning rate based on particle diameter had an estimated error of less than 15% for a 75 μm particle and less than 30% for a 2 μm particle.

Although the maximum experimental error for the laminar-premixed flame test was less than 5%, the possible experimental errors for the laminar-premixed flame test are substantially larger. Conventional error analysis gives the following possible average experimental error range: diameter ±10%, velocity ± 5%, axial location ± 20%, mass ± 28%, time ± 20% and temperature ± 10%.

The theoretical and experimental variation of burning rate as a function of particle diameter, with flame temperature as a parameter is illustrated in Figures 49 and 50. The predictions employ the empirical correlations for the reaction parameters discussed in the previous section. The agreement between theory and experiment is excellent, except in the small diameter region where experimental error is large. Note that the theoretical and experimental results for the various diameter cases at a constant equivalence ratio, as shown in Figure 50, line along a smooth continuous curve.
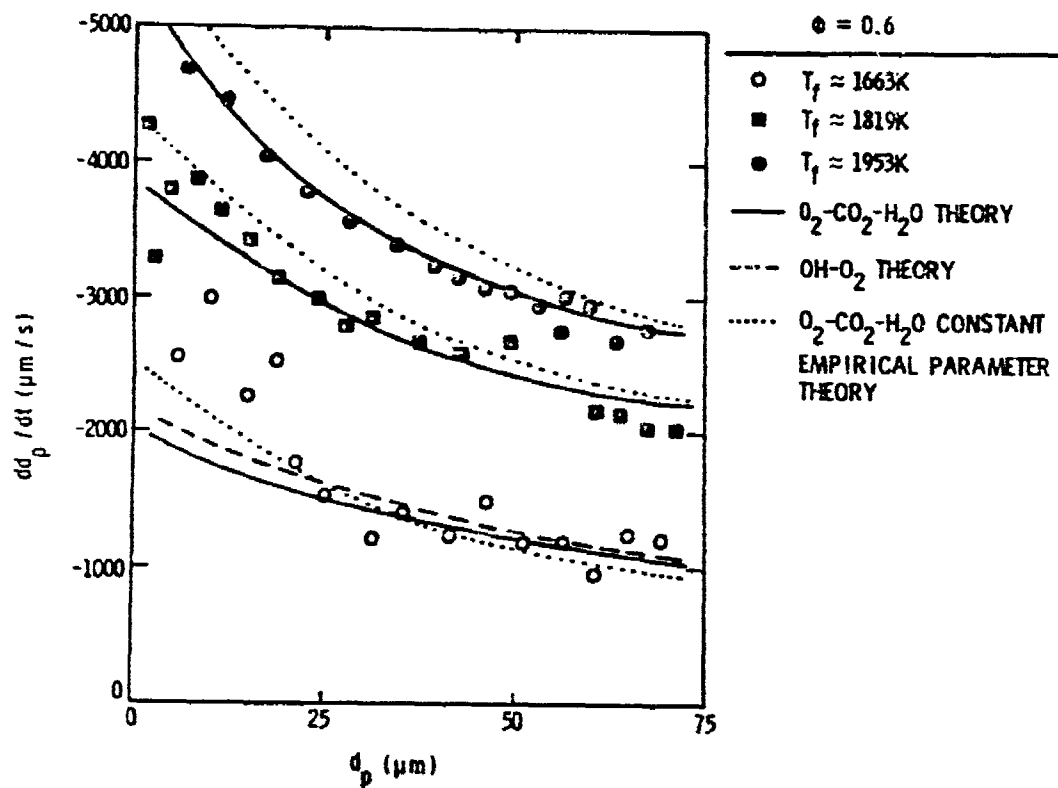
Figure 49. Variation of burning rate vs. particle diameter with
            temperature at a constant equivalence ratio of 0.6.
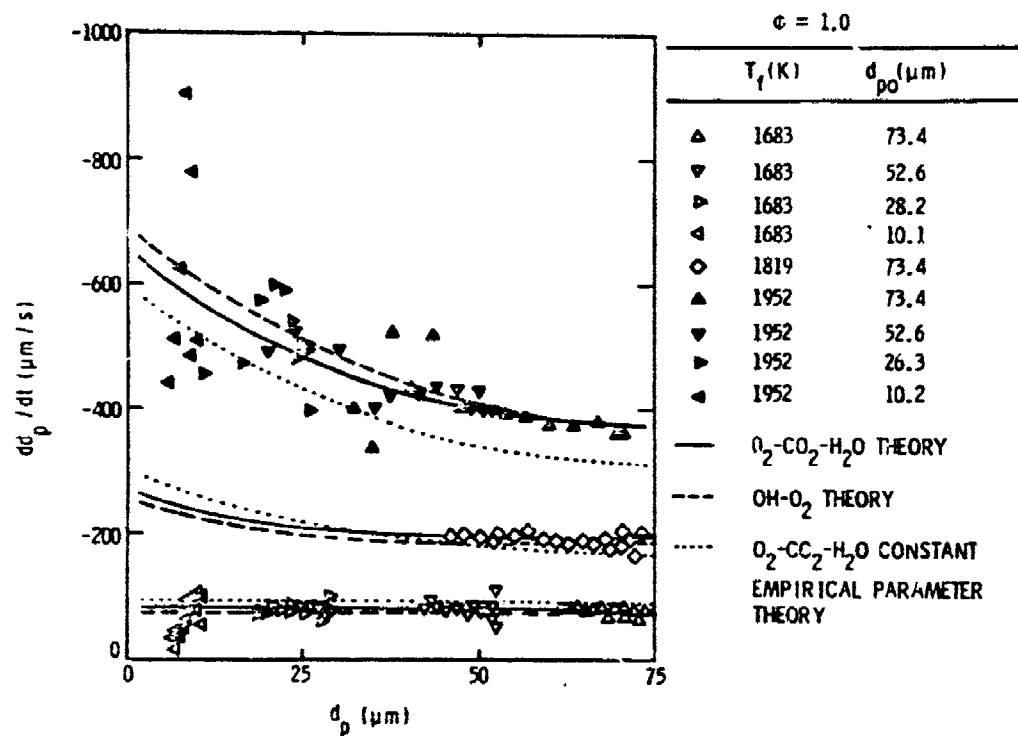
Figure 50. Variation of burning rate vs. particle diameter with temperature at a constant equivalence ratio of 1.0.

d
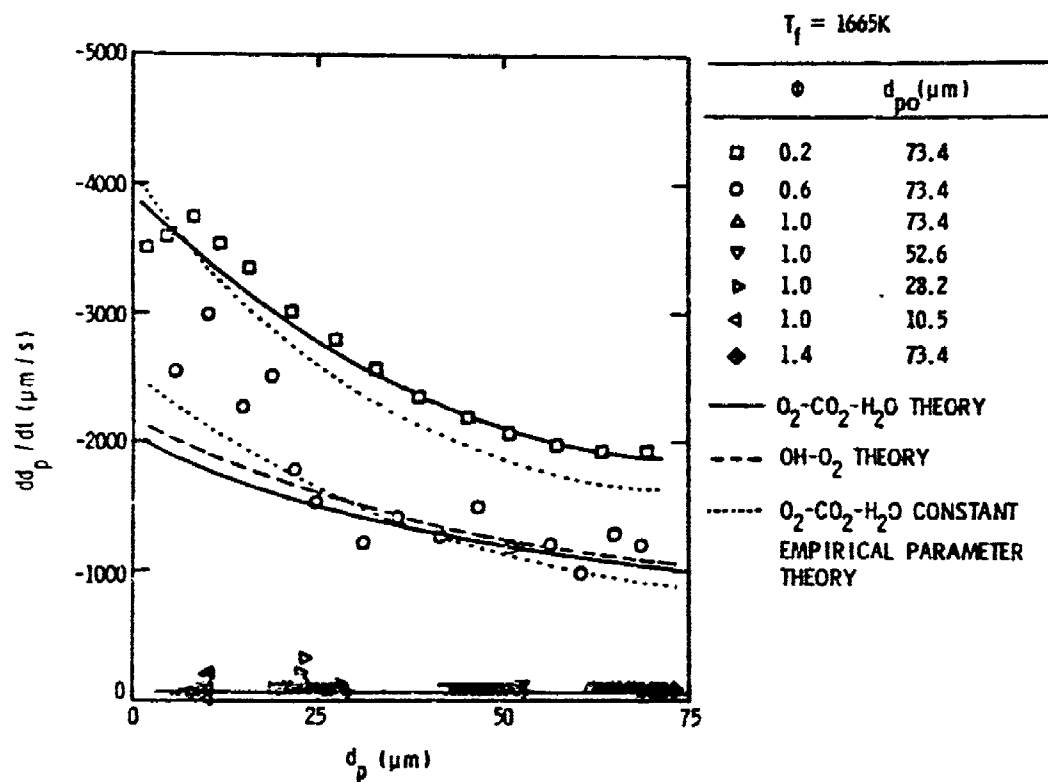
Figure 51. Variation of burning rate vs. particle diameter with
equivalence ratio at a constant temperature of 1665 K.
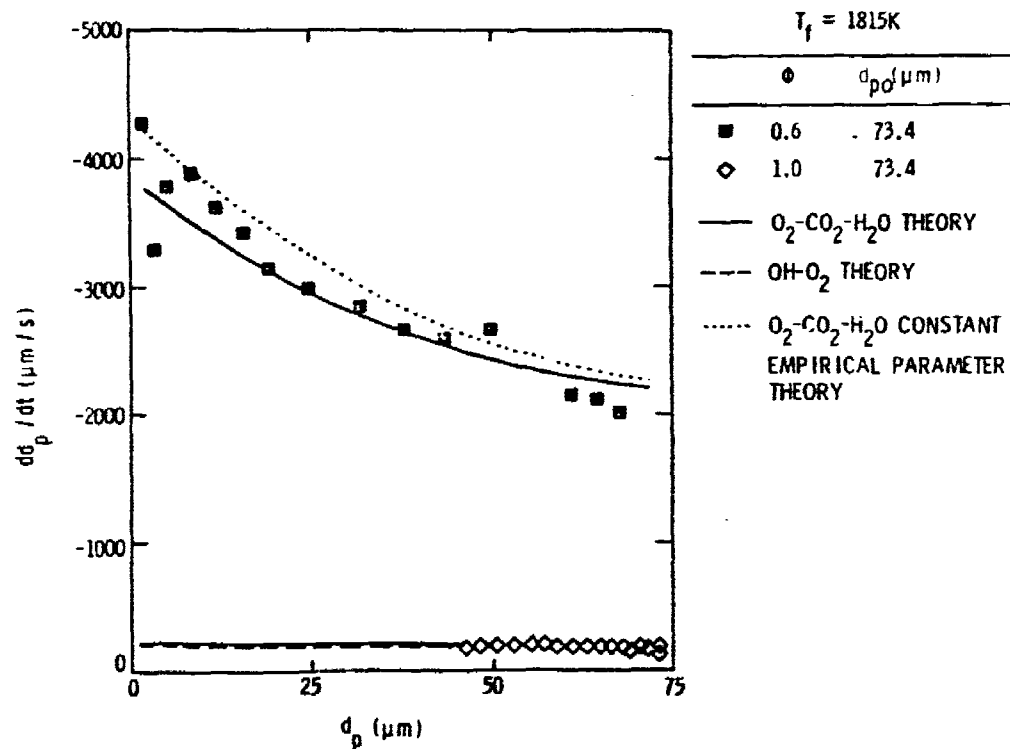
Figure 52. Variation of burning rate vs. particle diameter with
equivalence ratio at a constant temperature of 1815 K.
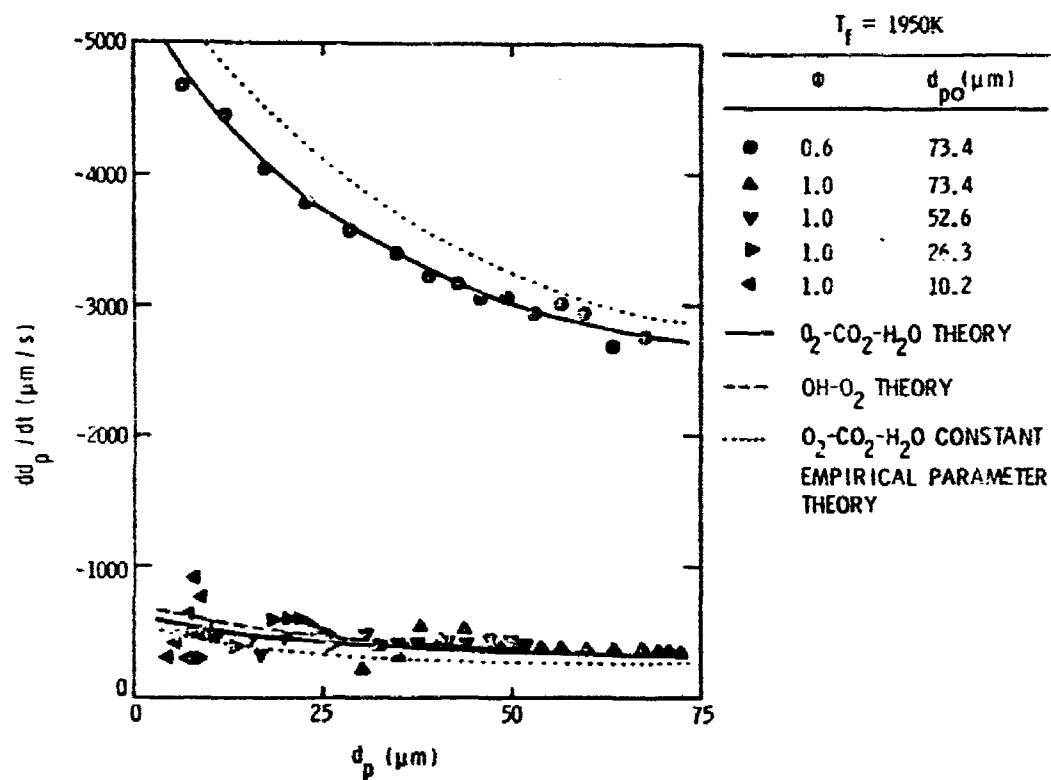
Figure 53. Variation of burning rate bs. particle diameter with
equivalence ratio at a constant temperature of 1950 K.

Recalling that the diffusion-controlled limit is characterized by an increasing burning rate with decreasing particle diameter, and that the kinetically controlled limit is characterized by a burning rate which is relatively indpendent of particle diameter, it is evident from the results in Figures 49 and 50 that increasing the temperature at a constant equivalence ratio increases the burning rate, and tends to shift the reaction into the diffusional-controlled regime.

The predictions employing either reaction mechanism are in exact agreement in all diffusion-controlled regimes, since the burning rate is independent of reaction mechanism in the diffusional controlled regime. The predictions of the two reaction mechanisms for the kinetically controlled cases agreed within 10%, which is comparable to experimental error. Therefore, either reaction mechanism seems quite capable of correlating the agglomerate reaction properties.

In order to evaluate the usefulness of the model which employed a more simple version of the empirical parameter presented in this investigation, a set of constant empirical parameters were chosen. The constant values chosen for the O_2-CO_2-H_2O empirical parameters are tabulated in Table 9. The parameters used were obtained from Equation $(4.4)-(4.6)$ using a particle diameter of 35 μm and a reacted mass fraction of 0.90. It was felt that these sets of parameters were representative and would give a reasonable prediction for most test conditions. In an attempt to further simplify the model, the drag coefficient for a smooth spherical particle was used to estimate the particle velocity. This simplified model was then used to calculate

Table 9.   Summary of Constant Valued Empirical Factors
           for the Laminar-Premixed Flame Tests.

Transport-Enhancement Factors:	
Mass	7.5
Energy	7.5
Area-Reactivity Multiplication Factors:	
O_2	82.9
CO_2	156.8
H_2O	205.7

the burning rates, using the $O_2-CO_2-H_2O$ reaction mechanism, and the results are presented in Figures 49-53. For all the conditions examined, the maximum error between predictions and measurements was 20%. These results indicate that the model has some ability to yield meaningful results even in this simplified form.

The variation of agglomerate burning rate with particle diameter at constant temperature, with equivalence ratio taken as a parameter, is shown in Figures 51, 52 and 53. The results indicate that increasing oxygen concentrations (or lower equivalence ratio) increases the burning rate, tending toward diffusionally-controlled conditions, for these temperature levels.

Predicted and measured reacted mass fraction as a function of time are illustrated in Figures 54 and 55, with temperature as a parameter. The agreement between predictions and measurements is good, suggesting adequate correlation of the empirical parameters. In general, increasing temperatures cause increasing mass burning rates, with the greatest increase occurring for equivalence ratios near unity.

The variation of reacted mass fraction as a function of time, with particle diameter as a parameter, is illustrated in Figure 56 for a fixed temperature and equivalence ratio. As expected, the results indicate that smaller particles burn more quickly, with the larger decrease in combustion time with reduced size occurring in the diffusionally-controlled regime -- at high temperatures.
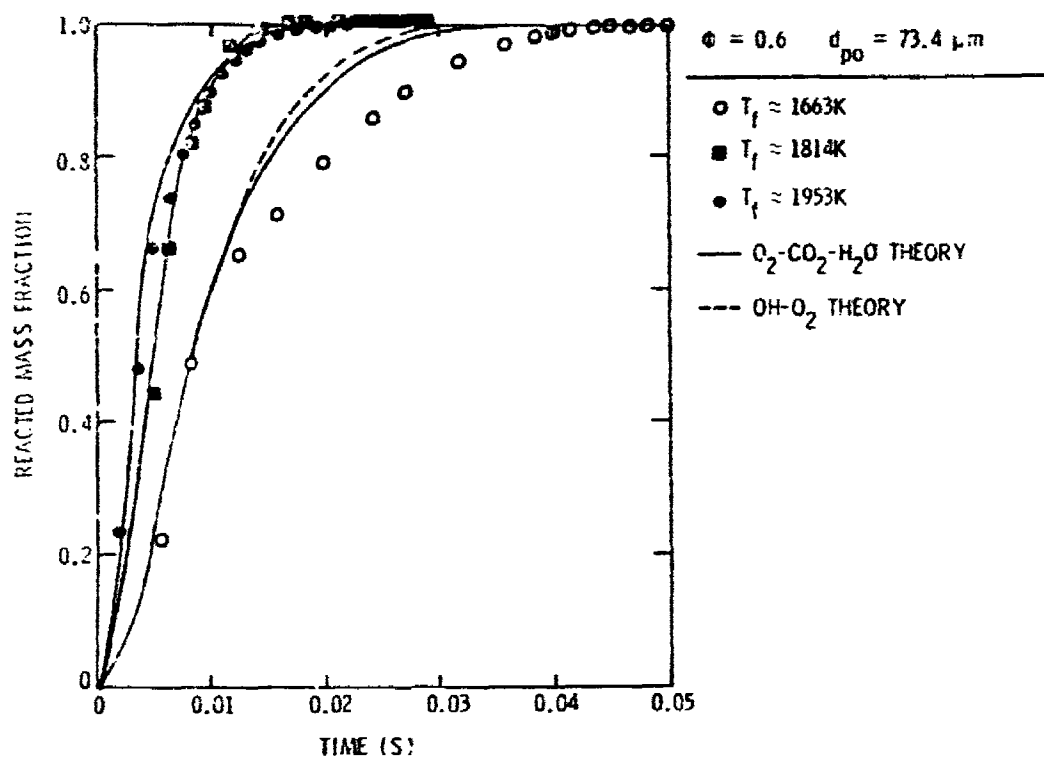
Figure 54. Variation of reacted mass fraction vs. time
with temperature at a constant equivalence
ratio of 0.6, and an initial particle 74.4 μm.
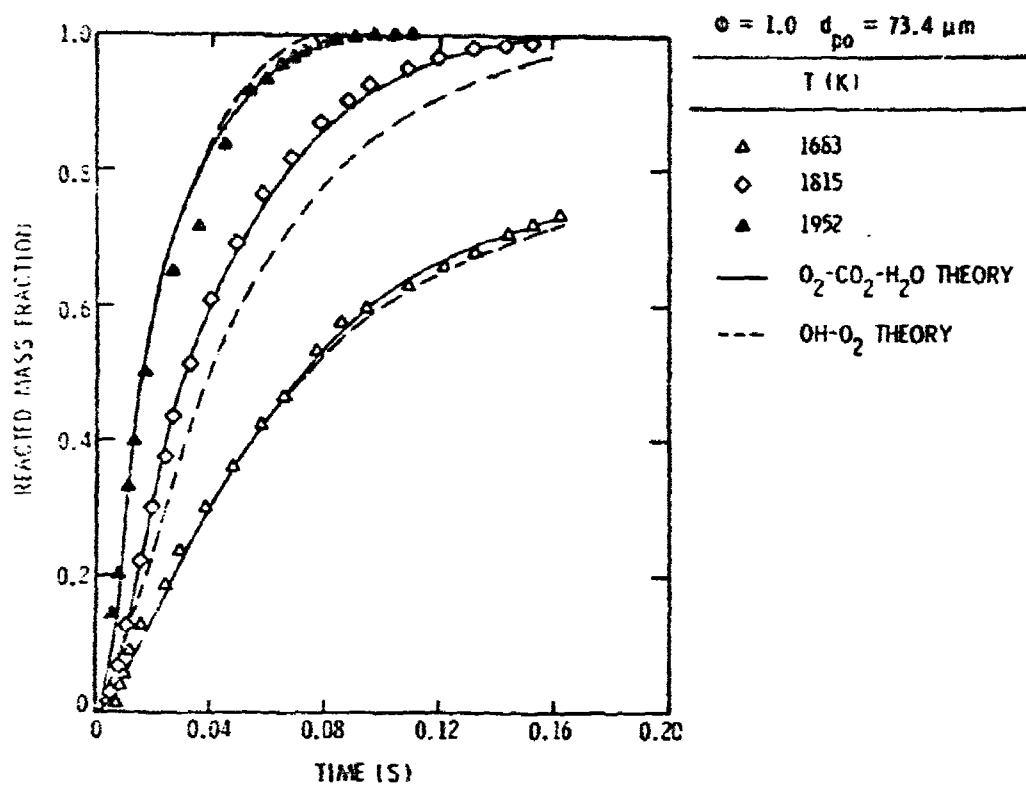
Figure 55.   Variation of reacted mass fraction vs. time
with temperature at a constant equivalence
ratio of 1.0, and an initial particle 73.4 µm.
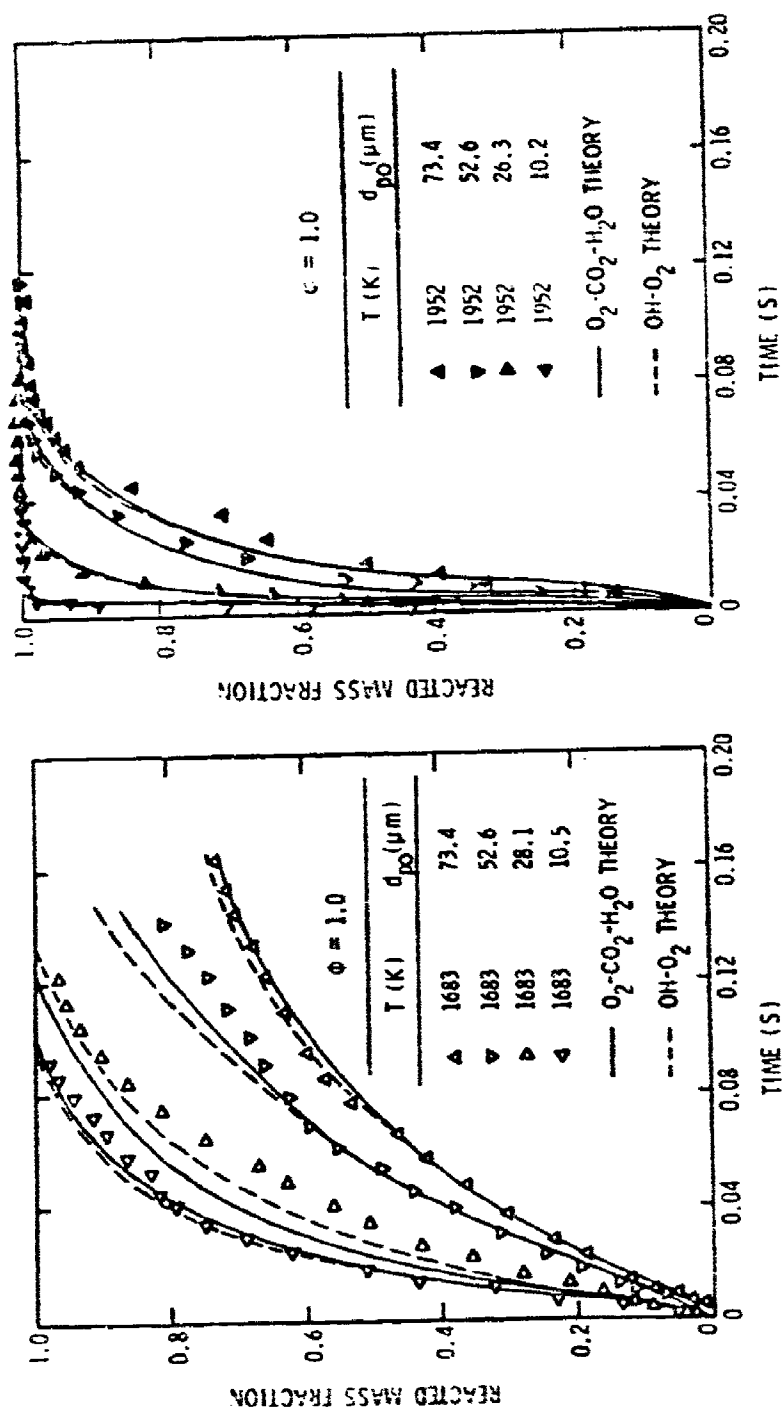
Figure 56. Variation of reacted mass fraction vs. time with particle diameter at a constant equivalence ratio of 1.0.

The reacted mass fraction as a function of time, at a constant temperature with equivalence ratio as a parameter, is plotted in Figures 57-59. Again it is observed that the agreement between theory and experiment is good. For these conditions, decreasing the equivalence ratio increases the burning rate; however, low equivalence ratios at these high temperatures are difficult to achieve for airbreathing combustion systems.

The final step in evaluating the model for the laminar-premixed flame tests involves comparison between the predicted and measured particle-life histories. These results are presented in Figures 60-73. Predicted and measured particle diameter (normalized by initial particle diameter), particle mass (normalized by initial particle mass) and particle temperature (normalized by the flame temperature) are plotted as a function of time for both reaction mechanisms. The data used in preparing the plots are tabulated in Appendix B. The agreement between theory and experiment, in general is excellent for both reaction mechanisms. An interesting feature of these results is that the particle mass decreases much more quickly than the particle diameter. The remaining trends are similar to the behavior discussed earlier for supported particles.

Experimental uncertainties were too large to yield an accurate determination of particle drag properties. Drag coefficients were of the same order of magnitude as the values for smooth spheres – but were widely scattered.
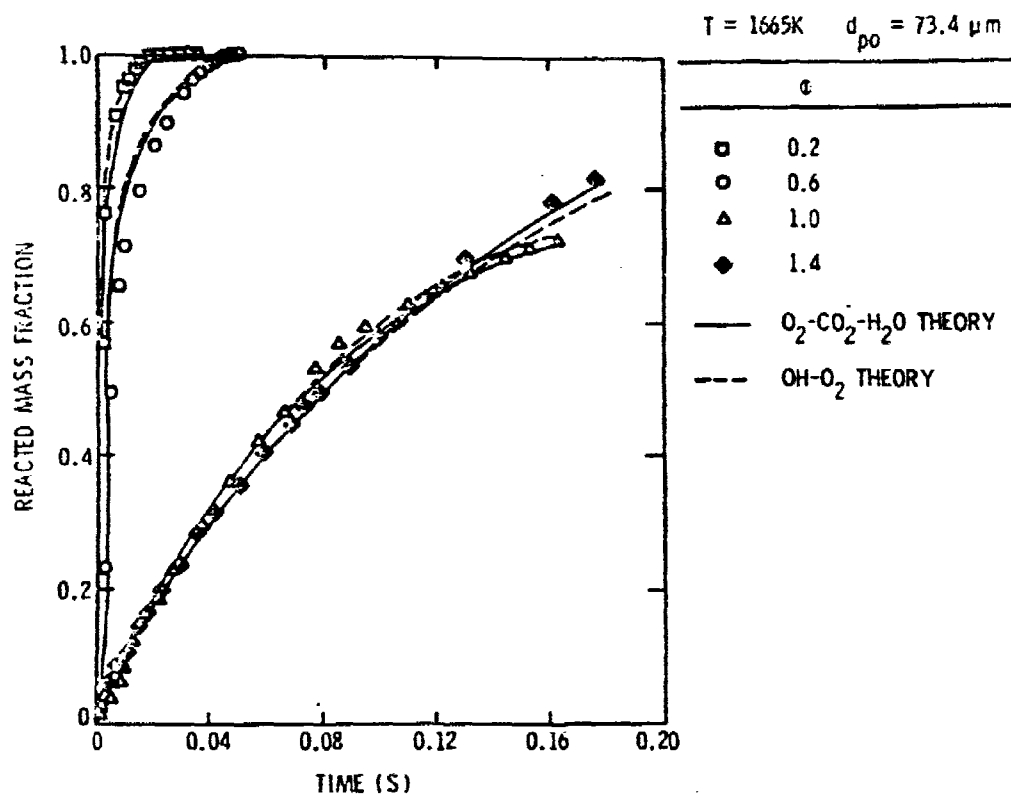
Figure 57. Variation of reacted mass fraction vs. time with equivalence ratio at a constant temperature of 1665 K and a constant particle diameter of 73.4 μm.
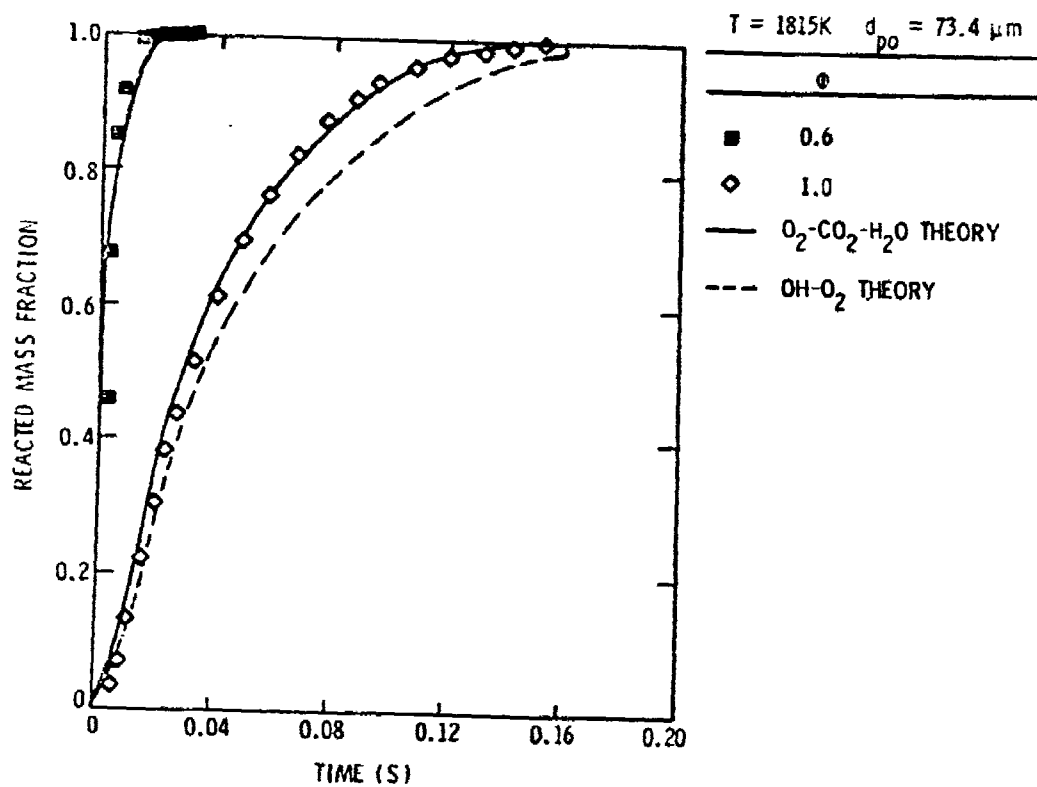
Figure 58. Variation of reacted mass fraction vs. time with equivalence ratio at a constant temperature of 1815 K and a constant particle diameter of 73.4 μm.
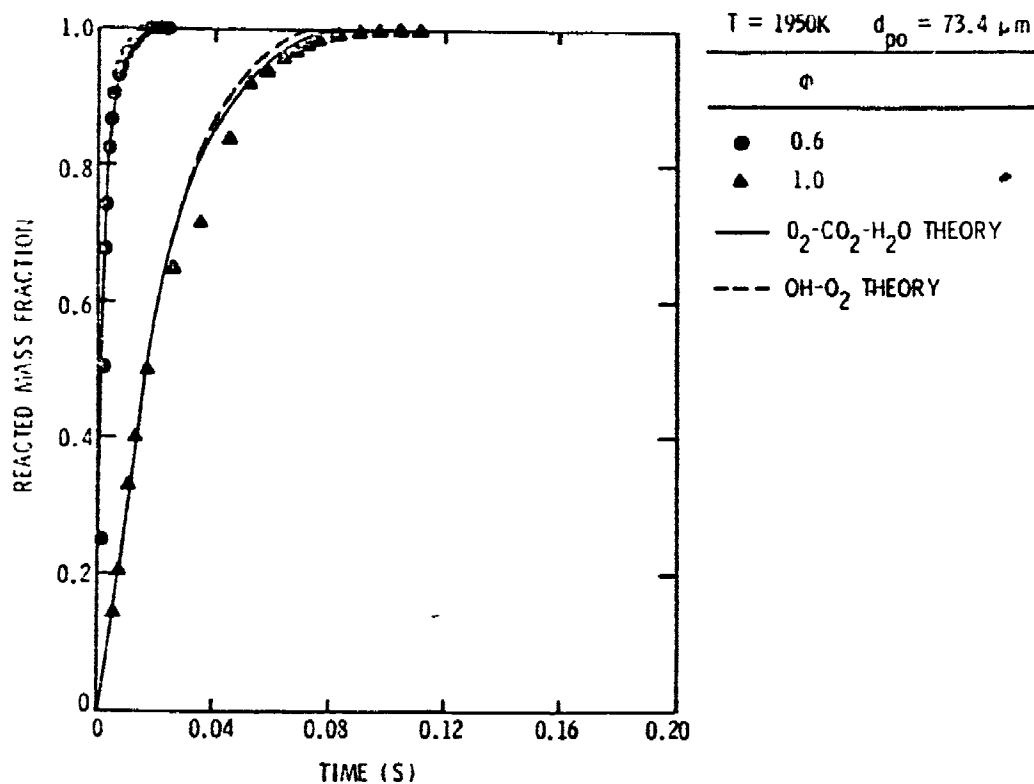
Figure 59. Variation of reacted mass fraction vs. time with
equivalence ratio at a constant temperature of
1950 K and a constant particle diameter of 73.4 μm.
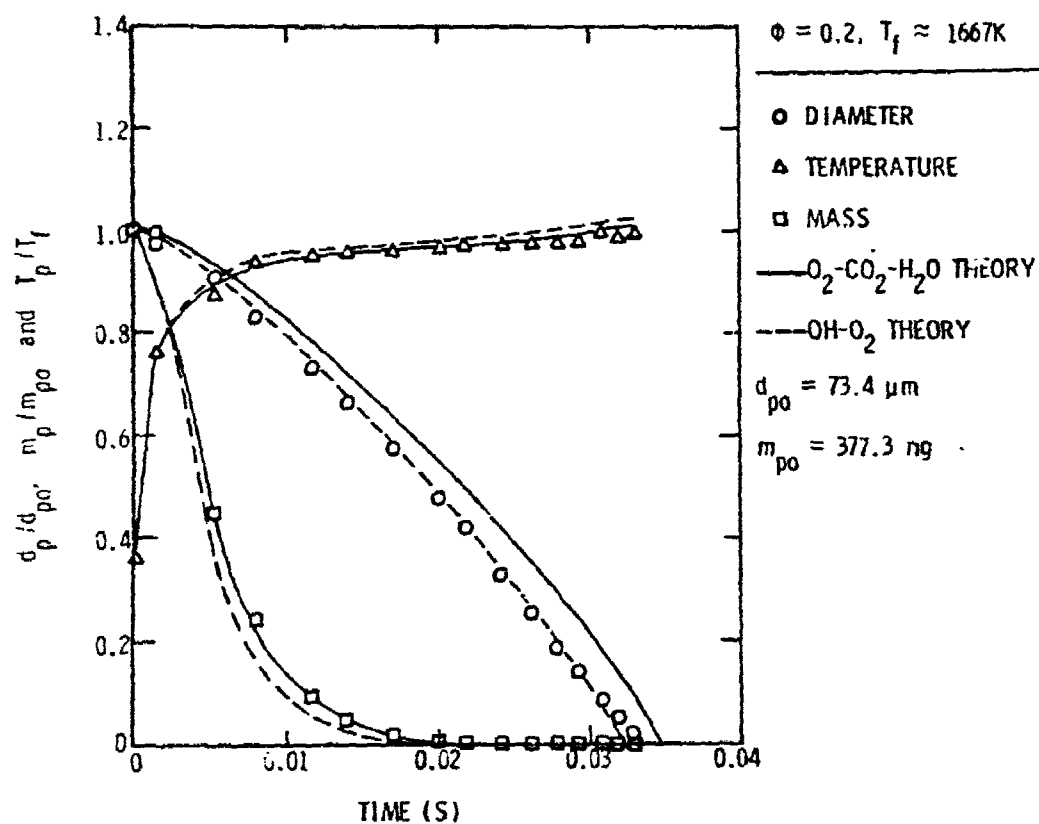
Figure 60.   Particle-life history for $\phi = 0.2$,
$T_f = 1667$ K and $d_{po} = 73.4$ μm.
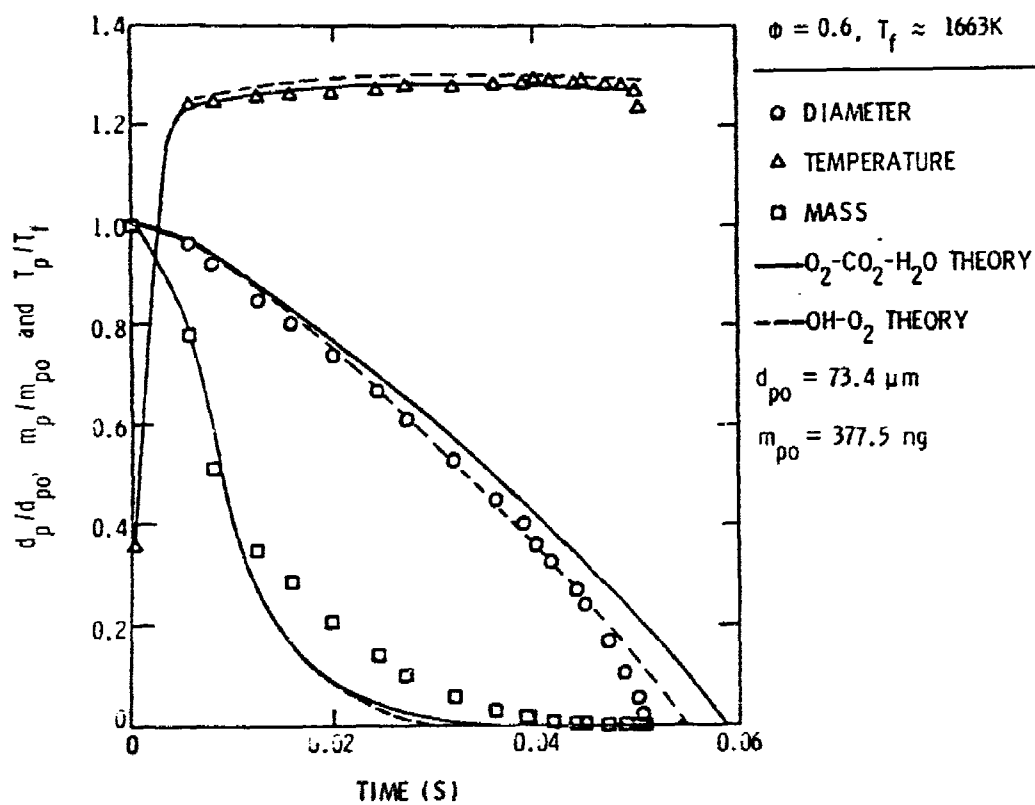
Figure 61. Particle-life history for ϕ = 0.6, T_f = 1663 K and d_{po} = 73.4 μm.
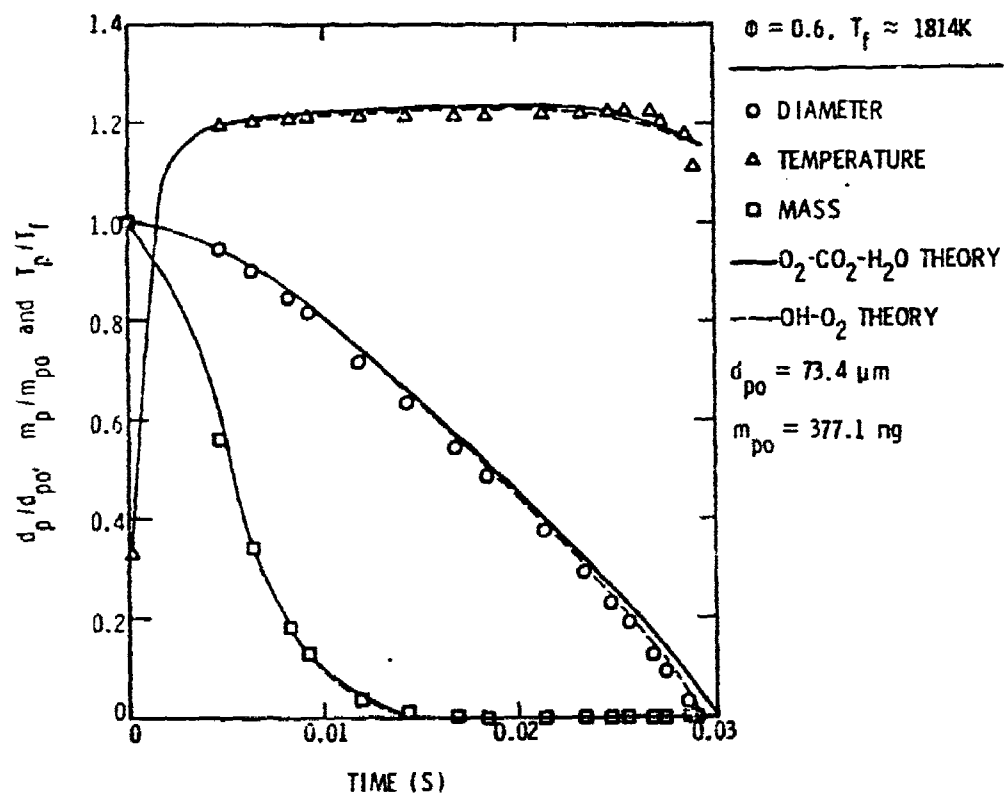
Figure 62. Particle-life history for ϕ = 0.6,
T_f = 1814 K and d_{po} = 73.4 μm.
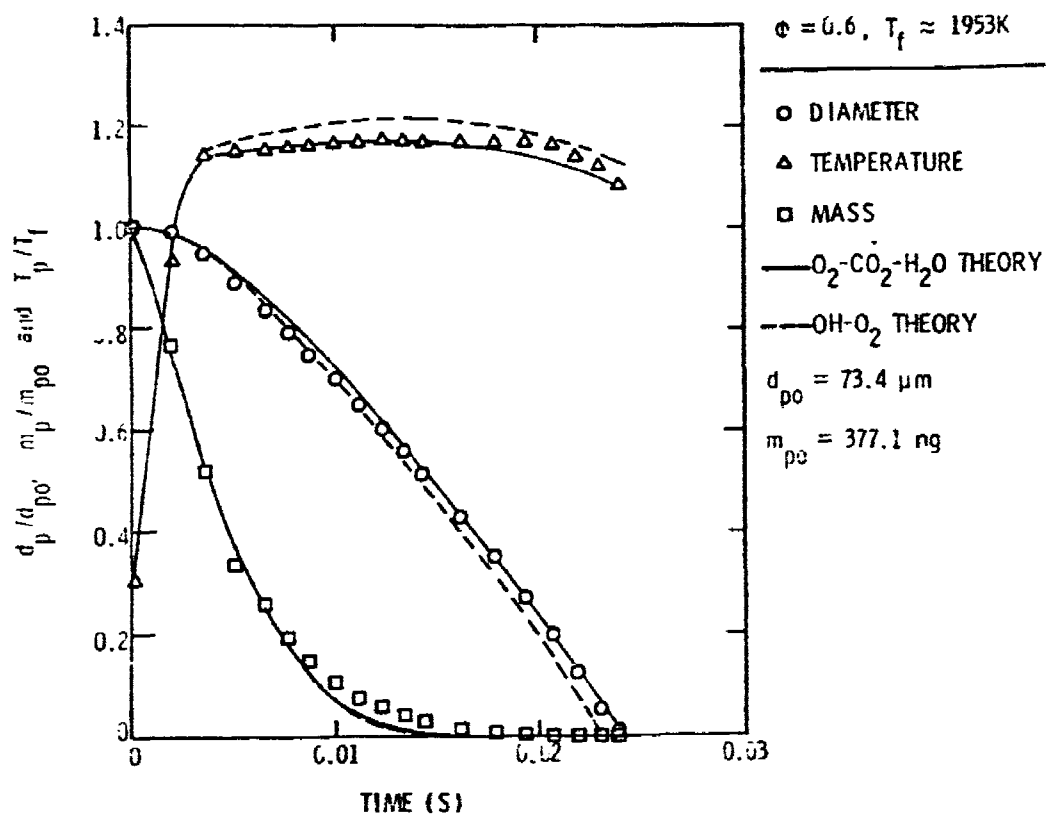
Figure 63.   Particle-life history for $\phi = 0.6$,
$T_i = 1953$ K and $d_{po} = 73.4$ μm.
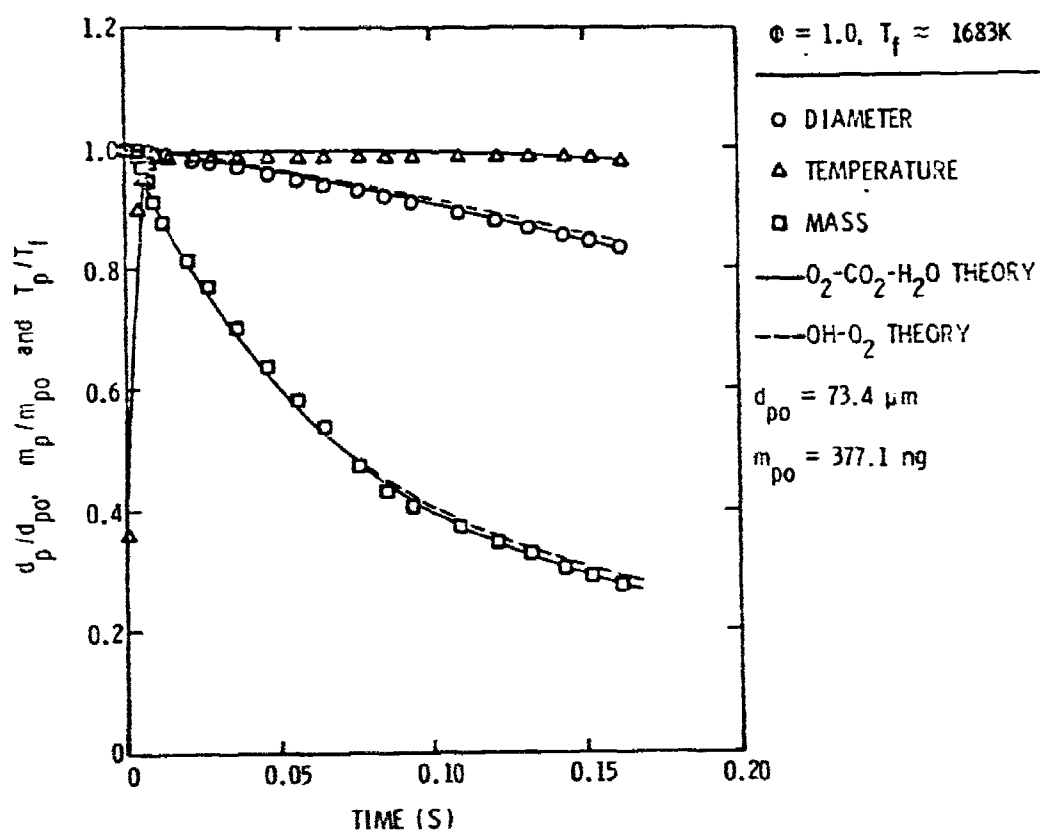
Figure 54. Particle-life history for $\phi = 1.0$, $T_f = 1683$ K and $d_{po} = 73.4$ μm.
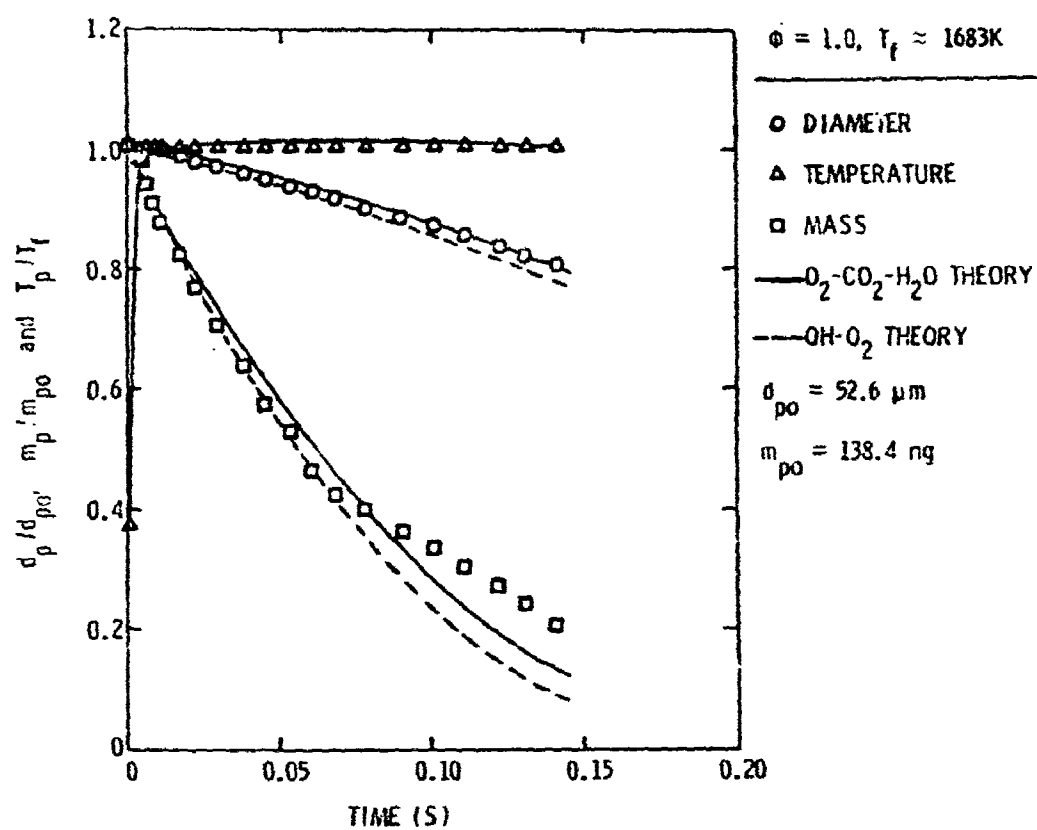
Figure 65. Particle-life history for $\phi = 1.0$, $T_f = 1683$ K and $d_{po} = 52.6$ μm.
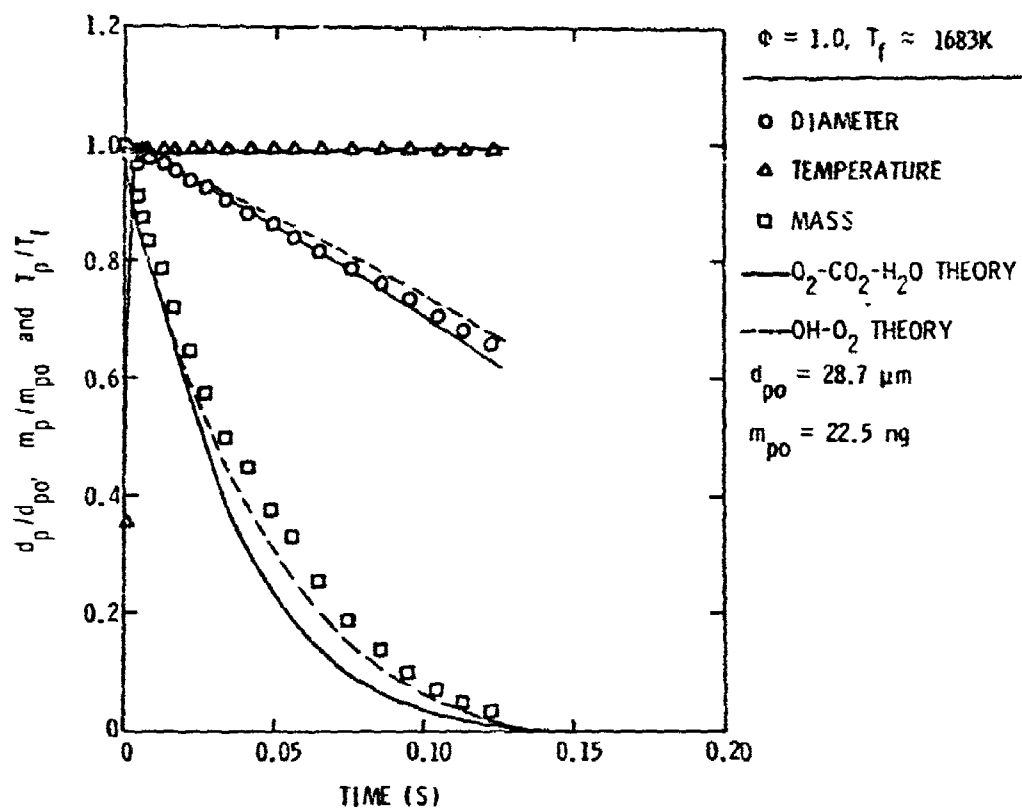
Figure 66. Particle-life history for ϕ = 1.0, T_f = 1683 K and d_{po} = 28.7 μm.
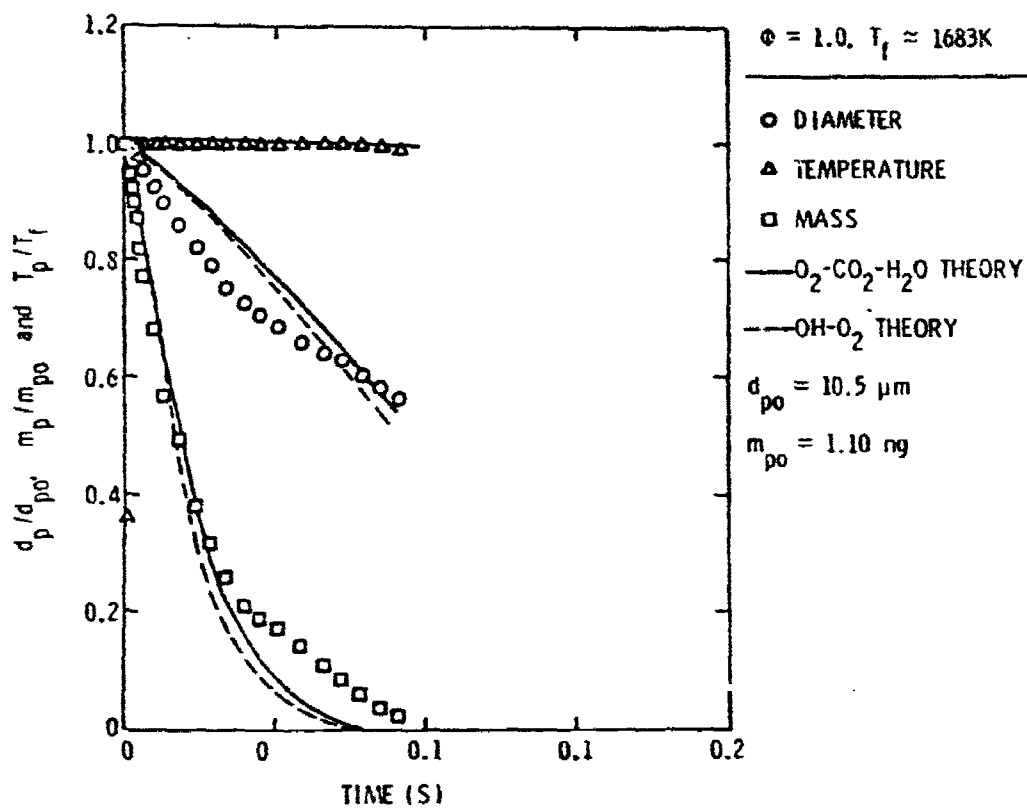
Figure 67. Particle-life history for $\Phi = 1.0$,
$T_f = 1683$ K and $d_{po} = 10.5$ μm.
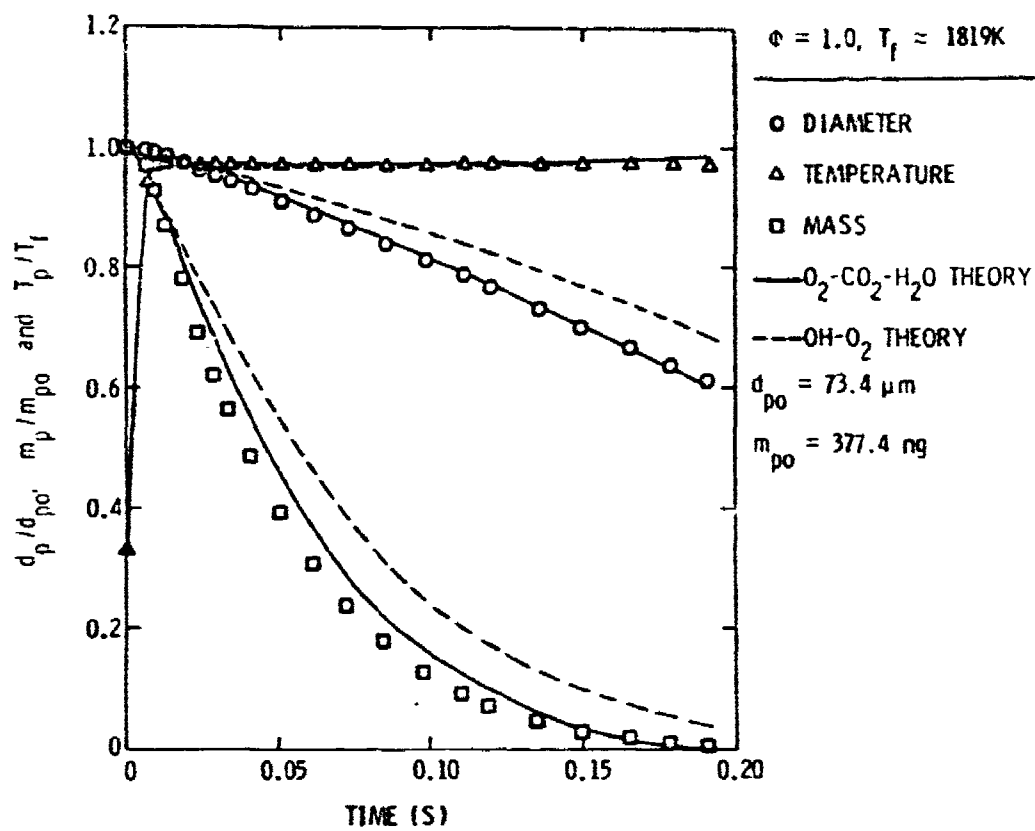
Figure 68. Particle-life history for $\phi = 1.0$, $T_f = 1819$ K and $d_{po} = 73.4$ μm.
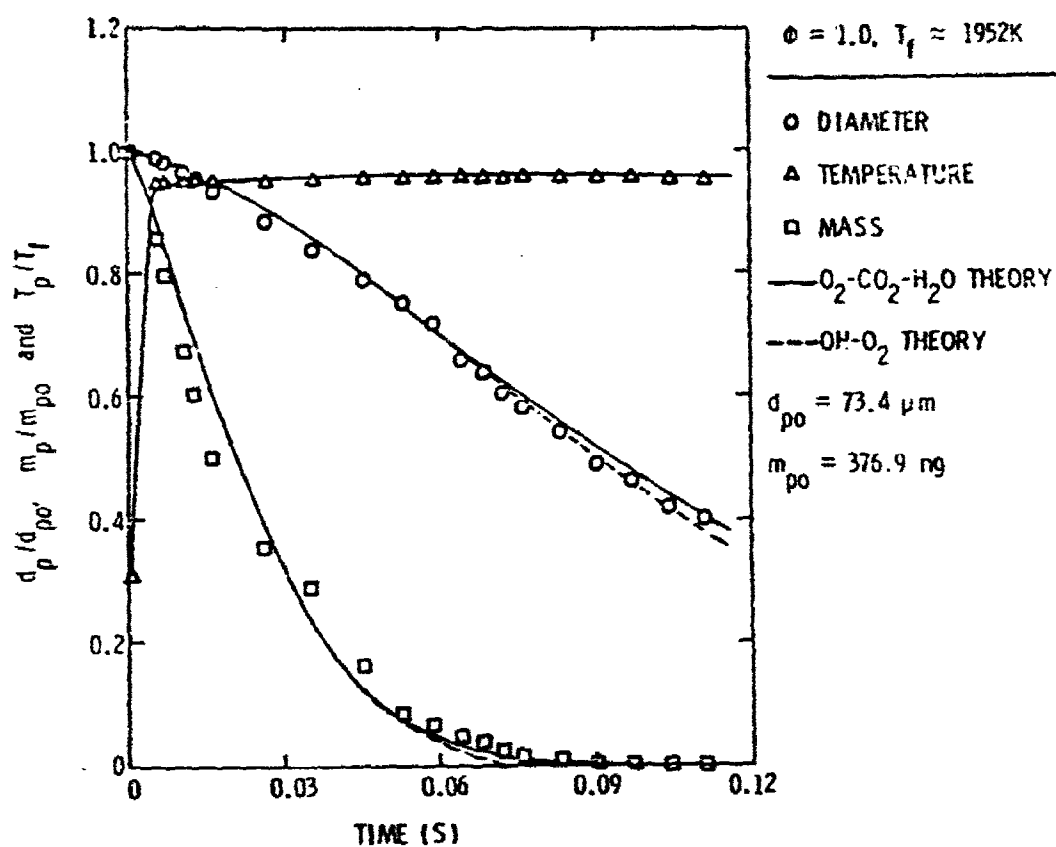
Figure 69.   Particle-life history for Φ = 1.0,
T_f = 1952 K and d_{po} = 73.4 μm.

Figure 70. Particle-life history for $\Phi = 1.0$,
$T_f = 1952$ K and $d_{po} = 52.6$ μm.
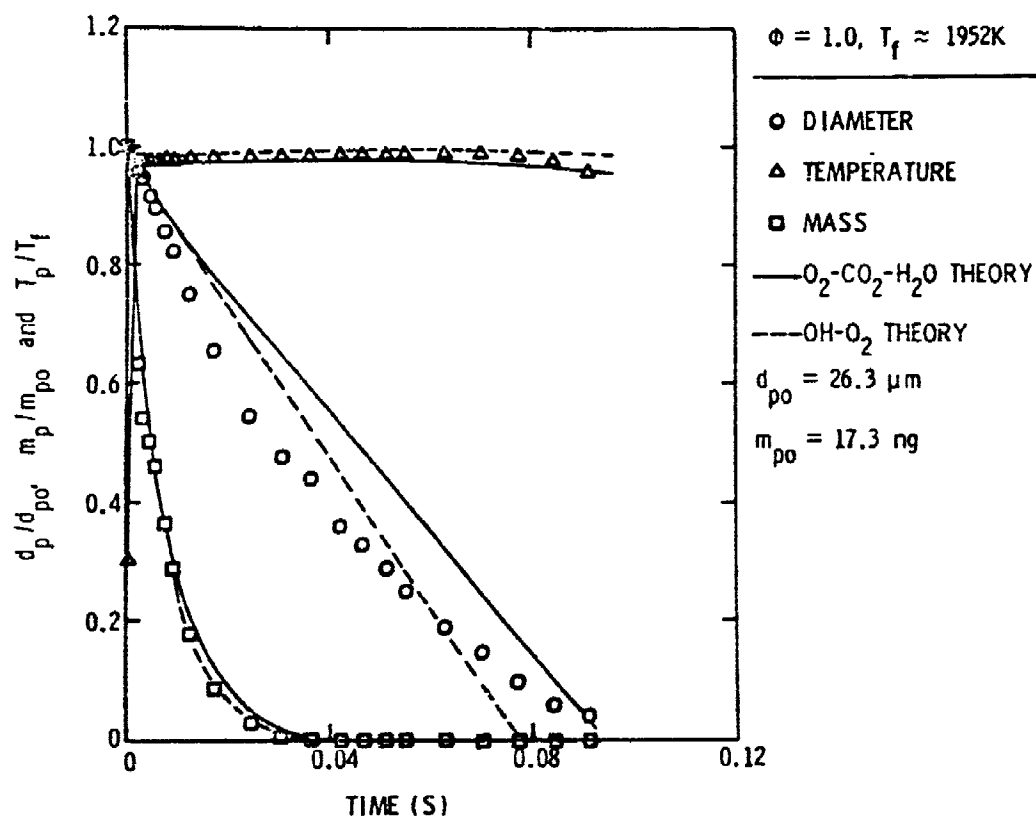
Figure 71. Particle-life history for ϕ = 1.0,
T_f – 1952 K and d_{po} = 26.3 µm.
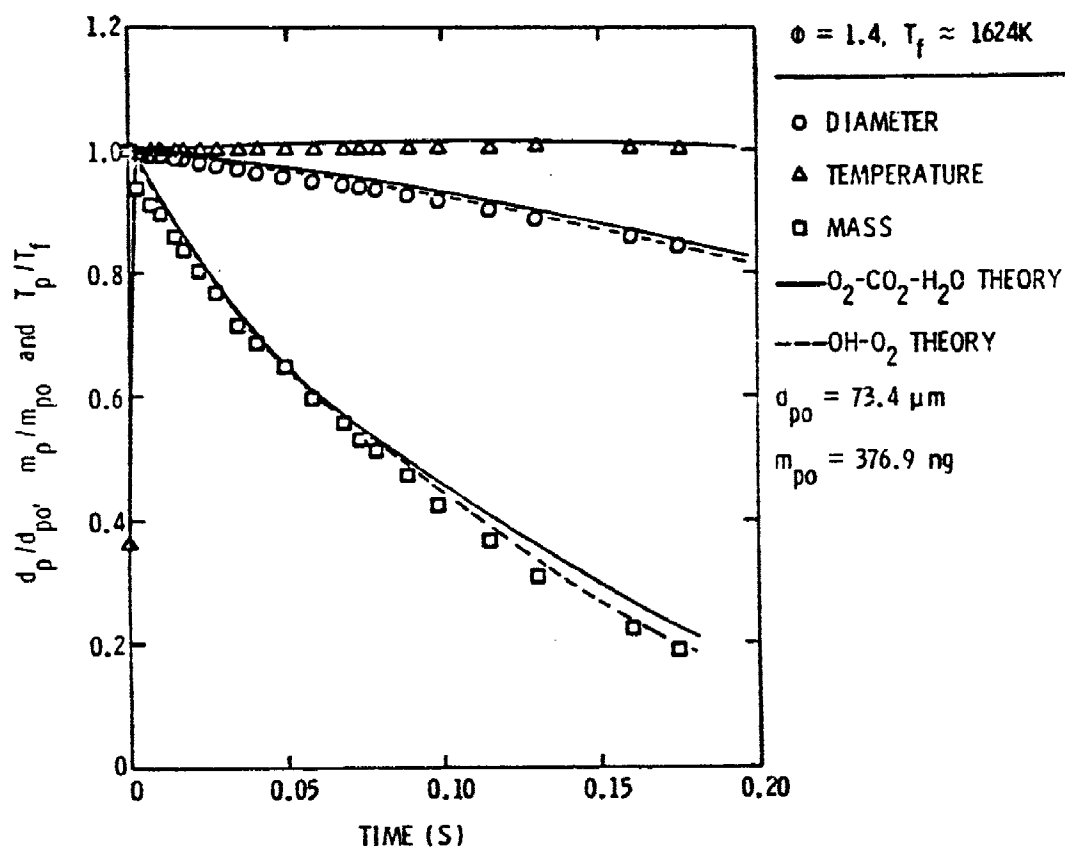
Figure 73. Particle-life history for ϕ = 1.4, T_f = 1624 K and d_{po} = 73.4 μm.

CHAPTER V

SUMMARY AND CONCLUSIONS

5.1 Summary

The overall objective of the present study was to experimentally observe and theoretically predict the heat-up and combustion processes of a slurry droplet. The carbon slurry fuels were formulated by mixing noncatalyzed and/or catalyzed medium-thermal carbon black (roughly 50% by weight) with JP-10 liquid fuel.

The combustion of individual-supported slurry drops, 400-1000 μm initial diameter, was observed in an open turbulent-diffusion flame at atmospheric pressure. The environment of the drops within the flame was known from measurements of mean velocity, temperature and composition. The drops were suspended from the junction of a thermocouple. Shadowgraph motion pictures were also obtained for the process. The data provided the variation of particle temperature and diameter as a function of time.

A two-stage combustion process was observed. The first stage involved heat-up and evaporation of the liquid, leaving a solid agglomerate of the carbon particles on the probe. The second stage involved heat-up and reaction or quenching of the agglomerate.

A model was constructed for both the liquid-evaporation process and the agglomerate-reaction process. This involved analysis of heat- and mass-transfer processes in the convective environment surrounding the droplet or agglomerate, and the chemical reaction of carbon with

oxygen, carbon dioxide, and water vapor; or oxygen and hydroxyl at the surface of the particle. Radiative heat transfer between the agglomerate and its surroundings was also considered. The predictions of both of the models were compared with measurements in the flame considering equivalence ratios in the range of 0.272-1.350. The liquid-evaporation model predictions for droplet size and temperature agreed very well with the experimental observations, except in regions where an envelope flame was observed (equivalence ratios of 0.761 and 0.870), where an extended model which considered the presence of an envelope flame was required for the actual predictions. Good agreement between predicted and measured agglomerate reaction properties was also obtained throughout the test range for both the $O_2-CO_2-H_2O$ and the O_2-OH agglomerate reaction model. Both models accurately predicted both particle temperature and size variations. Use of a catalyzed slurry was found to increase burning rates and extended the lean limit for agglomerate reaction.

A laminar-premixed flame apparatus was also constucted, in order to examine the variation of the empirical factors over a broader range of test conditions. These tests emphasized smaller freely moving particles, more representative of practical slurry sprays, and test conditions in the kinitically-controlled regime. The apparatus consisted of a particle genorator which produced a stream of carbon agglomerate particles, with initial initial diameters in the 10-100 µm range, which passed through the post flame region of a flat-flame burner. Measurements were made of particle size, mass, temperature and velocity as a function of position above the burner.

A relationship between apparent particle density and reacted-mass fraction was obtained which was relatively independent of particle size and local particle environment. The variation of both the transport-enhancement factors and the area-reactivity multiplication factors, for both reaction mechanisms, were found to depend on particle diameter and reacted-mass fraction to some degree. However, constant values similar to those found for the large supported particles, also yielded a reasonable correlation of the measurements. The burning rate increased with increasing flame temperature and with decreasing equivalence ratio.

5.2 Conclusions

The major findings of the study can be summrized as follows:

1. The life history of a carbon slurry drop can be broken down into four major stages:

    i. Heat up of the particle to temperature levels appropriate for evaporation of the liquid. Possible ignition of liquid fuel vapors.

    ii. Evaporation, and possibly combustion, of the liquid fuel in a relatively conventional manner accompanied by agglomeration of the carbon particles origianlly present within the droplet into a solid residue.

    iii. Further heating of the carbon residue once all the liquid has evaporated.

    iv. Ignition, or a gradually increasing reaction rate of the carbon, followed by combustion of the residue.

2. The behavior of the particles varied significantly throughout the flame. The various combustion regimes are identified in Table 6. They are characterized by the present or absence of envelope flames, residue reaction and residue breakup.

3. In general, the solid carbon in the slurry remained in the agglomerate, and the heat-up and reaction of the agglomerate required the bulk of the life-time of the particle (requiring 90-95% of the life-time even in locations where carbon reaction rates were fast). Agglomerate reaction was only observed for flame equivalence ratios of 0.37-1.4 for noncatalyzed slurries and 0.21-1.4 for catalyzed slurries.

4. The carbon residue broke up into smaller fragments in the high relative velocity region near the injector. Otherwise, most of the carbon formed a single residue particle whose size was controlled by the initial drop size. In this circumstance, the desirability of fine atomization for practical combustors is obvious.

5. Addition of the catalyst significantly increased the size of the region of the flame where reaction of the residue occurred. Catalyzed-slurry residue also reacted more completely.

6. Following active carbon combustion, the residue had an open lacey structure indicating that reaction was occurring to some depth in the particle. The sub-elements of this structure were approximately the same size as the ultimate particle size in the carbon black (0.3 μm).

7. Cenospheres were observed as carbon residue in some cases. It is postulated that they result from quenching of the reaction at the outer surface of the particle, due to excessive radiative and convective heat losses to the environment.

8. Similar to earlier work [11,150,151,155,156], good predictions of liquid-gasification rates and life histories were obtained by selecting a fixed reference condition for evaluating average properties. Drop gasification could be treated as a simple evaporation process, except for a narrow region where envelope flames were observed. The presence of an envelope flame resulted in an underestimation of gasification rates, when the drop was assumed to evaporate; however, a conventional extention of the model to consider envelope flames rectified this difficultly.

9. Good predictions of agglomerate reaction rates and life histories were obtained using either the Neoh et al. [121], or extended Libby and Blake [88,89] reaction approximations over a wide range of test conditions, including particle diameters between 0 and 1000 μm, flame equivalence ratios between 0.2 and 1.4, and flame temperatures between 500 and 2000 K. This agreement was obtained by selecting empirical area-reactivity factors which allow for effects of pores, intrinsic surface reactivity and catalyst, for each reaction; and transport-enhancement factors which accounted

for the ambient gas porcolating throught the porous particle.

These factors were significantly greater than unity,

suggesting that pore diffusion and reaction within pores was

important for present test conditions. The area-reactivity

multiplication and the transport enhancement factors were

found to depend on both particle diameter and reacted-mass

fraction to some degree. The values for the transport-

enhancement factors for the small particle test had values

reasonably close to the large particle values. The vallues

for the area-reactivity multiplication factors for the small

particle tests exhibit approximately a 20% overall increase

above the values used for the large particle tests.

10. Adding catalyst increased agglomerate burning rates, except

at the diffusion-controlled limit, and also extended the lean

limit for quenching. Agglomerate shattering in the lean

region of the flame was also occasionally observed for

catalyzed slurries.

5.3 Recommendations for Further Study

The present model employs an oversimplified treatment of

agglomerate structure; involving the assumption of a smooth surface

with empirical convection enhancement and area-reactivity factors to

allow for effects of flow penetrating the porous surface, pore

diffusion, intrinsic surface reactivity and catalyst. These empirical

factors were found to be nearly constant over the present test range.

Since the effects of surface structure probably vary with particle

size, percent reactivity, properties of the carbon black, and flow conditions, it is unlikely that the empirical factors found in the present study are generally appropriate.

In order to further expand the level of understanding of the carbon agglomerate combustion process the following items are recommended as possible areas of further study:

1. Evaluate the effect of ultimate carbon black particle size on agglomerate reaction. In particular, a bi-modal blend of ultimate particle particle size in the slurry should be considered since such formulations are likely to provide improved flow and stability properties.

2. Examine the effect of ambient pressure on the agglomerate combustion process, particularly emphasizing the higher pressure levels typically found in combustors.

3. Develope a pore structure model to aid in further understanding of the microscopic combustion processes.

REFERENCES

1. Burdette, G. W., Lander, H. R. and McCoy, J. R., "High Energy Density Fuels for Cruise Missiles," AIAA Paper No. 78-267, 1978.

2. Bruce, T. W., Mongia, H. C., Stearns, R. S., Hall, L. W. and Faeth, G. M., "Formulation Properties and Combustion of Carbon-Slurry Fuels," Proceedings of Sixteenth JANNAF Combustion Meeting, CPIA Publication No. 308, pp 679-717, December 1979.

3. Bruce, T. W. and Mongia, H., "Compound Cycle Turbofan Engine Task IX: Carbon-Slurry Fuel Combustion Evaluation Program," Technical Report AFWAL-TR-80-2-35, March 1980.

4. Salvesen, R. H., "Carbon-Slurry Fuels for Volume Limited Missiles," Technical Report AFAPL-TR-79-2122, November 1979.

5. Law, C. K., Lee, C. H. and Srinivasan, N., "Combustion Characteristics of Water-in-Oil Emulsions and Coal-Oil Mixtures," Paper No. 38, 1978 Fall Technical Meeting, Eastern Section of the Combustion Institute, Miami Beach, FL, November 1978.

6. Krazinski, J. L., Buckius, R. O. and Krier, H., "Coal Dust Flames: A Review and Development of a Model for Flame Propagation," Prog. Energy Combust. Sci., Vol. 5, p. 31, 1979.

7. Mulcahy, M. F. R. and Smith, I. W., "Kinetics of Combustion of Pulverized Fuel: A Review of Theory and Experiment," Rev. Pure and Appl. Chem., Vol. 19, pp. 81-108, 1969.

8. Walker, P. L., Rusinko, F. and Austin, L. G., "Gas Reactions of Carbon," "Advances in Catalysis 11, Academic Press, New York, pp. 133-221, 1959.

9. Gray, D., Cogoli, J. G. and Essenhigh, R. H., "Problems in Pulverized Coal and Char Combustion," Adv. Chem. Ser., No. 131, p. 72-91, 1973.

10. Field, M. A., Gill, D. W., Morgan, B. B. and Hawksley, P. G. W., Combustion of Pulverized Coal, British Coal Research Association Monograph, Leatherhead, England, 1967.

11. Faeth, G. M., "Current Status of Droplet and Liquid Combustion," Prog. Energy Combust. Sci., Vol. 3, pp. 191-224, 1977.

12. Levich, V. G., Physicochemical Hydrodynamics, Prentice-Hall, Englewood Cliffs, NJ, 1962.

13. Yuen, M. C. and Chen, L. W., "On Drag of Evaporating Liquid Droplets," Combust. Sci. Tech., Vol. 14, pp. 147-154, 1976.

14. Sirignano, W. A. and Law, C. K., A Review of Transient Heating and Liquid-Phase Mass Diffusion in Fuel Droplet Vaporization. Symposium on Evaporation—Combustion of Fuel Droplets, San Francisco, Aug. 29-Sept. 3, 1976.

15. Fendell, F. E., Coats, D. E. and Smith, E. B., "Compressible Slow Viscous Flow Past a Vaporizing Droplet," AIAA J., Vol. 6, pp. 1953-1960, 1968.

16. Hamielec, A. E., Hoffman, T. W. and Ross, L. L., "Numerical Solutions to the Navier-Stokes Equation for Flow Past Spheres," AIChE. J., Vol. 13, pp. 212-224, 1967.

17. Brounshtein, B. I., Zheliznyak, A. S. and Fishbein, G. A., "Heat and Mass Transfer in Interactions of Spherical Drops and Gas Bubbles with a Liquid Flow," Int. J. Heat Mass Trans., Vol. 13, pp. 963-973, 1970.

18. Ranz, W. E. and Marshall, W. R., Jr., "Evaporation from Drops, Parts I and II," Chem. Engr. Prog., Vol. 48, pp. 141-146, 173-180, 1952.

19. Williams, A., "Combustion of Droplets of Liquid Fuels: A Review," Combust. Flame, Vol. 21, pp. 1-31, 1973.

20. Williams, A., "The Mechanism of Combustion of Droplets and Sprays of Liquid Fuels," Oxidation Combust. Rev., Vol. 3, pp. 1-45, 1968.

21. Williams, A., "Fundamentals of Oil Combustion," Prog. Energy Combust. Sci., Vol. 2, pp. 167-179, 1976.

22. Hedley, A. B., Nuruzzaman, A. S. M. and Martin, G. F., "Progress Review No. 62: Combustion of Single Droplets and Simplified Spray Systems," J. Inst. Fuel, Vol. 44, pp. 38-54, 1971.

23. Wise, H. and Agoston, G. A., Burning of a Liquid Droplet, Advances in Chemistry Series, No. 20, American Chemical Society, Washington, DC, pp. 116-135, 1958, also Bahn, G. S., Ibid, pp. 104-115.

24. Williams, F. A., "Progress in Spray-Combustion Analysis," Eighth Symposium (International) on Combustion, Williams and Wilkins, Baltimore, MD, pp. 50-69, 1962.

25. Williams, F. A., Combustion Theory, Addison-Wesley, Reading, MD, 1965.

26. Harrje, D. T. and Reardon, F. H. (ed.), Liquid Propellant Rocket Combustion Instability, NASA SP-194, Washington, pp. 37-104, 1952.

27. Hubbard, G. L., Denny, V. E. and Mills, A. F., "Droplet Evaporation: Effects of Transients and Variable Properties," Int. J. Heat Mass Transfer, Vol. 18, pp. 1003-1008, 1975.

28. Bellan, J. and Summerfield, M., "Quasi-Steady Gas-Phase Assumption for a Burning Droplet," AIAA J., Vol. 14, pp. 973-975, 1976.

29. Williams, F. A., "On the Assumptions Underlying Droplet Vaporization and Combustion Theories," J. Chem. Phys., Vol. 33, pp. 133-144, 1960.

30. Kodata, T. and Hiroyasu, H., "Evaporation of a Single Droplet at Elevated Pressures and Temperatures," Bull.-JSME, Vol. 19, pp. 1515-1521, 1976.

31. Kent, J. C., "Quasi-Steady Diffusion Controlled Droplet Evaporation and Condensation," Appl. Scient. Res., Ser. A-28, pp. 315-359, 1973.

32. Faeth, G. M., "The Kinetics of Droplet Ignition in a Quiescent Air Environment," Ph.D. Thesis. The Pennsylvania State University, University Park, PA, 1964.

33. Spalding, D. B., "The Combustion of Liquid Fuels," Fourth Symposium (International) on Combustion, Williams and Wilkins, Baltimore, pp. 847-864, 1953.

34. Hottel, H. C., Williams, G. C. and Simpson, H. C., "Combustion of Droplets of Heavy Liquid Fuels," Fifth Symposium (International) on Combustion, Reinhold, NY, pp. 101-129, 1955.

35. Prubert, R. P., "The Influence of Spray Particle Size and Distribution in the Combustion of Oil Droplets," Phil. Mag., Vol. 37, pp. 94-105, 1946.

36. Berlad, A. and Hibbard, R., "Effect of Radiant Energy on Vaporization and Combustion of Liquid Fuels," NACA RME-52I09, Washington, DC, 1952.

37. Wolfhard, H. B. and Parker, W. G., "Evaporating Processes in a Burning Kerosene Spray," J. Inst. Petrol., Vol. 35, pp. 118-125, 1949.

38. Friedman, M. H. and Churchill, W.S., "The Absorption of Thermal Radiation by Fuel Droplets," Chemical Engineering Progress Symposium Series, Vol. 61, No. 57, pp. 1-4, 1965.

39. Lees, L., Third Combustion and Propulsion Colloquium, AGARD, Pergamon Press, New York, pp. 451-477, 1958.

40. Bird, R. B. Steward, W. E. and Lightfoot, E. M., Transport Phenomena, Part III. John Wiley, New York, 1960.

41. Faeth, G. M. and Lazar, R. S., "Fuel Droplet Burning Rates in a Combustion Gas Environment," AIAA J, Vol. 9, pp. 2165-2171, 1971.

42. Canada, G. S. and Faeth, G. M., "Combustion of Liquid Fuel in a Flowing Combustion Gas Environment at High Pressures," Fifteenth Symposium (International) on Combustion, The Combustion Institute, Pittsburgh, pp. 419-428, 1975.

43. Wood, B. J., Rosser, W. A., Jr. and Wise, H., "Combustion of Fuel Droplets," AIAA J., Vol. 1, pp. 1076-1081, 1963.

44. Wood, B. J., Wise, H. and Inami, S. H., "Heterogeneous Combustion of Multicomponents," Combust. Flame, Vol. 4, pp. 235-242, 1960.

45. Wise, H., Lorell, J. and Wood, B. J., "The Effects of Chemical and Physical Parameters on the Burning Rate of a Liquid Droplet," Fifth Symposium (International) on Combustion, pp. 132-141, Reinhold, New York, 1955.

46. Aldred, J. W., Patel, J. C. and Williams, A., "The Mechanism of Combustion of Droplets and Spheres of Liquid n-Heptane," Combust. Flame, Vol. 17, pp. 139-148, 1971.

47. Canada, G. S. and Faeth, G. M., "Fuel Droplet Burning at High Pressures," Fourteenth Symposium (International) on Combustion, pp. 1345-1354, The Combustion Institute, Pittsburgh, 1973.

48. Law, C. K. and Law, H. K., "Quasi-Steady Diffusion Flame Theory with Variable Specific Heats and Transport Coefficients," Combust. Sci. Tech., Vol. 12, pp. 207-216, 1976.

49. Tu, C. M. Davis, H. and Hottel, H. C., "Combustion Rate of Carbon," Ind. Eng. Chem., Vol. 26, pp. 749-757, 1934.

50. Essenhigh, R. H., Froberg, R. and Howard, J. B., "Combustion Behavior of Small Particles," Ind. Eng. Chem., Vol. 57, No. 9, pp. 33-34, 1965.

51. Mertens, E. and Hellincks, L., "Mechanism of Carbon Combustion," Third Symposium on Combustion, "Flame and Explosion Phenomena," Williams and Wilkins Company, Baltimore, pp. 474-475, 1949.

52. Wicke, E. and Wurzbacher, G., "Konzentrationsprofile vor einer in Sauerstoffstrom Verbunnenden Kohlenstoffoberflache - I. Experimentelle Ergebnisse," Int. J. Heat Mass Transfer, Vol. 5, pp. 227-289, 1962.

53. Hugo, P., Wicke, E. and Wurzbacher, G., Konzentrationsprofile vor einer in Sauerstoffstrom Verbunnen Kohlenstoffoberflache - II. Berechnung der Konzentrationsprofile," Int. J. Heat Mass Transfer Vol. 5, pp. 929-939, 1962.

54. Golovina, E. S. and Khaustovich, G. P., "The Interaction of Carbon with Carbon Dioxide and Oxygen at Temperatures up to 3000 K," Eighth Symposium (International) on Combustion, Williams and Wilkins, Baltimore, pp. 784-792, 1962.

55. Orenbakh, M. S., "The Reaction Surface of Brown Coal Cokes," Thermal Engineering, Vol 14, No. 6, pp. 40-43, 1967.

56. Orenbakh, M. S., "The Reaction Surface of Anthracite and its Coke," Thermal Engineering, Vol 14, No. 6, pp. 40-43, 1967.

57. Froberg, R. W., "The Carbon-Oxygen Reaction and Experimental Study of the Oxidation of Suspended Carbon Spheres," Ph.D. Thesis, The Pennsylvania State University, University Park, PA, 1969.

58. Kurylko, L., "The Unsteady and Steady Combustion of Carbon," Ph.D. Thesis, The Pennsylvania State University, University Park, PA, 1969.

59. Roberts, O. C. and Smith, I. W., "Measured and Calculated Burning Histories of Large Carbon Spheres in Oxygen," Combust. Flame, Vol. 21, pp. 123-127, 1973.

60. Kurylko, L. and Essenhigh, R. H., "Steady and Unsteady Combustion of Carbon," Fourteenth Symposium (International) on Combustion, The Combustion Institute, Pittsburgh, pp. 1375-1386, 1973.

61. Essenhigh, R. H. and Thuring, M. W., "Measurement of Burning Times of Single Coal Particles," Conference on "Science in the Use of Coal," Sheffield, 1958, D21-D27, Institute of Fuel, London, 1958.

62. Essenhigh, R. H., "Influence of Coal Rank on Burning Times of Single Captive Particles," J. Eng. for Power, Vol. 85, pp. 183-190, 1963.

63. Beeston, G. and Essenhigh, R. H., "Kinetics of Coal Combustion: The Influence of Oxygen Concentrtion on the Burning-Out Times of Single Particles," J. Phy. Chem., Vol. 67, pp. 1349-1355, 1963.

64. Essenhigh, R. H. and Yorke, G. C., "Reaction Rates of Single Coal Particles: Influence of Swelling, Shape, and Other Factors," Fuel, Vol. 44, pp. 177-189, 1965.

65. Anson, D. Moles, F. D. and Street, P. J., "Structure and Surface Area of Pulverized Coal During Combustion," Combust. Flame, Vol. 16, pp. 265-274, 1971.

66. Orning, A. A., "Combustion of Pulverized Fuel--Mechanism and Rate of Combustion of Low-Density Fractions of Certain Bituminous Coals," ASME Trans., Vol. 64, No. 1, pp. 497-508, 1942.

67. Saji, K., "Combustion Rate of Pulverized Coal in a Jet Stream," Fifth Symposium (International) on Combustion, Reinhold Publishing Corp., New York, pp. 252-260, 1955.

68. Wicke, E., "Contributions to the Combustion Mechanism of Carbon," Ibid, pp. 245-252.

69. Yagi, S. and Kunii, D., "Studies on Combustion of Carbon Particles in Flames and Fluidized Beds," Ibid, pp. 231-244.

70. Khitrin, L. N., "Fundamental Principles of Carbon Combustion and Factors Intensifying the Burning of Solid Fuels," Sixth Symposium (International) on Combustion, Reinhold Publishing Corp., New York, pp. 565-573, 1957.

71. Khitrin, L. N., Ravitch, M. B. and Kotova, L. L., "The Characteristics of the Combustion of the Coke Residual of Solid Fuels," Eighth Symposium (International) on Combustion, Williams and Wilkins, Baltimore, pp. 793-800, 1962.

72. Field, M. A., "Rate of Combustion of Size-Graded Fractions of Char From a Low-Rank Coal between 1200 K and 2000 K," Combust. Flame, Vol. 13, pp. 237-252, 1969.

73. Field, M. A., "Measurements of the Effect of Rank on Combustion Rates of Pulverized Coal," Combust. Flame, Vol. 14, pp. 237-248, 1970.

74. Smith, I. W., "Kinetics of Combustion of Size-Graded Pulverized Fuels in the Temperature Range 1200-2270 K," Combust. Flame, Vol. 17, pp. 303-314, 1971.

75. Smith, I. W., "The Kinetics of Combustion of Pulverized Semi-Anthracite in the Temperature Range 1400-2200 K," Combust. Flame, Vol. 17, pp. 421-428, 1971.

76. Hamor, R. J., Smith, I. W. and Tyler, R. J., "Kinetics of Combustion of a Pulverized Brown Coal Char Between 630 and 2200 K," Combust. Flame, Vol. 21, pp. 153-162, 1973.

77. Sergeant, G. D. and Smith, I. W., "Combustion Rate of Bituminous Coal Char in the Temperature Range 800 to 1700 K," Fuel, Vol. 52, pp. 52-57, 1973.

78. Buerin, H., Siemieniewska, T., Grillet, Y. and Francois, M., "Influence de la Chimisorption d'Oxygene sur la determination de l'Oxygen-reactivite des Combustibles Solides, I. Etude d'un Semi-Coke de Lignite Prepare a 550o," Carbon, Vol. 8, pp. 727-740, 1970.

79. Howard, J. B., "Mechanisms of Ignition and Combustion in Flames of Pulverized Bituminous Coal," Ph.D. Thesis, The Pennsylvania State University, University Park, PA, 1965.

80. Howard, J. B., and Essenhigh, R. H., "Pyrolysis of Coal Particles in Pulverized Fuel Flames," Ind. Eng. Chem. Process Design and Dev., Vol. 6, No. 1, pp. 74-84, 1967.

81. Howard, J. B. and Essenhigh, R. H., "Mechanism of Solid-Particle Combustion with Simultaneous Gas-Phase Volatiles Combustion," Eleventh Symposium (International) on Combustion, The Combustion Institute, Pittsburgh, pp. 399-408, 1967.

82. Dainton, A. D. and Elliot, M. A., "Researches into Combustion of Coal," Transactions of Seventh World Power Conference, pp. 525-546, 1968.

83. Spalding, D. B., Some Fundamentals of Combustion, Gas Turbine Series, Vol. 2, Butterworths, London, 1955.

84. Avedesian, M. M. and Davidson, J. F., "Combustion of Carbon Particles in a Fluidized Bed," Transact. Inst. Chem. Eng., Vol. 5i, pp. 121-131, 1973.

85. Ubhayakar, S. K. and Williams, F. A., "Burning and Extinction of a Laser-Ignited Carbon Particle in Quiescent Mixtures of Oxygen and Nitrogen," J. Electrochem. Soc., Vol. 123, No. 5, pp. 747-756, 1976.

86. Caram, H. S. and Amundson, N. R., "Diffusion and Reaction in a Stagnant Boundary Layer About a Carbon Particle," Ind. Eng. Chem. Fundam., Vol. 16, No. 2, pp. 171-181, 1977.

87. Mon, E. and Amundson, N. R., "Diffusion and Reaction in a Stagnant Boundary Layer About a Carbon Particle," Ind. Eng. Chem. Fundam., Vol. 17, No. 4, pp. 313-321, 1978.

88. Libby, P. A. and Blake, T. R., "Theoretical Study of Burning Carbon Particles," Combust. Flame, Vol. 36, pp. 139-169, 1979.

89. Libby, P. A. and Blake, T. R., "Burning Carbon Particles in the Presence of Water Vapor," Combust. Flame, Vol. 41, pp. 123-147, 1981.

90. Matalon, M., "Complete Burning and Extinction of a Carbon Particle in an Oxidizing Atmosphere," Combust. Sci. Tech., Vol. 24, pp. 115-127, 1980.

91. Lewis, P. F. and Simons, G. A., "Char Gasification: Part II. Oxidation Results," Combust. Sci. Tech., Vol. 20, pp. 117-124, 1979.

92. Khitrin, L. N. and Goloving, E. S., High Temperature Technology, IUPAC, Butterworths, London, p. 485, 1964.

93. Gadsby, J., Long, F. J., Slerghtholm, P. and Sykes, K. W., "The Mechanism of the Carbon Dioxide-Carbon Reaction," Proc. R. Soc. of London, Vol. A193, pp. 357-376, 1948.

94. Ergun, S., "Kinetics of the Reaction of Carbon Dioxide with Carbon," J. Phys. Chem., Vol. 60, pp. 480-485, 1956.

95. Ergun, S., "Kinetics of the Reactions of Carbon Dioxide and Steam with Coke," U. S. Bureau of Mines Bulletin 598, 1961.

96. Mentser, M. and Ergun, E., "A Study of the Carbon Dioxide-Carbon Reaction of Oxygen Exchange," U. S. Bureau of Mines Bulletin 664, 1973.

97. Strange, J. F. and Walker, P. L., Jr., "Carbon-Carbon Dioxide Reaction: Langmuir-Hinshelwood Kinetics at Intermediate Pressures," Carbon, Vol. 14, pp. 345-350, 1976.

98. Biederman, D. L., Miles, A. J., Vastula, F. J. and Walker, P. L., Jr., "Carbon-Carbon Dioxide Reaction: Kinetics at Low Pressures and Hydrogen Inhibition," Carbon, Vol. 14, pp. 351-356, 1976.

99. von Fredersdorff, C. G. and Elliot, M. A., "Coal Gasification," Chapter 20 of Chemistry of Coal Utilization, Supplementary Volume, (H. H. Lowry, Editor), Wiley, New York, 1963.

100. Lewis, W. K., Gilliland, E. R. and McBride, G. T., Jr., "Gasification of Carbon by Carbon Dioxide in Fluidized Powder Bed," Ind. Eng. Chem., Vol. 41, No. 6, pp. 1213-1226, 1949.

101. Reif, A. E., "The Mechanism of the Carbon Dioxide-Carbon Reaction," J. Phys. Chem., Vol. 56, pp. 785-788, 1952.

102. Gadsby, J. Hinshelwood, C. N. and Sykes, K. W., "The Kinetics of the Reactions of the Steam-Carbon System," Proc. R. Soc. of London, Vol. A187, pp. 129-151, 1946.

103. Johnstone, J. F., Chen, C. Y. and Scott, D. S., "Kinetics of the Steam-Carbon Reaction in Porous Graphite Tubes," Ind. Engr. Chem., Vol. 44, No. 7, pp. 1564-1569, 1952.

104. Long, F. J. and Sykes, K. W., "The Mechanism of the Steam-Carbon Reaction, Proc. R. Soc. of London, Vol. A193, pp. 377-399, 1948.

105. Strickland-Constable, R. F., "Some Comments on the Work of Key on the Reactions Between Coke and Carbon Dioxide and Between Coke and Steam," J. Chem. Phys., Vol. 47, pp. 356-360, 1950.

106. Wicke, E. and Rossberg, M., "Primar-und Sekundarreaktionen bei der Wasserdampfvergasung von Kohle," Z. Elektrochem, Vol. 57, pp. 641-645, 1953.

107. Binford, J. S., Jr. and Eryring, H., "Kinetics of the Steam-Carbon Reaction," J. Phys. Chem., Vol. 60, pp. 486-491, 1956.

108. Behrens, H., "Mechanismus und Kinetik der Wassergasreaktion in abkuklenden Verbrennungsgasen," Z. Physik, Chem., Vol. 195, pp. 24-36, 1950.

109. Nagle, J. and Strickland-Constable, R. F., "Oxidation of Carbon Between 1000-2000o," Proc. of Fifth Carbon Conf., Vol. 1, pp. 154-164, 1962.

110. Rosner, D. E. and Allendorf, H. D., "Comparative Studies of the Attack of Pyrolytic and Isotropic Graphite by Atomic and Molecular Oxygen at High Temperatures," AIAA J., Vol. 6, pp. 650-654, 1968.

111. Wright, F. J., "The Oxidation of Soot by O. Atoms," Fifteenth Symposium (International) on Combustion, The Combustion Institute, Pittsburgh, pp. 1449-1460, 1975.

112. Otterbein, M. and Bonnetain, L., "Carbon Reaction with the Oxygen Atom," Carbon, Vol. 7, pp. 539-544, 1969.

113. Walls, J. R. and Strickland-Constable, R. F., "Oxidation of Carbon Between 1000-2400 °C," Carbon, Vol. 1, pp. 333-338, 1964.

114. Olander, D. R., Siekhaus, W., Jones, R. and Schwarz, J. A., "Reactions of Modulated Molecular Beams with Pyrolytic Graphite. I. Oxidation of the Basal Plane," J. Chem. Phys., Vol. 57, pp. 408-420, 1972.

115. Appleton, J. P., "Soot Oxidation Kinetics at Combustion Temperatures," Paper presented at AGARD Propulsion and Energetics Panel 41st Meeting, London, England, April 1973.

116. Radcliffe, S. W. and Appleton, J. P., "Soot Oxidation Rates in Gas Turbine Engines," Combust. Sci. and Tech., Vol. 4, pp. 171-175, 1971.

117. Lee, K. B., Thring, M. W. and Beer, J. M., "On the Rate of Combustion of Soot in a Laminar Soot Flame," Combust Flame, Vol. 6, pp. 137-145, 1962.

118. Tesner, P. A. and Tsibuleusky, A. M., "Gasification of Dispersed Carbon in Hydrocarbon Diffusion Flames," Combust. Explos. Shock Waves, Vol. 3, pp. 163-167, 1967.

119. Fenimore, C. P. and Jones, G. W., "Oxidation of Soot by Hydroxyl Radicals," J. Phys. Chem., Vol. 71, pp. 593-597, 1967.

120. Park, C. and Appleton, J. P., "Shock-Tube Measurements of Soot Oxidation Rates," Combust. Flame, Col. 20, pp. 369-379, 1973.

121. Neoh, K. G., Howard, J. B. and Sarofim, A. F., "Soot Oxidation in Flames," Paper Presented at the General Motors Research Symposium on Particulate Carbon—Formation During Combustion, October 1980.

122. Thiele, E. W., "Relation Between Catalytic Activity and Size of Particle," Ind. Eng. Chem., Vol. 31, p. 916, 1939.

123. Wheeler, A., "Reaction Rates and Selectivity in Catalyst Pores," Advances in Catalysis, Vol. 3, Academic Press, New York, p. 249, 1951.

124. Hashimoto, K. and Silverston, P. L., "Gasification: Part I. Kinetic Control Model for a Solid with a Pore Size Distribution," AIChE J., Vol. 19, p. 259, 1973.

125. Hashimoto, K. and Silverston, P. L., "Gasification: Part II. Extension to Diffusion Control," AIChE J., Vol. 19, p. 268, 1973.

126. Kriegbaum, R. A. and Laurendeau, N. N., "Pore Model for the Gasification of a Single Coal Char Particle," 1978 Fall Technical Meeting, Eastern Section of the Combustion Institute, Miami Beach, FL, November 1978.

127. Beshty, B. S., "A Mathematical Model for the Combination of a Porous Carbon Particle," Combust. Flame, Vol. 32, pp. 295-311, 1978.

128. Simons, G. A. and Finson, M. L., "The Structure of Coal Char: Part I. Pore Branching," Combust. Sci. Tech., Vol. 19, pp. 217-225, 1979.

129. Simons, G. A., "The Structure of Coal Char: Part II. Pore Combination," Combust. Sci. Tech., Vol. 19, pp. 227-235, 1979.

130. Simons, G. A., "Char Gasification: Part I. Transport Model," Combust. Sci. Tech., Vol. 20, pp. 107-116, 1979.

131. Law, C. K., "Unsteady Droplet Combustion with Droplet Heating," Combust. Flame, Vol. 26, pp. 17-22, 1976.

132. Law, C. K. and Sirignano, W. A., "Unsteady Droplet Combustion with Droplet Heating - II: Conduction Limit," Combust. Flame, Vol. 28, pp. 175-186, 1977.

133. Law, C. K., "Multicomponent Droplet Combustion with Rapid Internal Mixing," Combust. Flame, Vol. 26, pp. 219-233, 1976.

134. Law, C. K., "Internal Boiling and Superheating in Vaporizing Multicomponent Droplets," AIChE J., Vol. 24, No. 4, pp. 626-632, 1978.

135. Sirignano, W. A. and Law, C. K., "Transient Heating and Liquid-Phase Mass Diffusion in Fuel Droplet Vaporization," ACS Adv. in Chem. Series, No. 166, American Chem. Soc., New York, pp. 1-25, 1978.

136. Greeves, G., Khan, I. M. and Union, G., "Effects of Water Introduction on Diesel Engine Combustion and Emissions," Sixteenth Symposium (International) on Combustion, Williams and Wilkins, Cambridge, MA, pp. 321-336, 1976.

137. Ivanov, V. M. and Nefedor, P. I., Experimental Investigation of the Combustion Processes in Natural and Emulsified Fuels, NASA Tech. Transl., TI F-258, January 1965.

138. Helion, Von R., Delatronchette, C., Sundermann, P. and Bandel, A., VGB Kraftwertstechnik, Vol. 55, p. 88, 1975.

139. Law, C. K., Lee, C. H. and Srinivasan, N., "Combustion Characteristics of Water-in-Oil Emulsions," Combust. Flame, Vol. 37, pp. 125-143, 1980.

140. Jacques, M. T., Jordan, J. B. and Williams, A., "The Combustion of Emulsions of Water and Fuel Oil," Twentieth European Symposium on Combustion, The Combustion Institute, pp. 397-4-2, 1975.

141. Dryer, F. L., "Water Addition to Practical Combustion Systems--Concepts and Applications," Sixteenth Symposium (International) on Combustion, Williams and Wilkins, Cambridge, MA, pp. 279-295, 1976.

142. Sjorgen, A., "Burning of Water-in-Oil Emulsions," Sixteenth Symposium (International) on Combustion, Williams and Wilkins, Cambridge, MA, pp. 297-305, 1976.

143. Jacques, M. T., Jordan, T.B., Williams, A. and Hadley-Coates, L., "The Combustion of Water-in-Oil Emulsions and the Influence of Asphaltene Content," Sixteenth Symposium (International) on Combustion, Williams and Wilkins, Cambridge, MA, pp. 307-319, 1976.

144. Law, C. K., Law, H. K. and Lee, C. H., "Combustion Characteristics of Droplets of Coal/Oil and Coal/Oil/Water Mixtures," Energy, Vol. 4, pp. 329-339, 1979.

145. Lasheras, J. C., Fernandez-Pello, A. C. and Dryer, F. L., "An Experimental Study of the Free Droplet Combustion of Hydrocarbon/Water Emulsions," Paper No. 78-45, 1978. Fall Meeting, Western States Section, The Combustion Institute, Lagana Beach, CA, 1978.

146. Lasheras, J. C., Fernandez-Pello, A. C. and Dryer, F. L., "Experimental Observations on the Disruptive Combustion of Free Droplets of Multicomponent Fuels," Paper presented at the 1979 Spring Meeting, Western States Section, The Combustion Institute, Provo, UT, 1979.

147. Lasheras, J. C., Fernandez-Pello, A. C. and Dryer, F. L., "On the Disruptive Burning of Free Droplets of Alcohol/n-Paraffin Mixtures and Emulsions," Paper No. 79-43, 1979 Eastern States Section Meeting, The Combustion Institute, Atlanta, GA,   .

148. Law, C. K., "Combustion and Agglomeration of Coal-Oil Mixtures in Furnace Environments," Paper No. 80-16, Presented at 1980 Spring Technical Meeting, Central States Section, The Combustion Institute, pp. 1-22, 1980.

149. Szekely, G. A., Jr., "Experimental Evaluation of a Locally Homogeneous Flow Model of Spray Combustion," Department of Mechanical Engineering, Master's Thesis, The Pennsylvania State University, University Park, PA, March 1980.

150. Mao, C-P., Szekely, G. A., Jr. and Faeth, G. M., "Evaluation of a Locally Homogeneous Flow Model of Spray Combustion," Energy, Vol. 4, No. 2, pp. 78-87, 1980.

151. Mao, C-P., Szekely, G. A., Jr. and Faeth, G. M., Evaluation of a Locally Homogeneous Flow Model of Spray Combustion, NASA CR-3202, April 1980.

152. Glass, M. and Kennedy, I. M., "An Improved Seeding Method for High Temperature Laser-Doppler Velocimetry," Combust. Flame, Vol. 29, pp. 333-335, 1977.

153. Kaskan, W. E., "The Dependence of Flame Temperature on Mass Burning Velocity," Sixth Symposium (International) on Combustion, Williams and Wilkins, New Haven, CT, pp. 134-143, 1956.

154. Daley, R. D., Withum, J. A., Warchol, J. J. and Reuther, J. J., "Combustion/Inhibition Physico-Chemistry of Coal-Derived Syngas/Air Flames," submitted for publication to Combustion and Flame.

155. Shearer, A. J., Tamura, H. and Faeth, G. M., "Evaluation of a Locally Homogeneous Flow Model of Spray Evaporation," J. of Energy, Vol. 3, pp. 271-278, Sept.-Oct. 1979.

156. Mao, C-P., Wakamatsu, Y. and Faeth, G. M., "A Simplified Model of High Pressure Spray Combustion," Eighteenth Symposium (International) on Combustion, The Combustion Institute, in press.

157. Faeth, G. M., "Spray Combustion Models—A Review," AIAA Paper No. 79-0293, 17th Science Meeting, New Orleans, 1979.

158. White, F. M., Viscous Fluid Flow, McGraw-Hill Book Co., New York, p. 209, 1974.

159. Stull, D. R. and Prophet, H., JANAF Thermochemical Tables, 2nd Ed., National Bureau of Standards, Washington, DC, 1971.

160. Laurendau, N. M., "Heterogeneous Kinetics of Coal Char Gasification and Combustion," Prog. Energy Combust. Sci., Vol. 4, No. 4, pp. 221-270, 1978.

161. Reid, R. C., Prausnitz, J. M. and Sherwood, T. K., The Properties of Gases and Liquids, 3rd Ed., McGraw-Hill, New York, 1977.

162. Shehla, R. A., "Estimated Viscosities and Thermal Conductivities of Gases at High Temperatures," NASA Technical Report R-132, 1962.

163. McCoy, J. R., Fuels Branch, Air Force Aero Propulsion Laboratory, Wright-Patterson AFB, OH, Personal Communication, July 1980.

APPENDIX A

COMPUTATION OF PROPERTIES

A.1 Mean Property State

The average properties of the gas surrounding the droplet were computed at the mean state, defined as follows:

$$\phi_{avg} = \alpha\phi_p + (1 - \alpha)\ \phi_\infty \tag{A.1}$$

where ϕ is a generic property at a specific temperature and mass fraction. α can range between 0 and 1 and a value of 0.9 was selected for the present investigation as suggested by Faeth and coworkers [15^,154,155].

A.2 Mixture Thermal Conductivity

The thermal conductivity of the gaseous mixture was calculated with the Mason and Saxena formulation of the Wassiljewa equation [160].

$$\lambda_m = \sum_{i=1}^{N} \left[\frac{X_i \lambda_i}{\sum\limits_{j=1}^{N} X_j \phi_{ij}} \right] \tag{A.2}$$

where

$$\phi_{ij} = \frac{1}{8^{1/2}} \left(1 + \frac{M_i}{M_j}\right)^{-1/2} \left[1 + \left(\frac{\mu_i}{\mu_j}\right)^{1/2} \left(\frac{M_j}{M_i}\right)^{1/4}\right]^2 . \tag{A.3}$$

The thermal conductivity and viscosity for gases other than JP-10 was obtained from Reference 161. The properties of JP-10 are derived in Section A.6. Equation (A.2) was evaluated at the average

temperature and composition of the gas phase in Equation (A.1). In Equation (A.3), ϕ_{ij} is set equal to 1, when $i = j$.

A.3 Mixture Viscosity

The viscosity calculations of mixture employed the method of Wilke, cited in Reference 160.

For a mixture of N components

$$\mu_m = \sum_{i=1}^{N} \left[\frac{X_i \mu_i}{\sum_{j=1}^{N} X_j \phi_{ij}} \right] \tag{A.4}$$

where ϕ_{ij} is given by Equation (A.3). The viscosity data used in the calculations was obtained in the same manner as described in Section A.2.

A.4 Mixture Diffusivity

Since only liquid vapor diffuses through the stagnant mixture, when liquid JP-10 is present the diffusion coefficient is given as

$$D_{1m} = \left[\sum_{j=2}^{N} \frac{X_j}{D_{1j}} \right]^{-1} = D . \tag{A.5}$$

Subscript 1 represents fuel vapor, and j indicates all other gases. Binary diffusivity calculations employed Chapman-Enskog theory along with Lennard-Jones characteristic energy and length concept (ε' and σ), cited in Reference 161. The data for σ and ε'/k' are listed in Table 10.

Table 10. Properties Used for Binary Diffusivity Calculations[a]

Substance	σ (A^o)	ϵ'/k' (K)
H_2O	2.641	809.1
CO	3.690	91.7
CO_2	3.941	195.2
N_2	3.798	71.4
H_2	2.827	59.7
O_2	3.467	106.7
JP-10[b]	6.927	531.5

[a]Taken from Reid et al. [161].

[b]Determined in Section A.6.

When all of the liquid fuel has evaporated and only a carbon-agglomerated particle remains the diffusion coefficient of the gas is given by:

$$D = \frac{1}{2} \left[\sum_{j=2}^{N} \frac{X_j}{D_{1j}} \right]^{-1} . \qquad (A.6)$$

A.5 Mixture Specific Heat

The mixture specific heat was calculated as a mole fraction weighted average of the specific heats of each contributing species

$$C_p = \frac{\sum_{i=1}^{N} X_i \overline{C_{p_i}}}{M} . \qquad (A.7)$$

A.6 Thermophysical and Transport Properties for JP-10

JP-10 or exo-tetrahydrodi (cyclopentadiene) has the chemical formula $C_{10}H_{16}$ and a molecular weight of 136.2, the chemical structure is shown in Figure 74.

The critical properties of JP-10 were calculated from the chemical structure using Lyderson's method discussed on page 12 of Reid, Prausnitz and Sherwood [161] to yield·

Critical Temperature, $T_c = 672.6$ K

Critical Pressure, $P_c = 27.84$ atm $\qquad (A.8)$

Critical Volume, $V_c = 3.605 \times 10^{-3}$ m^3/kg.
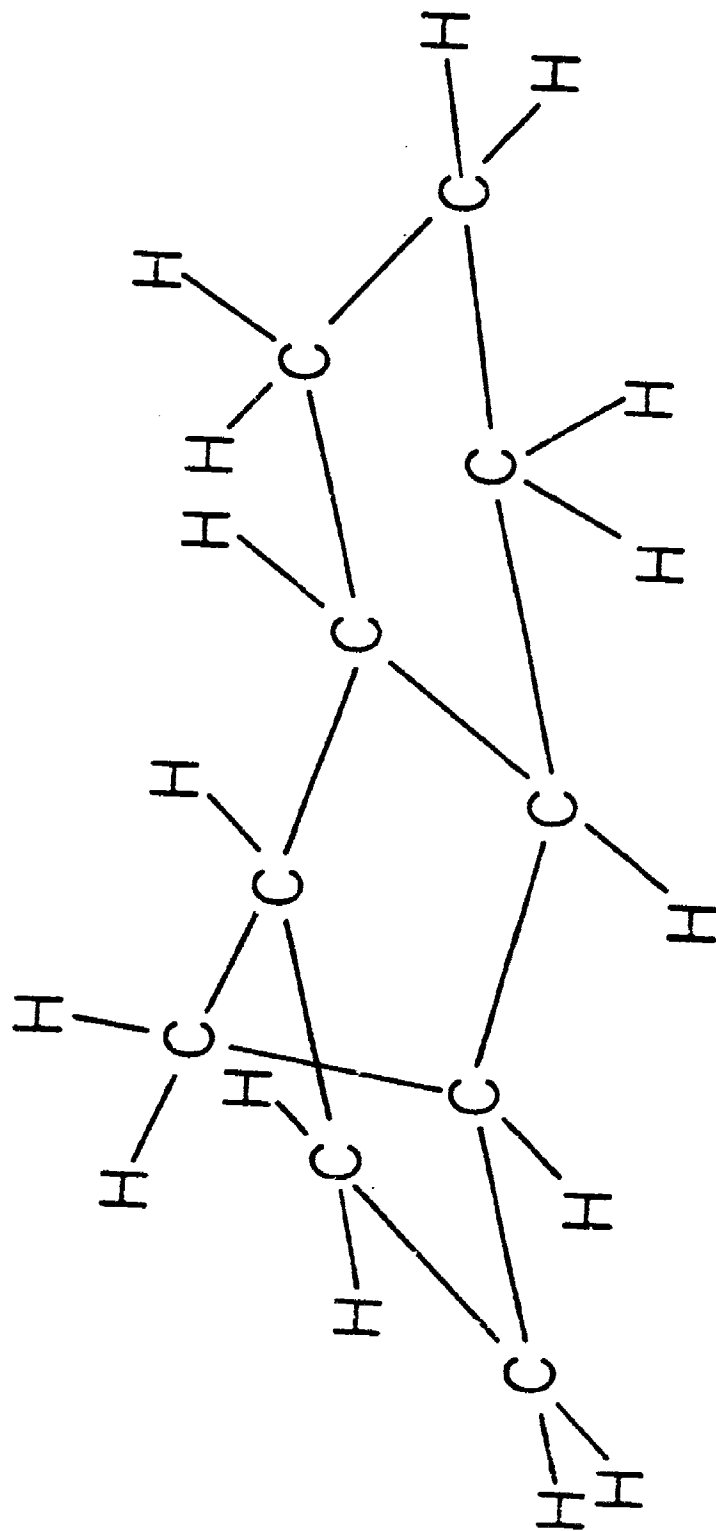
Figure 74. Chemical structure of JP-10.

The correlation for vapor pressure liquid density and liquid specific heat was obtained by curve-fitting experimental data obtained from McCoy [163]. The vapor pressure equation determined where the pressure is in N/m^2 was

$$P = 3.0690 \times 10^9 \exp(\frac{-4704.2}{T}) \;.$$ (A.9)

Liquid density in kg/m^3 was correlated as

$$\rho = 1166.4 - 0.792(T).$$ (A.10)

And, the liquid specific heat in units of $cal/gm°C$ was determined as

$$C_p = 0.0615 + 1.08 \times 10^{-3}(T)$$ (A.11)

where the temperature in Equation (A.9)-(A.11) is in degrees Kelvin.

The heat of vaporization was obtained using the Clausius-Clapeyron equation assuming ideal gas behavior, and that the vapor specific volume is much greater than the liquid specific volume, which leads to

$$i_{fg} = 286.7 \; kJ/kg.$$ (A.12)

The gas-phase specific heat was calculated using the method of Rehani and Doraiswany discussed on page 234 of Reid, Prausnitz and Sherwood [161] to give:

$$C_p = 0.35669 + 0.23542 \times 10^{-2} \, (T) - 1.5827 \times 10^{-6} \, (T)^2$$
$$+ 3.9699 \times 10^{-10} \, (T)^3 \qquad \text{(A.13)}$$

where temperature is again in degrees Kelvin.

The gas-phase viscosity for JP-10 was calculated using the Reichenberg method discussed in page 404 of Reid, Prausnitz and Sherwood [161]. The gas-phase viscosity equation determined was

$$\mu = 170.32(T_r)/[1 + 0.36(T_r)(T_r-1)]^{1/6} \qquad \text{(A.14)}$$

where

$$T_r = T/T_{cr} \qquad \text{(A.15)}$$

and T, T_{cr} are in degrees Kelvin and   has the units of micro-poise.

An equation for the gas-phase thermal conductivity was obtained by the Miscie and Thodos method discussed on page 480 of Reid, Prausnitz and Sherwood [161]. The resulting equation with thermal conductivity in units of cal/cm s K was

$$\lambda = 26.59 \times 10^{-8} \, [14.52(T_r) - 5.14]^{2/3} \, C_p \qquad \text{(A.16)}$$

where C_p and T_r are given in Equations (A.13) and (A.15) respectively.

The method discussed by Shehla [162] was used to obtain the Lennard-Jones characteristic energy and   length employed in the Chapman-Enskog binary diffusivity calculations.   The resulting Lennard-Jones parameters were:

$$\epsilon'/k' = 504.6 \text{ K}$$
$$\sigma = 6.927 \text{ A}^{o}. \qquad \text{(A.17)}$$

A.7 Equations Used to Calculate Transport and Thermophysical Properties of Each Species

The equations developed to determine the transport and thermophysical properties of the gas-phase for the species O_2, CO_2, CO, H_2O, H_2, OH, and N_2 were obtained by curve-fitting high temperature data tabulated by Shehla [161]. The equations used to determine the gas-phase properties for JP-10 were discussed in the previous section. The computer subroutine to calculate the gas-phase properties that was used in the carbon-agglomerate analysis is presented in the remainder of this section. The nomenclature used within the program is explained in the program comments.

```
      SUBROUTINE PROPG (YI,YS,TI,TS,P,VM,CDM,DFM,RHM,CPM,AVMS,
     $X02,XCO,XCO2,XH2,XH2O,XOH)
C------SPECIFY PROPERTIES OF AMBIENT GAS------------------------------
C---------SPECIES WHICH EXIST IN FLOW FIELD :
C         (1)----HYDROXYL (OH)
C         (2)----WATER VAPOR (H2O)
C         (3)----CARBON MONOXIDE (CO)
C         (4)----CARBON DIOXIDE (CO2)
C         (5)----NITROGEN    (N2)
C         (6)----HYDROGEN    (H2)
C         (7)----OXYGEN      (O2)
C-------------------------------------------------------------------
      IMPLICIT REAL*8(A-H,O-Z)
      DIMENSION AM(7),XS(7),XI(7),X(7),Y(7),YS(7),YI(7)
      DIMENSION DF(7,7), D(7), CP(7), V(7), CD(7)
      DIMENSION EDKC(7,7), SIGMA(7,7), OM(7,7), PHI(7), EDK(7), SIGM(7)
      DO 20 I=1,7
C     TO CHECK MASS FRACTION VALUES REMOVE C'S
C     IF ((YS(I).GT.1.0D0).OR.(YS(I).LT.0.0D0)) WRITE(6,10) I,YS(I)
C  10 FORMAT(' ',5X,'YS(',I1,') =',1PD13.6)
      IF (YI(I).LT.0.0D0) YI(I)=0.0D0
      IF (YS(I).LT.0.0D0) YS(I)=0.0D0
      IF (YI(I).GT.1.0D0) YI(I)=1.0D0
      IF (YS(I).GT.1.0D0) YS(I)=1.0D0
   20 CONTINUE
C---------LIST MOLECULAR WEIGHT OF EACH SPECIES
      AM(1)=17.0074D0
      AM(2)=18.016D0
      AM(3)=28.011D0
```

```
      AM(4)=44.011D0
      AM(5)=28.016D0
      AM(6)=2.016D0
      AM(7)=32.000D0
C-----COMPUTE MASS FRACTION OF FUEL AT SURFACE
      AVMI=0.0D00
      DO 30 I=1,7
      AVMI=AVMI+YI(I)/AM(I)
   30 CONTINUE
      AVMI=1.0D00/AVMI
      PRESS=P*101325.D0
      DO 40 I=1,7
      XI(I)=AVMI*YI(I)/AM(I)
   40 CONTINUE
      AVMI=0.0D00
      DO 50 I=1,7
      AVMI=AVMI+AM(I)*XI(I)
   50 CONTINUE
      RHI=PRESS*AVMI/TI/8314.3D00
      AVMS=0.0D00
      DO 60 I=1,7
      AVMS=AVMS+YS(I)/AM(I)
   60 CONTINUE
      AVMS=1.D0/AVMS
      DO 70 I=1,7
      XS(I)=AVMS*YS(I)/AM(I)
   70 CONTINUE
      XO2=XS(7)
      XCO=XS(3)
      XCO2=XS(4)
      XH2=XS(6)
      XH2O=XS(2)
      XOH=XS(1)
C-----A IS A MULTIPLICATION FACTOR APPEARS IN TB=A*TS+(1-A)*TI EQUATION
C-----IT WAS OBTAINED BY MATCHING WITH CALIBRATION TEST.----------------
      A=0.9D00
      TB=A*TS+(1.0D00-A)*TI
      DO 80 I=1,7
      X(I)=A*XS(I)+(1.0D00-A)*XI(I)
   80 CONTINUE
      AVM=0.0D00
      DO 90 I=1,7
      AVM=AVM+AM(I)*X(I)
   90 CONTINUE
      DO 100 I=1,7
      Y(I)=AM(I)*X(I)/AVM
  100 CONTINUE
C------SPECIFIC HEAT AND TRANSPORT PROPERTIES (UNIT)-------------------
C      CP          SPECIFIC HEAT AT CONST. PRESSURE (CAL/G-MOLE*DEG)
C                  ------------(KJ/KG*DEG)    WHEN RETURNING---------
C      V           VISCOSITY                      (MICRO POISE)
C                  ----------(KG/M*S OR PA*S) WHEN RETURNING----------
```

```
C    CD        THERMAL CONDUCTIVITY              (*1.0D-06 CAL/CM*S*DEG)
C              ------------(KJ/M*S*DEG)          WHEN RETURNING----------
C    DF        MASS DIFFUSIVITY                  (CM**2/S)
C              ----------(M**2/S)                WHEN RETURNING----------
C    RH        DENSITY                           (KG/M**3)
C              ----------(KG/M**3)               WHEN RETURNING----------
C
C------MEANING OF SUFFIX-----------------------------------------------------
C          I----INFINITE        M----MEAN VALUE      S----SURFACE
C          F----FUEL GAS        A----AMBIENT GAS     B----BULK GAS
C--------------------------------------------------------------------------
      IF (TB.GE.500.D0) GO TO 110
      CP(1)=7.674842D0-2.38931D-3*TB+2.2992D-6*TB**2
      CP(2)=7.972473D0-8.71300D-4*TB+3.5127D-6*TB**2
      CP(3)=7.182841D0-1.62840D-3*TB+3.0095D-6*TB**2
      CP(4)=4.798756D0+1.65402D-2*TB-9.6115D-6*TB**2
      CP(5)=7.174363D0-1.46168D-3*TB+2.5019D-6*TB**2
      CP(6)=6.274392D0+3.00860D-3*TB-3.1429D-6*TB**2
      CP(7)=6.875085D0-4.35900D-4*TB+3.0954D-6*TB**2
      GO TO 120
  110 TT=TB/1000.D0
      CP(1)=5.24639000D0+2.42980000D0*TT-5.66500000D-1*TT**2
     $      +4.90800000D-2*TT**3+1.8738000D-1/TT**2
      CP(2)=6.41074451D0+4.40994628D0*TT-8.87521069D-1*TT**2
     $      +6.28994081D-2*TT**3-9.2660052D-2/TT**2
      CP(3)=0.72635540D1+0.11035250D1*TT-0.235811400D0*TT**2
     $      +0.17634440D-1*TT**3-0.15939236D0/TT**2
      CP(4)=0.12226062D2+0.17893510D1*TT-0.380132200D0*TT**2
     $      +0.29171210D-1*TT**3-0.59083890D0/TT**2
      CP(5)=0.69731460D1+0.12742370D1*TT-0.274262700D0*TT**2
     $      +0.20276900D-1*TT**3-0.11855850D0/TT**2
      CP(6)=0.52903300D1+0.20241900D1*TT-0.352047000D0*TT**2
     $      +0.24859530D-1*TT**3+0.19386990D0/TT**2
      CP(7)=0.80211900D1+0.54604200D0*TT+0.77746000D-2*TT**2
     $      -0.61156400D-2*TT**3-0.21609740D0/TT**2
  120 IF(TB.GT.1.D3.AND.TB.LT.2.5D3) GO TO 130
      IF(TB.GE.2.5D3) GO TO 140
      GO TO 150
  130 TT=TB-1000.D0
      V(1)=443.2449D0+2.88315D-1*TT-4.1584D-5*TT**2+6.7434D-9*TT**3
      V(2)=358.5945D0+3.51007D-1*TT-5.3575D-5*TT**2+7.7015D-9*TT**3
      V(3)=405.7153D0+2.58971D-1*TT-3.1370D-5*TT**2+3.6138D-9*TT**3
      V(4)=393.1504D0+2.69698D-1*TT-4.5523D-5*TT**2+7.7199D-9*TT**3
      V(5)=397.1877D0+2.59811D-1*TT-4.0295D-5*TT**2+7.3183D-9*TT**3
      V(6)=197.6894D0+1.27990D-1*TT-1.9142D-5*TT**2+3.4007D-9*TT**3
      V(7)=480.9907D0+3.02530D-1*TT-3.3070D-5*TT**2+3.2938D-9*TT**3
      GO TO 160
  140 TT=TB-2500.D0
      V(1)=804.8804D0+2.07924D-1*TT-1.4765D-5*TT**2+2.0351D-9*TT**3
      V(2)=790.5020D0+2.42314D-1*TT-2.4886D-5*TT**2+5.1068D-9*TT**3
      V(3)=736.1011D0+1.90016D-1*TT-1.2502D-5*TT**2+1.1632D-9*TT**3
      V(4)=721.3639D0+1.83192D-1*TT+0.0200D-5*TT**2-5.7908D-9*TT**3
```

```
      V(5)=720.8079D0+1.85955D-1*TT-1.2555D-5*TT**2+1.3152D-9*TT**3
      V(6)=358.1956D0+9.17810D-2*TT-0.4861D-5*TT**2-2.1608D-10*TT**3
      V(7)=871.5132D0+2.26188D-1*TT-1.6785D-5*TT**2+2.4879D-9*TT**3
      GO TO 160
  150 V(1)=34.9350D0+6.2460D-1*TB-3.1150D-4*TB**2+9.5453D-8*TB**3
      V(2)=21.2350D0+2.5099D-1*TB+1.6890D-4*TB**2-8.2571D-8*TB**3
      V(3)=27.0290D0+5.8270D-1*TB-2.9570D-4*TB**2+9.1921D-8*TB**3
      V(4)=-8.5780D0+6.2144D-1*TB-3.1440D-4*TB**2+9.4699D-8*TB**3
      V(5)=32.7427D0+5.6251D-1*TB-2.9181D-4*TB**2+9.3694D-8*TB**3
      V(6)=16.3958D0+2.8675D-1*TB-1.6439D-4*TB**2+5.9090D-8*TB**3
      V(7)=22.5180D0+7.1790D-1*TB-3.8510D-4*TB**2+1.2550D-7*TB**3
  160 CONTINUE
C
      IF(TB.GT.1.D3.AND.TB.LT.2.5D3) GO TO 170
      IF(TB.GE.2.5D3) GO TO 180
      GO TO 190
  170 TT=TB-1000.D0
      CD(1)=274.4993D0+2.21650D-1*TT-0.8940D-5*TT**2-2.7137D-9*TT**3
      CD(2)=276.3345D0+3.60970D-1*TT+0.1080D-5*TT**2-9.8961D-9*TT**3
      CD(3)=164.5385D0+1.31915D-1*TT-1.8360D-5*TT**2+2.2402D-9*TT**3
      CD(4)=160.5447D0+1.44716D-1*TT-2.7369D-5*TT**2+4.6602D-9*TT**3
      CD(5)=158.8701D0+1.30969D-1*TT-2.0384D-5*TT**2+3.1328D-9*TT**3
      CD(6)=1021.868D0+7.86030D-1*TT+0.6080D-5*TT**2-1.7096D-8*TT**3
      CD(7)=178.8670D0+1.32902D-1*TT-1.2880D-5*TT**2+2.6768D-9*TT**3
      GO TO 200
  180 TT=TB-2500.D0
      CD(1)=577.9192D0+1.79665D-1*TT-1.3345D-5*TT**2+1.8819D-9*TT**3
      CD(2)=737.2119D0+3.04297D-1*TT-2.7674D-5*TT**2+4.3856D-9*TT**3
      CD(3)=328.7075D0+9.24140D-2*TT-0.7259D-5*TT**2+1.4081D-9*TT**3
      CD(4)=331.7312D0+9.31960D-2*TT-0.1311D-5*TT**2-2.4115D-9*TT**3
      CD(5)=319.9414D0+9.19400D-2*TT-1.0570D-5*TT**2+2.8529D-9*TT**3
      CD(6)=2157.398D0+6.98236D-1*TT-4.4289D-5*TT**2+5.2617D-9*TT**3
      CD(7)=358.1880D0+1.11655D-1*TT-0.4735D-5*TT**2-1.9153D-11*TT**3
      GO TO 200
  190 CD(1)=20.6530D0+3.7420D-1*TB-2.0540D-4*TB**2+8.5603D-8*TB**3
      CD(2)=19.4052D0+1.1330D-1*TB+1.9945D-4*TB**2-5.5305D-8*TB**3
      CD(3)=17.1240D0+1.5949D-1*TB-0.1020D-4*TB**2-1.7684D-9*TB**3
      CD(4)=-14.414D0+1.9866D-1*TB-1.7190D-5*TB**2-6.5668D-9*TB**3
      CD(5)=18.2390D0+1.6053D-1*TB-2.9930D-5*TB**2+1.0101D-8*TB**3
      CD(6)=99.7600D0+1.3812D+0*TB-7.9830D-4*TB**2+3.3980D-7*TB**3
      CD(7)=10.5004D0+1.8644D-1*TB-0.5740D-5*TB**2-1.2626D-8*TB**3
  200 CONTINUE
C
      SIGM(5)=3.798D0
      SIGM(7)=3.467D0
      EDK(5)=71.4D0
      EDK(7)=106.7D0
      I=5
      J=7
      EDKC(I,J)=DSQRT(EDK(I)*EDK(J))
      SIGMA(I,J)=(SIGM(I)+SIGM(J))/2.D0
      VBC=0.47635D0*(TB/EDKC(I,J))
```

```
      VBB=1.52996D0*(TB/EDKC(I,J))
      VBA=3.89411D0*(TB/EDKC(I,J))
      IF (VBC.GT.174.6D0) OM(I,J)=1.06036D0/(TB/EDKC(I,J))**0.1561
      IF (VBC.GT.174.6D0) GO TO 210
      IF (VBB.GT.174.6D0) OM(I,J)=1.06036D0/(TB/EDKC(I,J))**0.1561+
     $    0.193D0/DEXP(0.47635D0*(TB/EDKC(I,J)))
      IF (VBB.GT.174.6D0) GO TO 210
      IF (VBA.GT.174.6D0) OM(I,J)=1.06036D0/(TB/EDKC(I,J))**0.1561+
     $    0.193D0/DEXP(0.47635D0*(TB/EDKC(I,J)))+1.30587D0/
     $    DEXP(1.52996D0*(TB/EDKC(I,J)))
      IF (VBA.GT.174.6D0) GO TO 210
      OM(I,J)=1.06036D0/(TB/EDKC(I,J))**0.1561+0.193D0/DEXP(0.47635D0
     $      *(TB/EDKC(I,J)))+1.03587D0/DEXP(1.52996D0*(TB/EDKC(I,J)))
     $      +1.76474D0/DEXP(3.89411D0*(TB/EDKC(I,J)))
  210 DF(I,J)=1.858D-3*TB**1.5*DSQRT((AM(I)+AM(J))/(AM(I)*AM(J)))
     $      /P/SIGMA(I,J)**2/OM(I,J)
C-------CALCULATION OF MEAN VALUES---------------------------------
C-------VISCOSITY-------------------------------------------------
      VM=0.D0
      DO 230 I=1,7
      XPHI=0.D0
      DO 220 J=1,7
      PHI(J)=(1.D0+(V(I)/V(J))**.5*(AM(J)/AM(I))**.25)**2/
     $       (8.D0*(1.D0+(AM(I)/AM(J))))**.5
      IF(J.EQ.I) PHI(J)=1.D0
      XPHI=XPHI+X(J)*PHI(J)
  220 CONTINUE
      VM=VM+X(I)*V(I)/XPHI
  230 CONTINUE
      VM=VM*1.0D-07
C-------CONDUCTIVITY----------------------------------------------
      CDM=0.D0
      DO 250 K=1,7
      XPHI=0.D0
      DO 240 L=1,7
      PHI(L)=(1.D0+(V(K)/V(L))**.5*(AM(L)/AM(K))**.25)**2/
     $       (8.D0*(1.D0+(AM(K)/AM(L))))**.5
      IF(L.EQ.K) PHI(L)=1.D0
      XPHI=XPHI+X(L)*PHI(L)
  240 CONTINUE
      CDM=CDM+X(K)*CD(K)/XPHI
  250 CONTINUE
      CDM=CDM*1.0D-07
      CDM=4.1879D0*CDM
C-------DIFFUSIVITY----------------------------------------------
      DFM=DF(5,7)*1.D-4
C-------DENSITY--------------------------------------------------
      RHM=PRESS*AVM/TB/8314.3D00
C-------SPECIFIC HEAT--------------------------------------------
      CPM=0.0D00
      DO 260 I=1,7
      CPM=CPM+X(I)*CP(I)
```

```
  260 CONTINUE
      CPM=CPM/AVM
      CPM=4.1868D0*CPM
      IF (VM.LT.0.D0) WRITE(6,270) VM
      IF (CDM.LT.0.D0) WRITE(6,280) CDM
      IF (DFM.LT.0.D0) WRITE(6,290) DFM
      IF (RHM.LT.0.D0) WRITE(6,300) RHM
      IF (CPM.LT.0.D0) WRITE(6,310) CPM
      IF (AVMS.LT.0.D0) WRITE(6,320) AVMS
  270 FORMAT(' ',10X,'VM HAS THE VALUE',1PD15.6)
  280 FORMAT(' ',10X,'CDM HAS THE VALUE',1PD15.6)
  290 FORMAT(' ',10X,'DFM HAS THE VALUE',1PD15.6)
  300 FORMAT(' ',10X,'RHM HAS THE VALUE',1PD15.6)
  310 FORMAT(' ',10X,'CPM HAS THE VALUE',1PD15.6)
  320 FORMAT(' ',10X,'AVMS HAS THE VALUE',1PD15.6)
      RETURN
      END
```

APPENDIX B

EXPERIMENTAL DATA

B.1 Data From the Turbulent Diffusion Flame Test

B.1.1 Drop Environment Measurements

Temperature Measurements

x/d	Temperature (K)
21.3	558
42.5	825
74.5	1008
85.0	1053
127.5	1543
170.0	1841
212.5	1903
255.0	1824
297.5	1541
340.0	1271
382.5	1101
425.0	988
467.5	887
510.0	779
552.5	698
595.0	580

Velocity and Composition Measurements

x/d	ϕ	u (m/s)	Mass Fraction						
			O_2	N_2	CO_2	CO	H_2O	H_2	C_3H_8
74.5	8.716	22.01	0.000	0.662	0.068	0.020	0.060	0.002	0.172
170.0	1.350	9.93	0.006	0.615	0.101	0.079	0.161	0.000	0.013
212.5	0.939	8.14	0.021	0.689	0.094	0.051	0.145	0.000	0.000
255.0	0.870	6.15	0.076	0.677	0.079	0.039	0.129	0.000	0.000
297.5	0.761	4.82	0.093	0.688	0.075	0.031	0.113	0.000	0.000
340.0	0.557	4.35	0.122	0.699	0.066	0.016	0.097	0.000	0.000
382.5	0.484	4.21	0.136	0.705	0.057	0.013	0.0895	0.000	0.000
467.5	0.348	3.90	0.163	0.717	0.038	0.007	0.075	0.000	0.000
510.0	0.272	2.93	0.176	0.724	0.029	0.004	0.067	0.000	0.000

B.1.2 Particle Measurements

Particle-Life History, x/d = 170.0, ϕ = 1.350

Time (s)	d_p (μm)	T_p (K)
0.00	1230	294
0.01	1229	311
0.05	1224	321
0.08	1216	369
0.10	1190	384
0.13	1162	402
0.16	1112	410
0.19	1070	413
0.22	1056	414
0.26	1020	415
0.29	1002	416
0.45	996	417
0.52	987	449
0.63	985	506
0.78	981	628
0.84	973	974
1.14	951	1329
1.37	926	1369
1.56	914	1458
1.85	883	1484
2.07	855	1506
2.33	817	1502
2.52	783	1543
2.69	761	1587
2.86	746	1558
3.11	707	1584
3.24	667	1587
3.40	641	1595
3.61	625	1607
3.88	589	1618
4.26	524	1632
4.46	481	1661
4.73	432	1705
5.00	417	1743

Particle-Life History, x/d = 212.5, ϕ = 0.939

Time (s)	d_p (μm)	T_p (K)
0.00	1261	299
0.03	1258	344
0.07	1248	377
0.10	1226	410
0.14	1189	423
0.18	1154	431
0.22	1113	433
0.26	1081	434
0.29	1054	436
0.41	1023	480
0.52	1008	554
0.59	1006	685
0.74	1005	656
0.81	1004	784
0.85	1002	1030
0.91	993	1169
1.13	988	1272
1.22	960	1334
1.45	964	1395
1.66	927	1456
1.89	940	1444
2.05	909	1476
2.30	899	1484
2.50	864	1497
2.75	861	1479
2.97	822	1481
3.18	788	1526
3.45	779	1534
3.72	742	1537
3.98	705	1517
4.28	698	1559
4.64	655	1539
5.06	589	1541
5.37	582	1575
5.69	534	1601
5.92	502	1605
6.14	458	1682
6.27	447	1724

Particle-Life History, x/d = 255.0, ϕ = 0.870

Time After All Liquid has Evaporated (s)	d_p (μm)	T_p (K)
0.00	947	455
0.15	942	508
0.30	932	634
0.50	924	634
0.90	894	788
1.21	870	990
1.62	835	1229
2.01	826	1389
2.41	801	1471
2.83	771	1525
3.24	717	1594
4.01	687	1617
4.42	665	1635
4.79	629	1653
5.18	582	1677
5.62	552	1699
6.00	515	1737
6.30	471	1796

Particle Life-History, x/d = 297.5, ϕ = 0.761

Time After All Liquid Has Evaporated (s)	d_p (μm)	T_p (K)
0.00	921	461
0.23	916	517
0.41	913	588
0.59	897	807
0.78	881	939
1.01	867	1003
1.23	864	1094
1.38	847	1198
1.64	844	1244
1.81	821	1317
2.03	810	1364
2.37	794	1417
2.80	767	1473
3.21	754	1495
3.63	729	1509
4.03	691	1517
4.42	664	1539
4.77	652	1546
5.20	624	1559
5.81	583	1580
6.43	530	1607
6.84	483	1626
7.15	451	1642
7.41	420	1651
7.78	401	1657

Particle-Life History x/d = 340, ϕ = 0.557

Time (s)	d_p (μm)	T_p (K)
0.00	1081	303
0.04	1080	331
0.10	1077	353
0.13	1067	381
0.18	1048	390
0.22	1006	405
0.31	978	414
0.33	949	415
0.38	915	417
0.41	896	419
0.46	875	423
0.59	874	451
0.70	873	530
0.82	864	621
1.08	843	754
1.31	834	887
1.53	817	989
1.64	805	1074
1.96	796	1231
2.17	779	1264
2.34	763	1339
2.66	750	1384
2.98	723	1421
3.27	702	1487
3.69	665	1517
4.11	642	1545
4.61	601	1562
5.13	557	1597
5.78	498	1645
6.16	450	1669

Particle-Life History, $x/d = 382.5$, $\phi = 484$

Time (s)	d_p (μm)	T_p (K)
0.00	955	302
0.04	955	328
0.10	952	366
0.14	945	385
0.17	936	397
0.21	918	406
0.25	893	410
0.29	865	412
0.33	836	413
0.36	813	413
0.40	781	413
0.45	779	415
0.50	778	453
0.73	774	509
0.93	769	592
1.09	758	659
1.31	755	773
1.63	742	881
1.86	731	921
2.15	725	969
2.37	712	1008
2.54	703	1046
2.92	693	1089
3.33	685	1123
3.79	670	1154
4.31	661	1174
4.69	647	1183
5.17	638	1196
5.53	630	1202
5.97	604	1203
6.42	581	1208
6.87	575	1210
7.35	551	1211
7.74	533	1213
8.38	504	1215
9.71	477	1217
10.38	442	1220

Particle-Life History, $x/d = 467.5$, $\phi = 0.348$

Time (s)	d_p (μm)	T_p (K)
0.00	885	298
0.06	884	334
0.11	882	358
0.15	877	375
0.19	869	387
0.25	848	400
0.31	818	405
0.36	787	407
0.41	757	408
0.47	726	409
0.52	725	408
0.56	725	448
0.90	725	482
1.61	724	532
2.69	724	615
3.97	723	654
5.77	721	719
8.73	719	726
10.88	719	729
13.07	717	731
16.70	714	731
20.95	711	732
24.67	707	733
29.05	704	733
31.73	700	734
36.77	698	735
40.53	694	734

Particle-Life History, x/d = 510.0, ϕ = 0.272

Time (s)	d_p (μm)	T_p (K)
0.00	845.0	295
0.05	845.1	323
0.11	843.2	347
0.20	835.4	376
0.29	815.2	394
0.31	809.7	397
0.40	773.1	402
0.51	720.3	404
0.59	695.5	405
0.68	695.4	439
1.09	695.4	471
1.83	695.4	506
3.88	695.3	586
5.71	695.2	615
8.91	695.1	642
11.46	694.9	645
13.64	694.8	648
17.22	694.6	649
21.11	694.5	650
24.95	694.3	650
29.00	694.2	652
33.17	693.9	651
36.78	693.7	650
40.85	693.6	650

B.2 Data From the Laminar-Premixed Flame Tests

B.2.1 Particle Environment Measurements[A]

Gas Temperature and Composition, $\phi = 0.2$

x (mm)	T (K)	Mole Fraction						
		O_2	CO_2	CO	H_2O	N_2	H_2	OH
10	1667	0.5314	0.0664	--	0.1328	0.2691	--	0.0004
20	1668	0.5314	0.0664	--	0.1328	0.2691	--	0.0004
30	1667	0.5314	0.0664	--	0.1328	0.2691	--	0.0004
40	1667	0.5314	0.0664	--	0.1328	0.2691	--	0.0004
50	1667	0.5314	0.0664	--	0.1328	0.2691	--	0.0004

Gas Temperature and Composition, $\phi = 0.6$

x (mm)	T (K)	Mole Fraction						
		O_2	CO_2	CO	H_2O	N_2	H_2	OH
5	1662	0.0860	0.0637	--	0.1293	0.7208	--	0.0002
10	1663	0.0858	0.0640	--	0.1291	0.7208	--	0.0003
20	1663	0.0858	0.0644	--	0.1291	0.7208	--	0.0003
30	1664	0.0858	0.0644	--	0.1291	0.7208	--	0.0003
40	1663	0.0858	0.0644	--	0.1291	0.7208	--	0.0003
50	1664	0.0858	0.0644	--	0.1291	0.7208	--	0.0003

[A]OH mole fraction was obtained from CEC-72 equilibrium calculation. H_2O mole fraction was obtained from H and O element balances.

Gas Temperature and Composition, $\phi = 0.6$

x (mm)	T (K)	Mole Fraction						
		O_2	CO_2	CO	H_2O	N_2	H_2	OH
10	1810	0.0973	0.0730	0.0001	0.1458	0.6832	--	0.0007
20	1814	0.0973	0.0730	0.0001	0.1458	0.6832	--	0.0007
30	1815	0.0973	0.0730	0.0001	0.1458	0.6832	--	0.0007
40	1814	0.0973	0.0730	0.0001	0.1458	0.6832	--	0.0007
50	1814	0.0973	0.0730	0.0001	0.1458	0.6832	--	0.0007

Gas Temperature and Composition, $\phi = 0.6$

x (mm)	T (K)	Mole Fraction						
		O_2	CO_2	CO	H_2O	N_2	H_2	OH
10	1952	0.1096	0.0822	0.0002	0.1639	0.6425	0.0001	0.0017
20	1954	0.1095	0.0821	0.0002	0.1641	0.6425	0.0001	0.0017
30	1953	0.1096	0.0822	0.0002	0.1639	0.6425	0.0001	0.0017
40	1953	0.1096	0.0822	0.0002	0.1639	0.6425	0.0001	0.0017
50	1953	0.1095	0.0822	0.0002	0.1640	0.6425	0.0001	0.0017

Gas Temperature and Composition, $\phi = 1.0$

x (mm)	T (K)	Mole Fraction						
		O_2	CO_2	CO	H_2O	N_2	H_2	OH
5	1683	0.0002	0.0645	0.0003	0.1295	0.8054	0.0002	0.0001
10	1683	0.0002	0.0645	0.0003	0.1294	0.8054	0.0002	0.0001
20	1684	0.0002	0.0645	0.0003	0.1294	0.8054	0.0002	0.0001
30	1683	0.0002	0.0645	0.0003	0.1295	0.8054	0.0002	0.0001
40	1683	0.0002	0.0645	0.0003	0.1295	0.8054	0.0002	0.0001
50	1683	0.0002	0.0645	0.0003	0.1295	0.8054	0.0002	0.0001
60	1683	0.0002	0.0645	0.0003	0.1295	0.8054	0.0002	0.0001
70	1681	0.0002	0.0645	0.0003	0.1295	0.8054	0.0002	0.0001
80	1678	0.0002	0.0646	0.0003	0.1295	0.8054	0.0002	0.0001
90	1675	0.0002	0.0646	0.0002	0.1295	0.8054	0.0002	0.0001
100	1668	0.0002	0.0646	0.0002	0.1295	0.8054	0.0002	0.0001
110	1665	0.0002	0.0646	0.0002	0.1295	0.8054	0.0002	0.0001
120	1661	0.0002	0.0646	0.0002	0.1295	0.8054	0.0001	0.0001
130	1657	0.0002	0.0646	0.0002	0.1295	0.8054	0.0001	0.0001
140	1648	0.0002	0.0646	0.0002	0.1295	0.8054	0.0001	0.0001
150	1640	0.0001	0.0646	0.0002	0.1295	0.8055	0.0001	0.0001
160	1625	0.0001	0.0646	0.0002	0.1295	0.8055	0.0001	0.0
170	1606	0.0001	0.0647	0.0001	0.1295	0.8055	0.0001	0.0
180	1597	0.0001	0.0647	0.0001	0.1295	0.8055	0.0001	0.0
190	1578	0.0001	0.0647	0.0001	0.1296	0.8055	0.0001	0.0
200	1564	0.0001	0.0647	0.0001	0.1296	0.8055	0.0001	0.0

Gas Temperature and Composition, $\phi = 1.0$

x (mm)	T (K)	Mole Fraction						
		O_2	CO_2	CO	H_2O	N_2	H_2	OH
10	1816	0.0005	0.0722	0.0008	0.1455	0.7805	0.0004	0.0002
20	1819	0.0005	0.0722	0.0008	0.1455	0.7805	0.0004	0.0002
30	1819	0.0005	0.0722	0.0008	0.1455	0.7805	0.0004	0.0002
40	1820	0.0005	0.0722	0.0008	0.1455	0.7805	0.0004	0.0002
50	1819	0.0005	0.0722	0.0008	0.1455	0.7805	0.0004	0.0002
60	1819	0.0005	0.0722	0.0008	0.1455	0.7805	0.0004	0.0002
70	1817	0.0005	0.0722	0.0008	0.1455	0.7805	0.0004	0.0002
80	1817	0.0005	0.0722	0.0008	0.1455	0.7805	0.0004	0.0002
90	1815	0.0005	0.0722	0.0008	0.1455	0.7805	0.0004	0.0002
100	1812	0.0005	0.0722	0.0008	0.1455	0.7805	0.0004	0.0002
110	1809	0.0005	0.0722	0.0007	0.1456	0.7806	0.0004	0.0002
120	1805	0.0005	0.0723	0.0007	0.1455	0.7806	0.0004	0.0002
130	1801	0.0005	0.0723	0.0007	0.1455	0.7806	0.0004	0.0002
140	1793	0.0005	0.0723	0.0006	0.1456	0.7806	0.0003	0.0002
150	1785	0.0009	0.0724	0.0006	0.1456	0.7806	0.0003	0.0002
160	1773	0.0004	0.0724	0.0006	0.1457	0.7806	0.0003	0.0001
170	1754	0.0004	0.0725	0.0005	0.1456	0.7807	0.0003	0.0001
180	1742	0.0003	0.0725	0.0004	0.1458	0.7807	0.0003	0.0001
190	1730	0.0003	0.0726	0.0004	0.1457	0.7808	0.0002	0.0001
200	1718	0.0003	0.0726	0.0004	0.1457	0.7808	0.0002	0.0001

Gas Temperature and Composition, $\phi = 1.0$

x (mm)	T (K)	Mole Fraction						
		O_2	CO_2	CO	H_2O	N_2	H_2	OH
10	1949	0.0013	0.0806	0.0019	0.1641	0.7509	0.0009	0.0006
20	1952	0.0013	0.0806	0.0020	0.1641	0.7509	0.0009	0.0006
30	1953	0.0013	0.0806	0.0020	0.1641	0.7509	0.0009	0.0006
40	1952	0.0013	0.0806	0.0020	0.1641	0.7509	0.0009	0.0006
50	1952	0.0013	0.0806	0.0020	0.1641	0.7509	0.0009	0.0006
60	1951	0.0013	0.0806	0.0019	0.1642	0.7509	0.0009	0.0006
70	1950	0.0013	0.0806	0.0019	0.1642	0.7509	0.0009	0.0006
80	1948	0.0013	0.0806	0.0019	0.1642	0.7509	0.0009	0.0006
90	1946	0.0012	0.0806	0.0019	0.1644	0.7509	0.0009	0.0005
100	1944	0.0012	0.0807	0.0019	0.1643	0.7509	0.0009	0.0005
110	1940	0.0012	0.0807	0.0018	0.1643	0.7510	0.0009	0.0005
120	1935	0.0012	0.0808	0.0018	0.1643	0.7510	0.0008	0.0005
130	1930	0.0011	0.0808	0.0017	0.1644	0.7510	0.0009	0.0005
140	1924	0.0011	0.0809	0.0016	0.1644	0.7511	0.0008	0.0005
150	1913	0.0010	0.0810	0.0015	0.1745	0.7511	0.0007	0.0004
160	1901	0.0010	0.0811	0.0014	0.1645	0.7512	0.0007	0.0004
170	1891	0.0009	0.0812	0.0013	0.1645	0.7512	0.0007	0.0004
180	1879	0.0008	0.0813	0.0012	0.1647	0.0006	0.0006	0.0003
190	1860	0.0008	0.0814	0.0011	0.1647	0.7514	0.0006	0.0003
200	1851	0.0007	0.815	0.0010	0.1648	0.7614	0.0006	0.0003

Gas Temperature and Composition, $\phi = 1.4$

x (mm)	T (K)	Mole Fraction						
		O_2	CO_2	CO	H_2O	N_2	H_2	OH
5	1622	--	0.0421	0.0534	0.1432	0.7092	0.0542	--
10	1624	--	0.0427	0.0540	0.1412	0.7092	0.0563	--
20	1625	--	0.0428	0.0542	0.1409	0.7092	0.0566	--
30	1625	--	0.0428	0.0543	0.1408	0.7092	0.0566	--
40	1624	--	0.0427	0.0542	0.1409	0.7092	0.0566	--
50	1624	--	0.0427	0.0541	0.1410	0.7092	0.0566	--
60	1624	--	0.0428	0.0541	0.1410	0.7092	0.0567	--
70	1621	--	0.0428	0.0541	0.1410	0.7092	0.0566	--
80	1620	--	0.0429	0.0541	0.1408	0.7092	0.0566	--
90	1618	--	0.0430	0.0541	0.1407	0.7092	0.0567	--
100	1612	--	0.0430	0.0540	0.1407	0.7092	0.0568	--
110	1609	--	0.0430	0.0540	0.1406	0.7092	0.0569	--
120	1604	--	0.0431	0.0538	0.1406	0.7092	0.0569	--
130	1601	--	0.0432	0.0537	0.1405	0.7092	0.0571	--
140	1594	--	0.0434	0.0536	0.1403	0.7092	0.0572	--
150	1589	--	0.0435	0.0535	0.1402	0.7092	0.0573	--
160	1570	--	0.0439	0.0532	0.1397	0.7092	0.0577	--
170	1557	--	0.0442	0.0529	0.1394	0.7092	0.0580	--
180	1543	--	0.0444	0.0525	0.1393	0.7092	0.0583	--
190	1522	--	0.0449	0.0520	0.1388	0.7092	0.0588	--
200	1507	--	0.0450	0.0519	0.1387	0.7092	0.0589	--

B.2.2 Particle Measurements

Particle-Life History, $\phi = 0.2$, $T_f \approx 1667$ K

x (mm)	d_p (μm)	m_p (ng)	T_p (K)	Reacted Mass Fraction	Apparent Density (kg/m³)	u_p (m/s)	u_∞ with Particles Present (m/s)	u_∞ without Particles Present (m/s)
0.0	73.4	377.3	604	0.0	1822.2	0.349	0.623	1.478
0.6	73.2	368.5	1267	0.023	1794.3	0.467	0.749	1.494
2.5	66.0	169.6	1451	0.550	1126.7	0.504	0.842	1.510
3.9	60.8	91.7	1559	0.757	779.2	0.526	0.940	1.526
6.0	53.5	35.1	1574	0.907	437.8	0.601	1.038	1.543
7.5	48.7	17.4	1589	0.954	287.7	0.673	1.135	1.559
9.6	42.2	5.95	1597	0.984	151.2	0.723	1.233	1.575
12.9	35.0	1.456	1606	0.996	64.9	0.830	1.323	1.614
13.4	31.1	0.599	1614	0.998	38.0	0.994	1.412	1.654
16.0	24.1	0.089	1617	1.000	12.1	1.049	1.503	1.693
18.1	18.6	0.0133	1619	1.000	3.9	1.132	1.595	1.733
20.2	13.6	0.00123	1625	1.000	0.9	1.242	1.686	2.772
21.9	10.2	0.000144	1630	1.000	0.3	1.407	1.779	1.825
24.2	6.3	0.0000042	1633	1.000	0.03	1.555	1.861	1.877
26.1	3.6	0.0000001	1645	1.000	0.041	1.739	1.924	1.930
27.9	1.2	0.0	1657	1.000	0.0	1.972	1.976	1.983

Particle-Life History, $\phi = 0.6$, $T_E \approx 1663$ K

x (mm)	d_p (μm)	m_p (ng)	T_p (K)	Reacted Mass Fraction	Apparent Density (kg/m³)	u_p (m/s)	u_∞ with Particles Present (m/s)	u_∞ without Particles Present (m/s)
0.0	73.4	377.5	595	0.0	1823.2	0.439	0.613	1.513
2.6	70.6	293.3	2067	0.223	1591.8	0.476	0.707	1.521
3.8	67.6	193.3	2075	0.488	1195.1	0.479	0.839	1.557
5.9	62.2	131.2	2087	0.652	1041.3	0.483	0.942	1.563
7.5	59.0	96.3	2095	0.745	895.5	0.492	1.053	1.597
9.5	54.2	62.5	2100	0.834	749.7	0.501	1.172	1.631
11.8	48.9	37.0	2112	0.902	604.3	0.521	1.253	1.664
13.3	44.7	19.5	2120	0.948	416.7	0.539	1.342	1.697
15.9	38.7	11.4	2112	0.970	375.6	0.551	1.421	1.731
18.2	33.0	6.03	2133	0.984	320.5	0.581	1.497	1.765
19.9	29.5	3.64	2134	0.990	270.8	0.597	1.573	1.799
20.6	26.9	2.34	2145	0.994	229.6	0.657	1.684	1.832
21.7	23.9	1.55	2141	0.996	216.8	0.685	1.762	1.864
23.4	19.8	0.752	2132	0.998	185.0	0.782	1.821	1.887
24.1	17.6	0.333	2139	0.9991	116.7	0.811	1.871	1.903
26.1	12.4	0.0059	2128	0.99998	5.91	0.932	1.918	1.925
27.6	7.65	2×10^{-6}	2126	1.0	0.0085	0.949	1.943	1.949
29.0	4.01	0.0	2110	1.0	0.0	1.007	1.960	1.963
29.5	1.62	0.0	2051	1.0	0.0	1.974	1.975	1.979

Particle-Life History, ϕ = 0.6, $T_f \approx$ 1814 K

x (m)	d_p (μm)	m_p (ng)	T_p (K)	Reacted Mass Fraction	Apparent Density (kg/m³)	u_p (m/s)	u_∞ with Particles Present (m/s)	u_∞ without Particles Present (m/s)
0.0	73.4	377.1	601	0.000	1821.3	0.298	0.404	1.521
2.2	69.2	211.5	2166	0.439	1219.0	0.637	0.753	1.536
3.3	65.9	128.6	2174	0.659	858.2	0.711	0.842	1.550
4.7	61.9	68.6	2182	0.818	552.4	0.777	1.132	1.565
5.5	59.7	47.8	2187	0.873	429.0	0.797	1.195	1.579
7.6	52.6	13.4	2193	0.969	175.9	0.822	1.258	1.594
9.6	46.2	3.68	2195	0.990	71.3	0.839	1.321	1.608
11.7	39.8	0.827	2197	0.998	25.1	0.852	1.384	1.623
13.2	35.5	0.266	2199	0.999	11.4	1.001	1.467	1.663
16.1	27.4	0.0198	2202	1.000	1.8	1.025	1.551	1.705
18.3	21.3	0.00160	2205	1.0	0.316	1.199	1.634	1.743
20.1	16.8	0.00015	2210	1.0	0.0604	1.387	1.721	1.784
21.3	13.9	0.000023	2213	1.0	0.0164	1.442	1.814	1.857
23.2	9.1	0.0000005	2208	1.0	0.00126	1.489	1.584	1.929
24.1	6.9	0.0000003	2174	1.0	0.0	1.544	1.967	2.002
26.2	2.3	0.0000001	2127	1.0	0.0	1.902	2.052	2.074
27.1	0.4	0.0	2012	1.0	0.0	2.131	2.139	2.147

Particle-Life History, $\phi = 0.6$, $T_L \approx 1953$ K

x (mm)	d_p (μm)	m_p (ng)	T_p (K)	Reacted Mass Fraction	Apparent Density (kg/m³)	u_p (m/s)	u_∞ with Particles Present (m/s)	u_∞ without Particles Present (m/s)
0.0	73.4	377.1	603	0.0	1821.3	0.259	0.352	1.464
0.7	72.8	288.6	1828	0.235	1428.6	0.462	0.729	1.501
1.5	69.6	195.5	2233	0.482	1107.4	0.551	0.814	1.518
2.4	65.4	125.5	2246	0.667	856.9	0.632	0.924	1.534
3.4	61.4	98.0	2255	0.740	808.6	0.707	0.977	1.551
4.2	58.2	73.6	2264	0.805	713.0	0.764	1.023	1.568
5.0	55.1	56.2	2272	0.851	641.6	0.782	1.124	1.582
6.0	51.4	40.3	2281	0.893	566.8	0.807	1.246	1.596
7.0	47.8	28.6	2286	0.924	500.1	0.887	1.332	1.610
8.0	44.4	21.7	2289	0.942	473.5	0.913	1.417	1.625
9.0	41.0	15.3	2291	0.959	424.0	0.951	1.502	1.639
10.0	37.8	11.2	2290	0.970	396.0	1.072	1.587	1.653
12.0	31.6	6.01	2289	0.984	363.2	1.115	1.638	1.691
14.0	25.7	3.06	2288	0.992	344.3	1.312	1.689	1.728
16.0	20.0	1.31	2287	0.997	312.7	1.348	1.729	1.752
18.0	14.6	0.475	2276	0.999	291.5	1.645	1.759	1.778
20.0	9.3	0.0191	2231	1.000	45.4	1.702	1.827	1.853
22.0	4.1	0.00016	2195	1.000	4.4	1.883	2.111	2.111
24.0	0.9	0.0	2122	1.000	0.0	2.213	2.416	2.419

Particle-Life History, $\phi = 1.0$, $T_f \approx 1683$ K

x (mm)	d_p (μm)	m_p (ng)	T_p (K)	Reacted Mass Fraction	Apparent Density (kg/m³)	u_p (m/s)	u_∞ with Particles Present (m/s)	u_∞ without Particles Present (m/s)
0.0	73.4	377.1	608	0.000	1821.3	0.439	0.527	1.487
1.9	73.4	373.8	1515	0.0087	1805.3	0.583	0.721	1.508
2.7	73.3	366.2	1601	0.0289	1775.9	0.614	0.854	1.529
4.3	73.2	357.4	1645	0.0522	1740.3	0.665	0.984	1.548
5.6	73.0	344.2	1656	0.0872	1689.8	0.702	1.111	1.572
8.1	72.8	331.0	1660	0.122	1638.5	0.765	1.196	1.592
15.7	72.1	307.5	1661	0.185	1566.9	0.904	1.281	1.690
21.0	71.7	289.5	1660	0.232	1500.0	0.904	1.368	1.799
30.3	71.1	265.3	1661	0.296	1409.7	1.068	1.459	1.901
41.4	70.3	241.2	1661	0.360	1325.9	1.147	1.538	1.970
52.8	69.6	219.4	1661	0.418	1242.8	1.204	1.621	2.051
61.4	68.9	202.7	1661	0.462	1183.6	1.244	1.678	2.129
77.4	68.2	177.2	1660	0.530	1066.9	1.283	1.750	2.209
88.8	67.5	162.3	1661	0.570	1007.9	1.307	1.818	2.288
100.4	66.8	153.0	1661	0.594	980.3	1.343	1.895	2.364
121.1	65.6	140.1	1661	0.628	947.8	1.408	1.952	2.413
138.7	64.6	130.0	1660	0.655	921.0	1.417	2.018	2.460
154.2	63.7	123.2	1661	0.673	910.3	1.429	2.083	2.508
170.9	62.8	113.5	1660	0.699	875.2	1.521	2.148	2.563
184.3	62.1	109.1	1658	0.711	870.1	1.552	2.214	2.613
200.4	61.3	103.1	1651	0.727	854.8	1.558	2.232	2.658

Particle-Life History, $\phi = 1.0$, $T_f \approx 1683$ K

x (mm)	d_p (μm)	m_p (ng)	T_p (K)	Reacted Mass Fraction	Apparent Density (kg/m³)	u_p (m/s)	u_∞ with Particles Present (m/s)	u_∞ without Particles Present (m/s)
0.0	52.6	138.4	603	0.000	1816.3	0.464	0.578	1.489
1.8	52.6	137.1	1630	0.0094	1799.2	0.675	0.759	1.501
3.1	52.4	134.0	1665	0.0318	1778.7	0.752	0.942	1.534
4.1	52.3	128.8	1667	0.0694	1719.5	0.806	0.997	1.546
5.7	52.2	123.8	1667	0.105	1662.3	0.873	1.143	1.574
8.3	51.9	119.6	1667	0.136	1633.9	0.968	1.250	1.599
15.1	51.5	111.7	1668	0.193	1561.8	1.131	1.358	1.682
20.7	51.1	104.4	1667	0.246	1494.3	1.221	1.463	1.782
30.2	50.5	95.3	1667	0.311	1413.3	1.324	1.575	1.894
41.9	49.9	86.2	1668	0.377	1325.0	1.400	1.678	1.982
51.7	49.4	77.6	1667	0.439	1229.4	1.442	1.750	2.043
63.7	48.7	71.0	1666	0.487	1174.0	1.475	1.825	2.128
74.5	48.2	61.9	1667	0.553	1055.7	1.495	1.901	2.178
86.1	47.6	56.5	1668	0.592	1000.5	1.509	1.992	2.257
100.9	46.8	52.1	1668	0.624	970.7	1.521	2.054	2.369
118.7	45.9	47.6	1668	0.656	940.1	1.530	2.130	2.407
135.6	45.1	44.1	1667	0.681	918.1	1.542	2.207	2.452
151.2	44.3	39.7	1667	0.713	872.1	1.557	2.282	2.499
168.9	43.4	35.4	1666	0.744	827.1	1.584	2.354	2.532
183.2	42.6	31.5	1664	0.772	778.2	1.597	2.402	2.606
199.1	41.8	26.5	1662	0.809	693.0	1.602	2.427	2.654

Particle-Life History, $\psi = 1.0$, $T_f \approx 1683$ K

x (mm)	d_p (μm)	m_p (ng)	T_p (K)	Reacted Mass Fraction	Apparent Density (kg/m³)	u_p (m/s)	u_∞ with Particles Present (m/s)	u_∞ without Particles Present (m/s)
0.0	28.7	22.5	600	0.000	1817.8	0.562	0.592	1.485
1.8	28.6	22.1	1670	0.0178	1804.2	0.952	1.154	1.501
3.2	28.5	21.8	1674	0.0311	1789.6	1.096	1.212	1.518
4.1	28.4	20.5	1674	0.0889	1709.2	1.168	1.347	1.542
5.7	28.3	19.7	1674	0.124	1660.0	1.263	1.479	1.568
8.3	28.1	18.8	1675	0.164	1618.2	1.372	1.521	1.598
15.1	27.8	17.7	1674	0.213	1573.4	1.523	1.632	1.682
20.8	27.5	16.2	1675	0.280	1487.7	1.581	1.652	1.797
30.2	27.0	14.6	1675	0.351	1416.7	1.622	1.684	1.900
38.0	26.6	12.9	1675	0.427	1309.0	1.636	1.705	1.949
49.3	26.0	11.2	1675	0.502	1217.0	1.642	1.800	2.026
61.2	25.4	10.0	1675	0.556	1165.5	1.651	1.893	2.113
74.5	24.8	8.42	1676	0.626	1054.3	1.663	1.987	2.181
86.1	24.2	7.44	1675	0.669	1002.6	1.675	2.079	2.254
100.9	23.5	5.71	1675	0.746	840.3	1.684	2.173	2.332
118.7	22.7	4.21	1676	0.813	687.4	1.697	2.266	2.394
135.6	21.9	3.11	1676	0.862	565.5	1.703	2.359	2.497
151.2	21.2	2.21	1676	0.902	443.0	1.711	2.449	2.486
168.7	20.4	1.58	1677	0.930	355.4	1.719	2.482	2.551
183.3	19.7	1.10	1677	0.951	274.8	1.727	2.506	2.601
199.7	19.0	0.80	1677	0.964	222.8	1.735	2.531	2.656

Particle-Life History, ϕ = 1.0, T_f = 1683 K

x (mm)	d_p (μm)	m_p (ng)	T_p (K)	Reacted Mass Fraction	Apparent Density (kg/m³)	u_p (m/s)	u_∞ with Particles Present (m/s)	u_∞ without Particles Present (m/s)
0.0	10.5	1.10	602	0.000	1814.8	0.601	0.942	1.487
1.8	10.4	1.04	1680	0.0545	1765.8	1.387	1.487	1.502
3.2	10.3	1.01	1680	0.0818	1765.3	1.428	1.499	1.516
4.1	10.3	0.983	1680	0.106	1718.1	1.487	1.529	1.542
5.7	10.2	0.954	1680	0.133	1716.9	1.516	1.551	1.576
6.5	10.1	0.899	1680	0.183	1666.5	1.542	1.583	1.597
8.3	10.0	0.847	1680	0.230	1617.7	1.639	1.661	1.682
15.1	9.7	0.748	1680	0.320	1565.3	1.758	1.783	1.792
20.8	9.4	0.621	1680	0.435	1427.9	1.868	1.887	1.901
30.2	9.0	0.540	1681	0.509	1414.7	1.941	1.958	1.965
41.0	8.6	0.416	1680	0.622	1249.1	2.014	2.024	2.031
51.3	8.3	0.343	1680	0.688	1145.7	2.027	2.032	2.040
61.2	7.9	0.278	1680	0.747	1076.9	2.101	2.109	2.113
74.5	7.6	0.227	1680	0.794	987.6	2.200	2.208	2.211
86.1	7.4	0.205	1680	0.814	966.2	2.258	2.265	2.269
100.7	7.2	0.187	1681	0.830	956.9	2.361	2.368	2.370
113.7	6.9	0.153	1680	0.861	889.5	2.398	2.404	2.407
136.7	6.7	0.117	1680	0.894	743.0	2.444	2.448	2.452
151.0	6.6	0.0932	1681	0.915	619.1	2.480	2.484	2.489
163.4	6.3	0.0640	1681	0.942	488.8	2.543	2.548	2.551
184.1	6.1	0.0377	1681	0.966	317.2	2.597	2.608	2.611
199.8	5.9	0.0223	1681	0.980	207.4	2.614	2.643	2.654

Particle-Life History, $\phi = 1.0$, $T_f \approx 1819$ K

x (mm)	d_p (μm)	m_p (ng)	T_p (K)	Reacted Mass Fraction	Apparent Density (kg/m³)	u_p (m/s)	u_∞ with Particles Present (m/s)	u_∞ without Particles Present (m/s)
0.0	73.4	377.4	606	0.000	1822.7	0.299	0.413	1.513
1.9	73.2	365.5	1717	0.032	1779.7	0.479	0.767	1.533
3.0	72.9	350.8	1763	0.070	1729.3	0.533	0.851	1.553
4.4	72.4	327.7	1768	0.132	1649.2	0.589	1.097	1.572
7.5	71.6	293.1	1768	0.223	1525.0	0.687	1.185	1.594
10.6	70.8	261.7	1769	0.307	1408.3	0.765	1.274	1.612
13.7	70.0	233.8	1769	0.380	1301.8	0.829	1.363	1.677
17.1	69.3	211.7	1769	0.439	1214.8	0.889	1.451	1.748
22.4	68.3	182.6	1770	0.516	1094.6	0.962	1.539	1.814
30.3	66.8	146.8	1771	0.611	940.6	1.051	1.663	1.920
39.7	65.2	115.3	1771	0.694	794.5	1.128	1.783	2.030
50.2	63.5	88.7	1772	0.765	661.6	1.193	1.912	2.134
62.1	61.7	66.8	1773	0.823	543.2	1.249	2.036	2.211
75.6	59.7	47.5	1774	0.874	426.4	1.297	2.092	2.285
89.3	57.8	34.3	1775	0.909	339.2	1.495	2.160	2.360
103.4	56.3	26.4	1775	0.930	282.5	1.542	2.226	2.432
120.7	53.8	16.9	1776	0.955	207.3	1.632	2.292	2.467
139.2	51.6	11.4	1777	0.970	158.5	1.700	2.359	2.507
161.3	49.1	6.74	1778	0.982	108.7	1.741	2.427	2.548
180.4	47.0	4.37	1775	0.988	80.4	1.860	2.494	2.591
200.2	45.1	2.88	1771	0.992	60.0	2.183	2.549	2.625

Particle-Life History, $\phi = 1.0$, $T_f \approx 1952$ K

x (mm)	d_p (μm)	m_p (ng)	T_p (K)	Reacted Mass Fraction	Apparent Density (kg/m³)	u_p (m/s)	u_∞ with Particles Present (m/s)	u_∞ without Particles Present (m/s)
0.0	73.4	376.9	599	0.0	1820.3	0.260	0.304	1.543
1.9	72.7	323.2	1848	0.142	1606.5	0.45	0.561	1.567
2.6	72.2	300.6	1855	0.202	1525.4	0.487	0.784	1.582
4.4	71.0	252.9	1857	0.329	1349.5	0.564	0.997	1.618
5.7	70.2	227.1	1858	0.397	1253.7	0.611	1.142	1.645
8.2	68.8	189.0	1859	0.499	1108.4	0.687	1.232	1.665
15.8	65.1	133.2	1862	0.647	922.1	0.858	1.396	1.812
24.2	61.7	108.2	1865	0.713	879.8	0.986	1.560	1.971
35.8	58.0	60.7	1867	0.839	594.2	1.351	1.726	2.129
47.2	55.1	31.5	1870	0.916	359.6	1.682	1.889	2.285
58.3	52.8	24.3	1872	0.936	315.3	2.082	2.212	2.435
70.1	48.4	16.8	1873	0.955	283.0	2.291	2.378	2.547
80.0	47.0	13.4	1874	0.964	246.5	2.441	2.512	2.682
90.2	44.8	9.27	1874	0.975	196.9	2.651	2.721	2.814
100.2	42.6	6.38	1874	0.983	157.6	2.757	2.801	2.927
120.4	39.6	3.69	1873	0.990	113.5	2.861	2.887	2.940
140.3	36.0	1.82	1870	0.995	74.5	2.864	2.892	2.956
159.1	33.8	1.13	1868	0.997	55.9	2.868	2.903	2.973
180.7	30.8	0.59	1865	0.998	38.6	2.869	2.922	2.989
200.3	29.4	0.39	1861	0.999	29.3	2.870	2.954	3.001

Particle-Life History, $\phi = 1.0$, $T_f \approx 1952$ K

x (mm)	d_p (μm)	m_p (ng)	T_p (K)	Reacted Mass Fraction	Apparent Density (kg/m³)	u_p (m/s)	u with Particles Present (m/s)	u without Particles Present (m/s)
0.0	52.6	138.7	604	0.000	1820.2	0.381	0.462	1.549
1.8	51.9	117.0	1875	0.156	1598.4	0.607	0.704	1.561
2.6	51.4	103.6	1877	0.253	1457.0	0.661	0.821	1.591
4.4	50.4	89.6	1878	0.354	1336.7	0.760	1.004	1.617
5.7	49.7	79.1	1879	0.430	1230.6	0.822	1.157	1.647
8.1	48.6	65.2	1880	0.530	1084.8	0.915	1.264	1.661
15.7	45.4	45.3	1883	0.673	924.6	1.121	1.759	1.808
23.1	42.7	32.0	1887	0.769	785.0	1.249	1.857	1.963
35.9	38.5	19.2	1891	0.862	642.6	1.372	1.953	2.132
47.1	35.9	11.5	1895	0.917	474.7	1.487	2.055	2.281
58.3	34.1	6.7	1897	0.952	322.7	1.597	2.151	2.435
69.9	31.3	2.87	1898	0.979	178.8	1.721	2.249	2.539
80.4	29.5	1.84	1899	0.987	136.9	1.834	2.320	2.687
90.4	27.4	1.03	1900	0.993	95.6	1.947	2.391	2.818
100.3	25.2	0.57	1899	0.996	68.0	2.060	2.464	2.928
120.1	21.6	0.175	1899	0.999	33.2	2.173	2.538	2.936
140.7	18.1	0.047	1894	1.000	15.1	2.285	2.612	2.961
159.9	15.8	0.0169	1890	1.000	8.2	2.398	2.681	2.977
179.8	13.7	0.0058	1882	1.000	4.3	2.511	2.755	2.981
200.5	12.1	0.0023	1841	1.000	2.5	2.624	2.826	2.998

Particle-Life History, $\phi = 1.0$, $T_f \approx 1952$ K

x (mm)	d_p (μm)	m_p (ng)	T_p (K)	Reacted Mass Fraction	Apparent Density (kg/m³)	u_p (m/s)	u_∞ with Particles Present (m/s)	u_∞ without Particles Present (m/s)
0.0	26.3	17.3	597	0.000	1816.3	0.486	0.521	1.549
1.8	25.3	11.0	1913	0.364	1297.3	0.949	1.124	1.561
2.6	24.9	9.4	1913	0.457	1162.9	1.044	1.231	1.592
4.4	24.1	8.7	1914	0.497	1187.1	1.208	1.300	1.618
5.7	23.6	8.0	1915	0.538	1162.4	1.293	1.379	1.645
8.2	22.6	6.3	1917	0.636	1042.4	1.408	1.451	1.665
10.4	21.7	5.0	1918	0.711	934.5	1.478	1.526	1.707
15.4	19.8	3.1	1924	0.821	762.7	1.542	1.598	1.803
23.1	17.3	1.5	1926	0.913	553.3	1.698	1.714	1.963
35.8	14.4	0.53	1927	0.969	339.0	1.812	1.836	2.129
47.2	12.6	0.12	1929	0.993	114.6	1.901	1.959	2.282
58.1	11.6	0.034	1931	0.998	41.6	2.013	2.081	2.431
70.4	9.5	0.0089	1932	0.999	19.8	2.145	2.203	2.549
80.0	8.7	0.0042	1934	1.000	12.2	2.267	2.323	2.682
90.4	7.6	0.0017	1935	1.000	7.4	2.390	2.445	2.811
100.1	6.6	0.00072	1936	1.000	4.8	2.512	2.567	2.926
120.1	5.0	0.00031	1938	1.000	4.7	2.634	2.687	2.938
139.5	3.9	0.000092	1937	1.000	3.0	2.756	2.809	2.949
160.1	2.6	0.000024	1930	1.000	2.6	2.881	2.928	2.978
180.4	1.6	0.000004	1911	1.000	1.9	2.887	2.937	2.989
200.1	1.1	0.000001	1872	1.000	1.4	2.889	2.952	3.000

Particle-Life History, $\phi = 1.0$, $T_f \approx 1952$ K

x (mm)	d_p (μm)	m_p (ng)	T_p (K)	Reacted Mass Fraction	Apparent Density (kg/m³)	u_p (m/s)	u_∞ with Particles Present (m/s)	u_∞ without Particles Present (m/s)
0.0	10.2	1.01	598	0.000	1817.7	0.517	0.834	1.543
1.8	9.3	0.56	1940	0.446	1329.7	1.518	1.534	1.561
2.4	9.0	0.42	1940	0.584	1100.3	1.583	1.586	1.588
4.4	8.4	0.30	1940	0.703	966.7	1.607	1.612	1.618
5.7	7.7	0.11	1941	0.891	460.2	1.642	1.643	1.645
8.2	6.8	0.07	1941	0.931	425.2	1.663	1.664	1.665
10.3	6.2	0.02	1942	0.980	160.3	1.201	1.204	1.705
15.8	4.9	0.007	1943	0.993	113.6	1.804	1.808	1.812
23.2	3.8	0.002	1946	0.998	69.6	1.951	1.961	1.965
36.2	2.6	0.005	1997	1.000	54.3	2.131	2.135	2.138
47.1	1.8	0.000002	1949	1.000	0.7	2.278	2.280	2.283
58.4	1.4	0.000001	1951	1.000	0.7	2.431	2.434	2.437
70.2	1.0	0.0	1950	1.000	0.0	2.542	2.545	2.547
80.0	0.61	0.0	1947	1.000	0.0	2.679	2.680	2.682
90.1	0.41	0.0	1945	1.000	0.0	2.809	2.809	2.819
99.9	0.24	0.0	1942	1.000	0.0	2.879	2.922	2.924
120.1	0.06	0.0	1932	1.000	0.0	2.883	2.936	2.938

Particle-Life History, $\phi = 1.4$, $T_f \approx 1624$ K

x (mm)	d_p (μm)	m_p (ng)	T_p (K)	Reacted Mass Fraction	Apparent Density (kg/m³)	u_p (m/s)	u_∞ with Particles Present (m/s)	u_∞ without Particles Present (m/s)
0.0	73.4	376.9	592	0.000	1820.3	0.365	0.601	1.527
1.1	72.9	354.2	1613	0.060	1746.1	0.469	0.752	1.551
3.0	72.7	342.7	1627	0.091	1703.4	0.551	0.881	1.576
4.9	72.6	337.9	1627	0.103	1686.5	0.616	0.979	1.598
7.9	72.3	323.7	1627	0.141	1635.8	0.702	1.042	1.627
10.0	72.1	315.6	1627	0.163	1608.2	0.752	1.133	1.647
13.9	71.8	302.5	1627	0.197	1560.8	0.826	1.224	1.727
18.7	71.5	289.9	1628	0.231	1514.7	0.900	1.314	1.815
25.2	71.1	269.6	1629	0.285	1432.6	0.978	1.405	1.901
31.1	70.7	259.1	1626	0.313	1400.3	1.034	1.496	1.988
40.7	70.3	244.4	1627	0.352	1343.5	1.105	1.566	2.071
51.1	69.7	224.8	1627	0.404	1267.9	1.160	1.631	2.110
62.2	69.2	208.7	1628	0.446	1202.8	1.206	1.702	2.156
68.5	68.9	199.6	1630	0.470	1165.5	1.227	1.774	2.203
75.2	68.6	191.8	1631	0.491	1134.7	1.245	1.845	2.243
87.4	68.0	176.7	1632	0.531	1073.3	1.262	1.912	2.319
100.1	67.3	158.9	1634	0.578	995.6	1.281	1.984	2.385
121.2	66.3	137.4	1636	0.635	900.4	1.293	2.054	2.457
140.3	65.2	115.4	1637	0.694	795.2	1.299	2.123	2.538
179.7	63.1	83.7	1630	0.778	636.3	1.310	2.198	2.618
200.4	62.0	69.9	1627	0.815	560.1	1.315	2.263	2.691

VITA

Gerald A. Szekely, Jr. was born February 13, 1956, in Pittsburgh PA. He graduated in November of 1978 from The Pennsylvania State University, with a B. S. degree in Mechanical Engineering. From December 1978 to February 1981, the author was a Graduate Assistant with the Department of Mechanical Engineering of The Pennsylvania State University. From March 1981, to the present he has been employed as a Research Assistant by the Departments of Mechanical Engineering and Applied Research Laboratory of The Pennsylvania State University. He recieved a M. S. degree in Mechanical Engineering from The Pennsylvania State University, March 1980. The author is a member of Sigma Xi.

DISTRIBUTION LIST FOR TM 81-253

Commander (NSEA 0342)
Naval Sea Systems Command
Department of the Navy
Washington, DC 20362   Copies 1 and 2

Commander (NSEA 9961)
Naval Sea Systems Command
Department of the Navy
Washington, DC 20362   Copies 3 and 4

Defense Technical Information Center
5010 Duke Street
Cameron Station
Alexandria, VA 22314   Copies 5 through 10